Shock tube determination of the heat conductivity of non-ionized and partially ionized argon

Please check the document version of this publication:

SHOCK TUBE DETERMINATION OF THE HEAT CONDUCTIVITY OF NON-IONIZED AND PARTIALLY IONIZED ARGON

PROEFSCHRIFT

TER VERKRIJGING VAN DE GRAAD VAN DOCTOR IN DE
TECHNISCHE WETENSCHAPPEN AAN DE TECHNISCHE
HOGESCHOOL EINDHOVEN, OP GEZAG VAN DE RECTOR
MAGNIFICUS, PROF. IR. J. ERKELENS, VOOR EEN
COMMISSIE AANGEWEZEN DOOR HET COLLEGE VAN
DEKANEN IN HET OPENBAAR TE VERDEDIGEN OP
VRIJDAG 27 FEBRUARI 1981 TE 16.00 UUR
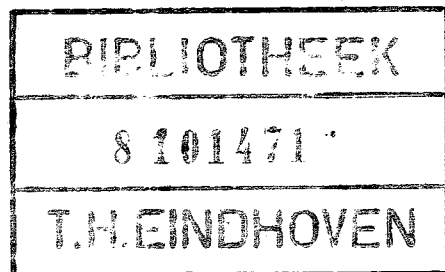
DOOR

AVRAHAM HIRSCHBERG

GEBOREN TE REHOVOT

DIT PROEFSCHRIFT IS GOEDGEKEURD

DOOR DE PROMOTOREN

Prof.Dr.Ir. G.Vossers

en

Prof.Dr.Ir. P.P.J.M.Schram

CO-PROMOTOR

Dr.Ir. M.E.H.van Dongen

STELLINGEN
A.Hirschberg
27 februari 1981

1. The use of a detailed atomic model by Katsonis for the
   development of a collision radiation model is overdone
   in view of the fact that the escape factors are assumed
   to be independent of the state of the plasma and that the
   influence of micro-fields on the atomic structure is
   neglected.

   Katsonis,K.
   Thèse Univ.Paris Sud, Centre d'Orsay(1976).

2. In the two step collision-radiation model of Hoffert and
   Lien the reaction rate for three body recombination by
   atom-ion-electron collisions depends only on the heavy
   particle temperature. However, this reaction rate depends
   certainly both on the electron- and heavy particle
   temperatures.

   Hoffert,M.I. and Lien,M.
   Phys.Fluids,10(1967)1769.

3. The hypothesis of Tumakayev and Lazovskaya that the waviness
   in the electron density profile after ionization relaxation
   behind a shock wave in Xenon is due to associative ionization,
   is contradicted by the experimental results of Glass and Liu
   showing that this effect depends on the shock tube diameter.

   Tumakayev,G.K. and Lazovskaya,V.R.
   proc.int.symp.: Phen.Ion.Gases(1967).
   Glass,I.I. and Liu,W.S.
   J.Fluid Mech.,84(1978)55.

4. The procedure of Asinovsky for the determination of the
   molecular contribution to the heat conductivity of a plasma
   from measurements in electric discharges with various diameters
   does not take the influence of the diameter of the discharge
   on the departure of the state of the plasma from local
   thermodynamic equilibrium into account. This may induce
   significant systematic errors in the heat conductivity data.

   Asinovsky,E.I.,Kirillin,A.V.,Pakhomov,E.P. and
   Shubashov,V.I., proc. IEEE,59(1971)592.

5. The statement of Mitchner and Kruger that the electron heat
   conductivity of an atmospheric argon plasma at low degrees
   of ionization calculated by means of the Frost-mixture rule
   is more accurate than the twelfth approximation in the Sonine
   polynomial expansion of the Chapman-Enskog procedure is not
   valid for the temperature range in which the Frost-value is
   lower than the twelfth approximation, because as demonstrated
   by Ferziger and Kaper the successive approximations converge
   monotonically towards an upper limit which is the exact value.

   Mitchner,M. and Kruger,C.H. Jr
   "Partially ionized gases",J.Wiley&Sons(1973).
   Ferziger,J.H. and Kaper,H.G.
   "Mathematical theory of transport processes in gasses"
   North Holland pub.cie(1972).

6. The procedure of Kicska and Smith for the experimental determination of the condensation coefficient by means of the formula of Schrage is based on the assumption that the condensation rate is determined by gas kinetic effects. However in the experimental conditions described the condensation rate appears to be determined by the heat transfer rate towards the wall.

> Kicska,P.A. and Smith,W.R.
> J.Chem.Phys.,$\underline{47}$(1967)1418.

7. The recovery factor of a shielded total temperature probe such as designed by Winkler depends strongly on the instationary flow phenomena inside the probe. Measurements with such probes are therefore unreliable.

> Winkler,E.M.
> NAVORD 3834(1954).

8. De vraag van Schweers en van Vianen om de vorm te construeren van een lopende golf in een vrij hangend vertikaal touw kan niet op basis van de in het boek behandelde stof worden beantwoord.

> Vraagstuk 4 van paragraaf 6.6 in:
> Schweers,J. en van Vianen,P.
> "Natuurkunde op corpusculaire grondslag"
> Deel 3 V, vierde druk,Mamberg Den Bosch(1973).

9. Belgen-moppen zijn niet onschadelijk. Deze moppen veroorzaken vooral bij kinderen in Nederland een vertekend beeld van de Belgische samenleving.

CONTENTS

ABSTRACT

A procedure for the determination of the heat conductivity of a monatomic gas, from measurements of the structure of the unsteady thermal boundary layer at the end-wall of a shock tube, is proposed.

In the non-ionized case the structure of the boundary layer determined by means of laser schlieren measurements appears to be self-similar. Improved analysis of the schlieren data and accurate pressure measurements yield heat conductivity data with an accuracy of 4% for temperatures up to 7000 K (argon, pressure 3×10^4 Pa to 10^5 Pa). There are still systematic errors of a few percent, due to the influence of side-wall boundary layers and to the simplifications in the procedure for the determination of the state of the gas outside the boundary layer.

In the ionized case a model for the development of the thermal boundary layer is proposed. The processes of ionization and thermal relaxation are considered. Experimental data on the electron and atom density profiles obtained from laser schlieren measurements agree within 10% with theory for a moderate degree of ionization (3%). At a higher degree of ionization the structure of the boundary layer is dominated by the influence of radiative cooling, which has been neglected in the model. Quantitative information on radiative cooling is obtained from absorption and pressure measurements outside the boundary layer. A considerable improvement of the accuracy of the measurements is still necessary in order to obtain quantitative information on the heat conductivity in the ionized case.

Additional experiments carried out in a 99.5% Ar + 0.5% H_2 mixture yield experimental information on the influence of ionization relaxation on the structure of the boundary layer and data on the ionization rate of hydrogen by collisions with argon atoms.

I.   INTRODUCTION

I.a.   Goal of the present study

Using a conventional shock tube one can generate for a period
of time of the order of magnitude of one millisecond a well defined
almost stagnant and approximately uniform high enthalpy gas.
This situation is achieved almost instantaneously after the reflection
of the so called incident shock wave at the end-wall of the tube.
The region of high enthalpy between the end-wall and the reflected
shock wave, the reflected shock region, is often used as a gas
reservoir for molecular beam devices (Thor 78, Teshima 79) and
hypersonic blow down tunnels (Oertel 73). For spectroscopic studies
the reflected shock region is used as a light source (Volkov 78,
Wilkerson 71). The reflected shock region is also well suited for
among others the studies of relaxation and transport phenomena in
gases at high temperatures (Baganoff 65, Smeets 65, Saxena 72).

The main research effort of the shock tube group of the
Laboratory for Fluid Dynamics and Heat Transfer of the Department of
Physics (Eindhoven University of Technology) has been directed to the
study of the transport properties of gases at high temperatures
(Jongen 71, Vrugt 76, Hutten-Mansfeld 76, van Dongen 78). The present
investigation is dedicated to the study of heat conductivity of
atmospheric argon in the temperature range $10^3 - 12 \times 10^3 K$.

In the past many attemps have been made to obtain quantitative
information on the heat conductivity of non-ionized gases by means of
shock tube experiments. Such studies were based on the investigation
of the end-wall thermal boundary layer. This boundary layer is
induced by the heat flux from the hot gas to the wall. The analysis
of the flow is simplified by the fact that viscous effects are
negligible. The boundary layer structure is well described by a
one-dimensional model if the tube cross section is large enough
compared to the boundary layer thickness. In the non-ionized case for
a : monatomic gas such as argon, when the heat conductivity is known as
a function of the temperature, the boundary layer structure is easily
calculated numerically. The inverse problem of obtaining information
on the heat conductivity of the gas from experimental data depends

strongly on the type of measurements considered.

From the reviews in the studies of Saxena (72) and Vrugt (76) one can conclude that heat flux measurements at the end-wall will not provide accurate data at high temperatures. The alternative of optical measurements of the boundary layer structure has not yielded any better result so far (Vrugt 76). However the shock tube method is to our knowledge the only source of experimental data on the heat conductivity of non-ionized gases above 2500 K. It is therefore worthwhile to improve this method.

In the case of partially ionized gases most of the data on transport properties have been obtained from the analysis of electric arc measurements (Emmons 67, Asinovsky 71, Kopainsky 71). There is still some discrepancy between the theory and the experimental data (Devoto 73).
The behaviour of the transport properties at high pressures, when a deviation from the ideal plasma behaviour is expected, is not well understood (Devoto 73). Independent shock tube data would be useful. Summarizing we can state that the main goal of our present study is to improve the shock tube method for measurement of the heat conductivity of gases at high temperatures.

We limited our investigation to experiments with argon. Reasons for this choice are:
Argon is a relatively cheap noble gas available at high degrees of purity. The use of a noble gas in the non-ionized case avoids complications due to the influence of internal degrees of freedom of the molecules. Argon has been extensively studied (Devoto 73, Aziz 77). The use of argon provides therefore an excellent test case for the shock tube method.

In the next sections we give a review of papers related to our study. In the last section of this introduction we give an outline of the present work.

I.b.   Review of recent studies of the heat conductivity of argon.

     The thermal conductivity of non-ionized argon can be calculated, on the basis of the kinetic theory of gases, starting from the intermolecular potential. Knowledge about the intermolecular potential on its turn, can be obtained from the analysis of spectroscopic data, studies of real gas effects, molecular beam measurements and data on the transport properties. In a recent review of Aziz and Chen (77) various expressions for the intermolecular potential are compared with experimental data. A particular feature of this study is that the thermal conductivity data are used in order to select an optimal expression. The data considered are those of Haarman (71) in the temperature range 328-468 K and those of Chen and Saxena (75) in the range 350-2500 K. The data of Chen (75) have also been used by Jain (80) in order to select optimal values for the parameters of a Lennard-Jones potential.

     Haarman (71), using the "transient hot wire" method, determined the thermal conductivity of argon with an accuracy of $\pm$ 0.3 %, which has been confirmed by de Groot (74) and Nieto de Castro (78).

     Chen and Saxena (75) used the "hot wire thermal diffusion column" method. They claim an accuracy of $\pm$ 1.5 %. Their data agree within 2 % with the independent data of Springer (73) and Shashkov (78), obtained with the same experimental method.

     The data of Chen and Saxena (75) are in agreement with the equivalent viscosity data. The results of Haarman (71) are not in agreement with the viscosity of Kestin (72). According to Aziz and Chen (77), the data of Haarman (71) are more reliable than the viscosity data.

     For temperatures above 2500 K, in the non-ionized case, all experimental data available have been obtained by means of shock tube experiments. A review of these studies is given in the next section. It appears that the uncertainty in these data is of the order of 10 %.

     The theory and experimental data for transport properties of partially ionized argon, in absence of magnetic field, have been reviewed by Devoto (73). The heat conductivity of a plasma consists of separate contributions from:
heavy particles, electrons, radiation and chemical reactions.

Below 7000 K the heat conductivity of atmospheric argon is almost exclusively due to heavy particles. In the range $10^4 - 1.5 \times 10^4$K the heavy particle, electron and reactive contributions are of the same order of magnitude. Above 1.5×10^4 K radiative heat conductivity is dominant.

The radiative heat conductivity is that part of the radiative contribution to the heat flux which is proportional to the temperature gradient. Such a model assumes that radiation is almost in equilibrium with the plasma. The radiative heat conductivity calculated with a Rosseland model (Vincenti 65) is roughly inversely proportional to the pressure and increases exponentially with the temperature (Kopainsky 71). The radiative energy transport which is not taken into account in the heat conductivity depends on the integral state of the plasma. A study of the influence of this effect on the analysis of electric arc data is given by Asinovsky (71).

In the low temperature range when radiative heat conductivity is negligible radiation escape can induce significant deviation of the state of the plasma from local thermodynamic equilibrium (Uhlenbusch 71, Biberman 71, Leclair 77, Rosado 79).

The reactive heat conductivity takes the influence of diffusion on the heat transfer into account. This approach is valid when the plasma is in a state close to local thermodynamic equilibrium if the pressure is uniform. In such a case the density gradient can explicitly be expressed into a temperature gradient by equilibrium relations.

The molecular heat conductivity is determined by the electrons, ions and atoms in the ground state. Due to the large mass ratio between the electrons and the heavy particles the two heat conductivities can be treated as independent.

A second order approximation in the first order Chapman Enskog theory should predict the heavy particle heat conductivity within 12 % (Devoto 73). Simplified formulas with a comparable accuracy are given by Capitelli (72).

In the fully ionized limit, when electron-ion collisions are dominant, the electron heat conductivity can be calculated by using the theory of Spitzer (53).

A third approximation in the first order Chapman-Enskog approximation yields a result which is 1 % lower than the result of Spitzer (53).

10

In the case of weak ionization when electron neutral collisions are dominant the Chapman-Enskog procedure fails to converge (Kruger 68). In order to overcome this problem Kruger (68) proposed a semi-empirical formula which has the mathematical form of the heat conductivity in the Lorentzian limit.
A similar approach is used by Devoto (73). Alternative mixture rules based on mean free path considerations are not better than an order of magnitude estimate (Mitchner 73).
At high electron densities and low temperatures additional uncertainties are due to the deviation of the gas from an ideal plasma behaviour (Itikawa 63, Williams 69, Daybelge 70, Luchina 78, Mondt 77).

The theory of Devoto (73) for a plasma in local thermodynamic equilibrium shows a discrepancy of about 30 % with the experimental data for atmospheric argon. This discrepancy might be significant.

Summarizing we conclude that data with an inaccuracy of a few percent can be expected to be useful in the non-ionized regime to improve the present knowledge of the intermolecular potential of argon.
In the partially ionized regime measurements with an inaccuracy of less than 30 % would be useful.

I.c.   Review of shock tube studies of the heat conductivity of

         non-ionized argon.

         The shock tube method for determination of the heat
conductivity of gases, by means of heat flux measurements at the
gas-wall interface, has been first used by Smiley (57).
The possibility of determining the heat conductivity of high
temperature gases by means of interferometric measurements of the
structure of the end-wall boundary layer was considered for the first
time by Smeets (65).
         Extensive reviews up to 1975 are given in the studies of
Saxena (72) and Vrugt (76). From those two studies it appears clearly
that the measurement of the heat flux at the end-wall will not yield
accurate information on the heat conductivity of gases at high
temperatures. The main reason for this is that although the heat flux
at the end-wall is an integral effect depending on the whole boundary
layer structure it appears to be mainly determined by the cold gas
layer close to the wall. This effect has been clearly demonstrated by
Lauver (64),who showed that variations of 20 % in the heat
conductivity at high temperatures would induce changes of only 2 % in
the heat flux at the wall. Optical methods yielding information on
the structure of the boundary layer in the high temperature region are
expected to be more sensitive to the heat conductivity behaviour at
corresponding temperatures.
         Interferometric studies of the boundary layer structure have
been performed by Smeets (65), Bunting (67), Kuiper (68) and Ewald
(71). The work of Ewald (71) is particularly interesting as it is an
attempt to obtain heat conductivity data by using the energy equation
directly.
This approach has the great advantage that no assumption has to be
made on the functional dependence of the heat conductivity on the
temperature. The results however show a scatter of 20 %. An important
problem is that the convective velocity cannot be obtained accurately
from the interferometric data. This is due to the fact that the
measurements close to the wall become rather inaccurate as a result
of diffraction and reflection of the light against the wall.
Vrugt (76) improved the method of Ewald (71) by making use of a self

similarity property of the boundary layer structure. This implies
that from measurements of the spatial gradient of the density at a
fixed position from the end-wall as a function of time one can obtain
an estimate of the time derivatives of the density.

Vrugt (76) measured the density profile of the boundary layer by
means of the laser schlieren method introduced by Kiefer (66)
This method appears to yield data with a high degree of
reproducibility (4 %). However the corresponding results for the heat
conductivity, based on theoretically determined convective velocities,
appear to be about 8 % lower than the data of Chen and Saxena (75).
(see previous section). In spite of Vrugt's considerable improvement
of the method we therefore had to reconsider the procedure in detail.
This is described in chapter II.

I.d.   Determination of the heat conductivity of partially ionized
        argon and flow induced by an ionizing shock wave.

When considering the possibility of the determination of the
heat conductivity of partially ionized argon from measurements of the
structure of the thermal boundary layer one is confronted with the
fact that no such work has been done before in shock tubes. However
the similar problem in electric arcs has been extensively studied
(Emmons 67, Kopainsky 71, Asinovsky 71, Uhlenbusch 71).
The analysis of the data is based on a determination of the integral
energy balance in a similar way as done by Vrugt (76) for the
analysis of shock tube data in the non-ionized case. Two major
differences between the electric arc and the thermal boundary layer
at the end-wall of a shock tube are:
The electric arc is stationary while the structure of the boundary
layer is time dependent.
The main source term in the energy balance for the arc is due to
dissipation while in the case of the thermal boundary layer it is due
to the time dependence of the enthalpy of the gas.

We consider further studies of the flow induced by the
reflection of an ionizing shock wave at the end-wall of a shock tube
and some papers on the related subject of the flow behind the
incident shock wave.

Kuiper (68) studied the thermal boundary layer at the
end-wall of a shock tube. From time resolved two-wavelength
interferograms he deduced the electron and atom density profiles.
Using two-wavelength streak interferometry Kuiper (68) obtained data
on the behaviour of the flow in the reflected shock region outside the
boundary layer as a function of time and space. Those data are
compared to calculations on the basis of integral conservation laws
by neglecting radiation losses and assuming local thermodynamic
equilibrium. The measured electron density agrees within 10 % with
the calculated one but as a result of radiation cooling it decreases
by as much as 30 % within 100 µ s for typical experimental conditions
(pressure 5 x 10^5 Pa, electron density 3 x $10^{23} m^{-3}$).
The boundary layer measurements are compared with calculations based
on the "thermal Rayleigh" problem assuming local thermodynamic

equilibrium. The discrepancy between theory and experiment could not be explained within the frame of this model by variation of the plasma conditions outside the boundary layer.

For this reason Hutten (76) developed a two temperature relaxation model. This model, also a Rayleigh problem, takes both temperature and chemical non-equilibrium into account. Radiation transport was not considered. At the wall a constant temperature was assumed for the heavy particles.
The behaviour of the electrons and the ions near the wall was described on the basis of the thin sheath model of Chen (65).
The wall was assumed to be fully catalytic and influence of photo-ionization was ignored. While the model can be expected to describe the outer part of the boundary layer quite well, some doubt arises about the consistency of the model and about the validity of the reaction model in the vicinity of the electric sheath at the wall (see chapter IV and Appendix IV).
The state of the gas outside the boundary layer was calculated according the procedure of Kuiper (68).
The numerical work included a study of the influence of various relaxation processes by consideration of limiting cases where the process is assumed infinitely rapid (equilibrium model) or infinitely slow (frozen model). Those calculations give quantitative information on the deviation from local thermodynamic equilibrium as a result of heat conduction and diffusion.

In his experiments Hutten (76) used a two-wavelength laser schlieren method and obtained electron density gradient measurements with a reproducibility of about 20 %. The atom density gradients showed a scatter of 100 %.
The choice of the wavelengths (0.6328 μm and 1.152 μm) makes the electron contribution to the schlieren effect dominant in the cases considered by Hutten (76).
The system of equations used to separate the contribution of electrons from that of the heavy particles turns out to be almost singular.

The reflected shock region has also been studied experimentally by Kon'kov (73, 74, 75, 76), Logan (77) and Volkov (78) for argon, by Bengtson (70) for neon and Ezumi (79) for krypton. Those studies yielded results similar to the results of Kuiper (68).

Numerical calculations based on a two step ionization model, including the influence of radiation cooling and side wall boundary layers have been presented by Takano (77, 79).

The side wall viscous boundary layer behind a shock wave has been studied experimentally in atmospheric argon by Liu (78). The model used is similar to the model of Hutten (76). Qualitative agreement between theory and experimental data has been achieved. At lower electron densities and low pressures, using spectroscopic diagnostic methods Vervisch (77, 79) obtained electron temperature and density data indicating an anomalous behaviour at the wall. In a theoretical analysis Vervisch (79) considered the possible influence of the production of electrons at the wall by Auger effect and photo-ionization.

Considering a boundary layer in a low temperature plasma Nishida (77) developed a model based on a five step reaction model including the influence of the escape of nonresonant radiation.

A great experimental and theoretical effort has been spent in the study of ionization relaxation behind a shock wave in argon. The influence of impurities on the initial phase of the ionization relaxation has been studied by Frohn (69), McLaren (68) and Schneider (79). The influence of side wall boundary layers is discussed by McLaren (68), Enomoto (73) and Takayama (79). In spite of those extensive studies little quantitative informations has been obtained at this time. Most attempts directed to the determination of the atom-atom ionization cross section are thwarted by the influence of impurities. The presence of instabilities (Glass 78) makes a comparison between theory and experiment rather difficult. Quantitative data on the radiation cooling behind the ionization relaxation front have been obtained by Horn (66) and Vaguin (78).

I.e.   Outline of the present study

        The present study can be considered as a continuation of the
investigations of Kuiper (68), Ewald (71), Vrugt (76) and Hutten (76).
As stated in section (I.a.) our main goal is to improve the shock
tube method for determination of the heat conductivity of gases at
high temperatures.

        In the non-ionized case this implies first a detailed
analysis of the methods proposed by Ewald (71) and Vrugt (76). This
analysis is given in chapter II.
In this treatment we derive formulas similar to the formulas of our
predecessors but we take the influence of pressure variations in the
reflected shock region into account. This effect which has been
neglected in all previous studies appears to be rather important.
In chapter III we consider the thermal Rayleigh problem as a model
for the boundary layer growth. This model yields some insight in the
behaviour of the boundary layer when pressure variations are
negligible. The influence of pressure variations is then considered
within the frame of a simplified model in which the thermal heat
conductivity is taken proportional to the temperature.

        In the partially ionized case (chapter IV) we derive formulas
for the experimental determination of the heat conductivity under the
assumption that the electron and heavy particle temperatures are
equal. We allow, however for the possibility of chemical non-
equilibrium. This procedure is justified by the study of the boundary
layer on the basis of the model developed by Hutten (76) (chapter V).
The behaviour of the flow outside the boundary layer is discussed on
the basis of experimental data in section V.b. In sections V.c. and
d. we consider the validity of the assumption of local thermodynamic
equilibrium outside the boundary layer.
The structure of the boundary layer is considered in section V.e.
The theoretical background of the laser schlieren method has been
considered with care. Special attention is given to the influence of
diffraction (chapter VI).
The experimental data obtained in the non-ionized case are analysed
in chapter VII.
The experimental data for the ionized case are presented in chapter
VIII.

II.   DETERMINATION OF THE HEAT CONDUCTIVITY OF A NON-IONIZED MONATOMIC GAS FROM MEASUREMENTS OF THE STRUCTURE OF THE THERMAL BOUNDARY LAYER AT THE END-WALL OF A SHOCK TUBE.

II.a.   Introduction

By measuring the deflection of a light beam propagating along the end-wall of a shock tube one can determine the density gradient at a fixed position in the boundary layer as a function of time. The experimental method, the laser schlieren technique, will be described further (chapter VI). In this chapter we assume that from a series of such measurements we have obtained the density profile of the boundary layer as a function of space and time. Assuming also the state of the gas outside the boundary layer to be known, we look for a procedure for the determination of the heat conductivity of the gas as a function of the temperature.

This problem has been first considered by Smeets (65) who used a linearised energy equation to derive a relation between the heat conductivity of the gas at a certain point of the boundary layer and the heat conductivity at an other point. Ewald (71) and Vrugt (76) obtained similar formulas without linearisation of the energy equation but assuming the pressure to be time independent. We reconsider the derivation of those formulas and take the influence of pressure variations into account (section II.c.).

The formulas obtained imply that the convective velocity should be estimated. This could in principle be done on the basis of the density profile measurements but it is not possible in practice. In order to determine the convective velocity additional information is necessary. We show that the determination of the heat flux at the gas-wall interface is sufficient. Vrugt (76) proposed as an alternative to use a theoretical evaluation of the convective velocity. In the next section we give a short description of the flow in the shock tube. In chapter III we will consider the thermal boundary layer structure more in detail.

II.b. Description of the flow in the shock tube and definition of
the reference frame.

The theory of the shock tube flow has been treated extensively
by Oertel (73). We consider here a simple model with the purpose of
clarifying the definition of the reference frame and of some reference
state of the gas.

The shock tube can be represented schematically as a closed
tube of uniform cross section. The tube is separated in two sections
by a membrane (figure II.1).
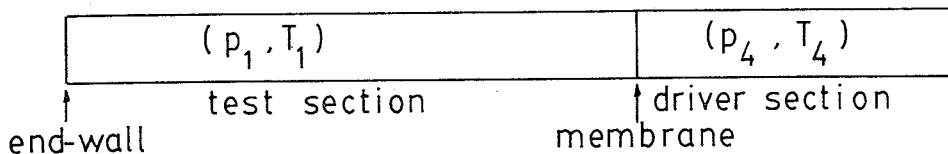
Figure II.1 : The shock tube.

One side of the tube, the test section, is filled with the test gas
(Ar) at a pressure p_1 and a temperature T_1.
The other part of the tube, the driver section, is filled with the
driver gas (N_2 or H_2) at a high pressure p_4 ($p_4 \gg p_1$) and a
temperature T_4. The gases are in equilibrium with the walls. They are
thus uniform, stagnant and at the same temperature as the walls.

The membrane is removed (collapses). The driver gas expands
into the test section pushing the test gas towards the end-wall (of
the test section). In our simplified model we assume that the
membrane has been removed instantaneously. We neglect viscous effects
and heat transport processes at the walls. We assume that ionization
processes are negligible. The flow which is one-dimensional can then
been seen as the desintegration of a discontinuity between two
stagnant gases with states (p_1, T_1, u_1) and (p_4, T_4, u_4). Such a
discontinuity desintegrates into a shock wave traveling through the
test gas towards the end-wall, an expansion fan propagating into the
driver gas and a contact discontinuity between the test gas and the
driver gas (Landau 71).

A space time diagram (x,t) is given in figure II.2.
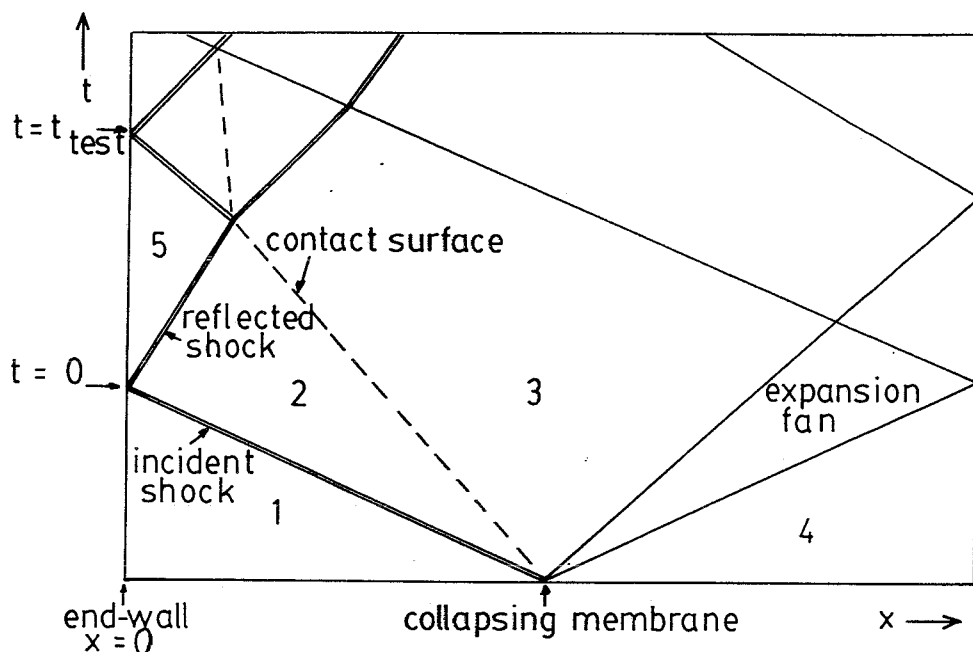
Figure II.2 : (x,t) diagram of the flow in the shock tube.

The shock wave (incident shock wave) is a region with a thickness of the order of magnitude of a mean free path of the molecules. Within the shock wave the test gas is compressed, heated and accelerated from the initial state (p_1, T_1, u_1) to a new uniform state (p_2, T_2, u_2). The relation between states 1 and 2 follows from the integral conservation laws for mass, momentum and energy completed with an equation of state. These so called Rankine-Hugoniot relations contain only one independent parameter. We use as parameter the shock wave Mach number M_s defined by:

$$M_s = v_s/c_1$$ II.1

where v_s is the shock speed measured in the reference frame of the tube and c_1 is the speed of sound in region 1.
The Rankine-Hugoniot relations are given in appendix I.

The incident shock wave reaches the end-wall at the instant t = 0. At this moment the gas in region 2 which has a uniform velocity u_2 directed towards the wall is stopped by the wall. A reflected shock wave is induced with a transition from state 2 to a new uniform state (p_5, T_5, u_5) determined by the condition:

$$u_5 = 0 \qquad\qquad\qquad\qquad\qquad II.2$$

The state 5 of the gas is thus determined by the initial state 1 and the shock wave Mach number M_s of the incident shock (see appendix I).

The gas between the end-wall and the reflected shock remains undisturbed until the arrival of waves generated by the interaction of the reflected shock with the contact surface or the reflection of the expansion fan at the end-wall of the driver section. The situation becomes then rapidly rather complicated. This limits the period of time t_{test} during which we can calculate the state of the gas at the end-wall.

In the actual situation the incident shock wave does not have a constant speed. This is due to the finite opening time of the diaphragm and the influence of the side wall boundary layers behind the shock. Regions 2 and 5 are in reality not uniform and they are time dependent. States 2 and 5 determined by the Rankine- Hugoniot relations, the initial state 1 and the Mach number M_s of the incident shock wave at $t = 0^-$ (just before shock reflection), are referred to as the ideal Rankine-Hugoniot states 2 and 5. The state of the gas at the end-wall, just outside the thermal boundary layer is denoted by $(p_\infty, T_\infty, u_\infty)$.

For reasons that will be discussed in chapter III we assume that state ∞ is uniform and follows from state 5 by an adiabatic pressure change. In such a case the temperature T_∞ can be determined from the knowledge of state 5 and the measurement of the end-wall pressure p_∞ as a function of time. The convective velocity u_∞ is the result of compression and the thermal boundary layer. The determination of u_∞ is discussed in the next section where we derive general formulas for the determination of the heat conductivity.

II.c. Determination of the heat conductivity.

Assuming the boundary layer to have a one dimensional structure we obtain the laws of conservation of mass, momentum and energy in the following form (Ewald 71):

$$\frac{d\,\rho}{d\,t} \;+\; \rho\,\frac{\partial\,u}{\partial\,x} \;=\; 0 \qquad\qquad \text{continuity} \qquad \text{II.3}$$

$$\frac{\partial\,p}{\partial\,x} \;=\; 0 \qquad\qquad \text{momentum} \qquad \text{II.4}$$

$$\rho\,\frac{d\,h}{d\,t} - \frac{d\,p}{d\,t} \;=\; \frac{\partial}{\partial x}\left(\lambda\,\frac{\partial\,T}{\partial\,x}\right) \qquad\qquad \text{energy} \qquad \text{II.5}$$

We have used here the so called boundary layer approximation. The velocity u of the gas is measured in the reference frame of the end-wall. The differential operator $\frac{d}{dt}$ stands for the Lagrangian time derivative which is defined by:

$$\frac{d}{d\,t} \;=\; \frac{\partial}{\partial t} \;+\; u\,\frac{\partial}{\partial x} \qquad\qquad \text{II.6}$$

As we limit ourselfs to a perfect monatomic gas the pressure p is related to the temperature T and the density ρ by the ideal gas law:

$$p \;=\; \rho\,R\,T \qquad\qquad \text{II.7}$$

and the enthalpy h is given by:

$$h \;=\; \frac{5}{2}\,R\,T \qquad\qquad \text{II.8}$$

R is the specific ideal gas constant which is related to the Boltzmann constant k and the mass m_a of an atom by:

22

$$R = k/m_a \qquad\qquad \text{II.9}$$

For atmospheric pressures and a temperature range 300 - 7000 K the
heat conductivity λ of Argon is accurately described by a function
of the temperature only.
Pressure dependence due to real gas effects in the low temperature
range has been studied by Nieto de Castro (78).
At high temperatures the pressure dependence is due to the ionization
which we assumed to be negligible in the temperature range considered.

Using II.3, 4, 7 and 8 we can write the energy equation II.5
in the form:

$$\lambda = \frac{5}{2} R \rho \; \frac{\{(\frac{\partial \rho}{\partial t})/(\frac{\partial \rho}{\partial x}) + u - \frac{3}{5}\frac{\rho}{p}(\frac{dp}{dt})/(\frac{\partial \rho}{\partial x})\}}{\{(\frac{\partial^2 \rho}{\partial x^2})/(\frac{\partial \rho}{\partial x}) - (2 + \frac{T}{\lambda}(\frac{d\lambda}{dT}))(\frac{\partial \rho}{\partial x})/\rho\}} \qquad\qquad \text{II.10}$$

In order to obtain an explicit relation for the heat conductivity
Ewald (71) approximated the right hand side of equation II.10 by
using a power law dependence of λ on T. In such a case we have:

$$\frac{T}{\lambda} \left(\frac{d\lambda}{dT} \right) = \nu \qquad\qquad \text{II.11}$$

The constant ν was taken by Ewald (71) to be $\nu = 0.66$. (We use the
value $\nu = 0.71$).
The value of λ obtained from equation II.10 is insensitive to the
exact value of ν as long as the condition:

$$\rho \left(\frac{\partial^2 \rho}{\partial x^2} \right) \gg \left(\frac{\partial \rho}{\partial x} \right)^2 \qquad\qquad \text{II.12}$$

is satisfied.
The restriction II.12 can be avoided when as proposed by Vrugt (76)
we integrate the energy equation. Considering two positions x_a and

x_b at a fixed time t we obtain from the integration of the energy
equation:

$$\lambda_b = \frac{\rho_b^2}{(\partial\rho/\partial x)_b} \left\{ \frac{\lambda_a}{\rho_a^2}(\partial\rho/\partial x)_a + \frac{5}{2}\frac{R}{}(u_a-u_b) + \frac{3}{2}\frac{R}{p}(dp/dt)(x_a-x_b) \right\}$$

II.13

Vrugt (76) obtained an explicit expression for λ_b by assuming that
$(\partial\rho/\partial x)_a$ and (dp/dt) vanish. We avoid those simplifications in order
not to restrict the validity of expression II.13.

In order to obtain an explicit expression for the heat
conductivity we assume that the points a and b have been chosen in
such a way that:

$$\frac{\lambda_b}{\rho_b^2} \left(\frac{\partial\rho}{\partial x} \right)_b \gg \frac{\lambda_a}{\rho_a^2} \left(\frac{\partial\rho}{\partial x} \right)_a$$

II.14

we can then use for λ_a a rough estimate.

Both expressions II.10 and 13 involve the convective velocity
u. This velocity might be determined, in principle, as proposed by
Ewald (71) by integration of the continuity equation II.3.
This yields:

$$u = -\frac{1}{\rho} \int_0^x (\partial\rho/\partial t) \, dx'$$

II.15

Such a procedure cannot be accurate because the optical determination
of the density close to the end-wall is inaccurate. This is due to
diffraction and reflection of the light against the wall as a result
of the bending of the light towards the wall. Due to the strong
compressibility of the inner part of the boundary layer the
extrapolation of the density profile measured in the outer part of
the boundary layer to the density (measured with light reflection
method (van Dongen 78)) at the wall is an inaccurate procedure.

We consider therefore as an alternative the procedure proposed by Vrugt (76). We apply equation II.13 between point a and the wall $x_b = 0$. This yields:

$$u_a = \frac{2}{5\,R}\,\{\,\frac{\lambda_i}{\rho_i^2}(\partial\rho/\partial x)_i \;-\; \frac{\lambda_a}{\rho_a^2}(\partial\rho/\partial x)_a\} \;-\; \frac{3}{5\,p}\,x_a(dp/dt) \qquad\qquad \text{II.16}$$

where the index i refers to the gas wall interface $(x = 0)$.
The term $(\lambda_i / \rho^2_i)(\partial\rho/\partial x)_i$ is proportional to the heat flux at the gas wall interface and can be deduced from measurements of the temperature T_i as a function of time.
Assuming the wall properties to be constant and the wall to be infinitely thick we have:

$$\frac{\lambda_i}{\rho_i^2}(\frac{\partial\rho}{\partial x})_i = \frac{R}{p}\,(\lambda_w\rho_w c_w/\pi)^{1/2}\,\{\,\frac{T_i(t)}{t^{1/2}} \;+\; \int_0^t \frac{T_i(t)-T_i(t')}{(t-t')^{3/2}}\,dt'\,\} \qquad \text{II.17}$$

where the index w refers to wall properties, c_w is the specific heat capacity of the wall.

The velocity u_b, in II.13, follows then from the integration of the continuity equation II.3 between points a and b. We obtain:

$$u_b \;=\; (\rho_a/\rho_b)\,u_a \;-\; \frac{1}{\rho_b}\,[\,\int_{x_a}^{x_b}(\partial\rho/\partial t)\,dx'] \qquad\qquad \text{II.18}$$

Combination of formulas II.13, 16 and 18 yields:

$$\lambda_b = \frac{\rho_b^2}{(\partial\rho/\partial x)_b}\{\,\frac{\lambda_i}{\rho_i^2}(\frac{\partial\rho}{\partial x})_i(1-\frac{\rho_a}{\rho_b}) \;+\; \frac{\lambda_a}{\rho_a\rho_b}(\frac{\partial\rho}{\partial x})_a +$$

$$\frac{5}{2}\frac{R}{\rho_b}(\int_{x_a}^{x_b}(\frac{\partial\rho}{\partial t})dx') \;+\; \frac{3}{2\rho_b p}\frac{R}{}(\frac{dp}{dt})(x_a\rho_a - x_b\rho_b)\,\} \qquad \text{II.19}$$

The corresponding temperature T_b is obtained from the ideal gas law:

$$T_b = p/R\rho_b \qquad\qquad II.20$$

and the pressure is obtained from end-wall pressure measurements.

A formula equivalent to II.19 is obtained by combining formulas II.10 and 16. We find:

$$\lambda = \frac{5R\rho}{2}\left\{\frac{[\,(\frac{\alpha(\rho-\rho_\infty)}{\partial t})/(\frac{\partial\rho}{\partial x}) + \frac{2}{5R}\frac{\lambda_i}{\rho_i^2}(\frac{\partial\rho}{\partial x})_i - \frac{3}{5p}(\frac{dp}{dt})(x + \frac{\rho-\rho_\infty}{(\partial\rho/\partial x)})]}{[\,(\partial^2\rho/\partial x^2)/(\partial\rho/\partial x) - (1+\upsilon)(\partial\rho/\partial x)/\rho\,]}\right\}\;II.21$$

with the corresponding temperature T given by:

$$T = p/R\rho \qquad\qquad II.22$$

In formula II.21 we made use of the assumption that p_∞ and ρ_∞ are related by the adiabatic ideal gas law:

$$\frac{p_\infty}{p_5} = (\frac{\rho_\infty}{\rho_5})^{5/3} \qquad\qquad II.23$$

Formulas II.19 and 21 should be equivalent. In practice formula II.19 is more sensitive to the time dependence of the pressure than II.21. Equation II.21, is restricted by condition II.12. In chapter III we give an estimate of the range of validity of II.12.
Equation II.21 is used in chapter VII for the determination of the heat conductivity of argon.

Formally we have solved the problem of obtaining formulas for the heat conductivity as a function of experimental data. We have seen that, in order to determine the heat conductivity as a function of the temperature from laser schlieren measurements of the structure of the outer part of the boundary layer at the end-wall of a shock

tube, we should also measure the temperature T_i and the pressure p at the gas wall interface as a function of time. However we will use, as done by Vrugt (76), a theoretical estimate of the heat flux at the end-wall.

In the next chapter we discuss the flow induced by the reflection of a shock wave at the end-wall of a shock tube more in detail.

III.   THE THERMAL BOUNDARY LAYER IN A NON-IONIZED MONATOMIC GAS.

III.a.   Introduction

In the previous chapter we derived formulas for the
determination of the heat conductivity from measurements of the
structure of the thermal boundary layer at the end-wall of a shock
tube. In this chapter we consider the structure of this boundary
layer. The main goal of this study is to deduce some general
properties of the flow, that are useful for the interpretation of
experimental data.

First we will see that when the state of the gas outside the
boundary layer is uniform and time independent (thermal Rayleigh
problem) the structure of the boundary layer is self-similar (III.b).
This property allows to reduce experimentally determined density
gradients from various positions and times to a single curve (Vrugt
76). The reduced density gradient appears to be rather insensitive
to the state of the gas outside the boundary layer. This property has
a restricted validity but yields in practice a powerful procedure for
the analysis of the data. It allows us to compare experimental data
with some variation in the initial conditions and the shock wave Mach
number.

Within the frame of the thermal Rayleigh problem we obtain an
analysis of the heat flux at the end-wall of the shock tube as a
function of the state of the gas outside the boundary layer.

The self-similarity of the boundary layer structure implies
that the set of partial differential equations II.3, 4 and 5 can be
reduced to an ordinary differential equation. However this equation,
the energy equation in Lagrangian coordinates, is nonlinear.
A quantitative discussion of the structure of the boundary layer can
only be obtained on the basis of numerical solutions of the problem.
We consider therefore a simplified model in which we assume the heat
conductivity to be proportional to the temperature. In such a case
the energy equation in Lagrangian coordinates is linear.

In section III.d we use this simplified model in order to
discuss the structure of the boundary layer. The influence of the
compressibility is analysed.

28

The relative magnitude of the various terms in the energy equation is estimated. This yields criteria for the validity of the boundary layer approximation and for the validity of the procedure of Ewald (71) for the determination of the heat conductivity.

In section III.e we discuss qualitatively the deviation of the flow from the thermal Rayleigh problem.

The main deviation of the flow from the thermal Rayleigh problem is due to the time dependence of the pressure.

The influence of pressure variations on the density gradient and the heat flux at the end-wall is analysed on basis of the simplified model in which the heat conductivity is assumed to be proportional to the temperature (III.f).

III.b.   The thermal Rayleigh problem

The thermal Rayleigh problem concerns a stagnant uniform gas
of semi-infinite extent (state (p_1, T_1)) in equilibrium with a semi-
infinite wall. At time t = 0 the gas is instantaneously compressed
and heated to a uniform, time independent, state (p_∞, T_∞). We use
this model to describe the shock reflection process at the end-wall
(section II.b). We assume thus that the boundary layer growth at the
end-wall can be clearly distinguished from the shock reflection
process. This implies that we consider only time scales that are much
greater than the mean free flight time τ_{col} of the molecules. The gas
can therefore be considered as a continuum. If we limit ourselfs to
times such that:

$$\sqrt{t/\tau_{col}} \quad \gg \quad 1 \qquad\qquad III.1$$

the convective velocity u_∞ induced by the thermal boundary layer
growth will be small compared to the speed of sound. (see section
III.d) This allows us to use the boundary layer approximation (II.3,
4 and 5).
It will be shown in section III.e that for the time scale considered
the temperature gradient at the wall is small enough to assume that
the temperature is continuous at the gas-wall interface. We assume
also that the wall properties are constant (Vrugt 76).
The use of this approximation excludes any independent length or time
scale. The structure of the thermal boundary layer is therefore self-
similar. An appropriate similarity coordinate S is defined by:

$$S \;=\; x/\sqrt{a_R\, t} \qquad\qquad III.2$$

where a_R is a reference thermal diffusivity.
Because of the self-similarity of the boundary layer structure
it is clear that the state of the gas (p, T_i) at the gas-wall
interface is time independent for t > 0.
We now consider the mathematical formulation of the thermal
Rayleigh problem. The energy equation II.5 can be uncoupled from the

continuity equation II.3 by considering the problem in Lagrangian coordinates (η, t).

The Lagrangian coordinate η is defined by:

$$\eta = \int_0^x \rho \, dx' \qquad\qquad III.3$$

The energy equation becomes, assuming that the pressure is uniform and time independent, in Lagrangian coordinates:

$$\frac{1}{\rho^2} \frac{\partial \rho}{\partial t} = \frac{2}{5R} \frac{\partial}{\partial \eta} \left(\frac{\lambda}{\rho} \frac{\partial \rho}{\partial \eta} \right) \qquad\qquad III.5$$

The boundary and initial conditions are:

$$\rho = \rho_i \quad ; \quad \eta = 0 \qquad t \geqslant 0$$

$$\rho \rightarrow \rho_\infty \quad ; \quad \eta \rightarrow \infty \qquad t \geqslant 0$$

$$\rho = \rho_\infty \quad ; \quad \eta \geqslant 0 \qquad t = 0$$

$$III.6$$

Again there is no independent scale for η so that the solution of the thermal Rayleigh problem must be selfsimilar. The Lagrangian similarity coordinate Z defined by:

$$Z = \frac{\eta}{\rho_R \sqrt{a_R \, t}} \qquad\qquad III.7$$

where ρ_R is a reference density, allows us to write the energy equation III.5 in the form:

$$\frac{d^2\bar{\rho}}{dZ^2} + \left(\frac{\bar{\rho}}{\bar{\lambda}} \frac{d\bar{\lambda}}{d\bar{\rho}} - 1 \right) \frac{1}{\bar{\rho}} \left(\frac{d\bar{\rho}}{dZ} \right)^2 + \frac{Z}{2\bar{\rho}\bar{\lambda}} \left(\frac{d\bar{\rho}}{dZ} \right) = 0 \qquad III.8$$

where the nondimensional density $\bar{\rho}$ and heat conductivity $\bar{\lambda}$ are defined by:

$$\bar{\rho} = \rho / \rho_R \qquad \text{III.9}$$

and

$$\bar{\lambda} = 5 \lambda / (2R\, a_R \rho_R) \qquad \text{III.10}$$

The temperature T is given by:

$$T = p/R\rho_R \bar{\rho} \qquad \text{III.11}$$

As the nondimensional heat conductivity $\bar{\lambda}$ depends also on T_∞, it is in general a function of both the pressure p and of $\bar{\rho}$.

When $\bar{\lambda}$ is known equation III.8 can be integrated (numerically) and the solution:

$$\bar{\rho} = f(Z) \qquad \text{III.12}$$

can be used to calculate the velocity u from the continuity equation II.3:

$$u = \frac{1}{2} \left(a_R / t \right)^{1/2} \int_0^Z \frac{Z'}{f(Z')} f^{(1)}(Z') dZ' \qquad \text{III.13}$$

From those results one can obtain the solution of the thermal Rayleigh problem:

$$\bar{\rho} = F(S) \qquad \text{III.14}$$

as a function of the laboratory similarity coordinate S by using the relation:

$$S = \int_0^Z \frac{dZ'}{f(Z')} \qquad \text{III.15}$$

While we have formally solved the thermal Rayleigh problem, we have ignored until now the problem of the determination of the state of the gas at the wall (p, T_i). We will show in section III.d that for a metal wall the temperature T_i is very close to T_1. An excellent

approximation for ρ_i is therefore given by:

$$\rho_i = p/R\,T_1 \qquad\qquad\qquad \text{III.16}$$

In the next section we consider the dependence of the solution of the thermal Rayleigh problem on the state of the gas outside the boundary layer.

III.c. Dependence of the solution of the thermal Rayleigh problem
on the state of the gas outside the boundary layer.

Taking as reference state R the state ∞ of the gas outside
the boundary layer, so that:

$$a_R = \frac{2 \; \lambda_\infty}{5 \; R \; \rho_\infty} \qquad \qquad \text{III.17}$$

and

$$\rho_R = \rho_\infty \qquad \qquad \text{III.18}$$

it is easy to see that equation III.8 is independent of (p, T_∞) if
the heat conductivity is given by a power law dependence of the
temperature:

$$\bar{\lambda} = (T/T_\infty)^\nu \qquad \qquad \text{III.19}$$

While such a power law dependence is not expected to describe
accurately the behaviour of the heat conductivity (Vrugt 76) it
yields a reasonable approximation (section VII.e).
The energy equation III.8 itself will therefore not strongly depend
on the state of the gas outside the boundary layer.

The dependence of the solution $f(Z)$ of the thermal Rayleigh
problem (III.12) on T_∞ is due to the dependence of the boundary
conditions on T_∞. The boundary conditions III.6 can be approximated,
using III.16 by

$$\begin{array}{lll} \bar{\rho} = T_\infty / T_1 & ; & Z = 0 \\[2mm] \bar{\rho} \rightarrow 1 & ; & Z \rightarrow \infty \end{array} \qquad \text{III.20}$$

In the next section we discuss the dependence of the solution of the
thermal Rayleigh problem on $\bar{T}_1 = T_1/T_\infty$.
As the energy equation III.8 and the boundary conditions
III.20 are independent of the pressure the solution of the thermal
Rayleigh problem is independent of the pressure. This statement is
confirmed by the experimental data of Saxena (72) for the heat

flux q_w at the end wall.

The heat flux q_w is related to $f(Z)$ by:

$$q_w = + (\frac{5 \quad p}{2 \, T_\infty \lambda_\infty t})^{1/2} \, \lambda_1 \, T_1 \, f^{(1)}(0) \qquad\qquad III.21$$

Formula III.21 is only valid if the pressure p is constant.

As shown by van Dongen (78) for test times of the order of magnitude of 200 μs and the initial pressures $p_1 = 2.7 \times 10^3$ Pa and 5.4×10^3 Pa considered by Saxena (72), the pressure p measured simultaneously by means of the light reflection technique and a piezo electrical gauge is constant and agrees within 2% with the ideal Rankine-Hugoniot value p_5 (section II.b). From our own experience it appears that for longer test times or lower initial pressures significant deviations of p from p_5 are observed. In section III.f we discuss the influence of the time dependence of the pressure on the structure of the boundary layer.

III.d. A simplified model.

In this section we consider a simplified model which yields an analytical solution for the thermal Rayleigh problem. In this model we assume that the heat conductivity is proportional to the temperature. From the studies of Saxena (72) and van Dongen (78) it appears that such a model yields a good qualitative idea of the structure of the thermal boundary layer.

Using the assumption:

$$\bar{\lambda} = \bar{T} \qquad\qquad\qquad III.22$$

we can write the energy equation III.8 in the form:

$$\frac{d^2\bar{T}}{dZ^2} + \frac{Z\,\bar{T}}{2\,\bar{\lambda}}\frac{d\,\bar{T}}{dZ} = 0 \qquad\qquad III.23$$

If we assume that the wall properties are constant the behaviour of $\bar{T}$ in the wall is described by:

$$\frac{\partial\,\bar{T}}{\partial\,t} = a_w\frac{\partial^2\bar{T}}{\partial\,x^2} \qquad\qquad III.24$$

The problem is defined by the initial conditions:

$$\bar{T}(x,0) = T_1/T_\infty \qquad ; \quad x < 0$$
$$\qquad\qquad\qquad\qquad\qquad\qquad\qquad III.25$$
$$\bar{T}(x,0) = 1 \qquad\qquad ; \quad x > 0$$

and the boundary conditions:

$$\lim_{x\to\infty}\bar{T}(x,t) = T_1/T_\infty$$
$$\qquad\qquad\qquad\qquad\qquad\qquad\qquad III.26$$
$$\lim_{x\to\infty}\bar{T}(x,t) = 1$$

The solution of the thermal Rayleigh problem g(Z):

$$\bar{T} = g(Z) \qquad\qquad\qquad III.27$$

is given by:

$$g(Z) = \bar{T}_i + (1 - \bar{T}_i)\,\text{erf}\,(Z/2) \quad ; \quad Z \geqslant 0 \qquad \text{III.28}$$

where the interface temperature $\bar{T}_i$ is constant and follows from:

$$\frac{\bar{T}_i - \bar{T}_1}{1 - \bar{T}_i} = \left(\frac{\lambda_i\,\rho_i\,c_p}{\lambda_w\,\rho_w\,c_w} \right)^{1/2} \qquad \text{III.29}$$

The dimensionless temperature $\bar{T}$ is related to the density by:

$$\bar{T} = 1/\bar{\rho} \qquad \text{III.30}$$

We use this solution of the thermal Rayleigh problem to check the validity of some assumptions introduced in the previous sections.

In section III.b we stated that T_i could be approximated by T_1. For the experimental conditions considered we have:

$$5 \times 10^{-2} \leqslant \bar{T}_1 \leqslant 2 \times 10^{-1} \qquad \text{III.31}$$

while for $T_1 = 3 \times 10^2 K$ and a steel wall we have:

$$\lambda_i\,\rho_i\,c_p = O(10)$$

and $\qquad \qquad \qquad \qquad \qquad \qquad \qquad \qquad \qquad \qquad$ III.32

$$\lambda_w\,\rho_w\,c_w = O(10^8)$$

From equation III.29 we obtain:

$$\frac{\bar{T}_i - \bar{T}_1}{\bar{T}_1} = O(10^{-3}) \qquad \text{III.33}$$

Because the uncertainty in the experimental determination of $\bar{T}_1$ is of the order of magnitude of 10^{-3}, we can neglect in III.28 the deviation of $\bar{T}_i$ from $\bar{T}_1$.

In section III.b we stated that the boundary layer approximation used (Equations II.3, 4 and 5) is valid if the convective velocity u_∞ induced by the thermal boundary layer is small compared to the speed of sound:

$$| u_\infty | \ll c_\infty \qquad\qquad \text{III.34}$$

The simplified model considered allows us to obtain a quantitative estimate of the time scale for which III.34 is valid. Using III.13 and III.28 we find:

$$u_\infty = - (a_\infty/t)^{1/2} \qquad\qquad \text{III.35}$$

With this expression the criterion III.34 becomes:

$$a_\infty/c_\infty^2 \ll t \qquad\qquad \text{III.36}$$

For our experimental conditions $a_\infty = 0(10^{-3} \, m^2 s^{-1})$ and $c_\infty = 0(10^3 \, m \, s^{-1})$ the boundary layer approximation is certainly valid for times larger than 10^{-6}s. We will see in the next section that this condition is not restrictive because the uncertainty in the moment of reflection of the incident shock wave at the end-wall is of the same order of magnitude.
A more detailed discussion including the estimation of the interaction between the thermal boundary layer growth and the reflected shock is given by van Dongen (78).

We now consider the influence of the compressibility on the structure of the boundary layer.

Due to the compressibility of the boundary layer the similarity coordinate S (III.2) will deviate from the Lagrangian similarity coordinate Z (III.7).
Using equations III.15 and III.28 we obtain the relation:

$$S = Z \, g(Z) - \frac{2}{\pi^{1/2}} \, (1 - \bar{T}_1)(1 - \exp(- Z^2/4)) \qquad \text{III.37}$$
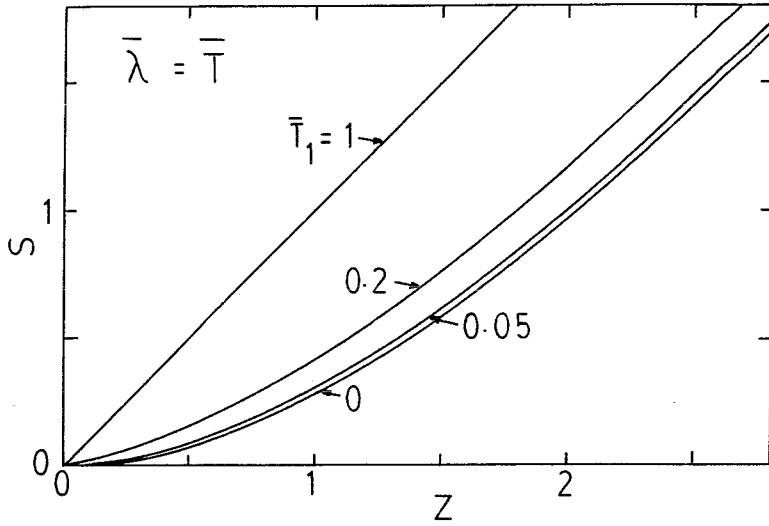
Figure III.2 : Relation between the laboratory
coordinate S and the Lagrangian similarity coordinate
Z for various values of $\overline{T}_1$.

In figure III.2 we give S as a function of Z for various values of $\overline{T}_1$.
In our experiments we measure the density gradient over the range:

$$0.4 \leqslant S \leqslant 3$$

From figure III.2 we see that strong compressibility effects should
be expected for $S \leqslant 1$. For large values of S the influence of the
compressibility on S can be seen as a shift, displacement thickness,
between the Lagrangian coordinate Z and the laboratory coordinate S:

$$\lim_{Z \to \infty} (Z - S) = \frac{2 (1 - \overline{T}_1)}{\pi^{1/2}} \qquad \text{III.38}$$

In our experiments we measure the density gradient at various
positions. The data show some scatter in $\overline{T}_1$. However the normalized

density gradient $F^{(1)}$ yields a single curve as a function of S.
We try to understand this insensitivity of $F^{(1)}$ to variations of $\bar{T}_1$.

In figure III.3 the influence of a relative change in $\bar{T}_1$ on
$F^{(1)}$ is shown as a function of S. We see that for small values of S
a relative change $\Delta\bar{T}_1/\bar{T}_1$ will induce a strong change of $F^{(1)}$.
This effect is due to the direct dependence of the density at the wall
on $\bar{T}_1$. For large values of S we observe a change of sign of $\Delta F^{(1)}/F^{(1)}$.
This can be understood, since the boundary layer thickness decreases
for decreasing $\bar{T}_1$. For S = 0(1) (our experimental range), the two
effects balance each other.
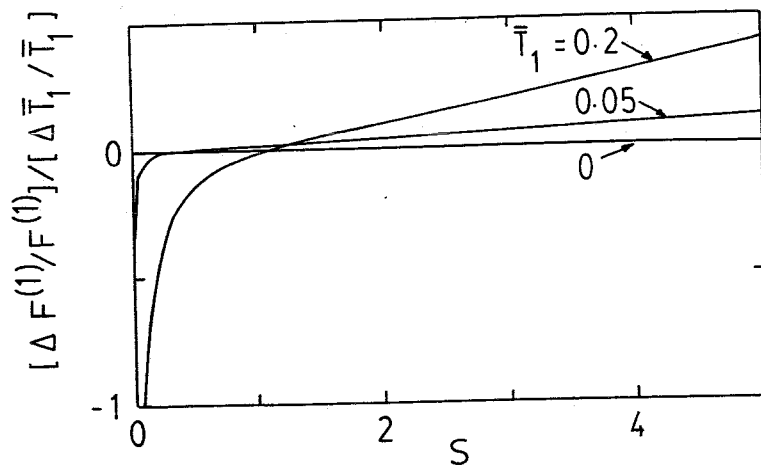
Figure III.3 : Sensitivity of the dimensionless
density gradient $F^{(1)}$ on $\bar{T}_1$, as a function of S.

We now consider the relative importance of various terms in
the energy equation.

First we discuss the validity of the procedure proposed by
Ewald (71) for the determination of the heat conductivity.
(equation II.22)

In section II.c we have seen that this formula is valid if condition
II.12:

$$\rho \left(\frac{\partial^2 \rho}{\partial x^2} \right) \quad \gg \quad \left(\frac{\partial \rho}{\partial x} \right)^2 \qquad\qquad II.12$$

is met.

The behaviour of $\rho(\partial^2\rho/\partial x^2)/(\partial\rho/\partial x)^2$ is given by:

$$\frac{\rho(\partial^2\rho/\partial x^2)}{(\partial\rho/\partial x)^2} = 3 + Z\frac{g(Z)}{g^{(1)}(Z)} \qquad \text{III.39}$$

From figure III.4 and II.10 we see that if the inaccuracy in $(T/\lambda)(d\lambda/dT)$ is 5%, the error in the determination of the heat conductivity will be less than the experimental uncertainty $O(10^{-2})$ if:

$$S \geqslant 1 \qquad \text{III.40}$$

In such a case the procedure of Ewald (71) can be used.

From figure III.4 we see also that for:

$$S \geqslant 3$$

the ratio $\rho(\partial^2\rho/\partial x^2)/(\partial\rho/\partial x)^2$ is of the order 10^2.

In this case one can use a linearised theory such as considered by Smeets (65).
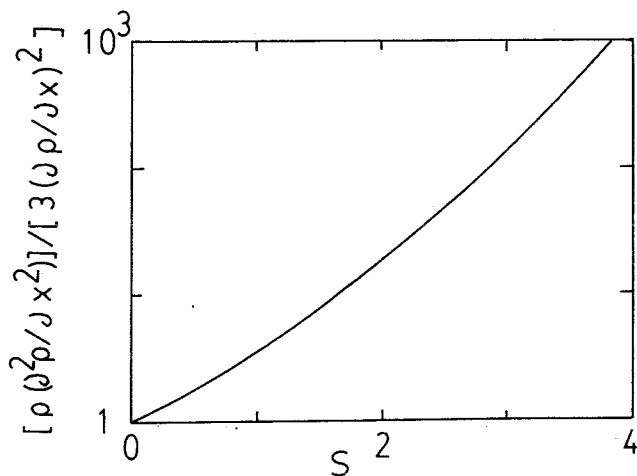
Figure III.4: $\rho(\partial^2\rho/\partial x^2)/(3(\partial\rho/\partial x)^2)$ as a function of S for $\bar{T}_1 = 0.2$.

When considering the experimental determination of the heat conductivity it is important to realise that the contribution of the convective term in the energy equation is of the same order of magnitude as the conductive term.

Therefore the heat flux at the end-wall should be determined with the same degree of accuracy as the density profile. This statement can be verified by considering the behaviour of the ratio:

$$\frac{u(\partial\rho/\partial x)}{(\partial\rho/\partial t)} \quad = \quad - \frac{2\,u}{S} \; (t/a_\infty)^{1/2} \qquad\qquad \text{III-41}$$

where u is determined by using equations III.13 and S is given by III.37 (see figure III.5).
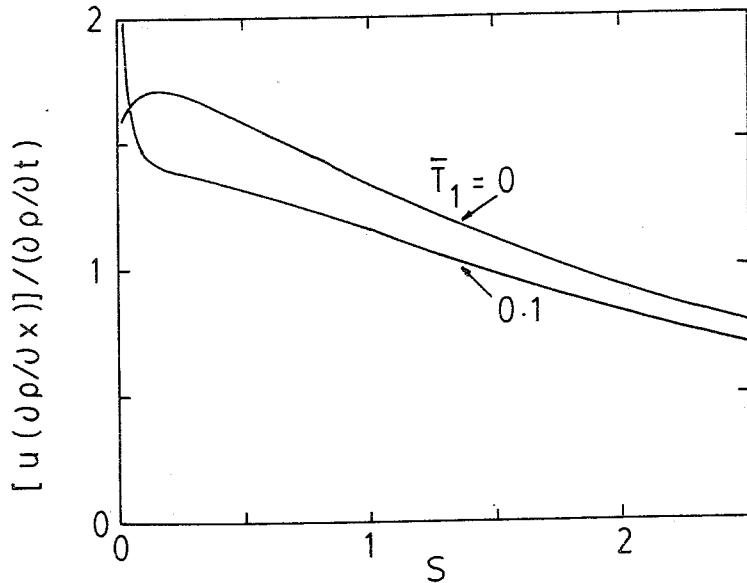
Figure III.5: Ratio $u(\partial\rho/\partial x)/(\partial\rho/\partial t)$
as a function of S.

III.e. <u>Deviation of the flow from the thermal Rayleigh problem.</u>

In the previous sections we have considered the thermal Rayleigh problem as a model for the boundary layer growth at the end-wall of a shock tube. We now consider the deviation of the flow from this model.

Roughly one can classify the deviations of the flow from the thermal Rayleigh problem into:

rarefaction effects,

interaction of the boundary layers with the main flow,

and instationarity due to pressure waves.

The rarefaction effects are important in the initial phase of the shock reflection process. For time scales of the order of magnitude of a mean free flight time τ_{col} of the atoms the thermal boundary layer at the end-wall cannot be distinguished from the reflected shock. This phase of the flow has been studied experimentally by Sturtevant (64), Hanson (73) and Meldau (77).

On an intermediate time scale ($\tau_{col}/t \leqslant 10^{-2}$) one can neglect the rarefaction effects in the flow in view of the inaccuracy of the experimental data $0(10^{-2})$.

The rarefaction effects at the wall can then be simulated by a temperature jump condition at the gas-wall interface.

The interaction of the reflected shock wave with the thermal boundary layer has been studied with such a model by Clarke (67). Using a linearized version of this theory van Dongen (78) shows that on the time scale we are considering ($(\tau_{col}/t)^{1/2} \leqslant 10^{-2}$) this interaction process will lead to the presence of an entropy gradient at the edge of the thermal boundary layer. For the experimental conditions ($M_s = 3$, $P_1 = 667$ Pa, $T_1 = 294$ K) considered this results in a lowering of T_∞ ($x_m = 5$ mm) in comparison to T_5 of the order of 10^{-2}.

The influence of the temperature jump on the boundary layer structure has an order of magnitude given by the estimate of the deviation of the heat flux at the end-wall:

$$\frac{\Delta q_w}{q_w} \sim (\lambda_1/c_p p\, t)^{1/2} \qquad\qquad \text{III.42}$$

This effect is negligible compared to the experimental inaccuracies $(O (10^{-2}))$ if we consider times larger than 10^{-5}s.

While the interaction of the end-wall boundary layer with the flow in the reflected shock region is negligible, the side wall boundary layers can have an important influence on the main flow. The side wall boundary layers behind the incident shock wave will act as a mass sink. The induced expansion will decelerate the incident shock wave and accelerate the contact surface.
Using the model of Mirels (66) one can obtain an order of magnitude estimate for the induced non-uniformity of the reflected shock region and the time dependence of the pressure at the end-wall. The actual flow appears to depend also strongly on the type of diaphragm used and on the driver gas. Those effects due to the finite opening time of the diaphragm are illustrated in figure III.6 where we compare the end-wall pressure measurements of two runs. In the two cases the initial conditions and the incident shock wave Mach numbers were identical.
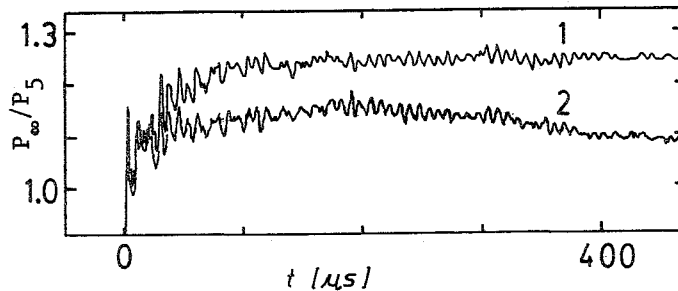
Figure III.6 : Influence of the diaphragm opening on the time dependence of the end-wall pressure p_∞.
1. Run (79101005/II), diaphragm (0.5 mm/0.4 mm), driver gas H_2. $(M_s)_1 = 4.175$, $(M_s)_2 = 4.171$, $p_1 = 667$ Pa, $T_1 = 296.3$ K.
2. Run (79101006/II), diaphragm (0.5 mm/0.4 mm), driver gas H_2. $(M_s)_1 = 4.180$, $(M_s)_2 = 4.163$, $p_1 = 667$ Pa, $T_1 = 296.3$ K.

(see notation chapter VII).

From figure III.6 we see that the end-wall pressure obtained at low
Mach numbers by using hydrogen as driver gas is not reproducible.
This effect due to the relative low pressure ratio (p_4/p_1) over the
diaphragm is also reported by Stupochenko (67) and Simpson (67).
From those data it should be clear that we should take the influence
of the time dependence of the pressure into account. In the next
section we consider the influence of the time dependence of the
pressure on the end-wall boundary layer structure.

The side-wall boundary layer behind the incident shock induces
a curvature of the shock wave (Stupochenko 67). From our experimental
data it appears that the shock wave curvature introduces an
uncertainty in the instant of reflection of the incident shock wave
at the end-wall of the order of 10^{-6} s.

Finally the side wall boundary layers behind the incident
shock wave can produce important deviations from the one-dimensional
character of the flow. Such effects are due to the difference between
the stagnation pressure in the boundary layer and the pressure in the
reflected shock region. When the stagnation pressure is lower than
the reflected shock region pressure, bifurcation of the reflected shock
wave may occur (Oertel (73)).
This effect has not been observed in non-ionized monatomic gases such as
argon. When region 2 is partially ionized bifurcation occurs (Kuiper
(68), Takano (79)).
In the present investigation no serious evidence of bifurcation has
been observed for the test times considered.
This however does not exclude a serious disturbance of the reflected
shock region by the penetration of the side wall boundary layers into
the reflected shock region.
The uncertainty due to such effects can be reduced by comparison of
the experimental data obtained in several shock tubes with different
cross sections.

III.f. Influence of pressure waves on the structure of the end-wall
        thermal boundary layer.

        In sections III.b, c and d we considered a model for the
thermal boundary layer in which we assumed that the initial conditions
were uniform and the boundary conditions constant (so called thermal
Rayleigh problem).
In section III.e we have discussed qualitatively the deviation of the
flow from this model. In this section we study the influence of
pressure waves on the structure of the thermal boundary layer.

        We distinguish two main effects of pressure waves: the
generation of a non-uniformity of the reflected shock region due to
the interaction of the waves with the reflected shock and the time
dependence of the pressure in the boundary layer.

        The first effect can be observed in measurements of the
density gradient outside the boundary layer.
In figure III.7 we show a typical laser schlieren record of the
density gradient as a function on time for x = 7 mm.
We see that the gas behind the reflected shock is non-uniform.
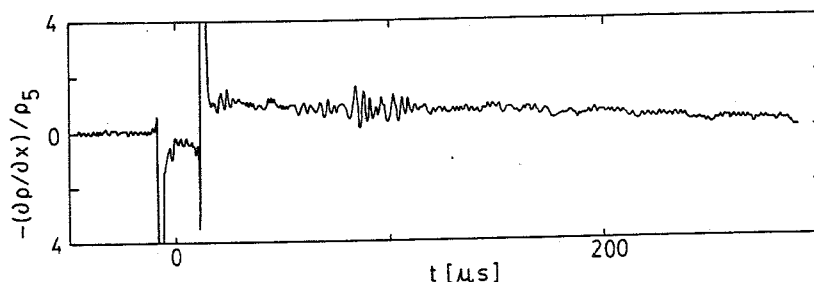
Figure III.7 : Laser schlieren record of the density
gradient at x = 7 mm.
Run (77091401/II), $(M_s)_1$ = 2.97, p_1 = 667 Pa,
T_1 = 294.9 K.

$$\frac{\partial \hat{T}}{\partial t} = \frac{\lambda_\infty \rho_\infty}{c_p} \; \frac{\partial}{\partial \eta} \; (\frac{\hat{\lambda}}{\hat{T}} \; \frac{\partial \hat{T}}{\partial \eta}) \qquad\qquad III.45$$

where the demensionless quantities $\hat{T}$ and $\hat{\lambda}$ are defined by:

$$\hat{T} = T/T_\infty(t)$$
$$\qquad\qquad III.46$$
$$\hat{\lambda} = \lambda/\lambda(T_\infty)$$

Introducing a stretched time coordinate τ defined by:

$$\tau = {_0\int^t} \; (\lambda_\infty/\lambda_5) \; (\rho_\infty/\rho_5) \; dt' \qquad\qquad III.47$$

and assuming that the heat conductivity is proportional to the temperature we obtain:

$$\frac{\partial \hat{T}}{\partial \tau} = \frac{\lambda_5 \, \rho_5}{c_p} \; \frac{\partial^2 T}{\partial \eta^2} \qquad\qquad III.48$$

The reference state 5 is defined by:

$$T_5 = T_\infty(0) \quad ; \quad p_5 = p_\infty(0) \qquad\qquad III.49$$

and is assumed to correspond to the "ideal" Rankine-Hugoniot state defined in section II.b.

We first study the influence of a non-uniformity in the initial conditions on the behaviour of the heat flux q_w at the end-wall.

We assume that the boundary conditions are constant (so that $\tau = t$) and given by:

$$\hat{T}(0,\tau) = T_1/T_5 \qquad\qquad III.50$$

$$\lim_{\eta \to \infty} \hat{T}(\eta,\tau) = 1$$

The boundary condition at the wall is justified by the order of

The influence of this non-uniformity of the reflected shock region is estimated by considering a model of the thermal boundary layer growth in a non-uniform gas at constant pressure. The influence of the time dependence of the pressure is considered in a second model in which we assume the initial conditions to be uniform.

In a similar way as for the thermal Rayleigh problem (section III.d) we use a simplified model in which the heat conductivity is proportional to the temperature.
In such a case we can obtain from the energy equation in Lagrangian coordinates a linear equation for the dimensionless temperature.
When a stretching of the time coordinate is applied this equation takes the form of the Fourier equation. Analytical solutions can be obtained for general initial and boundary conditions (Carslaw 48, Landau 71).

The main goal of this study is to obtain some insight in the behaviour of the heat flux at the end-wall.
We will see that the time coordinate stretching applied takes the influence of the "memory" of the boundary layer into account.
Replacing in formula III.21 the time t by a stretched time, one obtains a good approximation for the heat flux at the end-wall. This approach is refered to as the "local similarity" model.

We now derive the basic equation.
The behaviour of the gas in the boundary layer is described by the energy equation II.5 which in Lagrangian coordinates (η, t) can be written as:

$$\frac{c_p}{R\,T} \, \frac{\partial T}{\partial t} \;-\; \frac{1}{p} \, \frac{\partial p}{\partial t} \;=\; \frac{\rho}{R} \, \frac{\partial}{\partial \eta} \left(\frac{\lambda}{T} \, \frac{\partial T}{\partial \eta} \right) \qquad\qquad \text{III.43}$$

where η is defined by III.3. We assume that the state of the gas far from the wall ∞ is uniform. Using the assumption of the uniformity of the pressure we then have:

$$\frac{1}{p} \, \frac{\partial p}{\partial t} \;=\; \frac{c_p}{R\,T_\infty} \, \frac{\partial T_\infty}{\partial t} \qquad\qquad \text{III.44}$$

and we can write III.43 as:

magnitude estimate III.33. The general solution $\hat{T}(\eta,\tau)$ is given for general initial conditions by Landau (71).

We consider here the case of a stepwise discontinuity in the initial conditions:

$$\hat{T}(\eta,0) \quad = \quad 1 - \delta_0(1 - U(\eta - \eta_0))$$

$$\eta \geqslant 0$$

III.51

where δ_0 and η_0 are constants.

$U(\eta - \eta_0)$ is the Heaviside step function. In figure III.8 we give a schematic representation of $\hat{T}(\eta,0)$.
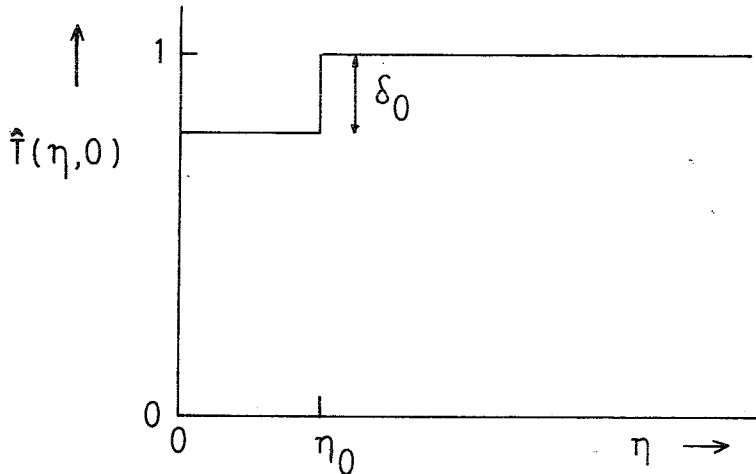
Figure III.8 : Schematic representation of $\hat{T}(\eta,0)$

The solution $\hat{T}$ of this problem can be expressed as the solution $g(Z)$ of the thermal Rayleigh problem (III.28) plus a deviation $\Delta\hat{T}$:

$$\hat{T} \quad = \quad g(Z) + \Delta\hat{T}$$

III.52

where Z is the Lagrangian similarity coordinate defined by III.7. $\Delta\hat{T}$ is given by:

$$\Delta\hat{T} = -\delta_0\left(\text{erf}(Z/2) - \frac{1}{2}\left(\text{erf}\frac{(Z + Z_0)}{2} + \text{erf}\frac{(Z - Z_0)}{2}\right)\right)$$

III.53

49

where Z_0 is defined as:

$$Z_0 = \frac{\eta_0}{\rho_5 (a_5 \, t)^{1/2}} \qquad \text{III.54}$$

The deviation $\Delta q_w / q_w$ of the heat flux at the end-wall induced by the non-uniformity in the initial conditions is given by:

$$\frac{\Delta q_w}{q_w} = \frac{\delta_0 (1 - \exp(-Z_0^2/4))}{(1 - \bar{T}_1)} \qquad \text{III.55}$$

where $\bar{T}_1$ is given by:

$$\bar{T}_1 = T_1/T_5 \qquad \text{III.56}$$

An order of magnitude estimate yields for typical experiments $\delta_0 = 0(10^{-1})$, $\eta_0 / \rho_5 = 0(10^{-3}m)$ and $a_5 = 0(10^{-3}m^2s^{-1})$. In such a case the relative deviation of the heat flux at the end-wall from the heat flux calculated on the basis of the thermal Rayleigh problem (equation III.21) should be less than $0(10^{-2})$ for times larger than $10^{-4}s$.

We now consider the influence of the time dependence of the pressure on the structure of the boundary layer. We assume that the initial conditions are uniform:

$$\hat{T}(\eta,0) = 1 \qquad ; \qquad \eta \geqslant 0 \qquad \text{III.57}$$

The boundary conditions are:

$$\hat{T}(0,\tau) = T_1/T_\infty$$

$$\lim_{\eta \to \infty} \hat{T}(\eta,\tau) = 1 \qquad \text{III.58}$$

where T_∞ is related to the pressure p by relation III.44. The solution $\hat{T}$ of this problem can be split in a "local similarity" solution $g(\hat{Z})$ and a deviation $\Delta \hat{T}$ from local similarity:

50

$$\hat{T} = g(\hat{Z}) + \Delta\hat{T} \qquad\qquad \text{III.59}$$

where

$$g(\hat{Z}) = \hat{T}(0,\tau) + (1 - \hat{T}(0,\tau))\,\text{erf}(\hat{Z}/2) \qquad\qquad \text{III.60}$$

and

$$\hat{Z} = \frac{\eta}{\rho_\infty(a_\infty \hat{t})^{1/2}} \qquad\qquad \text{III.61}$$

$g(\hat{Z})$ is the solution of the "local" thermal Rayleigh problem with (constant) boundary conditions corresponding to the instantaneous value of the boundary conditions III.58.

The normalized stretched time $\hat{t}$ is defined by:

$$\hat{t} = (\rho_5/\rho_\infty)^2 (a_5/a_\infty)\tau \qquad\qquad \text{III.62}$$

The departure of $\hat{T}$ from $g(\hat{Z})$ is given by:

$$\Delta\hat{T} = \int_0^\tau \frac{\hat{T}(0,\tau - \tau') - \hat{T}(0,\tau)}{(4\pi\rho_5^2\, a_5\, \tau')^{1/2}\, \tau'}\, \eta\, \exp\left(-\frac{\eta^2}{4\,\rho_5^2\, a_5\, \tau'}\right) d\tau'$$

$$\text{III.62\,a}$$

When we consider the problem in a laboratory reference frame we use in analogy to III.2 the similarity coordinate $\hat{S}$ defined by:

$$\hat{S} = x/(a_\infty \hat{t})^{1/2} \qquad\qquad \text{III.63}$$

$\hat{S}$ is related to the Lagrangian coordinate $\hat{Z}$ by:

$$\hat{S} = \hat{Z}\, g(\hat{Z}) - \frac{2}{\pi^{1/2}}\,(1 - \hat{T}(0,\tau))(1 - \exp(-\hat{Z}^2/4)\,) + \Delta\hat{S}$$

$$\text{III.64}$$

where:

$$\Delta\hat{S} = \frac{1}{(\pi\tau)^{1/2}}\int_0^\tau \frac{\hat{T}(0,\tau - \tau') - \hat{T}(0,\tau)}{\tau'^{1/2}}\,(1 - \exp(-\frac{\eta^2}{4\,\rho_5^2 a_5 \tau'})\,)\, d\tau'$$

$$\text{III.65}$$

51

$\Delta \hat{S}$ is the deviation of $\hat{S}$ from the local similarity value given by III.37.

Using relations III.59, 60 and 63 we obtain for the heat flux q_w:

$$q_w = - \frac{\rho_i \lambda_i \ T_\infty}{(\pi \ \rho_\infty^2 a_\infty \hat{t})^{1/2}} \ (1 - \frac{T_1}{T_\infty}) \ + \Delta q_w \qquad III.66$$

where the departure of q_w from the local similarity value is given by:

$$\Delta q_w = - \frac{\rho_i \lambda_i \ T_\infty}{(\pi \ \rho_\infty^2 a_\infty \hat{t})^{1/2}} \ \frac{\tau^{1/2}}{2} \int_0^\tau \frac{\hat{T}(0, \tau - \tau') - \hat{T}(0, \tau)}{\tau'^{3/2}} \ d\tau'$$

$$III.67$$

Applying III.67 to some simple cases such as a step wise change in $\hat{T}(0,\tau)$ or a linear variation of $\hat{T}(0,\tau)$ as a function of τ, one can show that for pressure variations of the order of magnitude of 10^{-1} (figure III.6) the deviation of q_w from local similarity should be of the order of magnitude of 10^{-2}.

We conclude therefore that for $t \geqslant 10^{-4}$ s the heat flux at the end-wall might be accurately estimated by using formula III.21 in which $f^{(1)}(0)$ is considered as a function of T_∞ and t is replaced by the stretched time $\hat{t}$

Because $f^{(1)}(0)$ is mainly determined by the behaviour of the heat conductivity in the low temperature region of the boundary layer (Vrugt 76), such a procedure should yield an accurate prediction of the heat flux at the end-wall without an accurate knowledge of the heat conductivity at high temperatures.

52

IV.   EQUATIONS FOR BOUNDARY LAYER FLOW, HEAT CONDUCTIVITY AND
        RADIATION LOSS IN A PARTIALLY IONIZED GAS.

IV.a.   Introduction

        In section IV.b we review the equations for a two temperature
model of the boundary layer.

        In section IV.c we consider a possible procedure to determine
the heat conductivity of a partially ionized monatomic gas. The
procedure is similar to the procedure for the analysis of non-ionized
experiments (section II.c) and to the standard procedure for the
analysis of electric arc data (Asinovsky 71). We allow departure from
local thermodynamic equilibrium in the chemical composition of the
plasma, but we limit ourselves to a single temperature for the
velocity distributions of the different species.

        When a single temperature is assumed, we can obtain a
determination of the thermodynamic state of the plasma in the
boundary layer from two-wavelength laser schlieren, continuum
absorption and end-wall pressure measurements.
The convective velocity can be estimated by means of the thermal
Rayleigh problem developed by Hutten (76). The heat conductivity is
determined by estimation of the various terms in the energy equation.

        Additional complications are the influence of radiation
transport and of diffusion. The radiation transport is split into a
conduction term and a transparent radiation loss term (Kopainsky 71).
The conduction term is included into the heat conductivity.
The transparent radiation loss term is determined experimentally
from the analysis of the behaviour of the plasma outside the boundary
layer (section IV.d).
The diffusion velocity is estimated from the assumption that diffusion
is ambipolar and a theoretical estimate of the diffusion coefficient.

IV.b.   Basic equations

The equations for a two-temperature non-equilibrium model of laminar boundary layer flows in a partially ionized monatomic gas have been derived by Knoös (68), starting from the conservation laws for mass, momentum and energy. A review of later studies and extensive discussions of these equations are given by Hutten-Mansfeld (76) and Liu (79). In the case of the thermal boundary layer, assumed to be one-dimensional, Hutten-Mansfeld (76) obtained the following set of equations for the electrons, ions and total mixture, respectively:

Continuity:

$$\rho \frac{d\,\alpha}{dt} + \frac{\partial}{\partial x}(\rho\alpha\,V) = M_i \qquad ; \qquad\qquad \text{IV.1}$$

$$n_e = n_i \qquad ; \qquad\qquad \text{IV.2}$$

$$\frac{d\,\rho}{dt} + \rho\frac{\partial\,u}{\partial x} = 0 \qquad ; \qquad\qquad \text{IV.3}$$

Momentum:

$$\alpha \;\; \rho\,e\,E = -m_h \frac{\partial\,P_e}{\partial x} \qquad ; \qquad\qquad \text{IV.4}$$

$$P_i = \frac{\partial}{\partial x}(p_e + p_i) \qquad ; \qquad\qquad \text{IV.5}$$

$$\frac{\partial\,p}{\partial x} = 0 \qquad ; \qquad\qquad \text{IV.6}$$

Energy:

$$\frac{5}{2}\frac{k}{m_h}\alpha\;\rho\frac{d\,T_e}{dt} - \frac{d\,P_e}{dt} = -\frac{\partial q_e}{\partial x} + \frac{5}{2}\frac{k}{m_h}T_e\frac{\partial}{\partial x}(\rho\;\alpha\;V)$$

$$-\frac{\rho\;\alpha\;V\,e\,E}{m_h} + \varepsilon_e \qquad ; \qquad \text{IV.7}$$

$$T_i = T_a(\,= T_h) \qquad ; \qquad\qquad \text{IV.8}$$

$$\frac{5}{2}\frac{k}{m_h}\rho \quad \frac{d}{dt}(\,T_h + \alpha T_e) - \frac{d\,p}{dt} = -\frac{\partial q_t}{\partial x} + \varepsilon_t \qquad ; \qquad \text{IV.9}$$

The definitions of the symbols in IV.1 to 9 are now considered in detail.

The plasma is considered here as an ideal gas mixture of electrons(e), singly ionized atoms (i) and neutral atoms (a). The partial pressure p_j of species j (j = e, i or a) is related to the number density n_j by:

$$p_j = n_j k T_j \qquad\qquad IV.10$$

where k is the Boltzmann constant and T_j the temperature of species j. The pressure p is given by:

$$p = \sum_j p_j \qquad\qquad IV.11$$

We assume that no external electric or magnetic field is applied to the plasma. The electric field E in equation(IV.4 and 7) is the field build up by the plasma. e is the elementary charge.

A consequence of the assumed quasi-neutrality (IV.2) is that the diffusion is ambipolar. The diffusion velocities V_j are thus related by:

$$V_e = V_i = - \frac{(1-\alpha)}{\alpha} V_a = V \qquad\qquad IV.12$$

where V is the ambipolar diffusion velocity and α is the degree of ionization:

$$\alpha = \frac{n_e}{n_a + n_i} \qquad\qquad IV.13$$

The diffusion velocities $\underline{V}_j$ are defined by:

$$\underline{V}_j = \underline{\bar{v}}_j - \underline{u} \qquad\qquad IV.14$$

where $\underline{\bar{v}}_j$ is the average of the velocity $\underline{v}_j$ of the particles of species j measured in the laboratory reference frame.

The mass average velocity $\underline{u}$ is given by:

$$\underline{u} = \frac{\sum_j m_j n_j \underline{\bar{v}}_j}{\sum_j m_j n_j} \qquad \text{IV.15}$$

The density ρ of the plasma is approximated by:

$$\rho = m_h (n_i + n_a) \qquad \text{IV.16}$$

where m_h is the mass of the heavy particles:

$$m_h = m_a = m_i \qquad \text{IV.17}$$

A characteristic length scale x_∞ for the boundary layer thickness is given by:

$$x_\infty = (\frac{\lambda_\infty \ t_\infty}{\frac{5}{2} \frac{k}{m_h} \rho_\infty})^{1/2} \qquad \text{IV.18}$$

where λ_∞ is the heat conductivity of the plasma and t_∞ is the characteristic time of observation. The index ∞ refers to the state of the gas outside the boundary layer.

The assumption of space charge quasi-neutrality is justified by the fact that for the conditions considered x_∞ is much larger than the Debye length.

In view of the uncertainties in the transport properties and the reaction rates (see appendix III) an inaccuracy in the model of the order of 10% is acceptable. This criterion is used in the derivation of equations IV.1 to 9. The shortest time scale appearing in the problem is t_h, the mean free flight time of the heavy particles. Terms of the order $(t_h/t_\infty)^{1/2} = 0(10^{-2})$ have been neglected. Terms of the order $(m_e/m_a)^{1/2}$ and $(V^2 m_h/k \ T_h)$ are also neglected.

The source terms M_i, P_i, ε_t, ε_e and the fluxes V, q_e, q_t are estimated on the basis of the Chapman-Enskog procedure (appendix II). We consider here only some general properties of the expressions used.

From the first approximation of the ion momentum source term

56

P_i we find:

$$V = - \frac{D_{ia}}{n_i k T_h} \frac{\partial}{\partial x} (p_e + p_i) \qquad \text{IV.19}$$

where D_{ia} is the ion-atom binary diffusion coefficient.
Within the same approximation one can write for the heat fluxes q_j:

$$q_j = - \lambda_j^m \frac{\partial T_j}{\partial x} + \frac{5}{2} n_j k T_j V_j \qquad \text{IV.20}$$

where λ_j^m is the heat conductivity of species j in the mixture.
The total heat flux q_t is given by:

$$q_t = \sum_j q_j \qquad \text{IV.21}$$

The energy source terms ε_e and ε_t are related to the ion-mass production source term M_i by:

$$\varepsilon_t = - M_i \frac{k}{m_h} T_{ion} - Q_r - \frac{\partial q_r}{\partial x} \qquad \text{IV.22}$$

and

$$\varepsilon_e = \varepsilon_{eh} - M_i \frac{k}{m_h} (T_{ion} + \frac{5}{2} T_e) - Q_r - \frac{\partial q_r}{\partial x} \qquad \text{IV.23}$$

where ε_{eh} is the electron energy source term resulting from the electron-heavy particles elastic collisions:

$$\varepsilon_{eh} = 4 \frac{k}{m_h} n_e (m_e/m_h) \rho (8 k T_e / \pi m_e)^{1/2} (\alpha Q_{ei}^{(1,1)} + (1-\alpha) Q_{ea}^{(1,1)}) (T_h - T_e)$$

$$\text{IV.24}$$

where the average cross sections $Q_{ei}^{(1,1)}$ and $Q_{ea}^{(1,1)}$ are given in appendix III.
Following Kopainsky (71) we assumed in IV.22 and 23 that the heat transfer by radiation is due to a radiative conduction term q_r and a transparent radiation loss Q_r. q_r is proportional to the temperature gradient:

57

$$q_r = -\lambda_r \frac{\partial T}{\partial x} \qquad\qquad \text{IV.25}$$

where λ_r is the Rosseland radiative heat conductivity.

The transparant radiation loss term Q_r is assumed to be a function of the local thermodynamic state of the plasma only.

Expressions for the ion-mass source term M_i are considered in appendices III and IV.

IV.c.   Formula for the determination of the heat conductivity

We assume a single temperature T:

$$T = p/k(n_a + 2n_e)$$

IV.26

We define the heat conductivity λ of the plasma by:

$$\lambda = \sum_j \lambda_j^m + \lambda_r$$

IV.27

In our definition the "reactive heat conductivity" is not included.
A definition of the total heat conductivity of the plasma including
the reactive heat conductivity (Devoto 73) is only meaningful in the
case of local thermodynamic equilibrium and for a plasma with a
uniform pressure

Using definition IV.27 we write the energy equation IV.9 as:

$$\frac{\partial}{\partial x} \lambda \frac{\partial T}{\partial x} = \frac{3}{2} \frac{dp}{dt} - \frac{5}{2} \frac{p}{n_h} \frac{dn_h}{dt} + n_h k T_{ion} \frac{d\alpha}{dt}$$

$$+ Q_r + \frac{\partial}{\partial x} (k n_e V (\frac{5}{2} T + T_{ion}))$$

IV.28

In order to obtain an explicit expression for λ Emmons (67)
and Asinovsky (71) use an integration procedure similar to the
procedure of Vrugt (76) (section II.c).
We consider here a differential approach similar to the formula of
Ewald (71) (section II.c) which follows directly from IV.28 and has
the advantage of being (more) local:

$$\lambda = \frac{\frac{3}{2}(dp/dt) - \frac{5p}{2n_h}(dn_h/dt) + n_h kT_{ion}(d\alpha/dt) + Q_r + \frac{\partial}{\partial x}(n_e kV(\frac{5}{2} T + T_{ion}))}{(\partial^2 T/\partial x^2) + \frac{1}{\lambda}(\partial\lambda/\partial T)(\partial T/\partial x)^2 + \frac{1}{\lambda}(\partial\lambda/\partial n_e)(\partial n_e/\partial x)(\partial T/\partial x)}$$

where:

IV.29

$$V = - (2 D_{ia}/(1 + \alpha))(\partial\alpha/\partial x)$$

IV.30

IV.d. Transparent radiation loss

The transparent radiation loss Q_r will be determined from the study of the behaviour of the plasma at the edge of the thermal boundary layer (chapter VIII). Assuming that the plasma is uniform we obtain from the energy equation:

$$Q_r = \frac{5}{2} \frac{p}{n_h} \frac{\partial n_h}{\partial t} - n_h k \, T_{ion} \frac{\partial \alpha}{\partial t} - \frac{3}{2} \frac{\partial p}{\partial t} \qquad\qquad \text{IV.34}$$

Outside the boundary layer we measure the pressure and the absorption of a light beam by the plasma. In order to determine the thermodynamic state of the plasma from these two quantities we must assume local thermodynamic equilibrium.

This assumption and the procedure for the determination of the thermodynamic state of the plasma outside the boundary layer are discussed in sections V.c and d.

60

V. FLOW INDUCED BY THE REFLECTION OF AN IONIZING SHOCK WAVE AT THE END-WALL OF A SHOCK TUBE.

V.a. Introduction

In the present chapter we give a qualitative description of the flow outside the boundary layer (section V.b).

In section V.c we consider the determination of the state of the plasma outside the boundary layer. An estimate of the state of the plasma just after ionization relaxation, is obtained from the Rankine-Hugoniot (RH) relations.

Combining these data with absorption and pressure measurements and assuming local thermodynamic equilibrium one can determine the state of the plasma outside the boundary layer.

The deviation of this state from local thermodynamic equilibrium as a result of radiation escape is considered in section V.d.

In section V.e we consider the thermal Rayleigh problem in partially ionized argon. This model developed by Hutten (76) is used in order to obtain some insight in the structure of the boundary layer and to calculate the convective velocity.

V.b.   Qualitative description of the flow outside the boundary
        layer

        We consider the flow induced by the reflection of a shock
wave at the end-wall of a shock tube for moderate Mach numbers,
$M_s \leqslant 10$. The ionization relaxation time behind the incident shock
is of the order of 1 ms (Kuiper 68).
The test time during which the pressure remains approximately constant
in the reflected shock region is about 0.3 ms.
We therefore can assume that the degree of ionization in region 2
(behind the incident shock wave) is negligible. We say that region 2
is frozen. The flow in the shock tube before reflection corresponds
to the flow described in section II.b.

        The flow after the reflection $(t \geqslant 0)$ is discussed on the
basis of an absorption measurement and two pressure measurements
(figures V.1, 2 and 3). We ignore the influence of the end-wall
boundary layer on the reflection process (section III.e).

        The light absorption in the continuum spectrum is roughly
proportional to the square of the electron density. A typical record
of the transmitted power P of a laser beam $(1 = 0.6328 \ \mu m)$ is given
in figure V.1. We see that in the initial phase, just after the
reflection $(t = 0)$, the ionization process is rather slow. This is
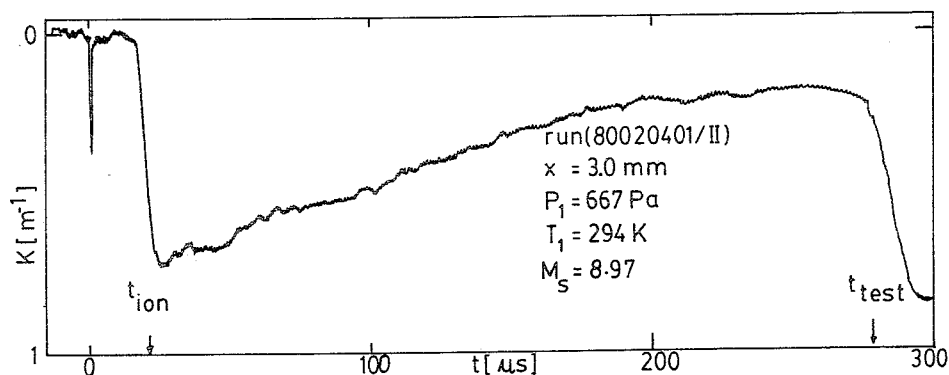due to the fact that atom-atom collisions are ineffective in the
ionization process.

run(80020401/II)
x = 3.0 mm
$P_1 = 667 \ Pa$
$T_1 = 294 \ K$
$M_s = 8.97$

Figure V.1 : Absorption of a light beam $(1 = 0.6328 \ \mu m)$
(see definition K equation V.1).

Therefore we may consider the initial phase of the flow in the reflected shock region to be frozen (fr) with respect to the ionization process. This frozen region 5 is denoted by 5_{fr}. The state of the gas 5_{fr} is calculated from the initial conditions (p_1, T_1) and the incident shock wave velocity by means of the (frozen) Rankine-Hugoniot relations (Appendix I).

When, after some time, the degree of ionization reaches the order of magnitude of 10^{-3}, the more effective electron-atom ionization process becomes dominant. The ionization rate suddenly increases. This phase, called the ionization front (Kuiper 68) occurs at $t = t_{ion}$ (figure V.1)

After the ionization front the state of the plasma is close to local thermodynamic equilibrium. The decrease of electron density as a function of time (figure V.1) is due to the escape of radiation. We call this period ($t \geq t_{ion}$) the radiation cooling region. We observe some waviness in the absorption signal. This corresponds to disturbances in the electron density that have also been observed by Kon'kov (75). A similar waviness of the electron density has been observed behind the incident shock wave in pure argon by Bristow (71) and Glass (78). These instabilities are strongly sensitive to the purity level of the argon. They might be caused by the interaction between the ionization process and transverse pressure waves. Bristow (71) noticed that the addition of 0.5% hydrogen to the argon has a strong stabilising influence. Some experiments in a 99.5% Ar + 0.5% H_2 mixture are described in chapter VIII.

At $t = t_{test}$ (figure V.1) we observe an increase of the electron density resulting from the compression of the plasma by the waves generated by the interaction between the reflected shock and the contact surface (section II.b).

At higher Mach numbers ($M_s \geq 12$) Kuiper (68) and Takano (79) observed a compression wave due to the interaction of the reflected shock with the ionization front behind the incident shock. In such cases bifurcation of the reflected shock occurs. No evidence of bifurcation was found in pure argon at low Mach numbers ($M_s < 10$). In the case of a 99.5% Ar + 0.5% H_2 mixture some experiments show evidence of bifurcation (chapter VIII).

An example of an end-wall pressure record is shown in figure V.2.

t_{ion}

P_{5fr} →

P/P_{5eq}

1

0

run (80100101/II)

x = 0 mm

P_1 = 667 Pa

T_1 = 295 K

M_s = 9.12

t_{test}

0   100   t [μs]   200   300
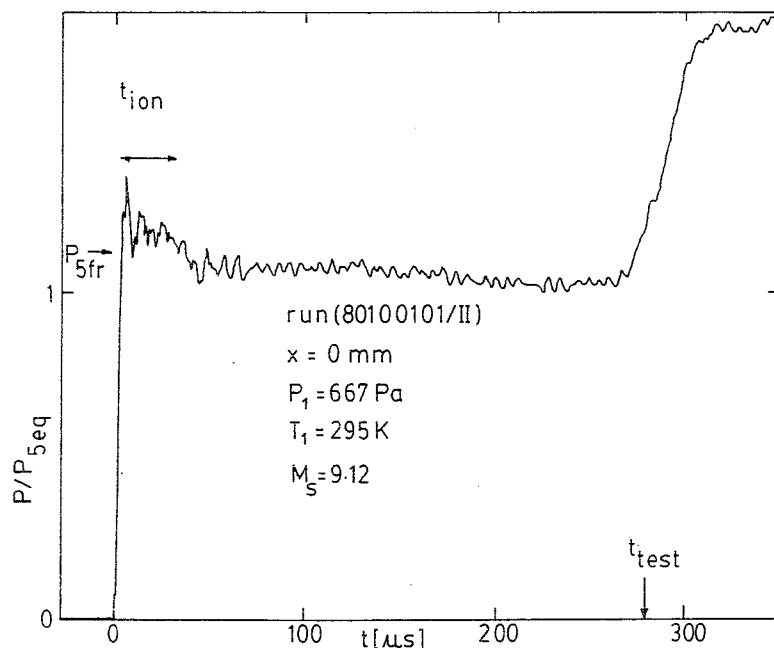
Figure V.2 : End-wall pressure record.

In the frozen region 5_{fr} (t $\leqslant$ t_{ion}) the pressure increases above P_{5fr} as a result of the influence of the inhomogeneity of region 2 (see section II.b and III.e).
During the ionization (t $\simeq$ t_{ion}) the pressure decreases.
This expansion wave is due to the temperature decrease of the gas in the ionization front resulting in a decrease of volume. The expansion waves generated in the ionization front and running away from the end-wall are absorbed by the reflected shock. This results in a deceleration of the shock. The expansion waves running towards the wall are reflected at the wall and then absorbed by the shock.

The increase of pressure for t $\geqslant$ t_{ion} is expected to be due to the influence of the inhomogeneity of region 2. The decrease

64

of pressure for 10^2 µs $\leqslant t \leqslant t_{test}$ is not well understood. Such a behaviour can be induced by radiation cooling or by waves generated by the diaphragm (see figure III.6).

A record of the side-wall pressure (x = 12 cm) is shown in figure V.3.
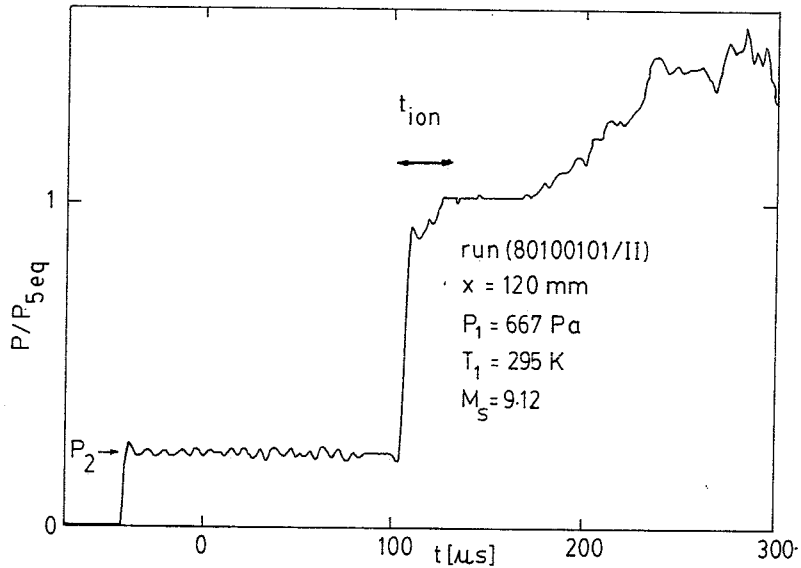
Figure V.3 : Side-wall pressure record.

After the compression by the incident and reflected shocks we observe at the side-wall a compression during the ionization relaxation. This effect is similar to the behaviour of the pressure behind a shock wave with constant velocity. Considering the ionization process in the reference frame of this "stationary" shock we observe a reduction of the velocity of the gas due to the increase of density. This deceleration implies an increase of the pressure as one can verify from the momentum conservation law (see for further details Glass 78). We conclude that at x = 12 cm, the reflected shock behaves qualitatively as the "ideal" reflected shock which would occur for $t \gg t_{ion}$ if region 2 were uniform and if radiation cooling would be negligible. Applying the integral conservation laws across this

"ideal" shock yields the Rankine-Hugoniot estimate of the equilibrium state of the plasma in region 5 (refered to as 5_{eq}). This model is described in section V.c.

On the basis of the previous observations we can draw a qualitative (x,t) diagram of the flow (figure V.4).
This diagram is similar to the diagram obtained by Kuiper (68).
In the diagram we show two particle paths (-----).
Following path 1 we observe the abrupt acceleration towards the end-wall which is induced by the incident shock, the deceleration by the reflected shock (stagnant region 5fr), the acceleration by the expansion wave induced by the ionization front and the deceleration in the ionization front itself.
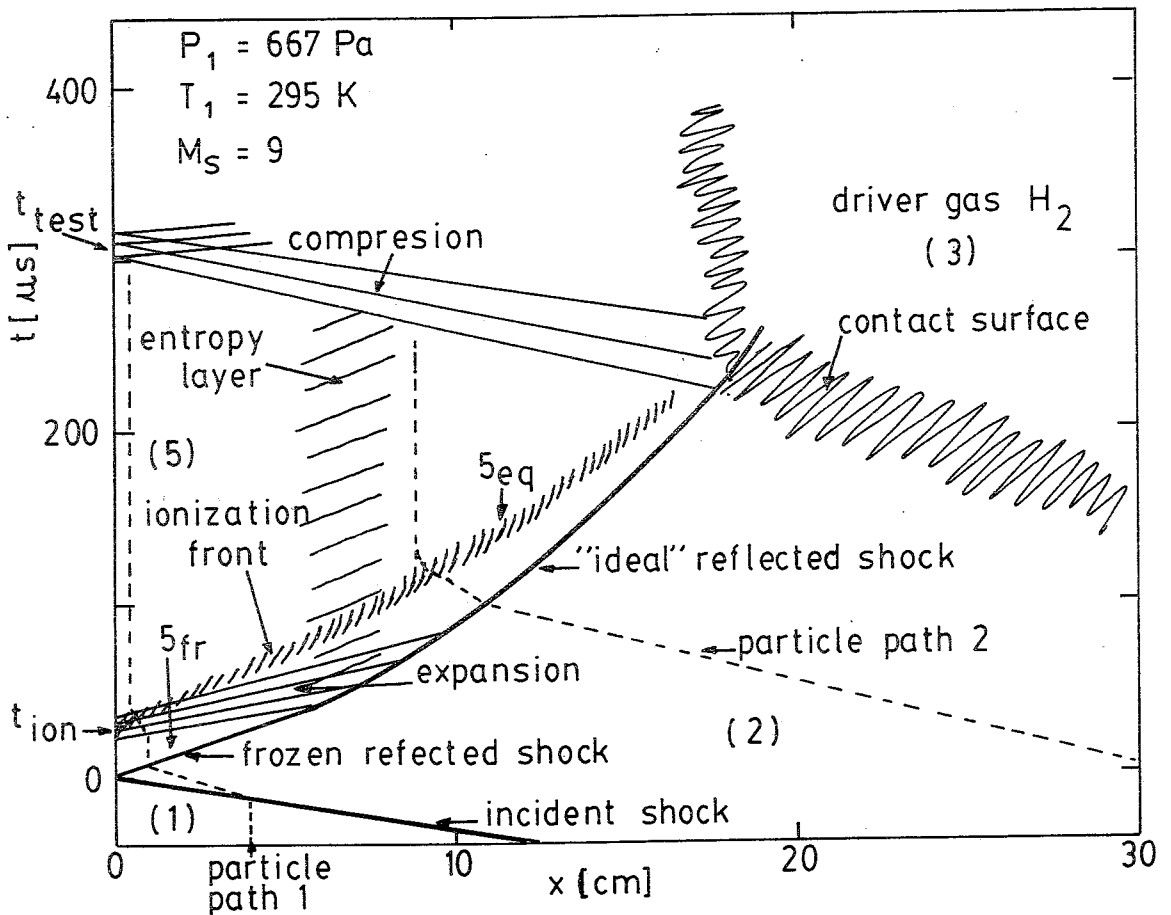
Figure V.4 : (x,t) diagram of the flow induced by the reflection of an ionizing shock wave in argon.

Following particle 2 we see that the gas in the frozen region behind the reflected shock is not stagnant.

The variation of the reflected shock velocity induced by the expansion wave results in a non-uniformity (entropy layer) of the reflected shock region. The flow is also complicated by the strong interaction between the expansion wave and the ionization front. Therefore a detailed description of the flow can only be obtained numerically as done by Takano (79).

Semi-linearized calculations as carried out by Smith (68) and Crespo-Martinez (68) can be used at low Mach numbers.

These models are rather inaccurate because of the large uncertainties in the reaction models used and in the influence of the inhomogeneity of region 2.

We can conclude from this discussion that the reflected shock region is in principle instationary and non-uniform and that a detailed determination of the state of the plasma at the edge of the boundary layer from measurements of the initial conditions, the incident shock speed and the end-wall pressure is a difficult proposition. In the next section we propose a procedure which should have an accuracy of 10%.

V.c.   Determination of the state of the plasma in the reflected
        shock region.

We assume that outside the boundary layer for $t > t_{ion}$, the
plasma is in a state of local thermodynamic equilibrium. In order to
determine the state of the plasma the measurement of two independent
state variables is sufficient. We consider here the determination of
the state of the plasma from measurements of the end-wall pressure
and the absorption of a light beam ($1 = 0.6328$ μm). [Ω]

The absorption coefficient K is defined by:

$$K = \frac{1}{P} \frac{d P}{d s} \qquad\qquad \text{V.1}$$

where P is the power of the light beam and s is the optical path
length. The absorption coefficient can be calculated when the plasma
is in a state of local thermodynamic equilibrium. For argon
calculations have been carried out by Schlüter (68) and Hoffsaess
(78). At high electron densities as considered here corrections have
to be made for the influence of microfields.
A considerable amount of experimental and theoretical studies are
devoted to this subject (Batenin (77), Erhardt (77), Goldbach (77),
Vorob'ev (78), Glasser (79) and Schlüter (80)). There is a rather
large scatter in the data presented.
For this reason we use the semi-empirical formula:

$$K = K_o (n_e/n_o)^2 \exp(T_o/T_e) \qquad\qquad \text{V.2}$$

in which (for $1 = 0.6328$ μm):
$T_o = 2.273 \times 10^4 K = h_p \omega/2 \pi k$
$n_o = 10^{23} m^{-3}$
and $K_o = 8.8 \times 10^{-2} m^{-1}$.

[Ω] Note:
  The determination of the state of the plasma in the reflected shock
  region from simultaneous absorption and emission of continuum
  radiation have been used in the studies of Kon'kov (73) and
  Hashiguchi (79).

The temperature dependence of K corresponds to the temperature dependence of the bound-free absorption assumed to be dominant. The experimental determination of K_o (in section VIII.b) is based on the assumption that just after ionization relaxation ($t = t_{ion}$) the state of the plasma corresponds to the Rankine-Hugoniot state 5eq.

This is the state of the plasma behind an "ideal" reflected shock (see V.b) which has a constant velocity v_r. The calculation of the state 5eq from the initial state (p_1, T_1) and the incident shock velocity v_s has been considered by Kuiper (68), Bengtson (70) and Hutten (76).

The state of the gas in region 2 is calculated by means of the Rankine-Hugoniot relations for a non-ionized gas (Appendix I). The state 5eq is related to the state 2 by the integral conservation laws:

$$(u_2 - v_r) \rho_2 = -v_r \rho_{5eq} \qquad\qquad V.3$$

$$p_2 + \rho_2 (u_2 - v_r)^2 = p_{5eq} + \rho_{5eq} v_r^2 \qquad\qquad V.4$$

$$h_2 + \frac{(u_2 - v_r)^2}{2} = h_{5eq} + \frac{v_r^2}{2} \qquad\qquad V.5$$

This set of equations is completed by the equations of state:

$$p = \rho RT (1 + \alpha) \qquad\qquad V.6$$

$$h = \frac{5}{2} R T + \alpha R(T_{ion} - \Delta T_{ion}) \qquad\qquad V.7$$

where the degree of ionization α is assumed to be given by the Saha relation:

$$\frac{\alpha^2}{1 - \alpha} = \frac{Z_e Z_i}{Z_a} \frac{m_a}{\rho} (2\pi m_e k \, T/h_p^2)^{3/2} \exp\left(- \frac{T_{ion} - \Delta T_{ion}}{T}\right)$$

$$V.8$$

where Z_j is the statistical weight of component j, h_p is the Planck constant and T_{ion} the ionization temperature. We used the approximation: $Z_e = 2$, $Z_i = 6$, $Z_a = 1$ and $T_{ion} = 1.83 \times 10^5 K$.

The lowering of ionization temperature ΔT_{ion} was calculated according to the Debye-Hückel theory (Drawin 71):   @

$$\Delta T_{ion} = 1.2 \frac{e^2 \, 2^{1/2}}{4\pi \, \varepsilon_o \, r_D \, k} \qquad\qquad V.9$$

where r_D is the Debye radius:

$$r_D = (\frac{\varepsilon_o \, k \, T}{e^2 \, n_e})^{1/2} \qquad\qquad V.10$$

e is the elementary charge and ε_o is the permittivity of vacuum.
The results of the calculations of the state 5eq are given in tables
(Appendix I).

The Rankine-Hugoniot state 5eq has been compared with
experimental data by Kuiper (68), Bengtson (70) and Kon'kov (73, 76).
Kuiper (68) mentions that the data on the electron density at 10 mm
from the end-wall agrees well with the calculations. The data at 4 mm
are about 10% higher. The results of Kon'kov (76) are similar to the
results of Kuiper (68). Bengtson (70) concludes that while the
average of the measured electron density agrees with the predicted
values an important scatter occurs as a result of the non-
reproducability of the flow in the shock tube (diaphragm opening, see
section III.e). Our own experience is in agreement with this
observation. The lower scatter in the electron density data of
Kuiper (68) is due to the fact that he only considered the average
of a few runs.
The electron temperature measured by Kon'kov (73) agrees well with
the Rankine-Hugoniot value.
While the electron density and the temperature agree within the
accuracy of the experiments with the predicted value, Bengtson (70)
obtained pressures significantly higher (7%) than the Rankine-Hugoniot
value. This effect is also observed in figure V.2 (see also section
VIII.b).

@ Note:
The calculated electron density and temperature are rather insensitive
to the lowering of ionization potential (Kuiper 68).

70

The fact that the average measured electron density and the
temperature are in agreement (within 10%) with the predicted values
is no clue for the validity of local thermodynamic equilibrium.
It is not impossible that various effects cancel. The deviation from
local thermodynamic equilibrium due to the instationarity of the state
of the plasma and to the influence of radiation escape on the reaction
rates is discussed in the next section.

Conclusion: Assuming local thermodynamic equilibrium one can use
equations V.2, 6 and 8 to determine the thermodynamic state of the
plasma from measurements of p and K.

V.d. Deviation from local thermodynamic equilibrium outside the
boundary layer.

As starting point for the study of the deviation of the state
of the plasma from local thermodynamic equilibrium we use the electron
continuity equation:

$$\frac{\partial n_e}{\partial t} + \frac{\partial}{\partial x}(n_e(u + V)) = \dot{n}_e \qquad\qquad V.11$$

Considering the plasma after ionization relaxation we assume that the
convective and diffusion velocities are negligible.

The source term $\dot{n}_e$ can be determined with the two step model
of Mitchner (73):

$$\dot{n}_e = n_e\, n_o\, {}_oS^1\, (1 - (n_e^2/n_o)/(n_e^2/n_o)_{st}) \qquad\qquad V.12$$

where ${}_oS^1$ is the reaction rate for excitation from the ground level
o to the first excited level 1 (see Appendix IV).
$(n_e^2/n_o)_{st}$ is the value of (n_e^2/n_o) which is found in a uniform and
stationary plasma.
The deviation of $(n_e^2/n_o)_{st}$ from the value $(n_e^2/n_o)_{Saha}$ calculated by
means of the Saha equation is due to radiation escape.

The continuity equation can be rewritten as:

$$\frac{(n_e^2/n_o)}{(n_e^2/n_o)_{Saha}} = \frac{1 - (\frac{\partial n_e}{\partial t})/(n_e n_o\, {}_oS^1)}{(n_e^2/n_o)_{Saha}\,(n_o/n_e^2)_{st}} \qquad\qquad V.13$$

The $(\partial n_e/\partial t)$-term can be estimated from absorption measurements
(figure V.1). The factor $(n_e^2/n_o)_{Saha}\,(n_o/n_e^2)_{st}$ can be calculated
with the collision-radiation model described in Appendix IV.
The results obtained are given in table V.1.

M_s	$(\partial n_e/\partial t)/(n_e n_o S^1)$	$(n_e^2/n_o)_{Saha}(n_o/n_e^2)_{st} - 1$
7	-10^{-1}	10^{-1}
8	-6×10^{-2}	3×10^{-2}
9	-5×10^{-2}	2×10^{-2}

Table V.1:
Deviation from local thermodynamic equilibrium outside
the boundary layer as a function of M_s.
$x = 1$ mm, $p_1 = 667$ Pa, $T_1 = 295$ K.

We see that the deviation from local thermodynamic equilibrium
induced by radiation escape and by the instationarity of the flow
counteract. Further we conclude that the deviation from local
thermodynamic equilibrium can be neglected in view of the uncertainty
in the experimental determination of the electron density (10%).

V.e.   The boundary layer structure.

Model

The studies of shock tube viscous (side-wall) and thermal
(end-wall) boundary layers by Knöös (68), Kuiper (68), Hutten-Mansfeld
(76) and Liu (78, 79, 80) have clearly demonstrated that such flows
cannot be described within the frame of an equilibrium theory
(section I.d).

In this section we use the relaxation model developed by Hutten (76)
in order to obtain some insight in the structure of the end-wall
thermal boundary layer.

The equations governing the flow have been given in section IV.b.
The equations used for the fluxes and the source terms are given in
Appendix III. We neglect here the influence of radiation transfer
so that equations IV.22 and 23 are replaced by:

$$\varepsilon_t = -M_i \frac{k}{m_h} T_{ion}$$

and

$$\varepsilon_e = \varepsilon_{eh} - M_i \frac{k}{m_h} (T_{ion} + \frac{5}{2} T_e) \qquad\qquad V.14$$

where ε_{eh} is given by IV.24.

Assuming that the ionization rate is determined by the electron atom
inelastic collisions we have:

$$M_i = m_h n_a n_e \, {}_0S^1 (1 - (n_e^2/n_a)/(n_e^2/n_a)_{eq}) \qquad\qquad V.15$$

where $(\frac{n_e^2}{n_a})_{Saha}$ is given by V.8 in which we neglect the lowering of
ionization temperature $(\Delta T_{ion} = 0)$.

${}_0S^1$ is a function of the electron temperature given in Appendix VI.
From equations IV.24 and V.15 we see that the source terms ε_{eh} and M_i
are the driving terms for the relaxtion of the state of the gas
towards local thermodynamic equilibrium.

In the model we consider the behaviour of a uniform partially
ionized monatomic gas which is suddenly (at t = 0) brought in contact

with a cold metal wall. The state of the gas outside the boundary layer is assumed to be constant and corresponds to a state of local thermodynamic equilibrium. This problem is a special case of the so called Rayleigh problem (Knöös (68)), it is therefore referred to as the "thermal Rayleigh problem".

When the problem is considered in Lagrangian coordinates the velocity u appears explicitly only in the continuity equation IV.3. Eliminating E by IV.4 and using the expressions of Appendix III for the source terms and the fluxes one obtains a closed set of equations for p, α, T_e and T_h.
Because the pressure is uniform, it is determined by the boundary conditions. We are thus left with a set of three equations for α, T_e and T_h. This set of equations is given in Appendix III. The formulation of the problem is completed by specification of the initial and boundary conditions.
The initial and outer boundary conditions are given by:

$$\alpha(x,o) = \lim_{x \to \infty} \alpha(x,t) = \alpha_\infty$$

$$T_e(x,o) = T_h(x,o) = \lim_{x \to \infty} T_e(x,t) = \lim_{x \to \infty} T_h(x,t) = T_\infty$$

$$\rho(x,o) = \lim_{x \to \infty} \rho(x,t) = \rho_\infty \qquad\qquad V.16$$

where (α_∞, T_∞, ρ_∞) are constants related by the Saha relation V.8. Values for (α_∞, T_∞, ρ_∞) are calculated from the initial conditions (ρ_1, T_1) and the incident shock Mach number M_s by means of the Rankine-Hugoniot relations (section V.c).

In order to obtain the boundary conditions at the wall a collisionless sheath model is used. We assume the wall to be non-emitting, fully catalytic and without net electric current at the wall. In the sheath a potential $\Delta\Phi$ is build up. From stability considerations Bohm (49) showed that the ion velocity at the edge of the sheath should satisfy the inequality:

$$(V(0,t))^2 \geqslant (k\, T_e/m_h) \qquad\qquad V.17$$

where we use the approximation obtained by Chen (65) for $T_e \gg T_h$.
Using the lower bound as an estimate for $V(0,t)$ and assuming a
Maxwellian velocity distribution for the electrons one finds:

$$\Delta\Phi \quad = \quad \frac{k\,T_e}{2\,e}\; \ln(m_i/2\,\pi\,m_e) \qquad\qquad \text{V.18}$$

Equating the molecular energy flux of those electrons at the edge of
the sheath which have sufficient energy to overcome the sheath
potential, to the energy flux $q_e(0,t)$, we obtain:

$$q_e(0,t) = -\,\frac{n_e(0,t)}{4}\,\left(\frac{8\,k\,T_e(0,t)}{\pi\,m_e}\right)^{1/2}\,(2kT_e(0,t) + e\Delta\Phi)\exp\left(-\,\frac{e\,\Delta\Phi}{k\,T_e(0,t)}\right)$$

$$\text{V.19}$$

where $\Delta\Phi$ is given by V.18.
Equation V.19 and the assumption that $V(0,t)$ is equal to the Bohm
velocity, yield two boundary conditions at the wall.
The boundary conditions are completed by:

$$T_h(0,t) \quad = \quad T_w \qquad\qquad \text{V.20}$$

where T_w is the wall temperature which is assumed to be constant
(T_w = 350 K). The numerical solution of the problem is described by
Hutten (76).

Comment on the boundary conditions at the wall.

Although the collisionless sheath model has been widely used
(see review in Liu (79))the validity of the model is not well
established. The Bohm criterion is in contradiction with the
assumption that the diffusion velocity is small compared to the
thermal speed of the heavy particles (Hutten-Mansfeld (76)).
The assumption that the wall is non-emitting is contradicted by the
experimental evidence obtained by Vervish (79) in his study of the
viscous boundary layer at low pressures. Recent research on the
theory of the electrical sheath at high pressures has shown that the
neccessity of the Bohm criterion might be questionable (Schram (80)).

For these reasons we decided to study the sensitivity of the
model to variations of the boundary conditions at the wall. Therefore
we used fixed value boundary conditions as an alternative to the
sheath model.

Boundary layer structure.

When a hot uniform partially ionized gas is suddenly brought
in contact with a cold metal wall the state of the gas in the vicinity
of the wall will be strongly modified by the presence of the wall.

The temperature of the heavy particles at the wall will be
close to the surface temperature of the wall if the time scale of
observation t_∞ is much greater than the mean free flight time t_h of
the heavy particles. As a result of the high value of the density and
the heat conductivity of the wall this contact temperature will be
close to the initial wall temperature. This induces a strong non-
uniformity of the gas temperature which implies a heat flux from the
hot gas towards the wall.

Due to the strong catalytic influence of the wall, the degree
of ionization of the gas at the wall will be very low. This induces
a strong non-uniformity in the composition of the gas which results
into a diffusion flux towards the wall.

The relative importance of the heat conduction and of the
diffusion on the structure of the boundary layer is given by the
Lewis number Le:

$$Le \quad = \quad \frac{2}{5} \quad \frac{m_h}{k \, \rho} \quad \frac{\lambda_a^m}{D_{ia}} \qquad\qquad V.21$$

At the outer part of the boundary layer $(Le)_\infty = 0(10)$ so that heat
conduction is dominant. Close to the wall $(Le)_w = 0(1)$ and we expect
therefore that in the inner part of the boundary layer diffusion and
heat conduction are of equal importance.

The structure of the boundary layer will also be determined
by the relaxation rate towards local thermodynamic equilibrium.
Close to the wall, as a result of the low electron density, the flow
is frozen and the electrons and heavy particles behave independently.
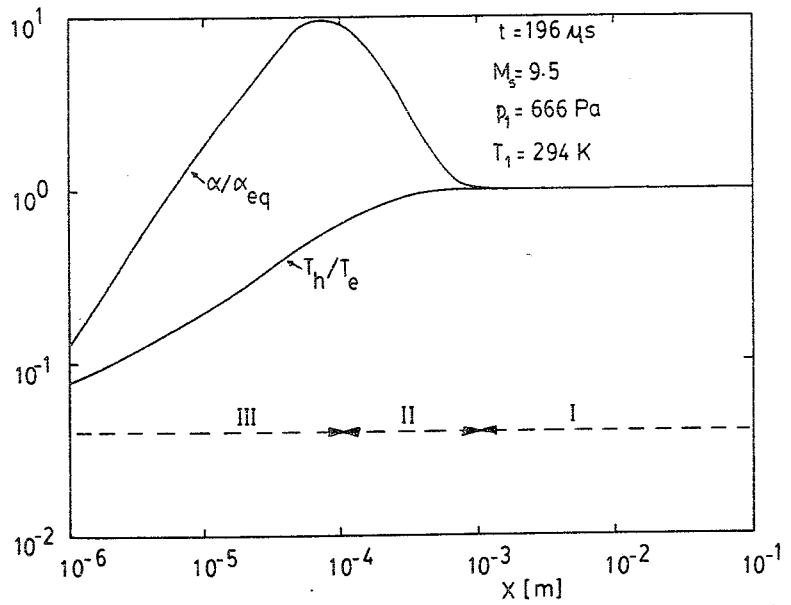Far from the wall due to the high electron density the relaxation

Figure V.5 : Deviation of the state of the plasma from local thermodynamic equilibrium as a function of the distance to the wall.
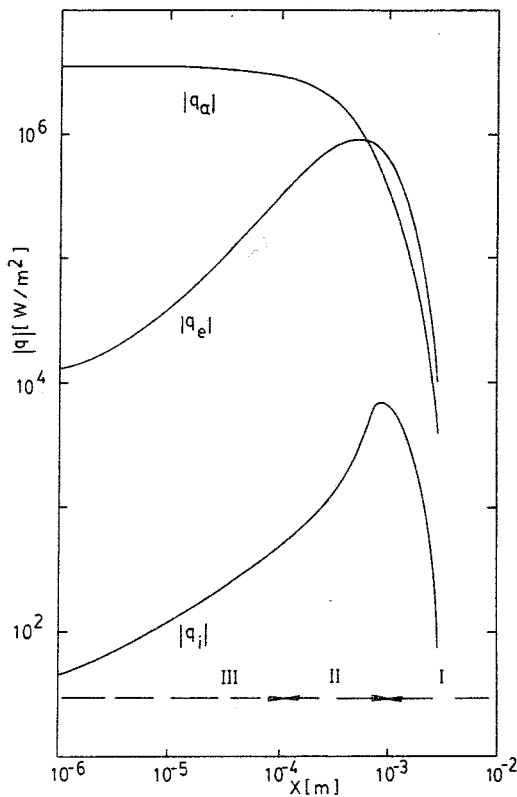

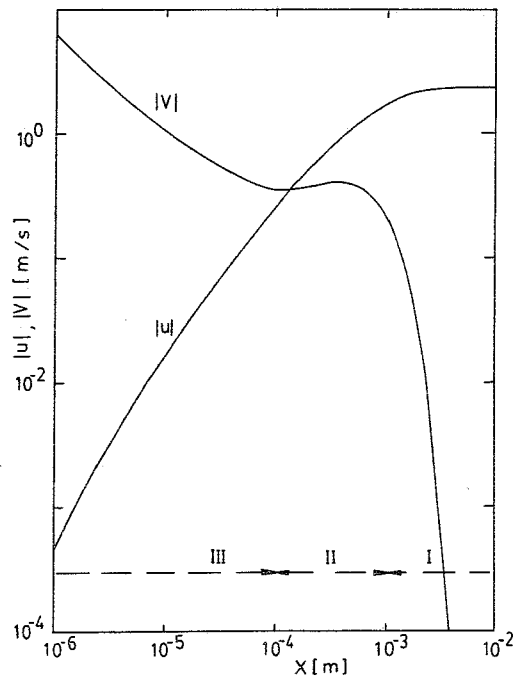Figure V.6 : Heat fluxes as functions of the position x. M_s = 9.5, p_1 = 666 Pa, T_1 = 294K.

Figure V.7 : Ambipolar and mass averaged velocity as functions of the position x. M_s = 9.5, p_1 = 666 Pa, T_1 = 294K.

78

time is small and local thermodynamic equilibrium is approached.
The high electron density implies also a high heat conductivity of
the mixture as a result of the electron contribution and a large
specific heat due to the energy involved in the ionization.
The various effects are clearly illustrated by the behaviour of α/α_{eq}
and T_h/T_e as a function of x for $t = 1.96 \times 10^{-4}$s (figure V.5).
The behaviour of the fluxes q_e, q_a, q_i and of the velocities V and u
are given in figures V.6 and 7.
For these data we see that the boundary layer can roughly be separated
into an equilibrium outer part dominated by heat conduction (region I,
$x \geqslant 1$ mm), a relaxation part (region II, 0.1 mm $\leqslant x \leqslant 1$ mm) and a
frozen inner part (region III, $x < 0.1$ mm).
More insight in the influence of the coupling between the various
processes is obtained by considering the limiting cases of the model
(section V.f).

Influence of the wall boundary conditions.

From the previous discussion we have seen that the electron
temperature and density profiles depend strongly on the coupling
between the transport processes and the relaxation phenomena.
However the discussion is obscured by the influence of the boundary
conditions. We consider therefore some calculations with fixed value
boundary conditions instead of the collisionless sheath model.
When a value of $\alpha(0,t) = 10^{-6} x \ \alpha_\infty$, lower than the value
predicted from the collisionless sheath model, is used, the deviation
of the n_e profile from the calculations with the collisionless sheath
model is negligible. A value for $\alpha(0,t) = 10^{-3} x \ \alpha_\infty$ corresponds to an
electron density $n_e(0,t)$ two orders of magnitude higher than the value
calculated with the collisionless sheat model.
This high electron density might not be physically unrealistic as the
photoionization can produce high electron densities at the wall
(Vervisch (79)). We are mainly concerned with the behaviour of the
electron density which we can determine experimentally, $x \geqslant 0.4$ mm.
From figure V.8 we see that for $\alpha(0,t) = 10^{-3} x \ \alpha_\infty$ and for
$0.2 \leqslant T_e(0,t)/T_\infty \leqslant 1.0$ there is no significant deviation (less than
10%) of n_e from the values calculated with the collisionless sheath

model for x $\geqslant$ 0.4 mm.

This result can be understood by the fact that the degree of ionization in the inner part of the boundary layer is relatively low. The heat flux at the wall and in the inner part of the boundary layer are determined by the atomic heat conduction.
Therefore the heat conduction dominated outer part of the boundary layer will not be sensitive to the behaviour of the electrons in the inner part.

In spite of the large uncertainties in the model for small distances from the wall it is certainly meaningfull to compare the experimentally determined electron density profiles with the calculated profiles.
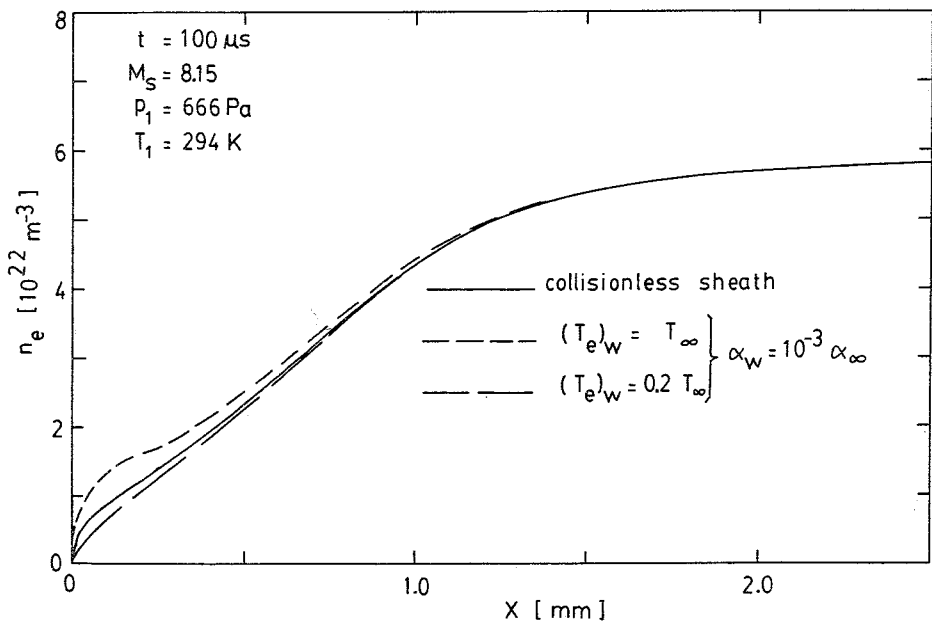
Figure V.8 : Influence of the boundary conditions at the wall on the electron density profile.

V.f.   Influence of relaxation processes on the structure of the
        boundary layer. &

We now consider limit cases of the thermal Rayleigh problem
discussed in the previous section. When the relaxation time for a
process is large compared to t_∞ the situation is said to be frozen
(fr), the corresponding source term is negligible i.e.:

$$M_i = 0 \qquad\qquad\qquad V.22$$

or

$$\varepsilon_{eh} = 0 \qquad\qquad\qquad V.23$$

The consideration of a frozen limit does not change the mathematical
formulation of the problem.

When the relaxation time for a process is small compared to
t_∞ (and t_h) equilibrium (eq) is achieved.
In such a case the corresponding equilibrium relation:

$$(n_e^2/n_a) = (n_e^2/n_a)_{eq} \qquad\qquad\qquad V.24$$

or

$$T_e = T_h \qquad\qquad\qquad V.25$$

can be used in order to eliminate one of the independent variables.
The corresponding differential equation (IV-1 or IV-7) is used to
eliminate the source term (M_i or ε_{eh}) from the other equations.

The two relaxation processes (M_i and ε_{eh}) are independent, we
obtain therefore from the combination of the three possibilities
frozen (fr), reaction (re) and equilibrium (eq) nine models.
The relation between the models is clarified in table V.2.

& Note:
The study of the equilibrium and frozen limits has been carried out
by R. van Panthaleon van Eck.

eqE-eqM	reE-eqM	frE-eqM
1 diff.eq	2 diff.eq	2 diff.eq
<u>b.c.:</u>	<u>b.c.:</u>	<u>b.c.:</u>
$T_e(0,t)=T_h(0,t)=T_w$	$T_e(0,t)=0.7\,T_\infty$	$T_e(0,t)=0.7\,T_\infty$
$\alpha(0,t)=\alpha_{eq}$	$T_h(0,t)=T_w$	$T_h(0,t)=T_w$
	$\alpha(0,t)=\alpha_{eq}$	$\alpha(0,t)=\alpha_{eq}$

eqE-reM	reE-reM	frE-reM
2 diff.eq	3 diff.eq	3 diff.eq
<u>b.c.:</u>	<u>b.c.:</u>	<u>b.c.:</u>
$T_e(0,t)=T_h(0,t)=T_w$	$T_h(0,t)=T_w$	$T_h(0,t)=T_w$
$V(0,t)=(kT_e/m_h)^{1/2}$	collisionless sheath	collisionless sheath

eqE-frM	reE-frM	frE-frM
2 diff.eq	3 diff.eq	3 diff.eq
<u>b.c.:</u>	<u>b.c.:</u>	<u>b.c.:</u>
$T_e(0,t)=T_h(0,t)=T_w$	$T_h(0,t)=T_w$	$T_h(0,t)=T_w$
$V(0,t)=(kT_e/m_h)^{1/2}$	collisionless sheath	collisionless sheath

<u>Table V.2.</u>

<u>Relation between the nine models.</u>

Abbreviations: eq = equilibrium, re = reaction, fr = frozen

$E = \varepsilon_{eh}$, $M = M_i$

diff.eq. = differential equation

b.c. = boundary conditions.

When equilibrium is assumed for a given process the number of
unknowns is reduced and one of the boundary conditions has to be
removed. The boundary conditions used are given in table V.2.
These boundary conditions must be considered as ad hoc assumptions. ⊗
In the reE-eqM and frE-eqM cases we used the fixed value boundary
condition:

$$T_e(0,t) = 0.7\ T_\infty \qquad\qquad V.26$$

in order to obtain values of $T_e(0,t)$ of the same order of magnitude
as the one obtained in the reE-reM model.

Comparison of the reaction model with the limiting cases.

In figure V.9 we compare the heavy particles temperature
profiles in the nine cases. We see that T_h is rather insensitive to
the relaxation model. The most striking difference between the various
models is the increase of the boundary layer thickness in the eqE
cases in comparison to the reE-reM model.
This is due to the increase in the electron heat flux q_e caused by
the strong electron temperature gradient as a result of the coupling
between the electron- and heavy particle temperatures (figure V.10).
In the eqE-frM case this effect is enhanced by the lower specific
heat capacity of the gas mixture (no recombination) and the higher
contribution of the electrons to the heat conduction (high degree of
ionization).

⊗ Note:
Instead of the fixed value boundary condition for the electrons (V.26)
we might have used in the reE-eqM and frE-eqM cases the Bohm criterion
as boundary condition $(V(0,t) = (kT_e/m_h)^{1/2})$.
However it is not correct to use equation V.19 without maintaining the
Bohm criterion since this is used to eliminate $\Delta\Phi$.
Such an erroneous boundary condition leads to the numerical
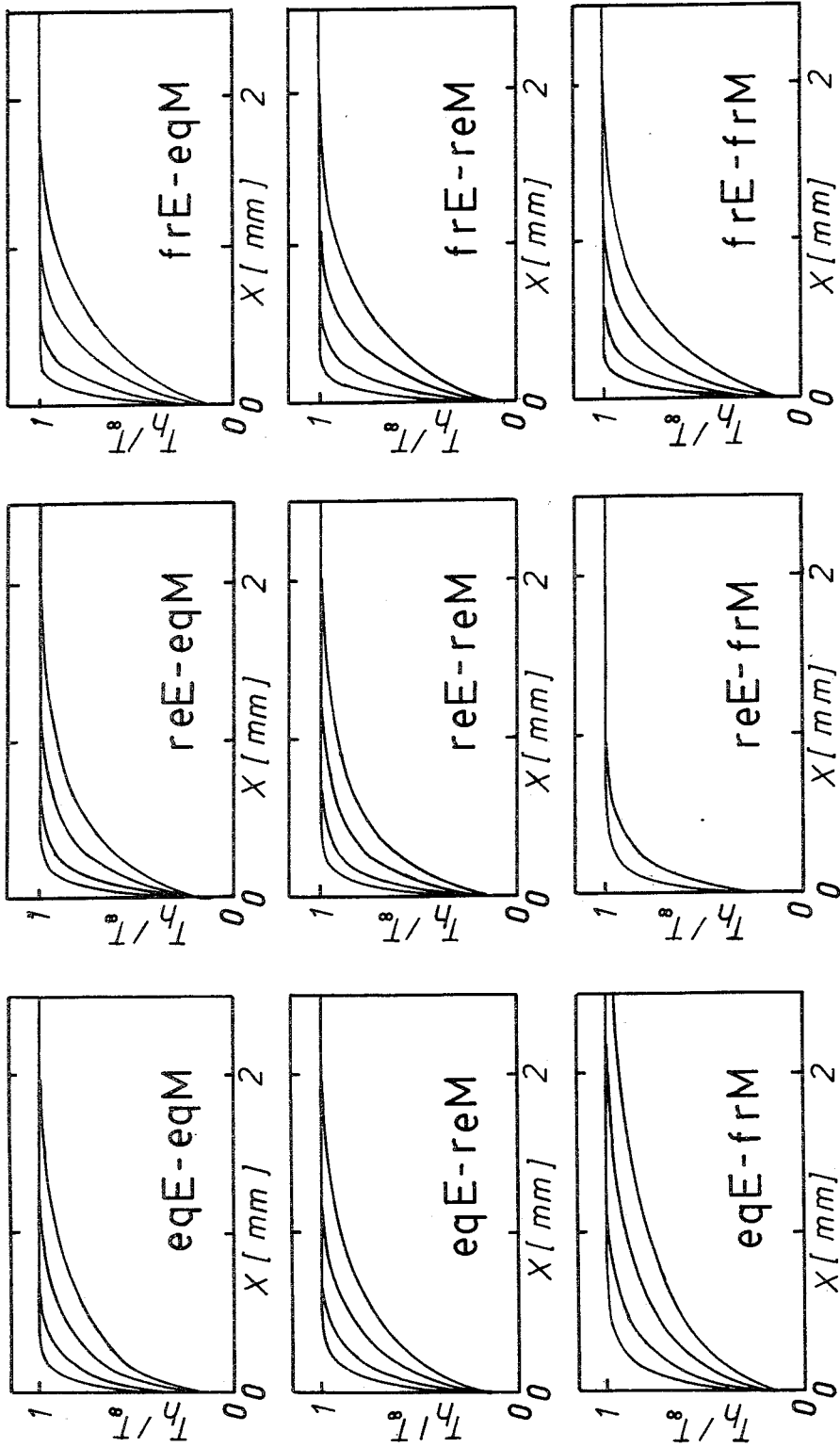instabilities reported by Hutten (76).

Figure V.9 : Reduced heavy particle temperature profiles of the boundary layer.

$t = 4, 16, 64$ and 196 µs. $M_s = 9.5$, $p_1 = 667$ Pa, $T_1 = 294$ K.

The calculations in the reE-frM case have only been carried out for t ⩽ 16 μs. Calculation for longer times is not possible without major modifications of the numerical model. The high density of relatively cold electrons close to the wall lowers considerably the thermal relaxation time and increases the already existing stiffness of the equations. The stiffness of the electron energy equation induces numerical instability so that in order to carry on the calculations one should use an eqE-frM approximation.
However in the reE-frM case the electron density close to the wall is so high that even the ideal gas law is not valid ($n_e = 0(10^{23} m^{-3}$),
$T_e = 0(10^3 K)$.
In such a case the expressions used for the transport coefficients are certainly not valid, hence the model has no physical meaning.

In figure V.10 the electron temperature profiles are given. Except for the frE-frM model the electron temperature is always higher than or equal to the heavy particle temperature. In the reE-reM case this is due to the weak coupling between the electron temperature and the heavy particle temperature combined with the fact that in our model the energy released in the recombination processes is transfered to the electrons. The absence of recombination in the reE-frM and frE-frM cases results in a lower wall temperature $T_e(0,t)$ than in the reE-reM and frE-reM cases.

In figure V.11 the electron density profiles are given. In the frM cases the electron density in the outer part of the boundary layer is proportional to the density and thus to T_h^{-1}. This explains the increase of n_e towards the wall. In the inner part of the boundary layer where diffusion is important the electron density decreases towards its value at the wall. In the eqE-frM model the diffusion dominated part of the boundary layer is thinner than in the reE-frM and frE-reM cases. This is due to the dependence of the diffusion velocity V(0,t) on the electron temperature $T_e(0,t)$ (Bohm criterion).

The frozen behaviour of n_e in the outer part of the boundary layer and the diffusion dominated inner part is still recognized in the frE-reM case. The reE-reM case has been discussed in section V.e.

The behaviour of n_e at the wall in the reE-eqM and frE-eqM
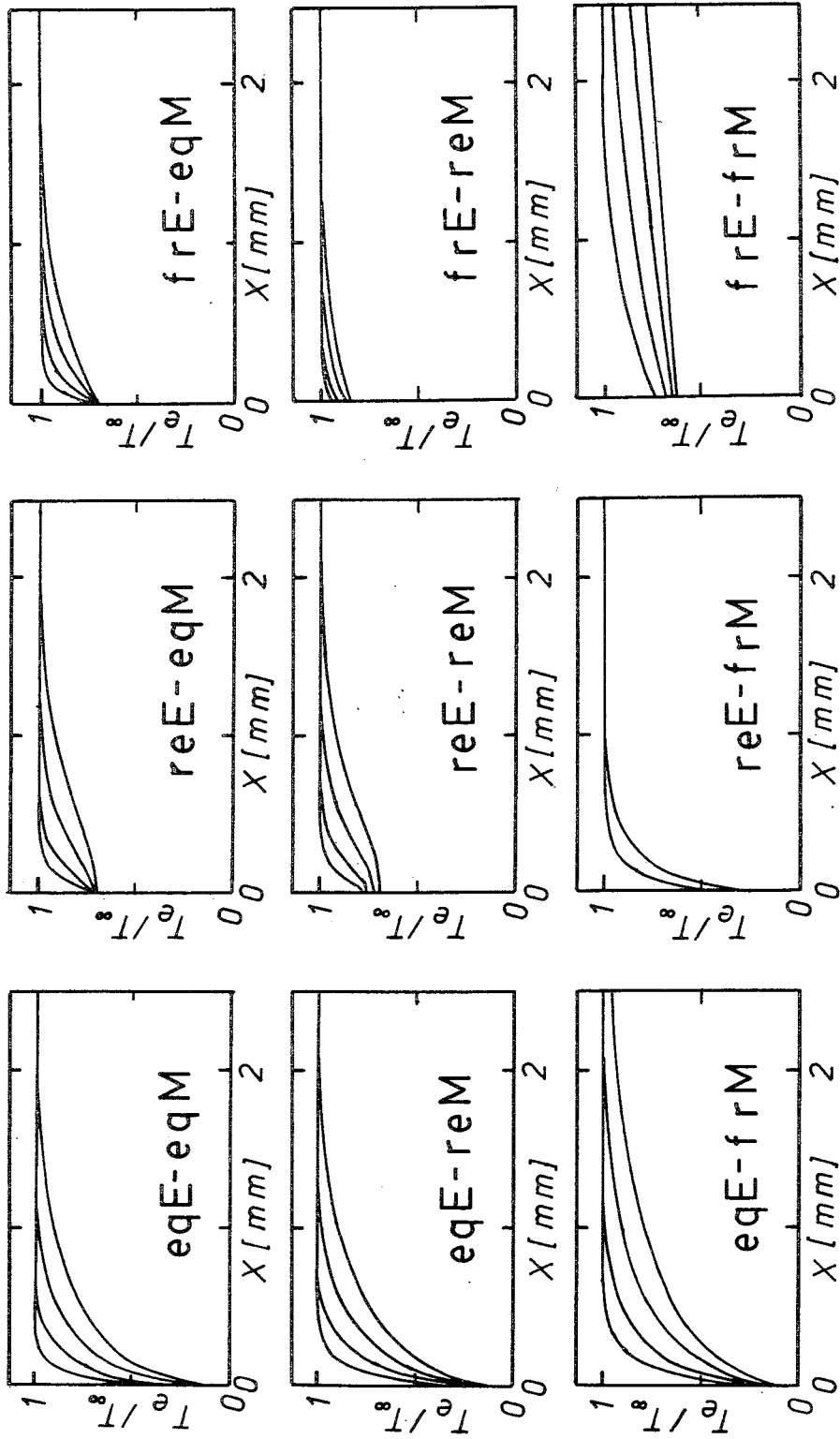
Figure V.10 : Reduced electron temperature profiles of the boundary layer.

$t = 4$, 16, 64 and 196 µs. $M_s = 9.5$, $p_l = 667$ Pa, $T_l = 294$ K.
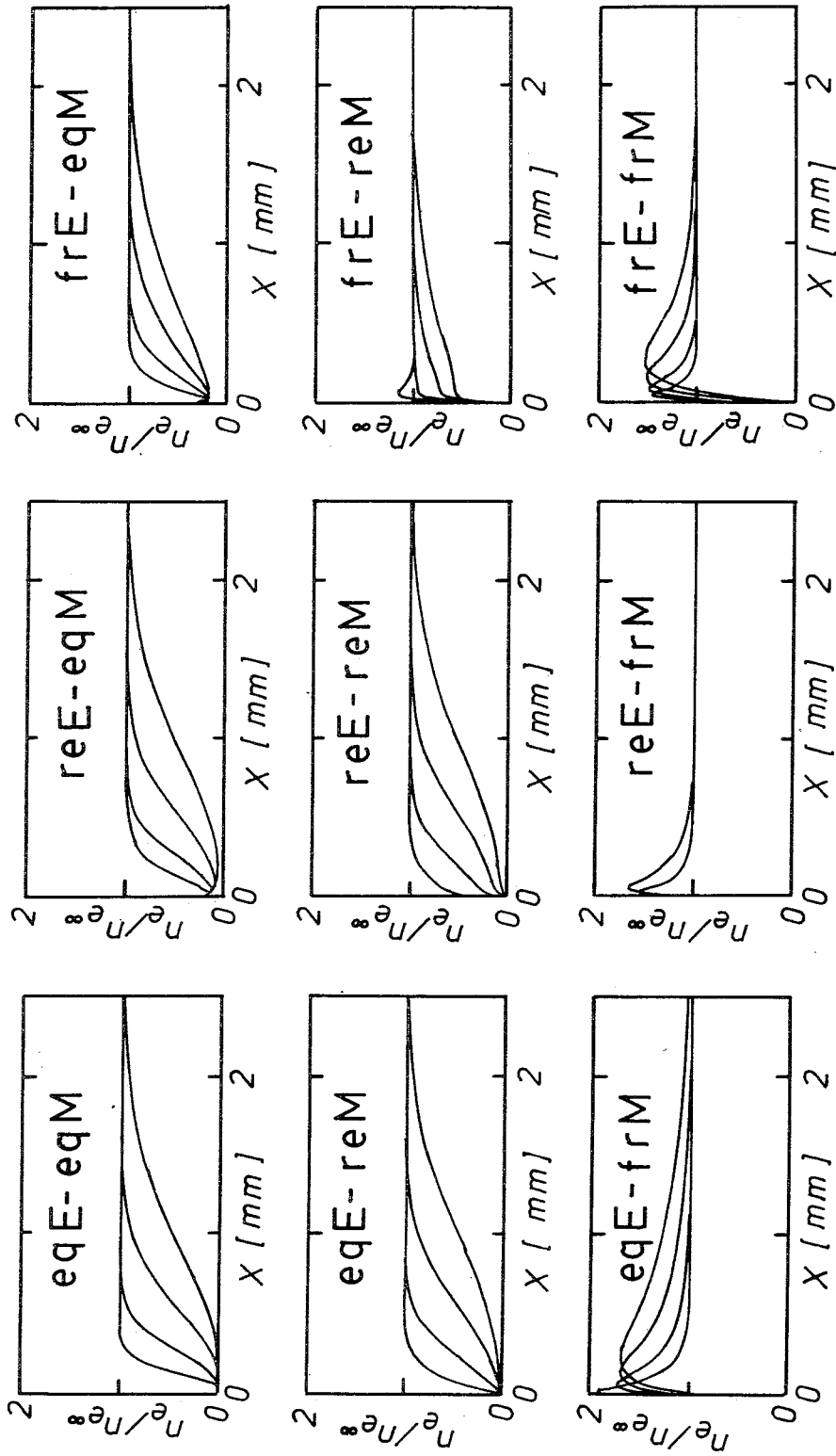
Figure V.11 : Reduced electron density profiles of the boundary layer.
t = 4, 16, 64 and 196 µs. M_s = 9.5, p_1 = 667 Pa, T_1 = 294 K.

M_s	α_∞ (10^{-2})	T_∞ $(10^4 K)$	P_∞ $(10^5 Pa)$
7.5	1.83	1.03	2.49
8.5	3.89	1.13	3.11
9.5	6.44	1.20	3.79

Table V.3:
State of the plasma outside the boundary
layer as a function of the Mach number for
the initial conditions: $p_1 = 666$ Pa, $T_1 = 294$ K.
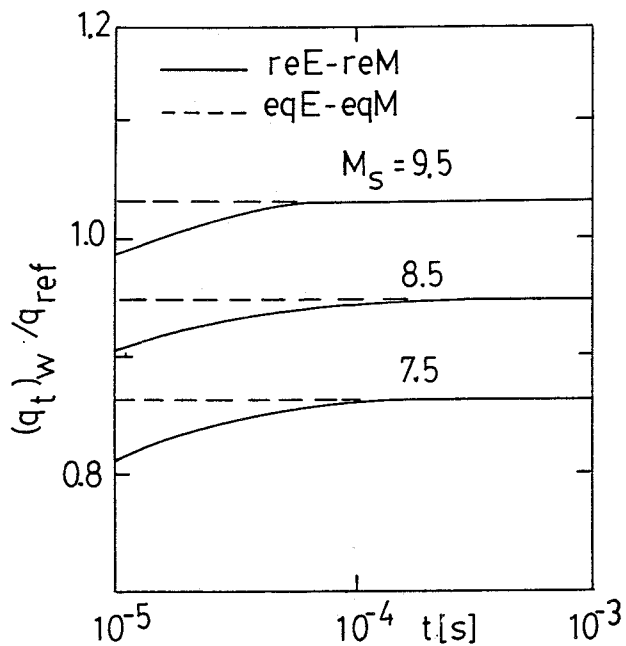
Figure V.12 : Heat flux at the wall as a function of
time. $p_1 = 667$ Pa, $T_1 = 294$ K.

cases is determined by the boundary conditions chosen for T_e and T_h.
No physical interpretation should be given to this behaviour because
it is a direct consequence of our choice of the value of $T_e(0,t)$
(eq. V.26).

Heat flux at the end-wall.

In figure V.12 we compare the molecular heat flux $(q_t)_w$ in the
reE-reM case with the heat flux in the eqE-eqM case, for various Mach
numbers.
The reference heat flux q_{ref} is defined by:

$$q_{ref} = - (T_\infty - T_w) \left(\frac{(\lambda_a^m \rho c_p)_w}{\pi t} \right)^{1/2} \qquad \text{V.27}$$

where c_p is the specific heat at constant pressure of the gas.
From these data we see that the eqE-eqM model yields an excellent
estimate of $(q_t)_w$ for $t \geqslant 10^{-5}$ s.

In table V.3. the state of the plasma outside the boundary
layer is given for the corresponding Mach numbers.

VI.   THE LASER SCHLIEREN METHOD

VI.a.   Introduction

        When a laser beam propagates through a refractive index
inhomogeneity it will undergo a "deflection" and a "deformation".
Measurements of the deflection can be used to determine the structure
of the inhomogeneity. Such a measurement method is called "laser
schlieren". The method developed by Kiefer (66) is often used for
the study of relaxation phenomena behind shock waves (Kiefer (79)).

        Vrugt (76) considered the use of the laser schlieren method
for the determination of the structure of the thermal boundary layer
at the end-wall of a shock tube in non-ionized gases. He estimated
the influence of diffraction and of deformation of the beam on the
schlieren signal using the theory of Kogelnik (65), that applies to
gaussian beams in a lens-like medium.

        Hutten (76) used the laser schlieren method as a plasma
diagnostic method. From simultaneous schlieren measurements at two
different wavelengths he could separate the electron contribution
to the schlieren signal from the atom contribution. This method is
similar to the two-wavelengths interferometry of Alpher (58).

        We give here an analysis of the laser schlieren method based
on the paraxial scalar wave theory. The basic equations are reviewed
in section VI.b. A model for the set-up and the definition of the
schlieren signal are given in section VI.c. We first neglect the
influence of diffraction and absorption and derive formulas based on
a geometrical optics analysis (VI.d.).
We show that for a lens-like medium and a suitable chosen
configuration of the laser beam, the schlieren signal is proportional
to the refractive index gradient at the center of the beam.
The influence of diffraction and absorption is discussed in section
VI.e.
In section VI.f we give a short review of the principle of the two-
wavelengths laser schlieren method.

VI.b. Basic equations and solutions

The analysis of the laser schlieren method given further is
based on geometrical optics and scalar wave theories of light.
These approximations are discussed by Born (75), Landau (69) and
Marcuse (72).

The scalar wave equation is derived from the Maxwell equations.
The fields are assumed to be weak so that linear constitutive
relations can be used. The plasma is assumed to be isotropic. The
electric fiel $\underline{E}$, the magnetic field $\underline{H}$ and the charge density ρ_e are
separated into a rapidly changing harmonic function of space and time
and a slowly varying amplitude:

$$\underline{E} = \underline{e} \exp(i(\omega t - \Sigma))$$
$$\underline{H} = \underline{h} \exp(i(\omega t - \Sigma))$$
$$\rho_e = \hat{\rho}_e \exp(i(\omega t - \Sigma)) \qquad\qquad VI.1$$

where $\underline{e}$, $\underline{h}$ and $\hat{\rho}_e$ are the amplitudes.
ω is the frequency which is assumed to be constant.
Σ is the phase.

From the Maxwell equations it appears that $\underline{e}$ and $\underline{h}$ are in
first approximation normal to $\nabla\Sigma$. For conditions such as considered
here the wave equations for the components of the field are identical.
The field can therefore be described by the amplitude e of the vector
$\underline{e}$.

The scalar wave equation is:

$$\nabla^2 e + (k^2 - (\nabla\Sigma)^2)e = i (2(\nabla\Sigma).(\nabla e) + e \nabla^2\Sigma) \qquad VI.2$$

The wave number k is defined by:

$$k^2 = \omega\mu(\epsilon\omega - i\sigma) \qquad\qquad VI.3$$

where μ is the magnetic permeability, ϵ is the permittivity and σ is
the conductivity.
The refractive index N of the plasma is related to k by:

$$N = k c /\omega \qquad\qquad VI.4$$

where c is the speed of light in free space.

Using a photo-detector we measure the average energy flux density $\underline{I}$ defined by:

$$\underline{I} = \frac{\omega}{2\pi} \int_{-\pi/\omega}^{\pi/\omega} \underline{E} \times \underline{H} \, dt' \qquad\qquad VI.5$$

In the scallar wave approximation $\underline{I}$ is given by:

$$\underline{I} = \frac{1}{2} e^{\overline{\ast}}e \ (\nabla\Sigma) \qquad\qquad VI.6$$

When the variations of $(\nabla\Sigma)$ are small it is useful to set:

$$\nabla\Sigma = (0,0,k_o) \qquad\qquad VI.7$$

where k_o is a constant. Using the arbitrariness in the definition (VI.1) of Σ and $\underline{e}$ we chose for k_o the value of k at the origin.

In the paraxial approximation (@) the wave equation becomes:

$$\boxed{\frac{\partial^2 e}{\partial x^2} + \frac{\partial^2 e}{\partial y^2} + (k^2 - k_o^2)e = 2 \, i \, k_o \frac{\partial e}{\partial z}} \qquad\qquad VI.8$$

In this approximation I is given by:

$$\boxed{\underline{I} = (0,0,\frac{1}{2} e^{\overline{\ast}} e \ k_o)} \qquad\qquad VI.9$$

The paraxial scalar wave approximation is used further when diffraction is expected to be important.

@ Note:

$$\left| \frac{\partial^2 e}{\partial z^2} \right| \ll k_o \left| \frac{\partial e}{\partial z} \right|$$

When diffraction can be neglected we use the geometrical optics approximation. In this approximation $\nabla\Sigma$ is determined from the so called Eikonal equation:

$$(\nabla\Sigma)^2 = k^2 \qquad\qquad\qquad \text{VI.10}$$

which follows from VI.2 by neglecting the other (higher order) terms. Light rays are defined as trajectories $\underline{r}_r = (x_r, y_r, z_r)$ for which:

$$d\,\underline{r}_r \quad x \quad \nabla\Sigma = \underline{0} \qquad\qquad\qquad \text{VI.11}$$

Using equations VI.10 and 11 Born (75) derives a relation between $\underline{r}_r$ and k which is refered to as the ray equation (see Appendix V).
In the <u>paraxial approximation of geometrical optics</u> and for the case of a <u>one-dimensional inhomogeneity</u>, e.i.

$$\boxed{k = k(x)} \qquad\qquad\qquad \text{VI.12}$$

the ray equation becomes:

$$\boxed{\begin{aligned}
\frac{d^2 x_r}{d\,z^2} &= \frac{1}{2}\left(\frac{d}{dx}(k/k_o)^2\right)_{x\,=\,x_r} \\[2mm]
\frac{d^2 y_r}{d\,z^2} &= 0
\end{aligned}} \qquad\qquad \text{VI.13}$$

where the direction of propagation of the light beam is parallel to the z axis.
The geometrical optics approach fails in focal points (where the light rays intersect each other) because $\nabla^2 e$ cannot be neglected in equation VI.2.
In the laser schlieren set-up considered the laser beam is focused in the test section. For this reason some features of the laser schlieren set-up can only be understood on the basis of the scalar wave approximation (VI.8). However it appears that the geometrical optics analysis is an excellent approximation which has the advantage

to be close to our intuition. We give therefore in section VI.d an analysis of the laser schlieren method based on geometrical optics. We now consider solutions of the scalar wave equation VI.8.

The initial conditions $e(x,y,0)$ are assumed to be given and we consider the behaviour of e for $z > 0$.

For a parabolic medium (lens-like) when $k^2(x)$ is a quadratic function of x, exact solutions can be obtained by using the mode theory of Carsperson (76). This theory includes the possibility of absorption and emission.

In the special case of a gaussian beam (single mode) the solution is identical to the approximation used by Vrugt (76). A detailed analysis is given by Carsperson (73).

An alternative solution is given by Arnaud (73) using Fresnel integrals.

When higher order terms in the series expansion of $k^2(x)$ are not negligible no exact solution is available. Calculations based on the W.K.B. method have been carried out for fiber optics by Marcatilli (67). Marcuse (72) used for the same problem a numerical procedure based on a thin lens discretisation scheme in combination with Fresnel integrals.

We use here a perturbation method based on the mode theory. This procedure is described in Appendix V.

In our further discussion we will mainly consider aspects of the laser schlieren method which have not been treated by Vrugt (76) or Carsperson (73).

94

VI.c. <u>Model of the set-up, definition of reference frame and signal</u>

A sketch of the experimental set-up is given in figure VI.1.
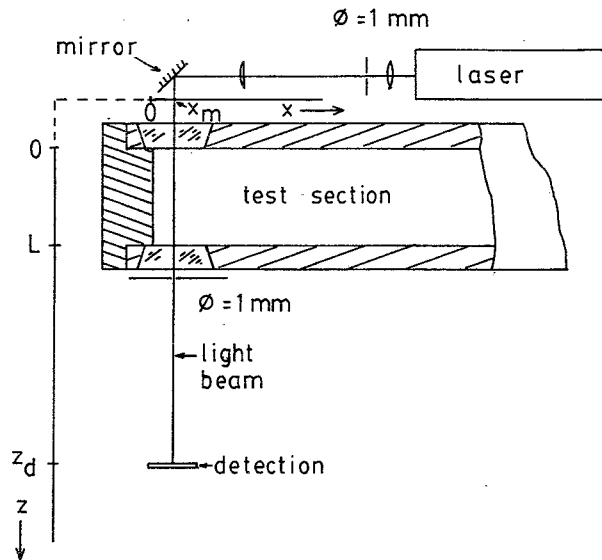
<u>Figure VI.1</u> : Sketch of the laser schlieren set-up
and definition of the reference frame.

The laser beam is positioned parallel to the end-wall of the
shock tube. The x axis is normal to the end-wall while the z axis is
taken along the median of the undisturbed beam (the gas in the test
section is uniform). The median x_m is given by:

$$\int_{-\infty}^{\infty}\int_{-\infty}^{x_m} I(x,y,z) \; dxdy \;\; = \;\; \int_{-\infty}^{\infty}\int_{x_m}^{\infty} I(x,y,z) \; dxdy$$

VI.14

In order to avoid complications due to the influence of reflections
at the windows the beam is tilted with respect to the direction
normal to the windows. The angle of incidence is chosen in such a way

that reflections can be intercepted by a diaphragm (figure VI.2).

reflected
beam

transmitted
beam

incident
light beam

test section
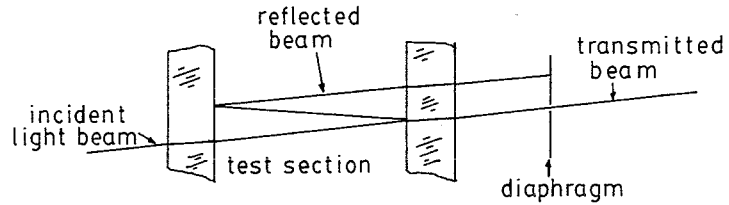
diaphragm

Figure VI.2 : Interception of the reflections at the
windows by a diaphragm.

The influence of the windows on the behaviour of the beam can be
described as a reduction of the distance from the test section to the
detection plane by the amount δz_d:

$$\delta z_d = ((N_w/N_o)-1) L_w \qquad\qquad VI.15$$

where:
N_w is the refractive index of the window
L_w is the thickness of the window.
We assume that the laser beam passes between $z = 0$ and $z = L$ through
a one-dimensional inhomogeneity.
The refractive index N is given by:

$$
\begin{aligned}
N &= N(x) & 0 \leqslant z \leqslant L \\
N &= N_o & \left\{ \begin{array}{l} L < z \\ z < 0 \end{array} \right.
\end{aligned}
\qquad VI.16
$$

L is the thickness of the test section.

The detection system @ placed at $z = z_d$ is assumed to yield a signal S given by:

$$S = \int_{-\infty}^{\infty} \int_{0}^{\infty} I(x,y,z_d) \, dxdy - \int_{-\infty}^{\infty} \int_{-\infty}^{0} I(x,y,z_d) \, dxdy$$

VI.17

In the following section we consider the relation between S and N(x).

@ Note:

Two different detection systems have been used.

They are described in Appendix VI.

In formula VI.17 we assume an ideal detector consisting of two equally sensitive half planes.

VI.d.   Geometrical optics analysis

The basis of the geometrical analysis of the laser schlieren method is the relation:

$$S = 2 \int_{-\infty}^{\infty} \int_{o}^{x_m} I(x,y,z_d) \, dxdy \qquad \text{VI.18}$$

which follows from the definitions VI.14 and 17.

From the definition of x_m it follows that within the geometrical approximation x_m satisfies the ray equation VI.13.

The initial conditions are:

$$x_m(0) = x_{mo}$$

$$(d \, x_m/dz)_{z=0} = 0 \qquad \text{VI.19}$$

Using a Taylor series expansion of N^2:

$$(N^2 - N^2(x_{mo}))/2N^2(x_{mo}) = \sum_{j=1}^{\infty} \frac{n_j}{j!} (x - x_{mo})^j \qquad \text{VI.20}$$

where n_j are the normalized derivatives of N^2:

$$n_j = \frac{1}{2 \, N^2(x_{mo})} \cdot (d^j N^2/dx^j)_{x=x_{mo}} \qquad \text{VI.21}$$

we obtain by integration of VI.13:

$$x_m(z) - x_{mo} = \frac{n_1 z^2}{2} (1 + \frac{n_2 z^2}{12} + \frac{n_3 z^4}{360} + \dots) \qquad \text{VI.22}$$

for $0 \leqslant z \leqslant L$

and

$$x_m(z) - x_m(L) = (z - L)(dx_m/dz)_{z=L} \qquad \text{VI.23}$$

for $L < z$.

For small deflections we can assume that for $0 \leqslant x \leqslant x_m$, $I(x,y,z_d)$ is independent of x and we obtain:

98

$$S = 2 x_m \int_{-\infty}^{\infty} I(0,y,z_d) \, dy \qquad\qquad \text{VI.24}$$

The value of $I(0,y,z_d)$ is slightly affected by the "deformation" of the beam due to the focusing effect of the inhomogeneity, it can be estimated by using a "thin lens" model for the inhomogeneity, e.i. we replace the inhomogeneity by a thin lens placed at $z = L/2$ with focal distance f:

$$f = -1/(\eta_2 L) \qquad\qquad \text{VI.25}$$

where we assume that $\eta_2 L^2 < 1$.

When the light beam is focused at $z = z_w$ and in the limit for:

$f \gg |z_w - L/2|$

$z_d \gg |z_w - L/2|$

$z_d \gg L$

Using the fact that the ratio of the apertures of the incoming and outcoming beams is equal to $((z_w - L/2)/f) - 1$, we find that the signal S is proportional to:

$$\eta_1 L \left(1 + \frac{\eta_2}{6} L^2\right)\left(1 + \eta_2 L(z_w - \frac{L}{2})\right) \qquad\qquad \text{VI.26}$$

We see that if the beam is positioned in such a way that:

$$\boxed{z_w - \frac{L}{2} = -\frac{L}{6}} \qquad\qquad \text{VI.27}$$

the schlieren signal is proportional to the refractive index gradient of the inhomogeneity along the z axis ($x = x_{mo}$).

The proportionality constant between S and η_1 is determined by the calibration of the system. The calibration signal S_{cal} is obtained by translating the detection along the x axis over a distance x_d.

For small deflection @ angles $\eta_1 L$ we obtain:

$$S = (-\frac{d\,S_{cal}}{d\,x_d})_{x_d=0} \quad \eta_1 L\,(z_d - \frac{L}{2})$$

VI.28

if VI.27 is fulfilled.

In addition to the simplifications introduced above, the validity of VI.28 is restricted by the assumption that the influence of diffraction is neglible. This effect is considered in the next section.

@ Note:

In some experiments the deflection was not small and a correction for the variation of $I(x,y,z_d)$ was introduced.

This correction is based on the assumption that the shape of the beam is gaussian. This correction was always less than 2%. For the calculation of this correction we neglected the influence of the distortion of the beam.

VI.e.   Diffraction and absorption

        Diffraction will cause the light beam to have a finite radius
at the focal plane and a related divergence at the detection.
The finite dimension of the beam in the test section yields a
limitation to the use of the schlieren method close to the end-wall
and a contribution of higher order derivatives of the refractive index
to the signal. The absorption of light in the test section will induce
a reduction of the beam power and, if the absorption is non-uniform,
a distortion of the beam shape. Both effects can be estimated with
the theory of Carsperson (73, 76). The influence of the reduction of the
beam power has been taken into account in the interpretation of the data.
The distortion of the beam (due to the absorption) has been neglected.

        We now discuss the influence of diffraction for the case of
a gaussian beam without absorption. A gaussian beam in free space
corresponds to the zeroth order mode e_{oo} (Appendix V):

$$e(x,y,0) = e_{oo} \qquad\qquad VI.29$$

The radius W of the undisturbed beam is defined as the distance from
the beam axis to the points where the power flux density has been
reduced by a factor e^2. W is given by:

$$W^2 = w_o^2 \left(1 + \left(\frac{z - z_w}{z_o} \right)^2 \right) \qquad\qquad VI.30$$

where w_o is the "waist" of the beam and z_w the position of the waist.
z_o is the "Rayleigh length" defined by:

$$z_o = (k_o w_o^2)/2 \qquad\qquad VI.31$$

Experimentally $W(z_d)$ is determined from:

$$W(z_d) = 2\left(\frac{2}{\pi}\right)^{\frac{1}{2}} \frac{\int_{-\infty}^{\infty} \int_{-\infty}^{\infty} I(x,y,z_d) \, dxdy}{\mid (d \, S_{cal}/dx_d)_{x_d = 0} \mid} \qquad\qquad VI.32$$

For other values of z ($z \neq z_d$), W is determined by measuring the power

of the beam intercepted by a knife as a function of the position x of the knife edge (formula similar to VI.32).

w_o and z_w are determined from measurements of W at various positions.

In Appendix V a relation between the signal S and the refractive index profile is obtained by means of the mode theory. We present here the results for the case:

$$z_w = L/2$$

$$z_d \gg L$$

and

$$z_d \gg z_o \qquad\qquad \text{VI.33}$$

The first two conditions are introduced in order to reduce the algebra involved in the calculations. The third condition is taken so that there is no influence of diffraction on the behaviour of the beam at the detection.

When the calculations are carried out up to the <u>first approximation</u> (in the mode expansion) we find:

$$S = (z_d - \frac{L}{2})(-\frac{dS_{cal}}{dx_d})_{x_d=0} \, L \, (n_1 + \frac{n_3 w_o^2}{6} + \frac{n_5 w_o^4}{2} (\frac{31}{30} + \frac{5}{18}(L/k_o w_o^2)^2 + \frac{1}{20}(L/k_o w_o^2)^4) + ..)$$

$$\text{VI.34}$$

for $n_1 L < \dfrac{2}{k_o w_o}$

In <u>second approximation</u> we find an additional correction, given by:

$$\Delta S = (z_d - \frac{L}{2})(-\frac{dS_{cal}}{dx_d})_{x_d=0} \, \frac{L^3}{6} (n_1 n_2 + n_3 w_o^2 \frac{n_2}{16} (7 + \frac{3}{5}(L/k_o w_o^2)^2 + \frac{1}{21}(L/k_o w_o^2)^4) + ...)$$

$$\text{VI.35}$$

for $n_1 L < \dfrac{2}{k_o w_o}$

Comparison of VI.34 to VI.22 and 23 confirms that the geometrical optics approach is valid for a parabolic medium.

This statement is demonstrated for more general conditions by Marcuse (72) and Carsperson (73). We also see that in order to minimise the influence of the higher order derivatives we should chose w_o such that:

$$w_{op} \leqslant w_o \leqslant w_{min} \qquad\qquad VI.36$$

where w_{min} corresponds to the beam configuration for which the beam radius at the windows $W(L)$ is minimal:

$$w_{min} = (k_o/L)^{\frac{1}{2}} \qquad\qquad VI.37$$

and w_{op} corresponds to the beam configuration for which the average beam radius $\bar{W}$ in the test section is minimal:

$$\bar{W} = \frac{1}{L} \int_0^L W \, dz' \qquad\qquad VI.38$$

For $z_w = L/2$ we have:

$$w_{op} = (1/3)^{\frac{1}{4}} (L/k_o)^{\frac{1}{2}} \qquad\qquad VI.39$$

Vrugt (76) showed that for $z_w = L/2$ and $w_o = w_{op}$ the influence of the second order derivative on the distortion of the beam is minimised. Formula VI.38 has been used for the correction of the signal for the influence of η_3. This correction was always smaller than 3%.

The sensitivity Γ of the schlieren set-up can be defined by:

$$\Gamma = \frac{z_d - L/2}{\int_{-\infty}^{\infty} \int_{-\infty}^{\infty} I \, dxdy} \left(\frac{dS}{dx_m}\right)_{\substack{z=z_d \\ x=x_{mo}}} \sim \frac{z_d - L/2}{W(z_d)} \qquad VI.40$$

From this definition we see that the sensitivity of the set-up can be increased by focusing the beam at the detection.

Due to the divergence of the beam a high sensitivity will correspond

to a large beam radius in the test section.

For a given beam radius in the test section there is therefore a limit to the sensitivity of the set-up which is obtained when the beam is focused at the detection and $(z_d - L/2) = z_o$.

VI.f.   Principle of the two-wavelengths laser schlieren method

We now consider the dispersion relation VI.3.
Using definition VI.4 we can write VI.3 as:

$$N^2 = (\mu/\mu_o)((\varepsilon/\varepsilon_o) - i(\sigma/\varepsilon_o\omega))$$ VI.41

where μ_o is the permeability of vacuum and ε_o the permittivity of vacuum. Following Landau (69) we can state:

$$(\mu/\mu_o) = 1$$ VI.42

The dissipative (real) part of the electric conductivity σ can be neglected for the wavelength considered because the electron-heavy particle collision frequency is much smaller than ω.
Then we can write (Born (75)):

$$\sigma = - i \frac{n_e e^2}{m_e \omega}$$ VI.43

$(\varepsilon/\varepsilon_o)$ is estimated by assuming that the contribution of each particle is independent of the contribution of the other particles:

$$(\varepsilon/\varepsilon_o) - 1 = 4 \pi \sum_j n_j P_j$$ VI.44

where P_j is the polarisability of a particle j.
From the experimental studies of Alpher (65) and Bristow (71) it follows that the contribution of excited argon atoms can be neglected. Following Peck (64) we use the polarisability P_a of argon atoms:

$$P_a = C_1 + C_2\omega^2$$ VI.45

with:

$$2\pi C_1 = 10.326 \times 10^{-30} \ m^3$$

$$8 \pi^3 c^2 C_2 = 5.417 \times 10^{-44} \ m^5$$

The value of P_i of singly ionized argon has been determined by

Bristow (71):

$$P_i = (0.65 \pm 0.08) P_a \qquad\qquad VI.46$$

This value agrees with the estimates of Alpher (65) and Baum (75).
Using VI.42 to 45 we can write VI.41 as:

$$N^2(\omega_i) - 1 = 2 (A_i n_a + E_i n_e) \qquad\qquad VI.47$$

and

$$\boxed{\eta_1(\omega_i) = A_i n_a' + E_i n_e'} \qquad\qquad VI.48$$

Using VI.48 we can determine the electron and aton density gradients
n_e' and n_a' from two simultaneous measurements of η_1 at two-wavelengths
$(\omega_1$ and $\omega_2)$.

Note:
$1_1 = 6.328 \times 10^{-7}$m ;
$A_1 = 1.046 \times 10^{-29}$ m^3;
$E_1 = -1.727 \times 10^{-28}$ m^3;

$1_2 = 1.152 \times 10^{-6}$m ;
$A_2 = 1.036 \times 10^{-29}$m^3 ;
$E_2 = -5.887 \times 10^{-28}$m^3 ;

VII.   EXPERIMENTAL DETERMINATION OF THE HEAT CONDUCTIVITY OF

        NON-IONIZED ARGON

VII.a.   Introduction

     In this chapter we present experimental data on the structure
of the thermal boundary layer for cases in which ionization is
negligible. Using the procedure described in chapter II we obtain
heat conductivity data as function of the temperature. The basic idea
is to determine the state of the gas as a function of position and
time and to use the energy equation to determine the heat conductivity
λ.

     Because the flow is one-dimensional, the state of the gas is
determined by (p, ρ, u). The pressure p is measured at the end-wall
by means of a piezo-electrical transducer. The density gradient
$(\partial \rho / \partial x)$ is measured with the laser schlieren method (chapter VI).
Integration of the density gradient yields the density difference
$(\rho - \rho_\infty)$. The density ρ_∞, outside the boundary layer, is estimated as
described in section II.b; $\rho_\infty(0)$ is assumed to be equal to the
Rankine-Hugoniot value ρ_5. The velocity u is related to the velocity
u_∞ outside the boundary layer, through the continuity equation
(II.18). The velocity u_∞ can be calculated with equation II.16 when
the heat flux at the end-wall q_w is known. For q_w we use a
theoretical estimate based on the thermal Rayleigh problem
(section III.b) and the local similarity approximation discussed in
section III.f. As will be shown in section VII.b the estimate for q_w
is rather insensitive for variations in the expression used for heat
conductivity.

     As suggested by Vrugt (76), the procedure outlined above is
considerably simplified when the structure of the boundary layer is
self-similar. Deviation from the self-similarity resulting from the
time dependence of the pressure appeared to be negligible (section
VII.d) for the conditions considered.

     In section VII.b we describe the experimental procedure for
the determination of $(p, \rho_\infty, u_\infty)$. In section VII.c we consider the
non-uniformity of the flow in the reflected shock region.
The laser schlieren data on the structure of the boundary layer are

given in section VII.d. The heat conductivity data are presented in section VII.e.

Technical notes:

Set-up:

The principle of the set-up and the accuracy of the measurements are discussed. Some additional technical information is given in Appendix VI.

Shock tubes:

Most of the experiments presented in this chapter have been carried out with the same shock tube facility as used by Vrugt (76). This shock tube (cross section 10 x 10 cm^2) is refered to as shock tube I. Additional experiments have been carried out in a smaller shock tube with a cross section in the shape of a racing track (4.2 x 8 cm^2) refered to as shock tube II.

Diaphragms:

Aluminum diaphragms of 0.5 and 1 mm thickness were used.
In order to achieve a specific Mach number the diaphragms were encarved following a pattern given in Appendix VI. The diaphragm is characterized by: (thickness/depth of encarving).

Driver gas:

For $M_s < 3.5$ we used N_2, for $M_s > 3.5$ we used H_2 as driver gas.

Run:

Each run is denoted by the date followed by a series number and the shock tube number (I, II): (date, number/shock tube number).

VII.b. State of the gas outside the boundary layer

Using the procedure outlined in section II.b we determine $(p_\infty, \rho_\infty, u_\infty)$ from the measurement of the initial state (p_1, ρ_1), the incident shock Mach number M_s and the end-wall pressure which is equal to p_∞.

$\underline{p_1}$: Before each experiment the test section of the shock tube was evacuated to a pressure p_{oo} of less than 10^{-2}Pa. The test section was filled with argon (N50 of Aga/Air liquide, impurity level about 10 ppm). The initial pressure p_1 was measured by means of a van Essen oil filled micro-manometer of the Betz type (absolute accuracy better than 2 Pa). For some measurements with p_1 higher than 10^4 Pa a Bourdon type Wallace-Tiernan manometer was used (accuracy better than 1%).

The leakage (outgasing) rate of the shock tube was about 2×10^{-3}Pa/s. The time between the closing of the pump and the shot was about 3 min. The partial pressure p_o of the impurities (mainly air) was thus of the order of magnitude of 0.4 Pa.

$\underline{T_1}$: The temperature T_1 was measured with a mercury thermometer in thermal contact with the shock tube wall (accuracy 0.2 K).

$\underline{M_s}$: The Mach number M_s was calculated from equation II.1 where c_1 is given by:

$$c_1 = (\gamma R T_1)^{1/2} \qquad\qquad \text{VII.1}$$

with $\gamma = 5/3$, $R = 208.13 \text{ m}^2\text{s}^{-2}\text{K}^{-1}$.

$\underline{v_s}$: The speed of the incident shock wave v_s was determined from the measurement of the travel time of the shock between two piezo-electrical transducers (Kistler type 603 B) mounted flush in the side-wall at distances x_1 and x_2 from the end-wall (see table VII.1). An additional pressure transducer is mounted at x_3.

Shock tube	x_1 (mm)	x_2 (mm)	x_3 (mm)
I	995	30	945
II	615	125	190

Table VII.1: Positions of side-wall pressure transducers.

The pressure signals triggered electronic counters.

The inaccuracy in the time measurement, about 0.2 μs, was estimated by the simultaneous use of various counters (Systron and Donner type 7034 or HP type 5345 A) in combination with various triggering systems.

The value of v_s measured in this way is referred to as $(v_s)_1$ and has an accuracy of 0.1%. The corresponding value of M_s is $(M_s)_1$.

p_∞: The end-wall pressure p_∞ was measured by means of a piezo-electrical transducer (Kistler 603 B) mounted flush at 2 cm from the middle of the end-wall surface. The charge amplifier (Kistler 5001) was used in the position "long" corresponding to a RC-time of ca 1 s for leakage of the charge from the crystal. In order to avoid heating of the gauge, the sensitive surface was coated with a non-transparent layer (ca 0.2 mm) of black silicon rubber.

The coated transducer was calibrated dynamically in combination with the charge amplifier over the range 10^5 to 2×10^5 Pa. The calibration pressure step, released by the opening of a magnetic valve, was measured by means of a calibrated bourdon type manometer (Wallace – Tiernan, model n^oD 62-A).

The finite opening time of the valve and the wave phenomena in the system restricted the validity of the calibration procedure to times greater than 2 ms. The reproducibility of the calibration was better than 0.1%. The response of the gauge appeared to be linear within 0.4%. The short time dynamical response of the gauge was checked by using shock tube experiments with high initial pressures. A typical signal is shown in figure VII.1.

Figure VII.1 : End-wall pressure measurement. Run (80020705/II), Diaphragm (1 mm/0.35 mm)
$(M_s)_1$ = 5.160;
p_1 = 6665 Pa;
T_1 = 294.4 K.
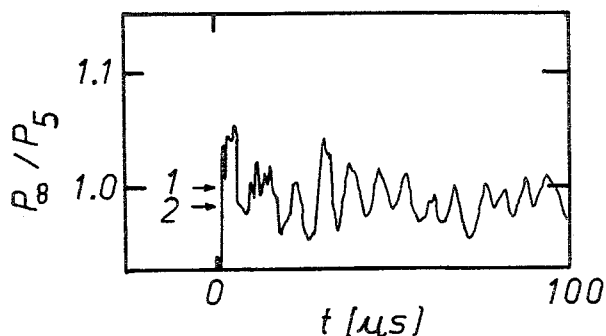
The registration of the signals is described in Appendix VI.
Because of the resonances (see figure VII.1) one can only measure the
pressure accurately by averaging over a period of ca 10 μs.
From figure VII.1 we see in this way that the end-wall pressure agrees
within 2% with the Rankine-Hugoniot value p_5. (See for additional data
chapter VIII). The overshoot in the pressure signal in the first 3 μs
depends strongly on the gauge.
The accuracy of the pressure measurements(2%) has been confirmed by
the study of van Dongen (78) in which the response of piezo-electrical
transducers is compared with pressure data obtained by means of the
light reflection method (van Dongen 75,77).

In figures VII.2, 3 and 4 we give the pressure data for the
conditions at which boundary layer measurements have been carried out.

Figure VII.2 : End-wall pressure as function of time.
average Mach number M_s = 2.73, shock tube I.
p_1 = 667 Pa, T_1 = 295 K.
End-wall configuration of figure VII.5a.
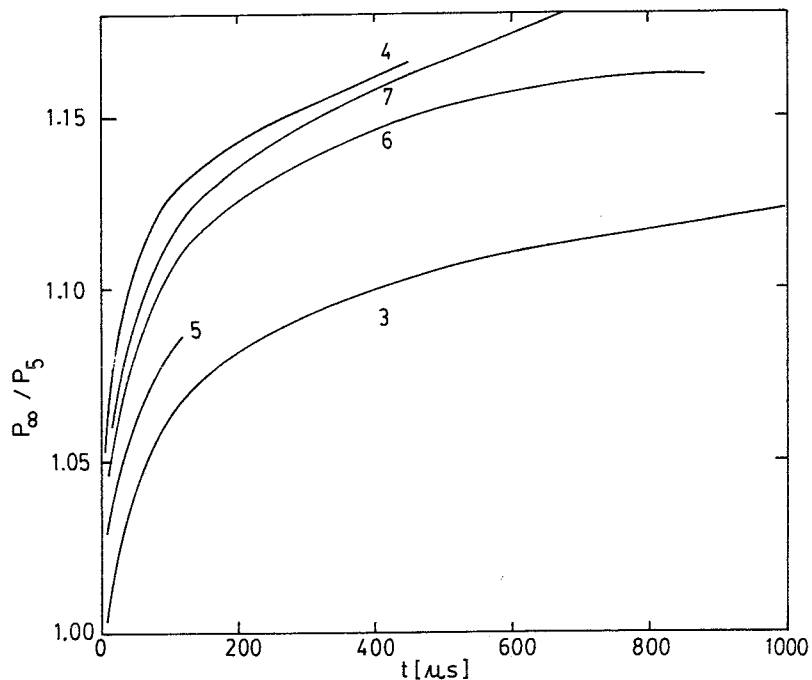
Figure VII.3 : End-wall pressure as function of time.
average Mach number M_s = 3.0, shock tube I.
End-wall configuration of figure VII.5b.
Details about the initial state and Mach number data are
given in table VII.2.
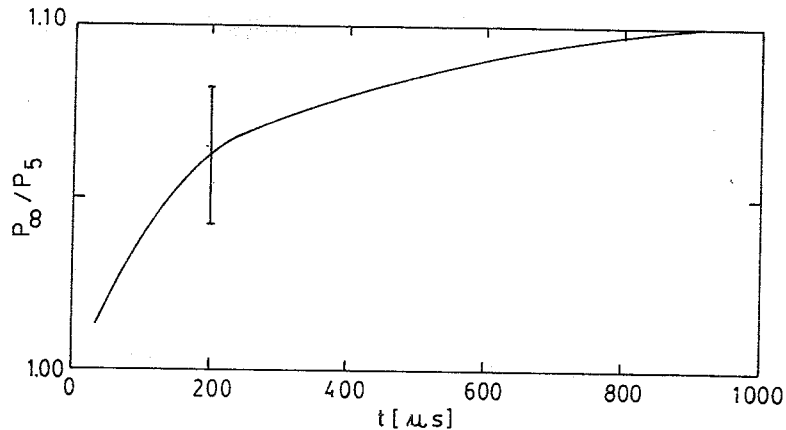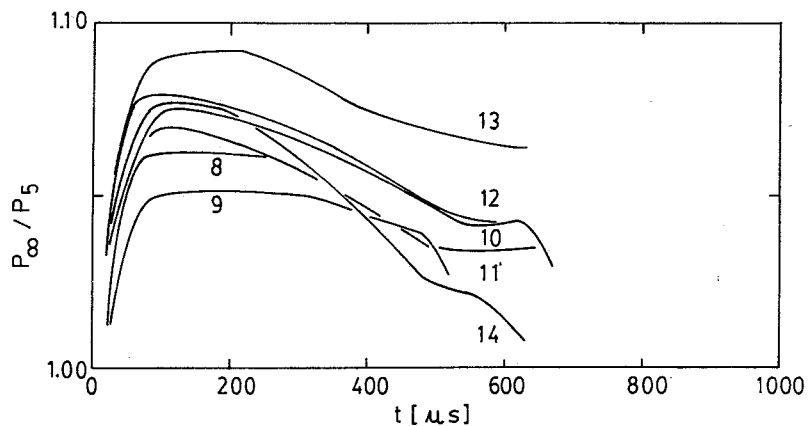

Figure VII.4 : End-wall pressure as function of time.
average Mach number M_s = 5.3, shock tube I.
End-wall configuration of figure VII.5b.
Initial conditions and Mach number data are given in
table VII.2.

N°	run	P_1 (Pa)	T_1 (K)	$(M_s)_1$	diaphragm ((mm)/(mm))
1	80062701/I	660	291.4	2.991	(0.5/0.15)
2	80062702/I	665	292.2	3.007	(0.5/0.15)
3	80063001/I	671	294.2	3.022	(0.5/0.15)
4	80063003/I	668	292.9	2.998	(0.5/0.15)
5	80070101/I	664	292.1	2.849	(0.5/0.25)
6	80070102/I	670	292.4	2.834	(0.5/0.25)
7	80070103/I	667	292.4	2.826	(0.5/0.25)
8	80070302/I	666	292.9	5.914	(0.5/0.15)
9	80070401/I	667	292.6	5.310	(0.5/0.25)
10	80070701/I	663	292.3	5.319	(0.5/0.25)
11	80070801/I	667	292.4	5.292	(0.5/0.25)
12	80070802/I	667	292.8	5.324	(0.5/0.25)
13	80070901/I	667	293.1	5.333	(0.5/0.25)
14	80070902/I	668	292.9	5.374	(0.5/0.25)

Table VII.2 : Initial conditions and Mach numbers corresponding to figures VII.3 and 4.

We observe that the data of figure VII.2 are lower than the data of figure VII.3. The data of figure VII.2 have been presented in our previous study (Hirschberg 78).

The main difference between these two series of measurements is the configuration of the end-wall of the shock tube. (see figure VII.5 a and b).
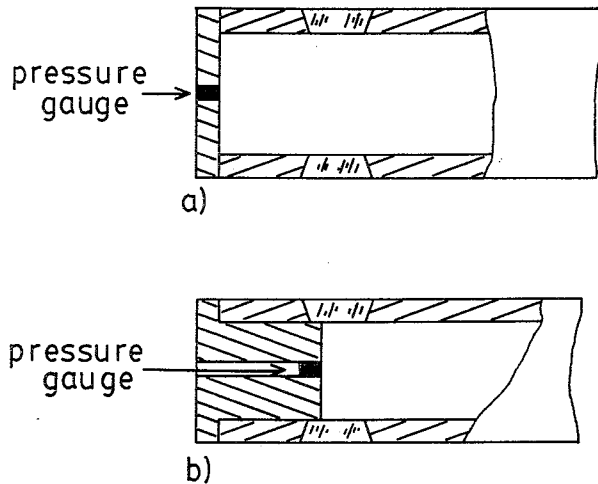
End-wall configurations corresponding to the data of figure VII.2, 3 and 4.

This suggests that the discrepancy between the behaviour of the pressure measurement series might be due to variations in transition from a laminar to a turbulent side-wall boundary layer induced by the windows.

q_w : The heat flux q_w at the end-wall of the shock tube was estimated on basis of the thermal Rayleigh problem (section III.b). The influence of the time dependence of the pressure was taken into account by means of the local similarity approximation (section III.f).

For the calculation of $(q_w)_{th}$ we used a λ_{fit} based on the heat conductivity data available (see figure VII.6). &

Figure VII.6 : Comparison of the expression used for the heat conductivity in the calculations of $(q_w)_{th}$ with data on the heat conductivity.

& Note:

λ_{fit} is slightly discontinuous at T = 500 K.

For the calculation of $(q_w)_{th}$ we used a λ_{fit} based on the heat conductivity data available (see figure VII.6). &

$$\lambda_{fit} = 0.0172\,(T/290)^{0.8} \quad ; \quad T \leqslant 500 \text{ K}$$
$$= 0.0568\,(T/1500)^{0.7} \quad ; \quad T > 500 \text{ K}$$

- - - - Touloukian (70)

x   Haarman (73)

——— Chen (75)

λ / λ_{fit} versus $T\ [10^3 K]$
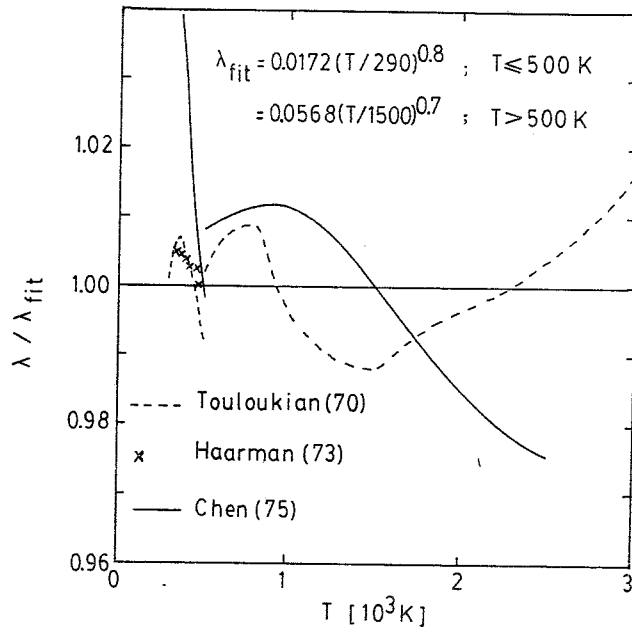
Figure VII.6 : Comparison of the expression used for the heat conductivity in the calculations of $(q_w)_{th}$ with data on the heat conductivity.

& Note:

λ_{fit} is slightly discontinuous at T = 500 K.

In order to obtain some insight in the influence of the uncertainty in the expression used for the heat conductivity we compare in figure VII.7 $(q_w)_{th}$ to the calculated values of q_w for various expressions for the heat conductivity.
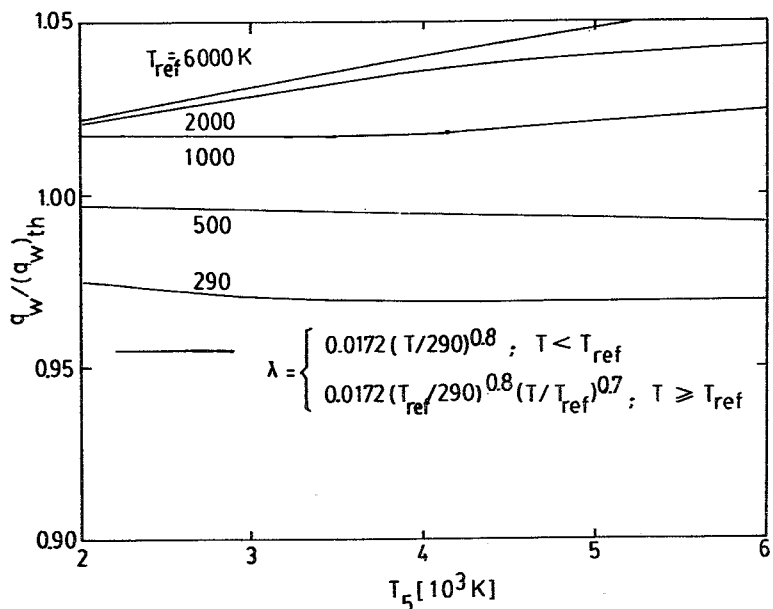
Figure VII.7 : Influence of the expression used for the heat conductivity on the heat flux at the end-wall.

These expressions yield values of the heat conductivity at high temperatures $(T_5 \geqslant 6000K)$ that differ by 30% (see figure VII.8),while the data on q_w show a corresponding variation of 8%.

Further more we see that in agreement with the conclusion of Lauver (64) the heat flux q_w is rather insensitive to variations on the heat conductivity in the outer part of the boundary layer.
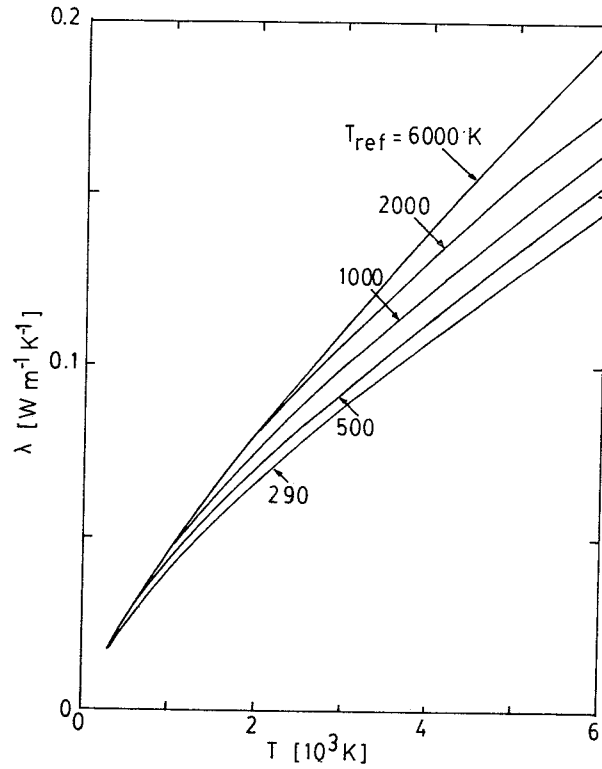

Figure VII.8 : Expressions for the heat conductivity used in the calculations of the heat flux q_w shown in figure VII.7.

VII.c. Non-ideal behaviour of the flow outside the boundary layer

The procedure described in the previous section for the determination of the state of the gas outside the boundary layer is based on the model of section II.b in which we assumed that the incident shock has a constant speed and that the gas outside the boundary layer is uniform.

In section III.e we reviewed the main sources of deviation of the flow from this model. In the present section we give the corresponding experimental data collected.

M_s: As a result of the influence of the finite opening time of the diaphragm and of the side-wall boundary layers the incident shock wave does not have a constant speed (Mirels (66), Stupochenko (67), Simpson (67), Boer (75), Reese (77), Zeitoun (79)). Using a third piezo-electrical pressure gauge placed at a distance x_3 from the end-wall (table VII.1) we obtain a second speed measurement refered to as $(v_s)_2$.

In shock tube I the traject $x_1 - x_3$ was used for the measurement of $(v_s)_2$. In shock tube II the traject $x_3 - x_2$ was used.

The data collected on $(M_s)_1/(M_s)_2$ are given in figure VII.9.

The order of magnitude of the deceleration of the incident shock measured (figure VII.9) corresponds to the order of magnitude of the data found in the literature (see above).

From the scatter in $(M_s)_1$ for a given initial pressure and diaphragm one can get an estimate of the reproducibility of the experiments (figure VII.9).

Neglecting the deceleration of the incident shock in the procedure for the determination of the state of the gas outside the boundary layer (section VII.b) we overestimate M_s by about 0.5%. This results in an overestimation of p_5 by 1% which induces an underestimation of ρ_∞ by about 0.6%.
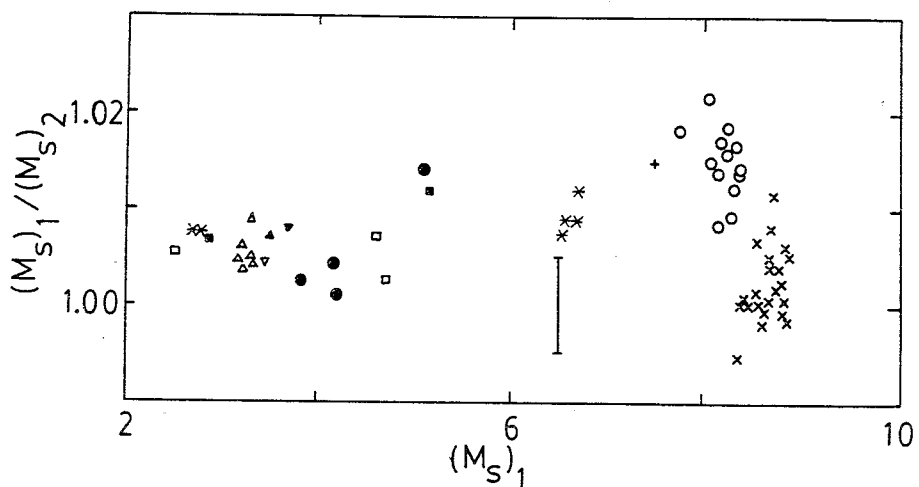
Figure VII.9 : deceleration of the incident shock wave in shock tube II as a function of $(M_s)_1$ for various pressures (see table VII.3).

Symbol	diaphragm ((mm)/(mm))	driver gas	P_1 (Pa)
△	(0.5/0.20)	N_2	667
▽	(0.5/0.35)	N_2	667
▲	(1.0/0.85)	N_2	667
▼	(1.0/0.65)	N_2	667
●	(0.5/0.40)	H_2	667
+	(1.0/0.45)	H_2	667
o	(1.0/0.40)	H_2	667
x	(1.0/0.25)	H_2	667
✳	–	–	2666
■	–	–	6665
□	–	–	13330

Table VII.3 : Symbols of figure VII.9

v_r : In a similar way as the incident shock wave the reflected shock does not have a constant speed. In the initial phase of the reflection process the reflected shock wave strongly interacts with the end-wall thermal boundary layer (Piva (69), Sturtevant (64),

Meldau (77)).

This effect is clearly observed in measurements of v_r carried out for M_s = 7.7 in a mixture of 99.5% Ar + 0.5% H_2. These data are described in section VIII.c.

For longer times (t $\geq$ 20 μs) the reflected shock velocity appears to be about 10% lower than the velocity predicted by the Rankine-Hugoniot relations. This effect is due to the non-uniformity of region 2 and should therefore be closely related to the time dependence of the end-wall pressure (section VII.b) and the non-uniformity of the reflected shock region.

ρ_∞: Information on the non-uniformity of the reflected shock region can be obtained from the laser schlieren data. A typical laser schlieren record for x_m = 7 mm is shown in figure III.7. Similar data for 0.6 mm $\leq x_m \leq$ 1.0 mm are shown in figure VII.10
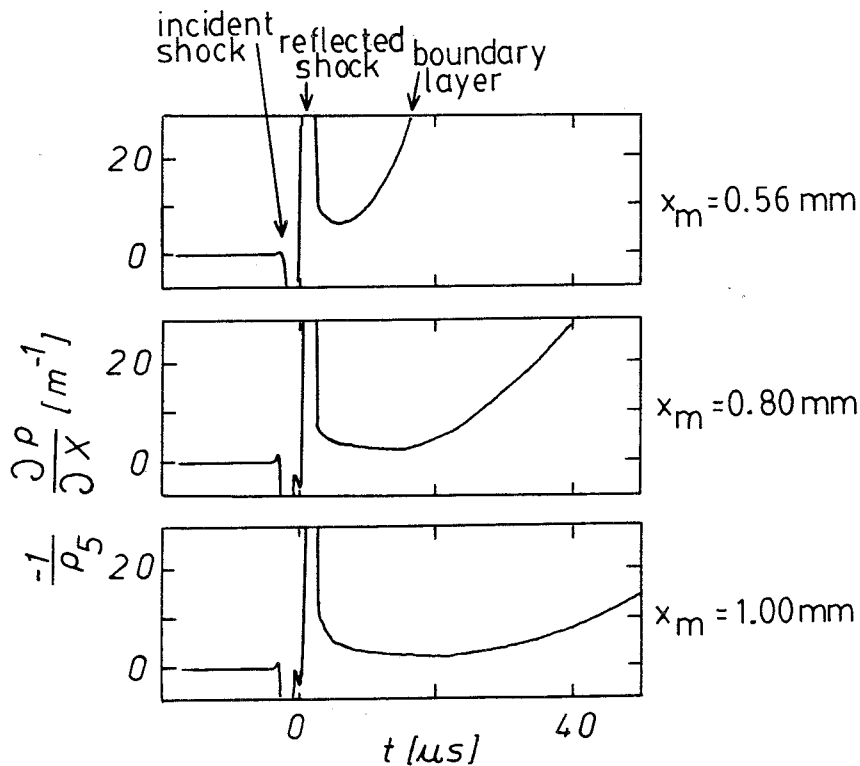
Figure VII.10 : Short time behaviour of the laser schlieren data.

M_s = 2.83, p_1 = 667 Pa, T_1 = 292 K.
Shock tube I.

In figure VII.10 we observe successively in time the incident and
reflected shocks and the thermal boundary layer growth. In a similar
way as in figure III.7 between the shock compression and the "arrival"
of the boundary layer the laser schlieren signal does not vanish.
The schlieren signal measured is thus due to a gasdynamic
inhomogeneity. @

This fact is confirmed by the correlation between the time dependence
of the pressure and the schlieren signal shown in figure VII.11. The
steeper increase of the pressure in experiment 1 corresponds to a
higher density gradient just behind the reflected shock.
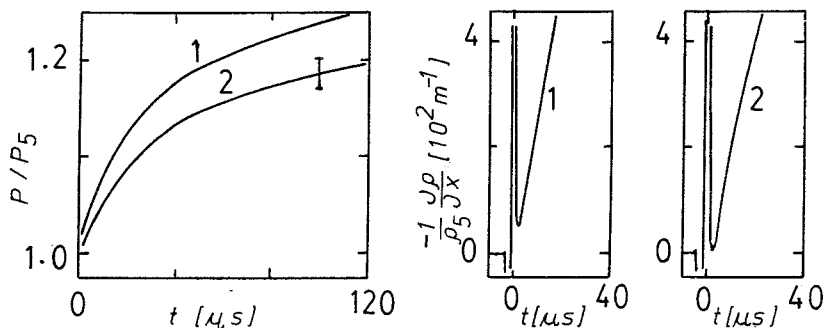
Figure VII.11 : Correlation between the time
dependence of the pressure and the laser schlieren
signal (x_m = 0.6 mm), M_s = 3.4, p_1 = 266 Pa,
T_1 = 294 K, shock tube II.

@ Note:

  A possible influence of the windows on the signal was excluded by
  considering the schlieren signal obtained with Helium as a test gas.
  In such a case for x_m = 7 mm there was no significant schlieren
  effect as we expected because of the lower refractivity of Helium.
  Fused quartz windows were used.
  BK 7 Crown glass used earlier shows significant schlieren effect.
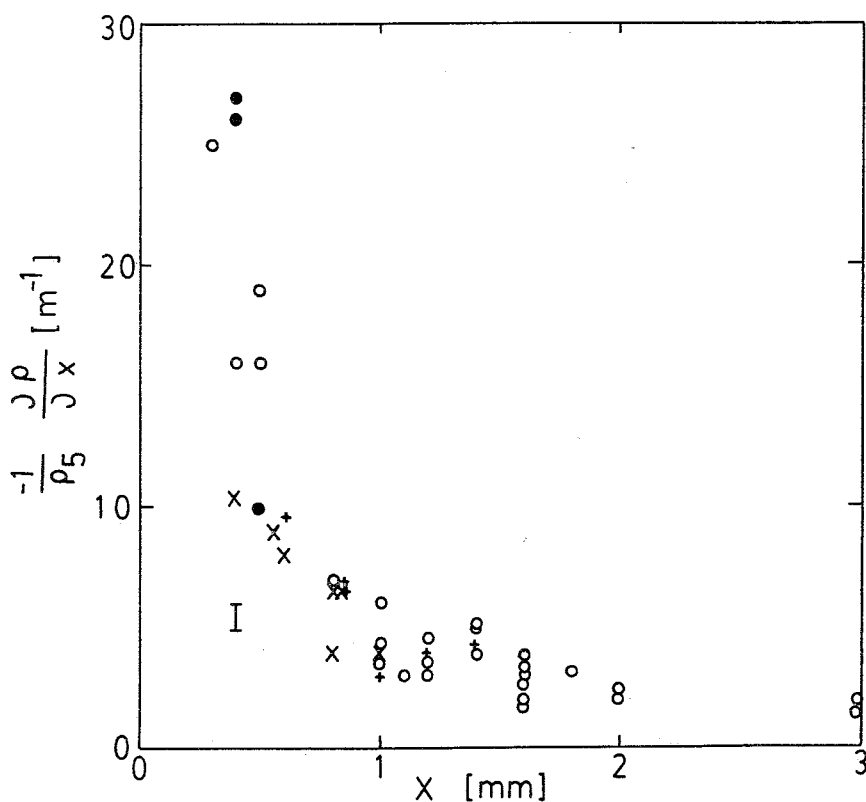
Figure VII.12 : Density gradient measured 10 µs after compression by the reflected shock as a function of the distance from the end-wall.

Symbol	shock tube	p_1 (Pa)	M_s
o	II	667	3.2
●	II	267	3.4
+	I	667	2.9
x	I	667	5.3

In figure VII.12 we give the data on the density gradient measured 10 µs after the shock compression as a function of the distance x from the end-wall. From these data we can estimate the non-uniformity of the reflected shock region.

We conclude that for x ≥ 0.5 mm the density variations are of the

order of magnitude of 2%. The order of magnitude of this inhomogeneity agrees with the calculations based on a one-dimensional linearized theory (see section III.e).

On the basis of the data presented by Gardiner (61), Kuiper (68) and Bunting (67) one can exclude deviation of $\rho_\infty(0)$ from ρ_5 of more than 5%.

Conclusion: From the data presented here we conclude that using the procedure described in section VII.b we may underestimate the density ρ_∞ by about 2% and that we can not exclude systematic errors up to 5%.

VII.d   **The structure of the boundary layer.**

Presentation of the data:

The structure of the boundary layer has been determined with measurements of the density gradient, by means of the laser schlieren method (chapter VI), as a function of time for various distances x_m from the end-wall.

As demonstrated by Vrugt (76) from a series of measurements (with 0.94 mm $\leqslant x_m \leqslant 1.74$ mm) the structure of the boundary layer is self-similar within the accuracy of the measurements. Deviations from self-similarity can be estimated with the simplified model of section III.f. For times greater than 100 µs no significant deviation from selfsimilarity was observed in our data. We therefore present the data in the normalised form:

$$F^{(1)} = \frac{(a_5 t)^{1/2}}{\rho_5} \, (\partial\rho/\partial x) \qquad\qquad \text{VII.2}$$

as a function of S :

$$S = x_m/(a_5 t)^{1/2} \qquad\qquad \text{VII.3}$$

For the calculation of a_5 we used the formula:

$$\lambda_5 = 0.0568 \, (T_5/1500)^{0.68} \qquad\qquad \text{VII.4}$$

The main advantage of this presentation of the data is that it allows us to compare data obtained at various positions x_m and with some scatter in the initial conditions and the incident shock wave Mach number.

Accuracy:

The absolute accuracy in the position of the beam is of the order of 6 µm (see Appendix VI). The time measurements has an uncertainty of about 1 µs in the origin of time and an additional 0.5 % relative uncertainty due to the registration procedure (see Appendix VI).

The uncertainty in the measured density gradient is of the order of magnitude of 3%, mainly due to the inaccuracy of the calibration of the schlieren system. As pointed out before (section III.e) there may

be an additional uncertainty due to the influence of the side-wall boundary layers on the signal.

Survey of the data :

We performed six series of measurements of the structure of the thermal boundary layer in non-ionized argon (see table VII.3).

Series N^o	P$_1$ (Pa)	M$_s$	x$_m$ (mm)	shock tube	data	number of runs
1	667	2.7	0.4 to 1.8	I	780227 to 780301	9
2	667	3.0	0.4 to 1.2	I	800627 to 800701	7
3	667	5.3	0.6 to 1.4	I	800701 to 800709	7
4	667	3.2	0.3 to 1.4	II	790907 to 791005	30
5	267	3.4	0.4 to 0.8	II	791015 to 791017	5
6	2666	2.8	0.6 to 0.8	II	791018	4

Table VII.3 :   Survey of the measurements series.

The purpose of the first series (1) was to confirm the results of Vrugt (76). The second and third series (2 and 3) have been carried out with special care and have been used for the determination of the heat conductivity data presented in section VII.e.
Measurement series 1 and 2 cover the low temperature range (T ≤ 2500 K) for which accurate data on the heat conductivity are available. These two series of measurements are used in order to estimate the accuracy of the determination of the heat conductivity.

Measurement series 3 is used to obtain heat conductivity data in a temperature range for which no accurate data are available (T ≥ 4000 K).

The other series (4, 5 and 6) were mainly meant to verify the influence of the side-wall boundary layers on the schlieren signal.

As a result of an error [a] in the use of the registration system these data are less accurate than the data of the previous series (about 5%).

Series 1 :

In the set up used for series 1 the laser beam was focused as done by Vrugt (76) at the center of the test section ($z_w = L/2$).

The laser schlieren signal obtained in such a case is related to the structure of the boundary layer by formulas VI.34 and 35. The refractive index gradient N_1 is determined by iterative correction of the signal for the influence of the second and third derivatives N_2 and N_3 (see Hirschberg (78)). The density gradient is given by:

$$\partial\rho/\partial x = N_1 /K \qquad\qquad\qquad \text{VII.5}$$

in which $\underline{K \text{ is the Gladstone-Dale coefficient}}$ ($K = 1.582 \times 10^{-4} m^{-3} kg^{-1}$). A correlation formula for the data with $x_m \geqslant 0.6$ mm was determined by linear regression:

$$F^{(1)} = 0.04791 - 0.4768\ S^{-2} + 0.02487\ S^{-4} \qquad\qquad \text{VII.6}$$

valid for $0.4 \leqslant S \leqslant 1.5$.

The determination coefficient [b] of the fit is $r^2 = 0.9993$.

For $x_m \leqslant 0.5$ mm deviations of 10% from selfsimilarity were observed. Further analysis and comparison with the second measurement series (2) showed that the deviation of the data from selfsimilarity was due to a misalignment of the waist of the laser beam, $\Delta z_w = 8$ mm.

In later measurements series an improved determination of z_w excludes uncertainties in z_w of more than 2 mm.

In the experiments of series 1 the pressure was not measured simultaneously with the schlieren signal.

The pressure data shown in figure VII.2 have been obtained from a

[a] Note :

  An A-C filter was used

[b] Note :

  Definition of the determination coefficient is taken following Wonnacott (72).

series of experiments with the end-wall configuration shown in
figure VII.5a while the schlieren measurements were carried out with
the end-wall configuration of figure VII.5b. In series 2 and 3 the
end-wall pressure was measured simultaneously with the schlieren
signal.

From figure VII.2 we see that the end-wall pressure increases
from p_5 to $1.1 \times p_5$. We therefore compared the data of series 1 to the
solutions of the thermal Rayleigh problems for $p_\infty = p_5$, $T_\infty = T_5$ and
$p_\infty = 1.1\ p_5$, $T_\infty = 1.04\ T_5$. In those calculations we used the data of
Chen (75) for the heat conductivity.
From figure VII.13 we see that a quantative agreement between theory
and experiment may be expected when the influence of the time
dependence of the pressure is taken into account.
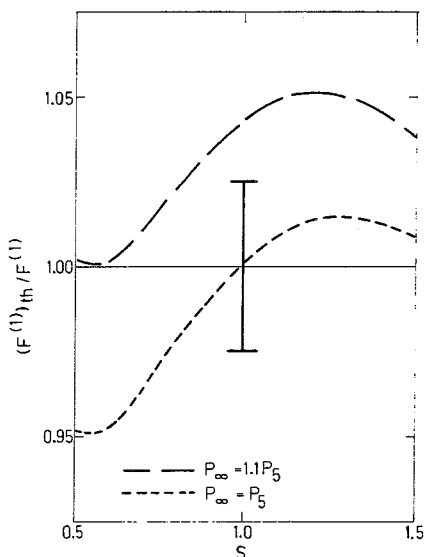
Figure VII.13 : Comparison of the experimental data
of series 1 (equation VII.6) with the solutions of
the thermal Rayleigh problems with $p_\infty = p_5$, $T_\infty = T_5$
and $p_\infty = 1.1\ p_5$, $T_\infty = 1.04\ T_5$.

Series 2 :
As noticed before series 2 was performed for the purpose of
determining heat conductivity. Special attention was dedicated to the
measurement of z_w and the pressure was measured simultaneously with

the schlieren signal. We restricted ourselves to signals small
enough so that the non-linearity of the response of the schlieren
system (due to the gaussian shape of the beam) does not involve
corrections of more than 1.5%.

In addition we focused the beam at z_w = L/3 so that in first
approximation the contribution of the second derivative N_2 to the
deflection of the beam is compensated by the influence of the
deformation of the beam (equation VI.28).

The correction for the influence of N_3 was performed on the basis of
formulas VI.34 and 35. This correction was not more than 2% in the
data used for the determination of the heat conductivity. In order to
illustrate the influence of the third order derivative N_3 on the
signal we compare in figure VII.14 the data on $F^{(1)}$ for x_m = 0.4 mm
with and without correction, with the average of the data of series 2.

Figure VII.14 : Influence of N_3 on the schlieren
signal. Comparison of run (80070301/I) with the
average of the data of series 2. (X: equation VI.28;
o : equation VI.28 corrected for the influence of N_3).

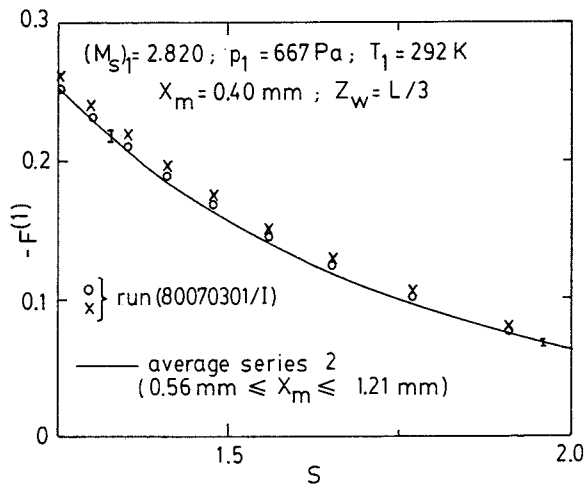When a misalignement Δz_w = 8 mm is assumed in the experiments of series 1, the data on $F^{(1)}$ of series 1 and 2 agree within 1%. The reproducibility of individual experiments is about 2%. Within this uncertainty no deviation of similarity was observed in the range $0.7 \leqslant S \leqslant 2$.

In view of the determination of the heat conductivity a fit of the data of each run was obtained by linear regression. The expression used is:

$$F^{(1)} = A_0 + \sum_{j=2} A_j S^{-j}$$ VII.7

The coefficients A_j and the determination r^2 are given in table VII.4. In order to achieve an optimal fit we used a rather large number of terms. As a result of the rather large correlation between some powers of S the individual coefficients A_j have a low significance.

Note : For runs (80062701/I) and (80062702/I) the pressure data are not available. For the determination of the heat conductivity we used the average of the pressure data of the series 2 (figure VII.3).

Series 3 :
The experimental procedure followed for series 3 is identical to the procedure followed for series 2. The fits of the data are given in table VII.5.

Series 4 :
In order to obtain an estimate of the influence of the side-wall boundary layers on the laser schlieren data we performed in shock tube II (optical path length L= 4.2 cm) a measurements series similar to series 1 and 2 (shock tube I, optical path length L = 10 cm).
In figure VII.15 we compare the averages of the data of series 2 and 4. The data of series 4 appears to be about 7% lower than the data of series 2!!

N°	run	A_0	A_2	A_3	A_4	A_5	A_6	r^2
1	80062701/I	1.2506-2	2.0514-1	-1.6558	1.5825	-6.4781-1	9.9348-2	0.999947
2	80062702/I	-1.9353-4	7.5512-1	-3.5128	3.9776	-2.0033	3.8052-1	0.999942
3	80063001/I	**8**.8265-3	3.2353-1	-2.0181	2.0075	-8.6824-1	1.4244-1	0.999984
4	80063003/I	-2.3435-2	1.4514	-6.0642	7.7670	-4.5760	1.0420	0.999985
5	80070101/I	9.4915-3	2.7270-1	-1.7610	1.4540	-3.8179-1	-	0.999674
6	80070102/I	1.8737-2	2.1946-1	-1.8603	1.9593	-9.0137-1	1.5813-1	0.999985
7	80070103/I	-1.5948-2	1.2220	-5.2771	6.5690	-3.7172	8.0412-1	0.999986

Table VII.4: Fits of the $F^{(1)}$ data of series 2($0.7 \leqslant S \leqslant 3.0$)[⊗].

N°	run	A_0	A_2	A_3	A_4	A_5	A_6	r^2
8	80070302/I	-8.5522-3	7.3525-1	-3.0811	3.2265	-1.5209	2.7572-1	0.999978
9	80070401/I	-2.4422-3	5.8754-1	-2.7075	2.8319	-1.3163	2.2937-1	0.999989
10	80070701/I	-1.7550-3	8.3535-1	-3.9764	5.1853	-3.1870	7.6796-1	0.999967
11	80070801/I	-2.2906-2	1.4150	-5.8199	7.4728	-4.4424	1.0151	0.999968
12	80070802/I	-3.9125-3	6.7375-1	-3.0552	3.3514	-1.6594	3.1789-1	0.999986
13	80070901/I	-1.1749-2	9.8208-1	-4.1150	4.8077	-2.5713	5.2852-1	0.999944
14	80070902/I	-1.8973-2	1.1306	-4.5339	5.2169	-2.7227	5.4302-1	0.999993

Table VII.5: Fits of the $F^{(1)}$ data of series 3 $(0.7 \leqslant S \leqslant 3.0)$[⊗].

⊗ Note:
$$F^{(1)} = A_0 + \sum_{j=2} A_j \, S^{-j} \; ;$$
$$1.2506\text{-}2 = 1.2506 \times 10^{-2}.$$
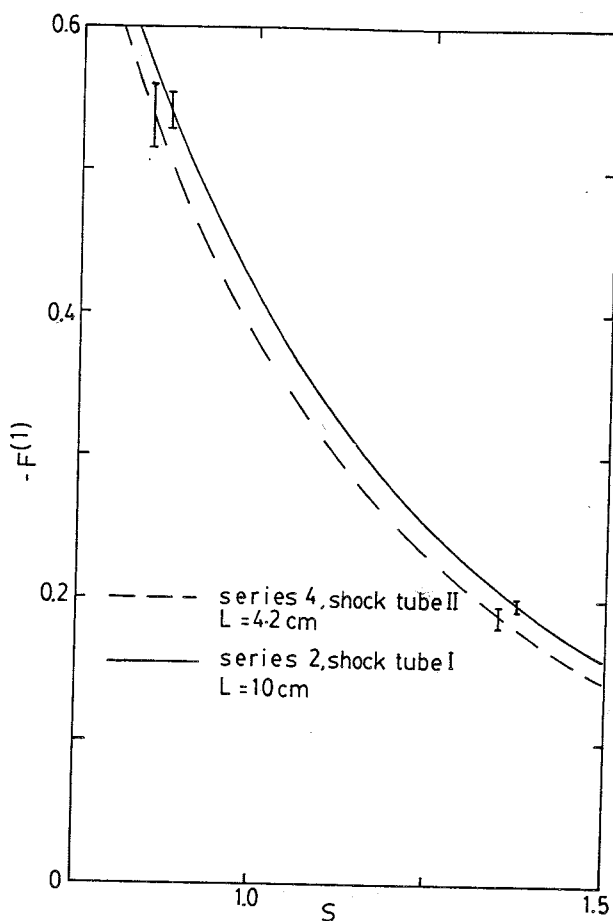
Figure VII.15 : Comparison of the data obtained in shock tube I (L = 10 cm) with the data obtained in shock tube II (L = 4.2 cm).

Translated in terms of effective optical path such a discrepancy implies an error of about 5% in the data of series 2 (shock tube I).

Series 5 :

In order to obtain some insight in the influence of the side-wall boundary layer we performed a series of measurements at lower pressures p_1 = 267 Pa. Unlike the data of series 1, 2, 3 and 4 the experimental results show a large scatter (20%) for similar experiments.

<u>Series 6 :</u>

An additional series of measurements was carried out for high initial pressures p_1 = 2666 Pa. The data obtained agree within the experimental accuracy with the data of series 4.

<u>Conclusions :</u>

Within the experimental accuracy the structure of the boundary layer is self-similar.

A significant influence of side-wall boundary layers cannot be excluded (Additional experiments are necessary).[x]

[x] <u>Note</u> : As stated in section III.e the side wall boundary layers might penetrate into the reflected shock region. This might induce a complex turbulent flow. Because of the complexity of this problem measurements in shock tubes with different cross sections and at various pressures are certainly necessary in order to obtain high accuracy data on the heat conductivity.

VII.e. Heat conductivity data

Using the selfsimilarity of the boundary layer structure one can write formula II.21 in the form:

$$\lambda = \lambda_5\left(\frac{\rho}{\rho_5}\right)\frac{\left[\ -\frac{S}{2} + \frac{2(q_w)_{th}}{5\,p}\left(\frac{t}{a_5}\right)^{1/2} - \frac{3}{5}\frac{t}{p}\left(\frac{d\,p}{d\,t}\right)\ \left(S + \dfrac{\displaystyle\int_\infty^S F^{(1)}\,dS'}{F^{(1)}}\right)\ \right]}{\left[\ \frac{1}{F^{(1)}}\left(\frac{d\,F^{(1)}}{d\,S}\right) - (1+\nu)\,F^{(1)}\left(\frac{\rho_5}{\rho}\right)\ \right]} \qquad\text{VII.8}$$

where [a] :

$$(\rho/\rho_5) = (p/p_5)^{0.6} + \int_\infty^S F^{(1)}\,dS' \qquad\qquad\text{VII.9}$$

and λ_5 is the reference value calculated with formula VII.4. For ν we used the value $\nu = 0.71$ expected to approximate $(T/\lambda)(d\lambda/dT)$ within 5% for $T > 10^3$K.

We first neglect the (dp/dt) term and the time stretching in the local similarity approximation of $(q_w)_{th}$. In figure VII.16 we compare calculations of λ with these corrections (—— —— ——) to the calculations without these corrections (- - - - - -).
In both cases we used the "global fit" of the schlieren data (equation VII.7 and table VII.4). In order to get an impression of the sensitivity of the procedure for the fit used, we show in figure VII.16 the data obtained by using a "local fit" (linear regression) in order to estimate $(dF^{(1)}/dS)$. In view of the accuracy of the experimental data (ca 3%) the discrepancies between the three procedures are negligible.

[a] Note :
  The integration bound "∞" was replaced by $S' = 3$.
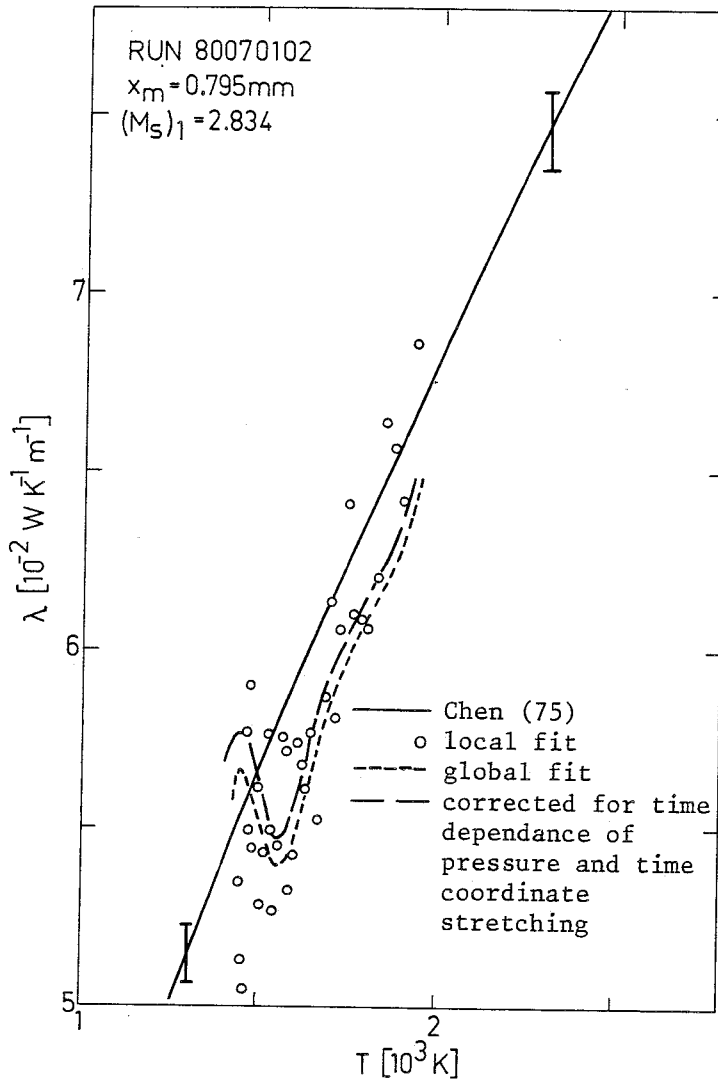
Figure VII.16 : Influence of the fit of the $F^{(1)}$ data, of the (dp/dt) term in equation VII.8 and of the time coordinate stretching in the local similarity approximation of $(q_w)_{th}$ on the determination of the heat conductivity.

In figures VII.17 and 18 we compare the data of series 2 (section VII.d) to the data of Chen (75). The corresponding pressure data are given in figure VII.3. The initial state and Mach number data are given in table VII.2. The fits of the $F^{(1)}$ data are given in table VII.4.

For low temperatures (T ⩽ 1900 K) the data show no significant
dependence on x_m. At higher temperatures the data tend to be higher.
This effect is expected to be due to the non-uniformity of the
reflected shock region (section VII.c and figure VII.10). The non-
uniformity of the reflected shock region induces a deviation of the
structure of the boundary layer from the similarity structure assumed
in equation VII.8 (section III.f).

The average of the data for T ⩽ 2100 K (including all terms
in the energy balance) are compared in table VII.6 to data calculated
on the basis of the intermolecular potential of Aziz (77). ⍺
We conclude that the data are lower than the heat conductivity data
of Chen (75) by 4%. In view of the accuracy of the data of Chen (75)
(1.5%) and the reproducibility of our data (3%) this discrepancy is
significant. The main source of systematic error in the procedure for
the determination of the heat conductivity is the underestimation of
the density $\rho_\infty(0)$. (section VII.c).
Further the influence of the side-wall boundary layers is not well
understood and might induce errors of a few percent (section VII.d).

⍺ Note :

  Private communication Aziz (80).
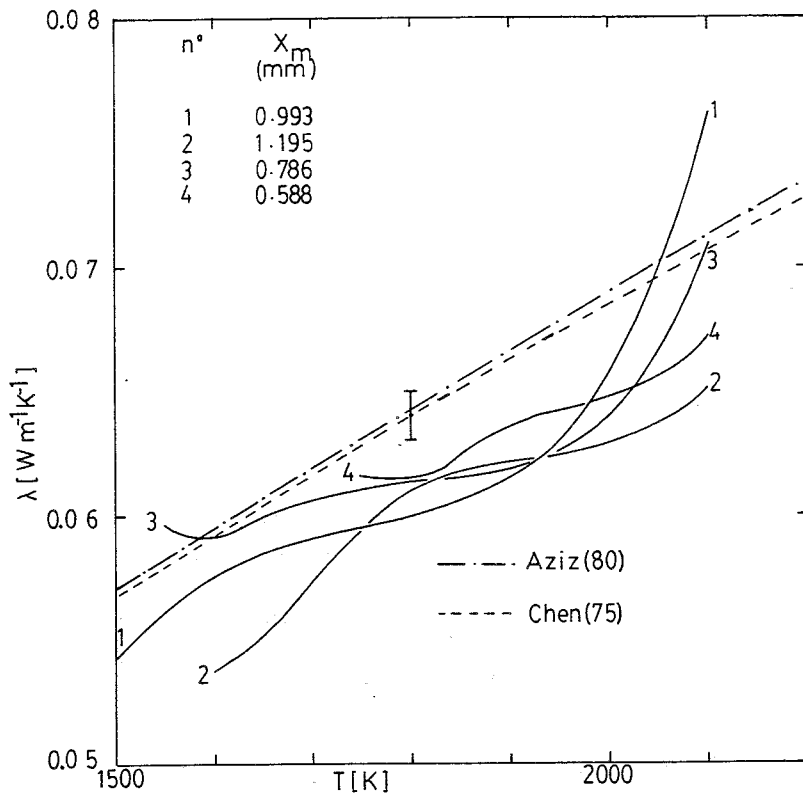
Figure VII.17 : Heat conductivity data without $(\frac{dp}{dt})$ term and time stretching.
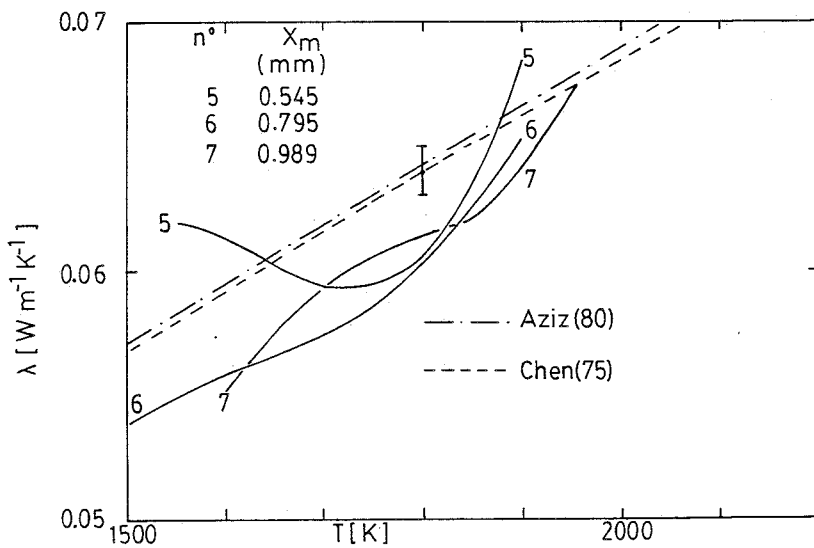
Figure VII.18 : Heat conductivity data without (dp/dt) term and time stretching.

T	λ	σ_λ	λ_{th}	$(\lambda_{th}/\lambda) - 1$
(K)	$(10^{-2}W/m\ K)$	$(10^{-2}W/m\ K)$	$(10^{-2}W\ m\ K)$	
1400	5,67	–	5.430	−0.042
1450	5.38	–	5.559	0.033
1500	5.41	–	5.687	0.051
1550	5.86	0.27	5.813	−0.008
1600	5.80	0.25	5.938	0.023
1650	5.89	0.18	6.062	0.028
1700	5.98	0.12	6.184	0.033
1750	6.09	0.10	6.305	0.034
1800	6.17	0.06	6.425	0.040
1850	6.29	0.08	6.544	0.039
1900	6.47	0.22	6.661	0.029
1950	6.40	0.07	6.778	0.056
2000	6.53	0.11	6.894	0.053
2050	6.75.	0.21	7.009	0.037
2100	7.09	0.42	7.123	0.005

Table VII.6

Comparison of the average of the experimental data λ
with the theoretical data λ_{th} of Aziz (80).
σ_λ is the standard deviation of the experimental data.

In figure VII.19 we compare the data of series 3 to the data of Devoto (73) and Aziz (80). Our data are about 15% lower than the data of Devoto (73) but agree within the experimental accuracy (3%) with the data of Aziz (80).
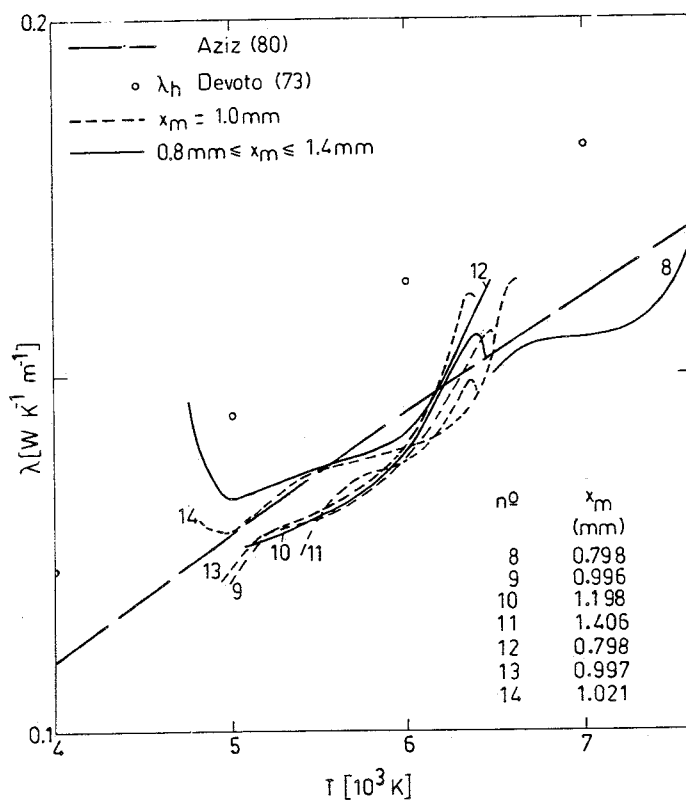
Figure VII.19 : Heat conductivity data without (dp/dt) term and time stretching.

In table VII.7 we compare the average of our data (including all terms) with the data of Aziz (80).

T	λ	σ_λ	λ_{th}
(K)	(W/m K)	(W/m K)	(W/m K)
5000	0.127	0.04	0.1279
5200	0.129	0.03	0.1313
5400	0.131	0.04	0.1348
5600	0.134	0.03	0.1382
5800	0.137	0.02	0.1415
6000	0.140	0.02	0.1449
6200	0.145	0.04	0.1482
6400	0.149	0.06	0.1515
6600	0.151	-	0.1547
6800	0.152	-	0.1579
7000	0.153	-	0.1611
7200	0.155	-	0.1643
7400	0.158	-	0.1675
7600	0.164	-	0.1706

Table VII.7.

Comparison of the average of the experimental data λ
with the theoretical data λ_{th} of Aziz (80).

Comments:

The data below 6600 K are the average of 6 experiments.

Above 6600 K only one experiment is available.

σ_λ is the standard deviation.

The pressure is 1.3×10^5 Pa.

In figure VII.20 we give an overall view of the data.

Figure VII.20 : Comparison of the data obtained from shock tube experiments with data of previous studies.

The data presented by Vrugt (76) are about 5% lower than our data. A further analysis of the procedure used by Vrugt (76) <u>did not</u> reveal any systematic error of this order of magnitude.

This discrepancy is expected to be due to:

    a. the time dependence of the pressure which is not taken into account by Vrugt (76).

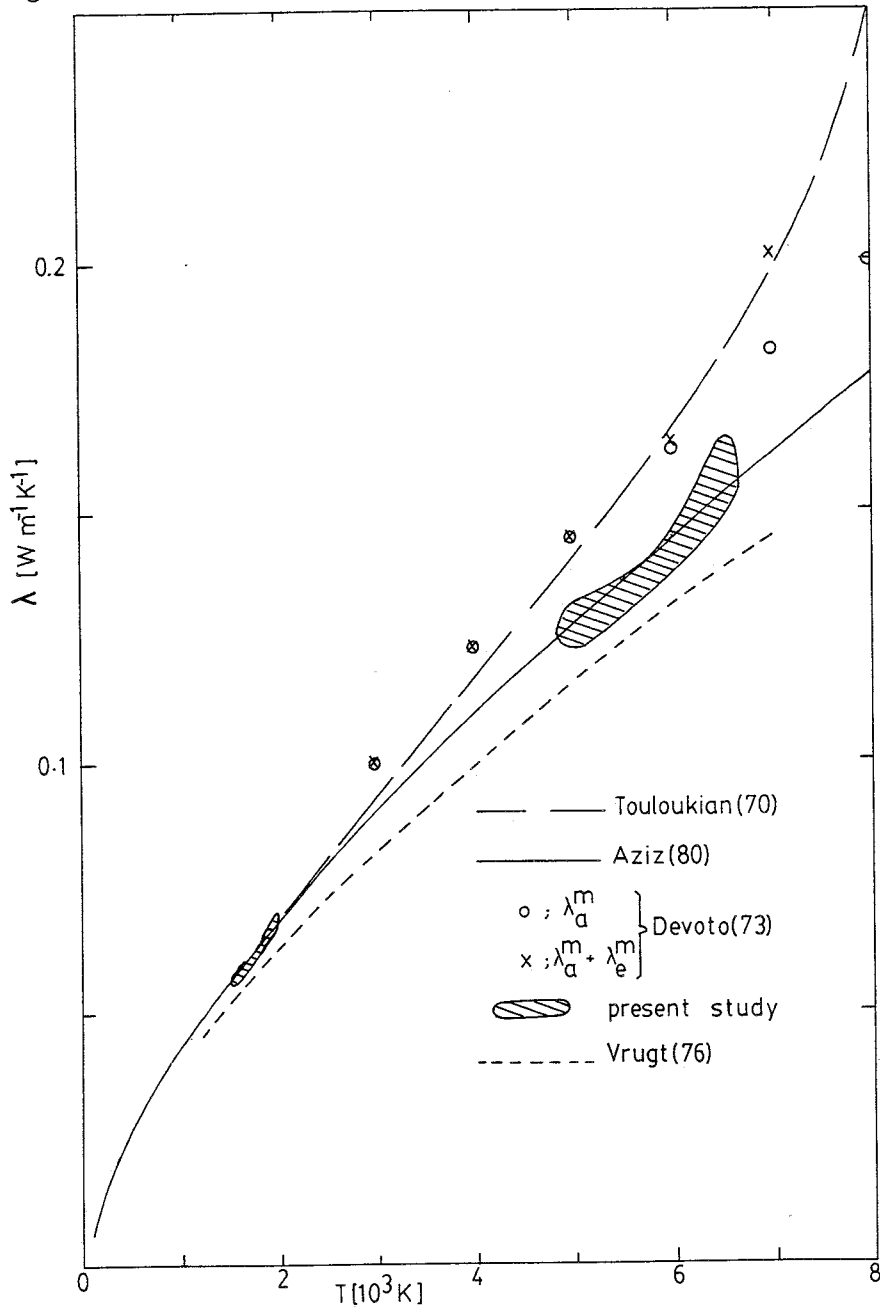   b. a different estimate of $(q_w)_{th}$.

    c. influence of the third derivative of the refractive index.

    d. schlieren effect of the windows [Ω].

    e. different Mach number measurement.

       It is interesting to calculate lower and upper bounds for the heat conductivity by comparing the various intermolecular potentials $V(r)$ available.

       The heat conductivity data of Devoto (73) were calculated on the basis of the repulsive exponential potential of Colgate (69). This potential appears to be "softer"[ΩΩ] than the corresponding part of the potential of Aziz (77) (see table VII.8). The Lennard-Jones potential of Clifford (77) selected by Jain (80) on the basis of the data of Chen (75) is "harder"[ΩΩ] than the potential of Aziz (77). In a restricted temperature range a power law fit of the temperature dependence of the heat conductivity should be rather accurate. Because the Lennard-Jones potential would yield a value of $\nu \geqslant 0.67$ while a fit of the data of Devoto (73) yields $\nu = 0.71$ we expect that:

$$0.67 \leqslant \nu \leqslant 0.71 \qquad\qquad\qquad VII.10$$

[Ω] Note :

  In the present study considerable attention has been given to the quality of the windows. The windows were checked both statically (translation of a light beam along the window) and dynamically (run with $x_m = 7$ mm, section VII.c).

[ΩΩ] Note :

  The expressions soft and hard refer to small and large slope respectively of the curve $V(r)$.

Combining this estimate with the data of Chen (75) we find the estimate:

$$0.0568(T/1500)^{0.67} \leqslant \lambda \leqslant 0.0568(T/1500)^{0.71} \quad \text{VII.11}$$

for $10^3 K \leqslant T \leqslant 10^4 K$. The data of Aziz (80) and our data agree with this estimate.

r	Colgate (69)	Aziz (77)	Jain (80)
	V/k	V/k	V/k
(:nm)	(K)	(K)	(K)
0.20	3.56+4	6.09+4	2.50+5
0.22	1.64+4	2.96+4	7.66+4
0.24	7.55+3	1.38+4	2.53+4
0.26	3.48+3	6.19+3	8.72+3
0.28	1.60+3	2.59+3	3.01+3
0.30	7.38+2	9.48+2	9.51+2
0.32	3.40+2	2.41+2	2.06+2
0.34	–	−3.82+1	−5.43+1
0.36	–	−1.21+2	−1.31+2
0.38	–	−1.43+2	−1.40+2
0.40	–	−1.28+2	−1.26+2
0.42	–	−1.05+2	−1.06+2
0.44	–	−8.34+1	−8.69+1
0.46	–	−6.50+1	−7.02+1
0.48	–	−5.04+1	−5.65+1
0.50	–	−3.91+1	−4.54+1

Table VII.8.

Comparison of various intermolecular potentials V(r).
r is the distance.

In view of the systematic error in the estimate of the state of the gas outside the boundary layer (about 3%) and the discrepancy between the data obatained in different shock tubes (7%) it should be clear that the actual power of the shock tube method has not yet been fully

exploited. In view of the high reproducibility of the data (3%) the shock tube method might, when improved have an accuracy comparable to the hot wire colomn method (2%).

VIII.   EXPERIMENTAL DATA ON THE STRUCTURE OF THE FLOW INDUCED BY
         THE REFLECTION OF AN IONIZING SHOCK WAVE

VIII.a. Introduction

         While in the non-ionized case the shock tube method has been
used before for the determination of the heat conductivity of gases
(chapters II, III and VII) no similar attempt has been reported in
the ionized case (section I.d). The present study, a first attempt,
has an exploring character. The data obtained are not accurate enough
to improve our knowledge about the heat conductivity of partially
ionized argon. However our insight in the structure of the reflected
shock region and the end-wall boundary layer in partially ionized
argon has been considerably improved.
The attempted determination of the heat conductivity presented in
section VIII.e can be used in order to estimate the relative
importance of the various terms in the energy equation. This yields
an estimate of the accuracy which must be achieved in order to obtain
valuable heat conductivity data by means of the shock tube method.
         In section VIII.b we give the data collected on the flow
outside the boundary layer in pure argon. In section VIII.c we
consider the influence of the addition of 0.5% hydrogen to the argon.
The hydrogen appears to be a powerful catalyzer for the initial
ionization relaxation process. The shortening of the ionization
relaxation time t_{ion} improves the agreement between the experiment
and the thermal Rayleigh problem (section V.e).
Further the addition of hydrogen suppresses the instability of the
ionization front (section V.b). In section VIII.d we present the data
on the structure of the thermal boundary layer.

Note :

The flow induced by the reflection of an ionizing shock wave has been
described in chapter V. A review of related studies has been given in
section I.d. The experimental procedure used is similar to the
procedure in the non-ionized case (chapter VII). In this chapter we
limit ourselves to the presentation of experimental data.

VIII.b. Flow outside the boundary layer in pure argon

In order to determine the state of the gas outside the boundary layer we carried out a series of simultaneous pressure, absorption and laser schlieren measurements (0.6328 μm). Typical records are shown in figure VIII.1.
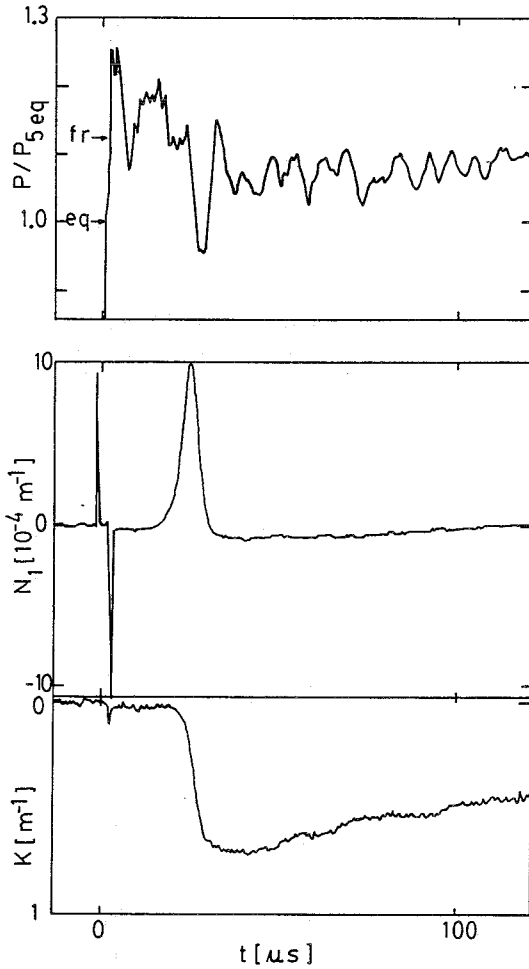

Figure VIII.1 : Pressure p, absorption coefficient K and refractive index gradient N_1 measured in run (80030403/II):
x_m = 3.00 mm; p_1 = 666 Pa, T_1 = 293.4 K; p_o = 10^{-1} Pa; $(M_s)_1$ = 8.90; $(M_s)_2$ = 8.88.

A systematic study of the ionization relaxation process in argon is

difficult because the flow is strongly sensitive to the purity level
of the argon.

At high purity levels (10 ppm) the ionization front shows
instabilities similar to the instabilities observed by Glass (78)[Ω]
behind the incident shock wave. This effect is illustrated in figure
VIII.2 in which we show a typical schlieren record obtained in a first
measurement series with $p_o = 3 \times 10^{-3}$ Pa and $p_{oo} = 10^{-4}$ Pa.
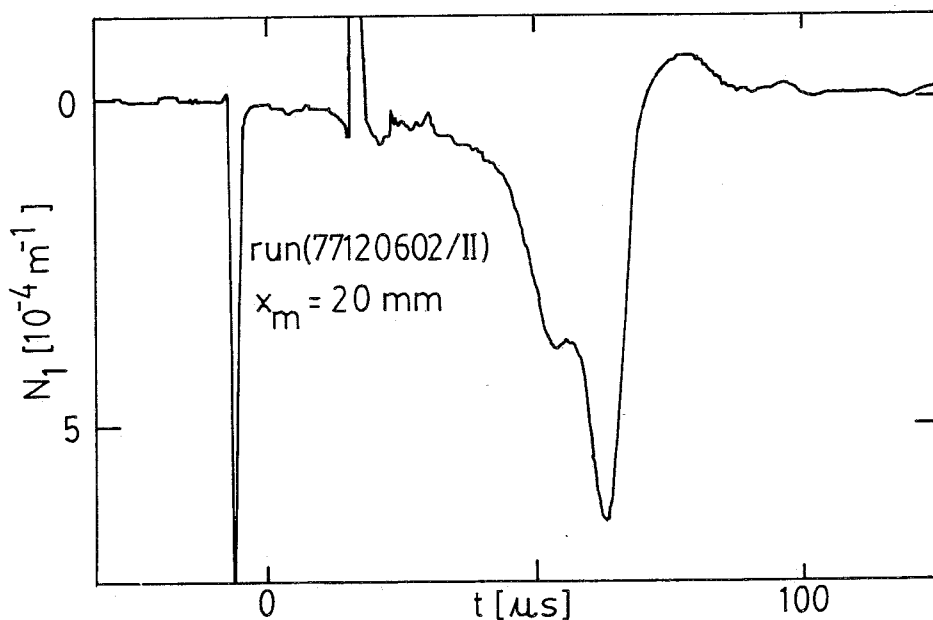
Figure VIII.2. : Laser schlieren record of the
ionization relaxation process showing instability
(impurity level 10 ppm).
run (77120602/II)
$M_s = 8.53$; $p_1 = 667$ Pa, $T_1 = 294$ K, $p_o = 3 \times 10^{-3}$ Pa,
$p_{oo} = 10^{-4}$ Pa.

In order to improve the reproducibility of the flow we carried out
experiments in argon with a small amount of impurities.

A measurement series was carried out in argon with about 150 ppm air.

[Ω] Note : See also Baryshnikov (79).

146

This measurement series is refered to as "pure argon".

An additional measurement series was carried out in a 99.5% Ar + 0.5% H_2 mixture (sections VIII.c and d).

Pressure data :

The pressure p at the end-wall was measured as described in section VII.b. In figure VIII.3 we compare the pressure measured at t = 200 μs with the value calculated with the Rankine-Hugoniot relations (Appendix I), as a function of $M_s p_1$.

As noticed in section V.b the data show significant discrepancy from the Rankine-Hugoniot value at low initial pressures ($p_1 \leqslant 10^3$ Pa).

Symbol	P_1 [10^2 Pa]
x	2.67
●	4.00
o	6.67
+	9.33
△	13.33
▽	20.0
✳	26.7
■	66.7
□	133.3
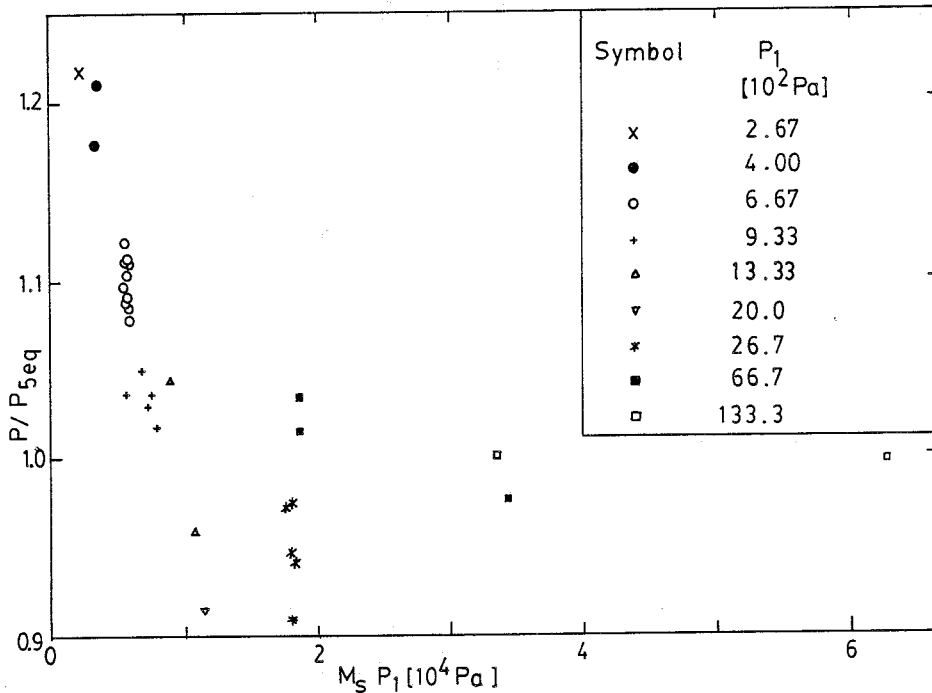
Figure VIII.3 : End-wall pressure at t = 200 μs in shock tube II.

Diaphragm thickness 1 mm.

Absorption coefficient :

The maximum of the absorption signal (figure VIII.1) is given as a function of the square of the calculated electron density $(n_e^2)_{RH}$ in figure VIII.4 (wave-length 0.6328 μm). From those data we obtained the value of the coefficient K_o in equation V.2 :

$$K_o = 8.8 \times 10^{-2} m^{-1}$$

The uncertainty in the determination of K_o is of the order of 20% mainly as a result of the uncertainty in the estimate of the electron density (section V.c). [x]
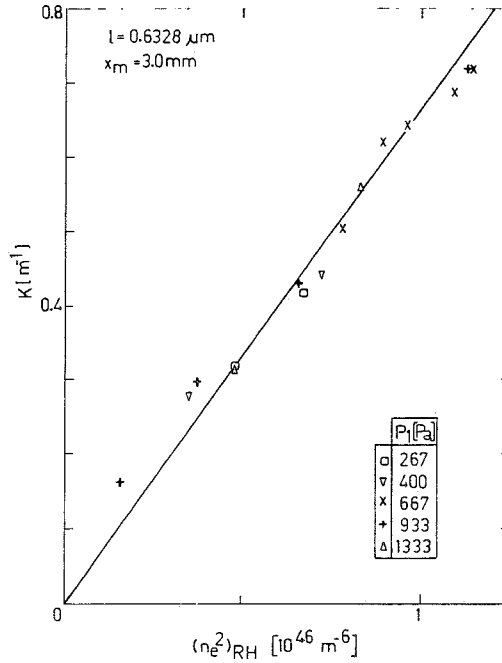
Figure VIII.4 : Absorption of a light beam (0.6328 μm) as a function of the calculated electron density. Equation V.2; T_e = 11.300K.

[x] Note:

By lineair regression we obtain the fit of the data:
$$K = [\ 0.0424 + 0.601\ (n_e/10^{23})^2 - 0.314\ ((T_e - \bar{T}_e)/10^4)\ ] m^{-1}$$
where:
$$\bar{T}_e = 1.126 \times 10^4 K$$
and
$$r^2 = 0.986$$

For the Biberman factor $\zeta(\lambda_1 T_e)$ defined by (Hofsaess (78)):
$$K = 1.367 \times 10^{-27}\ \frac{1^3 n_e^2}{\sqrt{T_e}}\ \exp\ (T_o/T_e)\ \zeta(1,T_e)$$
we find: $\zeta(1,T_e) = 2.74$.

Radiation loss :

Using the procedure described in section V.c we can determine the
state of the plasma after the ionization relaxation ($t > t_{ion}$) from
the absorption and pressure measurements.

Using the energy equation (section IV.d) we calculated the radiation
loss Q_r from those data.

In figure VIII.5 we compare our data with the data of Kopainsky (71)
on Q_r and the continuum contribution Q_c to Q_r.

Within the accuracy of the measurements all our data appeared to be
a function of the electron density only.

The difference between our data and the data of Kopainsky (71) is due
to the difference of the geometry of the plasmas. The measurements of
Kopainsky (71) were carried out in a cylindrical electric discharge
(radius 3 mm).
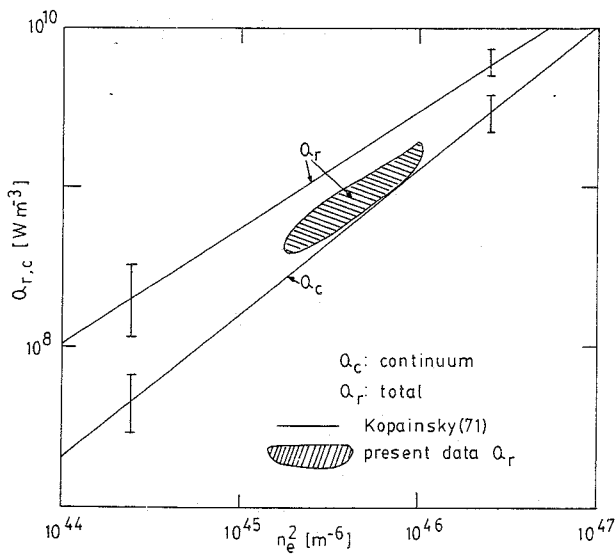
Figure VIII.5 : Comparison of the radiation loss Q_r
measured at x_m = 3 mm and the data of Kopainsky (71).
$10^5 Pa \leqslant p \leqslant 5 \times 10^5 Pa$; $10^4 K \leqslant T \leqslant 1.3 \times 10^4 K$.

In a similar way as described above one can determine Q_r from simultaneous pressure and light emission measurements (Petchek (53), Logan (77)). Measurements of Q_r performed in this way agree within the experimental accuracy with the data of figure VIII.5. Further the data obtained in shock tube I agree well with the data of shock tube II.

VIII.c. Flow outside the boundary layer in a 99.5% Ar + 0.5% H₂ mixture [Ω]

Influence of the hydrogen :

As noticed in sections V.b and VIII.a the addition of hydrogen to the argon improves the reproducibility and the stability of the flow in the reflected shock region. This is due to the strong catalytic influence of the hydrogen in the initial phase of the ionization relaxation.

This effect is illustrated in figure VIII.6 where we compare the laser schlieren signal at x_m = 3.0 mm in pure argon to the signal in a 99.5% Ar + 0.5% H₂ mixture.
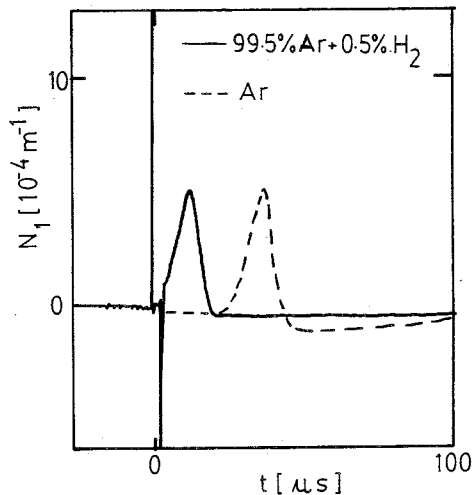
Figure VIII.6 : Refractive index gradient (0.6328 µm) at x_m = 3.00 mm.

————— 99.5% Ar + 0.5% H₂; $(M_s)_1$ = 8.37; p_1 = 669 Pa; T_1 = 294.8 K; run (80042502/II).

-------- pure Ar; $(M_s)_1$ = 8.40; p_1 = 667 Pa; T_1 = 293.8 K; p_o = 10⁻³ Pa; run (78092201/II).

[Ω] Note :

The work presented in this chapter has been carried out by S. Bruinsma.

As we will see in the next section the reduction of the ionization relaxation time t_{ion} improves the agreement between the structure of the boundary layer and the thermal Rayleigh model.

The hydrogen is not expected to influence the transport properties of the plasma significantly but the energy and ion-mass production source terms ε_{eh} and M_i are increased by approximately a factor 2. The addition of hydrogen appears also to induce bifurcation like phenomena in about one run out of ten.

This effect is illustrated in figure VIII.7.
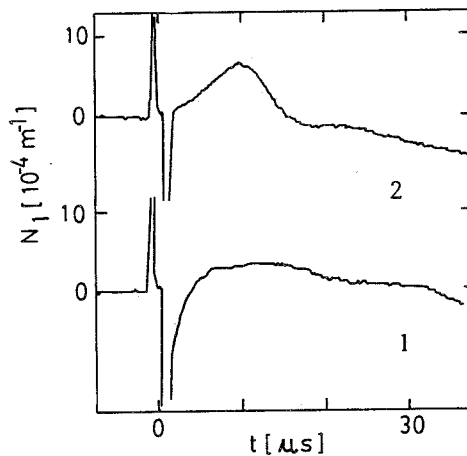
Figure VIII.7 : Comparison of a laser schlieren signal
showing bifurcation like behaviour (1) to a normal
signal (2). 99.5% Ar + 0.5% H_2.
(1) : x_m = 1.20 mm; p_1 = 670 Pa; T_1 = 294.6 K; $(M_s)_1$ = 8.21
      run (80042403/II)
(2) : x_m = 1.20 mm; p_1 = 670 Pa; T_1 = 294.6 K; $(M_s)_1$ = 8.30
      run (80042404/II).

(x,t) diagram of the flow :

In figure VIII.8 an (x,t) diagram of the flow made out of laser schlieren signals at various positions is shown.

The corresponding end-wall and side-wall pressure records are shown in figure VIII.9.
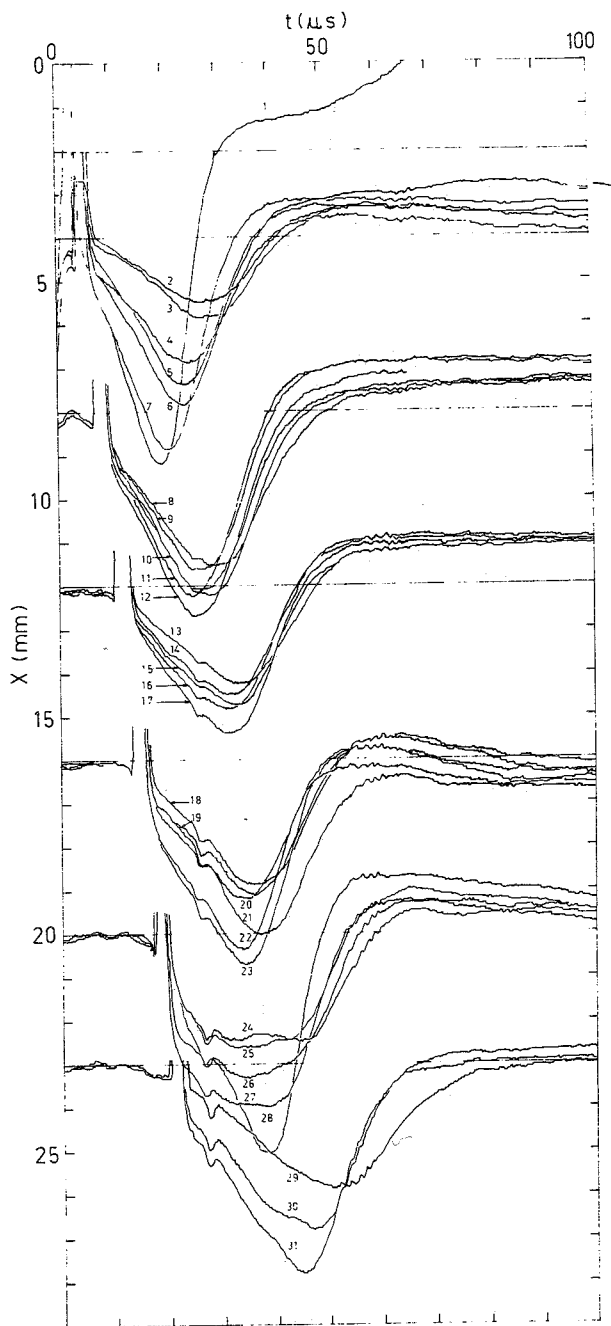
N°	M_s	x_m (mm)
1	7.82	2.0
2	7.24	4.0
3	7.24	4.0
4	7.62	4.0
5	7.74	4.0
6	7.78	4.0
7	7.80	4.0
8	7.57	8.0
9	7.78	8.0
10	7.70	8.0
11	7.74	8.0
12	7.74	8.0
13	7.67	12.0
14	7.78	12.0
15	7.71	12.0
16	7.74	12.0
17	7.71	12.0
18	7.67	16.0
19	7.60	16.0
20	7.67	16.0
21	7.68	16.0
22	7.78	16.0
23	7.71	16.0
24	7.78	20.0
25	7.86	20.0
26	7.72	20.0
27	7.79	20.0
28	7.94	20.0
29	7.49	23.0
30	7.67	23.0
31	7.72	23.0

Table VIII.1:

M_s and x_m data of figure VIII.8.

Figure VIII.8 : Laser schlieren signals as function of x and t. (x,t) diagram of the ionization relaxation in the reflected shock region. Shock tube I; 99.5% Ar + 0.5%H_2 mixture; p_1 = 667 Pa; T_1 = 294 K; see Mach number data table VIII.1.

The corresponding data on the reflected shock velocity v_r are shown in figure VIII.10. These data clearly show the influence of the end-wall boundary layer on the reflected shock. The order of magnitude of the measured change of the reflected shock velocities agree with the data presented by Sturtevant (64). The change of the reflected shock velocity is responsible for the non-uniformity of the reflected shock region discussed in section VII.c.

Q_r :

No significant influence of the hydrogen addition on the radiation loss Q_r has been observed.

k_{H-Ar}:

In the initial phase of the ionization relaxation process the ionization rate is determined by the excitation of hydrogen by collisions with argon atoms. This reaction rate k_{H-Ar} can be estimated from the measured electron density gradient $(n_e')_o$ just behind the reflected shock with the approximation:

$$k_{H-Ar} = \frac{(v_r)_{fr}}{n_H \, n_{Ar}} (n_e')_o \qquad\qquad VIII.1$$

where $(v_r)_{fr}$ is the frozen reflected shock velocity and n_H, n_{Ar} are the hydrogen and argon atom densities.

For the measurement of $(n_e')_o$ we used a laser schlieren set-up with a wavelength of 3.39 μm. In such a case the heavy particles contribution to the schlieren signal is negligible.

The data on k_{H-Ar} obtained in this way are shown in figure VIII.11.

154

run(78011205/I)

M_s = 7.73

P_1 = 667 Pa

T_1 = 294 K

99.5% Ar + 0.5% H_2

X = 0 mm

X = 80 mm

100 μS
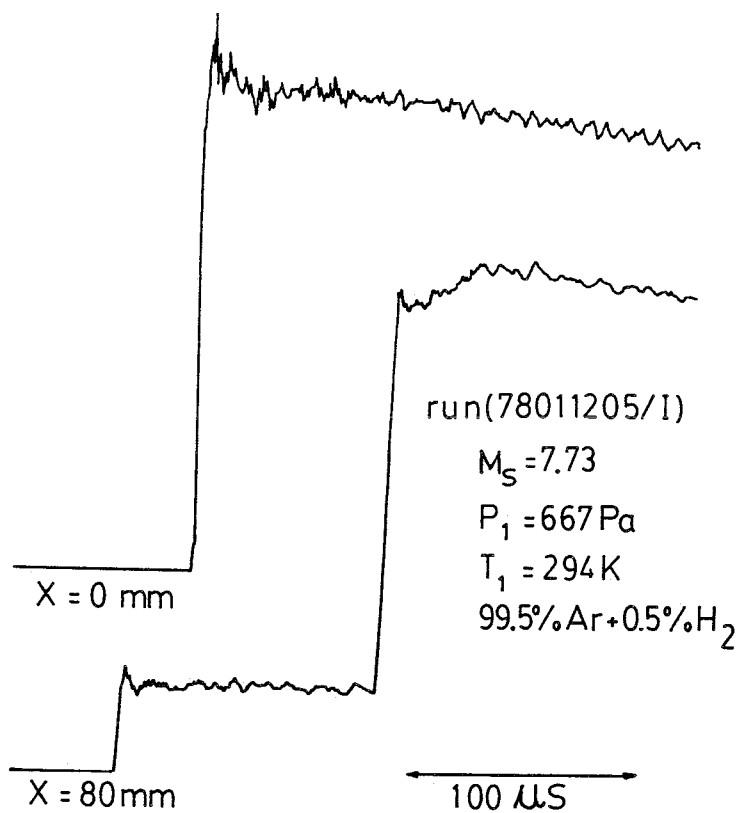
Figure VIII.9 : End-wall and side-wall pressure records corresponding to the (x,t) diagram of figure VIII.8.
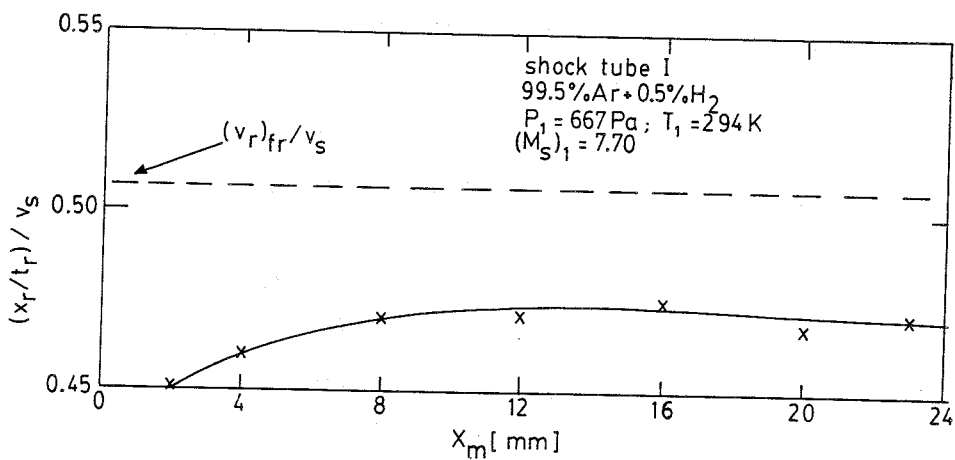
Figure VIII.10 : Comparison of the measured reflected shock position (x_r, t_r) and of the calculated reflected shock velocity $(v_r)_{fr}$.

Figure VIII.10 (continuation)

In the calculation of $(v_r)_{fr}$ we assumed that the hydrogen in region 2 is fully dissociated.

Each point (x) has been obtained as the average of about 5 measurements (a linear dependence of (x_r/t_r) on M_s for a given value of x_m has been assumed.
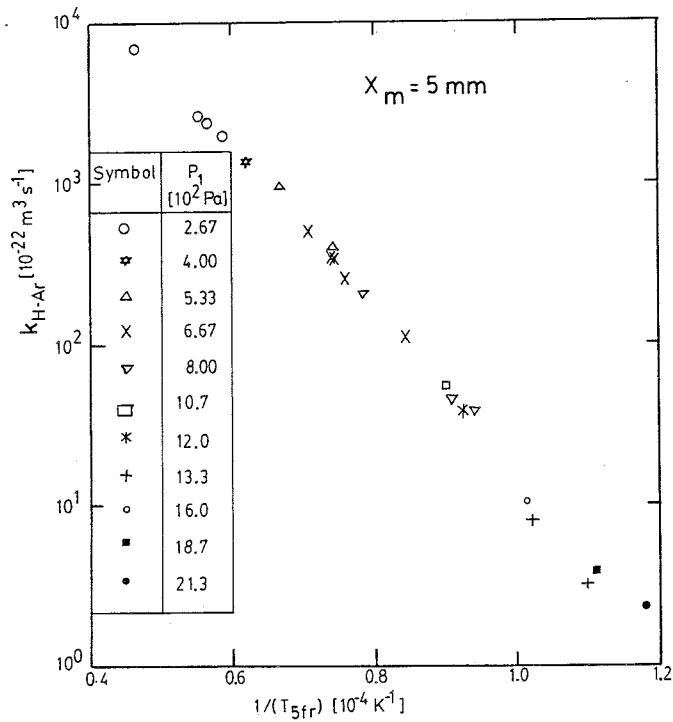
Figure VIII.11 : Reaction rate k_{H-Ar} for excitation of hydrogen by collision with argon atoms as a function of the temperature.

VIII.d. Boundary layer structure

Laser schlieren measurements :

Measurements of the structure of the boundary layer were carried out
with a two-wavelength laser schlieren set-up.
The wavelengths are: l_1 = 0.6328 μm and l_2 = 1.152 μm (He-Ne laser;
Spectra Physics type 120).
Simultaneously with the schlieren measurements we measured the end-
wall pressure, the absorption of the laser beam (0.6328 μm), and the
displacement of the shock tube.
All the data presented in this chapter have been obtained in shock
tube II. The set-up is shown in figure VIII.12. Additional technical
details are given in Appendix VI. The experimental procedure is
similar to the procedure followed in the non-ionized case (chapter
VII).

Typical laser schlieren records are shown in figure VIII.13.
From the response of the schlieren system to the passage of the
incident and reflected shocks one can estimate the response time τ of
the detection systems.
We found: $\tau_1 \leq$ 0.2 μs for l_1 = 0.6328 μm and $\tau_2 \approx$ 0.6 μm for
l_2 = 1.152 μm.

The contribution of light emission of the plasma to the
infrared signal (l_2)(of the order of 2%) was determined experimentally.
The influence of the absorption of light by the plasma leads to
similar corrections. The absorption of the red light beam (l_1) was
measured. The absorption of the infrared light beam was calculated by
using formula V.2 in which: K_o = 0.32 m^{-1}, T_o = 1.25 x 10^{4}K,
n_o = 10^{23}m^{-3}. ☒

☒ Note :

  This estimate was obtained on the basis of a series of measurements
  of the absorption outside the boundary layer. The contribution of
  the light emission by the plasma was of the same order of magnitude
  as the absorption signal. This is the reason why no absorption
  measurements of the infrared light beam were carried out in the
  boundary layer.
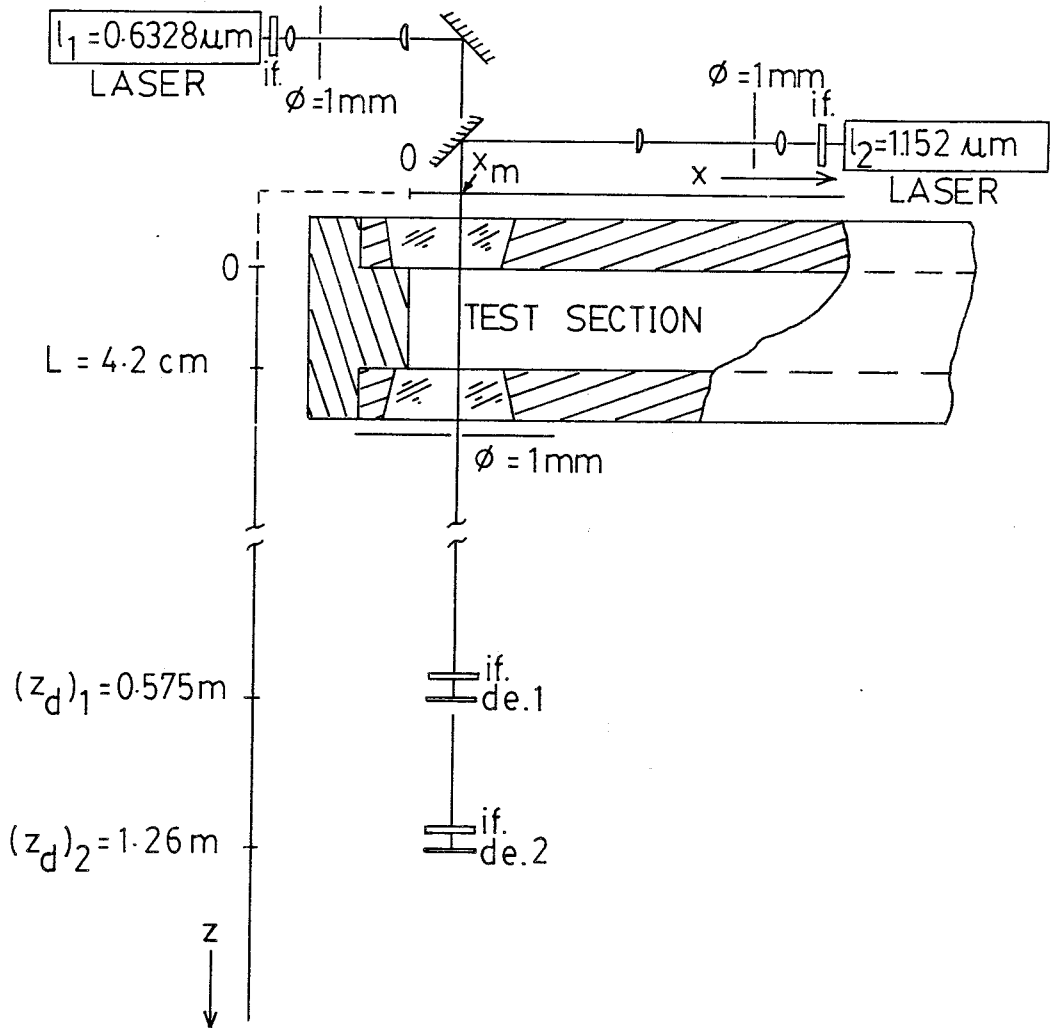
Figure VIII.12 : Principle of the two-wavelength laser schlieren set-up.

In order to reduce the influence of the light emitted by the plasma on the schlieren signal an interference filter (if,) was placed in front of each detection system (de.). The two light beams cross each other just after the test section. The diaphragm placed at this position reduces also the influence of the light emission.
The interference filters in front of the lasers protect the laser for

the light emission from the plasma.

The diaphragm in front of each laser improve the gaussian shape of the beam by filtering out higher order modes.

run(80041501/II); $X_m = 0.80$ mm $(M_s)_1 = 8.06$

$P_1 = 670$ Pa

$T_1 = 295.4$ K

$(\Delta N_1)_{l_1} = 10^{-2}$ m^{-1}

$(\Delta N_1)_{l_2} = 10^{-2}$ m^{-1}

$\Delta t = 100 \, \mu s$
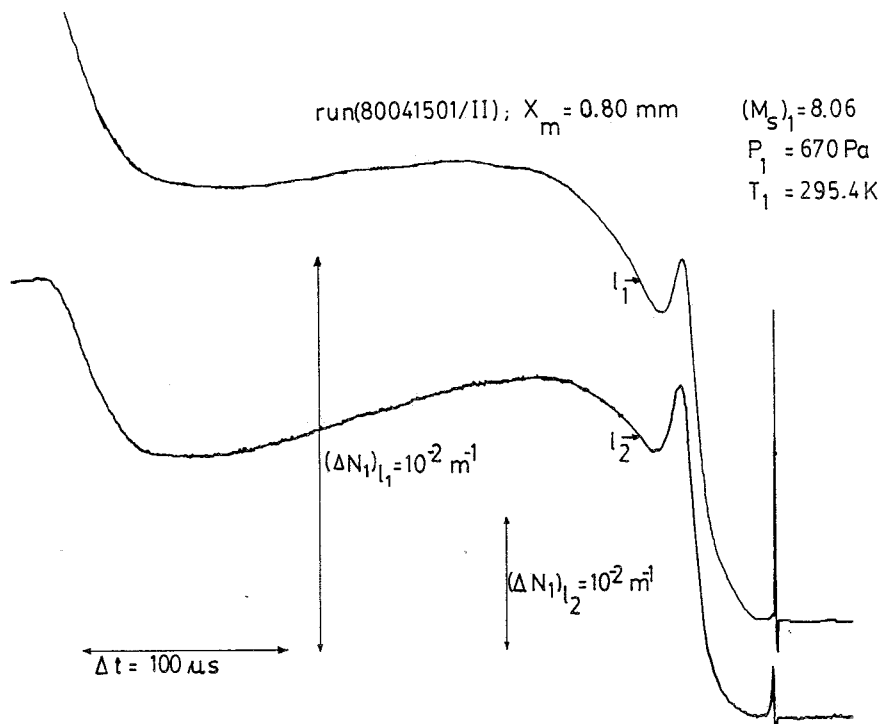
Figure VIII.13 : Laser schlieren records.
$l_1 = 0.6328$ µm, $l_2 = 1.152$ µm.

The shock tube displacement, due to the recoil of the driver section was of the order of 3 µm. This effect is the same for the two light beams and was neglected in view of the uncertainty of 6 µm in the position of the beams. The set-up used for the measurement of the shock tube displacement was similar to the set-up described by Vrugt (76).

Both laser beams were focused at $z_w = L/3$ so that in first approximation the laser schlieren signal is proportional to the refractive index gradient N_1 (section VI.d). Corrections for higher order effects were not carried out. From the refractive index

gradients we obtained the electron and atom density gradients
(n_e' and n_a') by means of formula VI.48.

An estimate of the accuracy of the determination of n_e' and n_a'
was obtained from experiments in which ionization is negligible
(M_s = 3.2, p_1 = 667 Pa, T_1 = 294 K). The uncertainties $\Delta n_e'$ and $\Delta n_a'$
are estimated to be:

$$\frac{\Delta n_e'}{n_e'} = 5\% \qquad\qquad \Delta n_e' \geqslant 10^{24} m^{-4}$$

$$\frac{\Delta n_a'}{n_a'} = 10\% \qquad\qquad \Delta n_a' \geqslant 10^{26} m^{-4}$$

These estimates correspond to the reproducibility of the experiments.
In addition one must take into account the uncertainty due to the
influence of the side-wall boundary layers (see section VII.d).

Electron density from absorption measurements :

The electron density n_e was estimated from the absorption measurements
with formula V.2. The temperature T_e in this formula was determined
from the ideal gas law assuming a single temperature :

$$T = p/(k(n_a + 2n_e)) \qquad\qquad\qquad VIII.2$$

n_a was estimated by integrating the laser schlieren data on n_a'.
The integration constant $(n_a)_\infty$ was determined from the measurement
of the state of the plasma outside the boundary layer described in
section V.c. (absorption and pressure measurements + assumption about
local thermodynamic equilibrium. The accuracy of the determination of
n_e is about 10% with $\Delta n_e \geqslant 5 \times 10^{21} m^{-3}$.

Pure argon : (Ar + 150 ppm air)

In figure VIII.14 the data on n_e' and n_a' for M_s = 8.15 are compared
with the calculations of two thermal Rayleigh problems:
the two temperature relaxation model (reE-reM) and the
local thermodynamic equilibrium model (eqE-eqM) (sections V.e and f).
We see that the eqE-eqM model overestimates the electron density
gradient n_e' significantly while after the ionization relaxation the

reE-reM model agrees well with the experimental data.

The behaviour of n_e' and n_a' during the ionization relaxation
($t \leqslant 60$ μs) is due to the combination of various effects. As a result
of the thermal boundary layer growth the gas has a non-uniform
temperature. The resulting position dependence of the ionization rate
yields high positive values of n_e' for $t = 40$ μs. While the initial
phase of the ionization relaxation, controled by atom-atom ionization
processes, is slow, the final phase of the ionization relaxation
dominated by electron-atom ionization processes is abrupt.
This sudden increase of the ionization degree induces a considerable
decrease of temperature and a mass flux towards the wall (The
pressure decreases only slightly (figure VIII.1)).
This convective effect is observed in our data by a sudden decrease
of the gradients at $t = 45$ μs.

After ionization relaxation is completed a fair agreement
between the reE-reM model and the experimental data is observed for
$x_m < 1.0$ mm. For $x_m \geqslant 1.0$ mm the measurements of both n_e' and n_a' give
significantly lower values than the theory(for $t > 100$ μs).
This is due to the flattening of the outer part of the boundary layer
by the radiation cooling. This is confirmed by the comparison of the
electron density n_e (determined from the absorption measurements)
with the theory in figure VIII.15.

The effects described above are also observed in figures
VIII.16 and VIII.17 in which we show the dependence of n_e' on the
Mach number for $x_m = 0.80$ mm and $x_m = 1.20$ mm.

In figure VIII.17 we observe also negative values of n_e'
during the ionization relaxation ($M_s = 9.27$). In such a case the
ionization occurs in a more uniform gas. The electron density
gradient measured is due to the dependence on the position of the
onset of ionization.

In figures VIII.18 and 19 we give the data obtained for
$M_s = 8.7$. In figure VIII.19 we compare the data on n_e obtained from
the absorption measurements with the integrated laser schlieren data.
The integration constant was determined by setting n_e at $x_m = 1.20$ mm
equal to the average of the absorption measurement data for
1.0 mm $\leqslant x_m \leqslant 1.4$ mm.
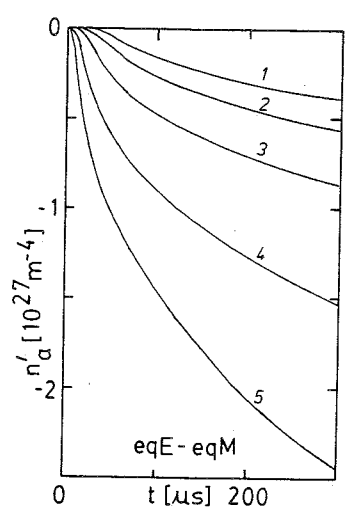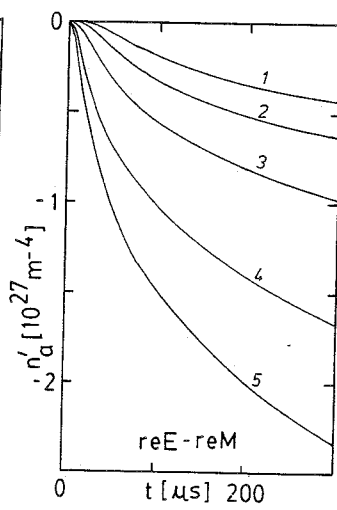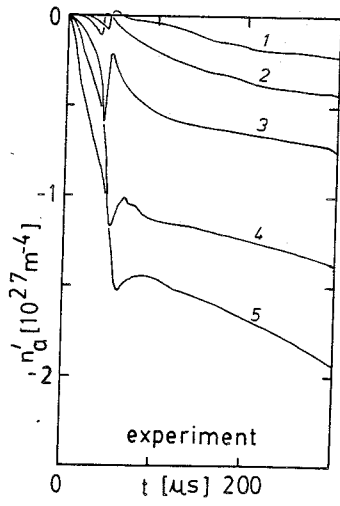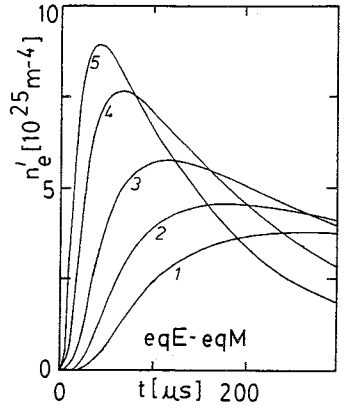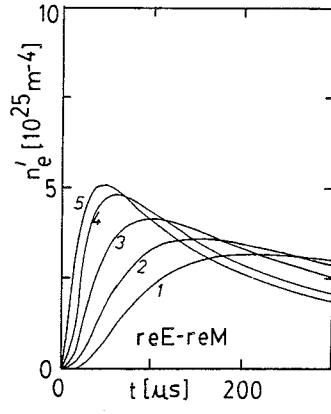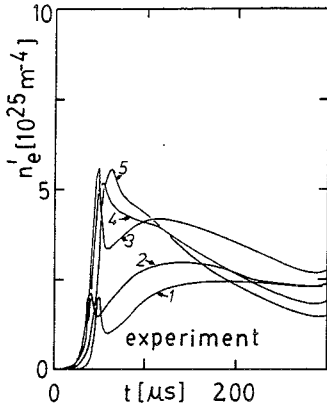
Figure VIII.14 :

Comparison of the measured and theoretical electron and atom density profiles of the thermal boundary layer in pure argon (Ar + 150 pmm air).

Theory :

$M_s = 8.15$, $p_1 = 666.5$ Pa, $T_1 = 294$ K.

N^o	x_m (mm)
1	1.20
2	1.00
3	0.80
4	0.60
5	0.50

Experiment :

N^o	run	x_m (mm)	$(M_s)_1$	$(M_s)_2$	p_1 (pa)	T_1 (K)
1	80041602/II	1.20	8.25	8.12	667.9	295.5
2	80041601/II	1.00	8.15	8.08	667.4	295.5
3	80041503/II	0.80	8.33	8.24	666.5	295.5
4	80041102/II	0.60	8.25	8.19	667.0	295.3
5	80041402/II	0.50	8.19	8.14	666.5	294.5
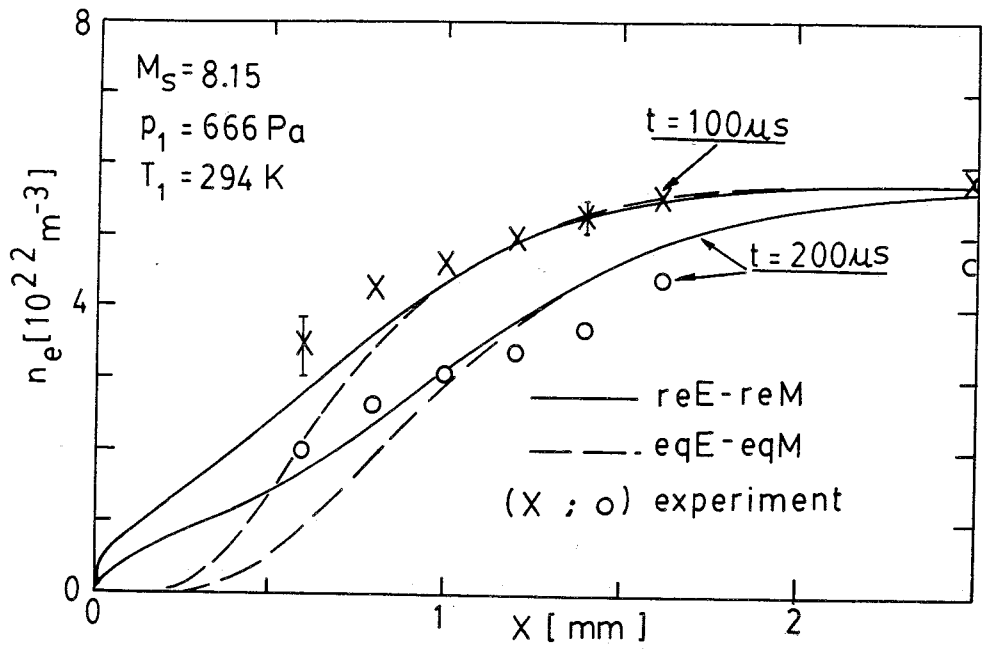
Figure VIII.15 : Comparison of the electron density determined by means of absorption measurements with the theoretical profiles.
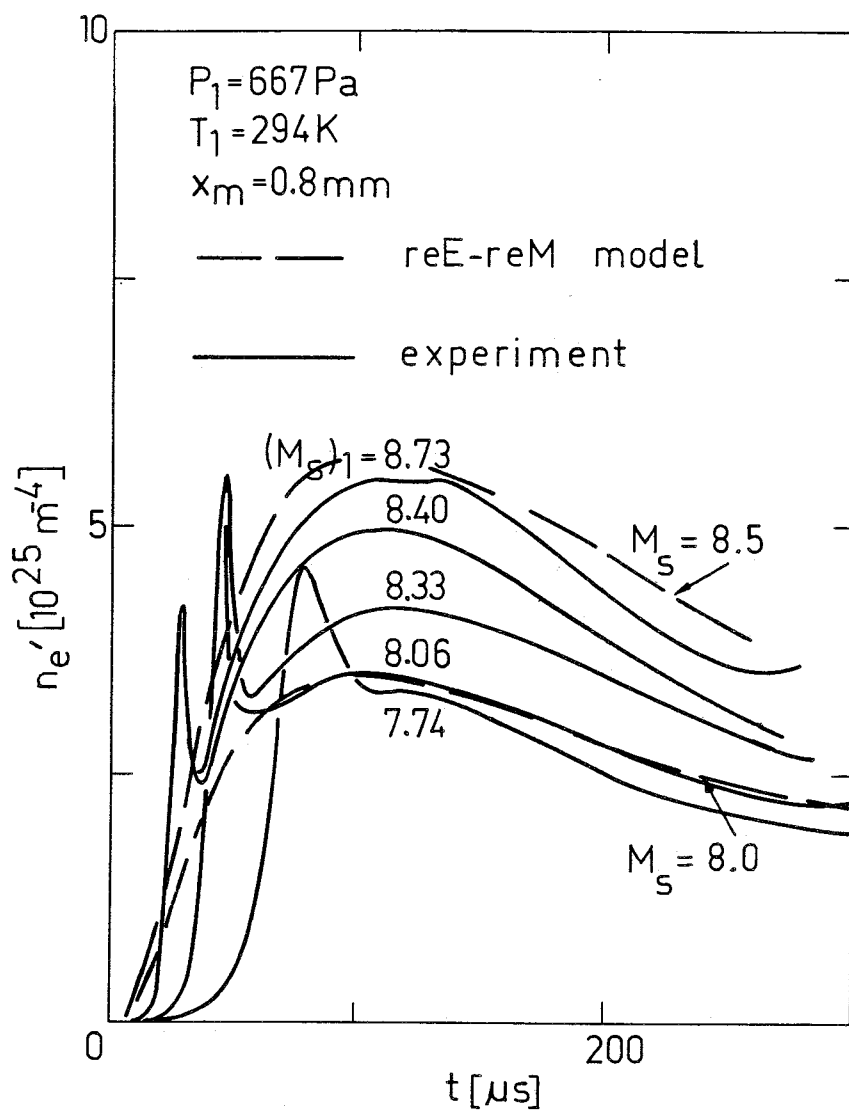
Figure VIII.16 : Mach number dependence of the
electron density at x_m = 0.80 mm.

166
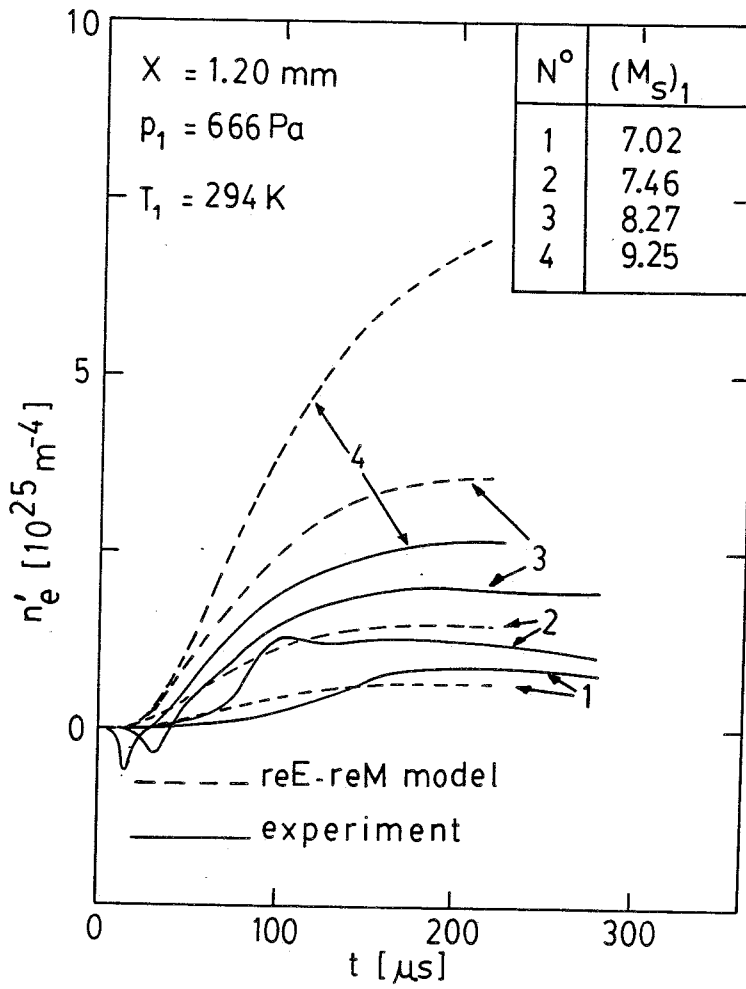
Figure VIII.17 : Mach number dependence of the electron density at x_m = 1.20 mm.

$M_S = 8.70$
$P_1 = 667 \, Pa$
$T_1 = 294 \, K$

$reE - reM$

$x_m = 0.4 \, mm$

$n_e' \, [10^{25} \, m^{-4}]$

experiment

$t \, [\mu s]$

$t \, [\mu s]$

$x_m = 1.2 \, mm$

$n_a' \, [10^{27} \, m^{-4}]$

experiment

$M_S = 8.70$
$P_1 = 667 \, Pa$
$T_1 = 294 \, K$

$reE - reM$

$t \, [\mu s]$

$t \, [\mu s]$
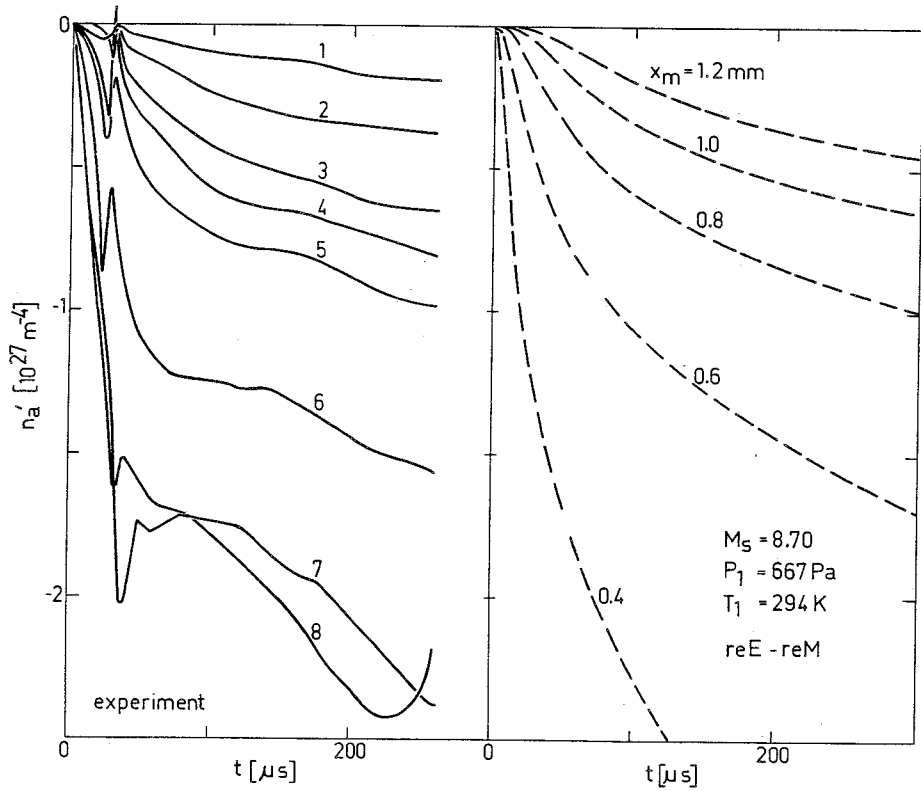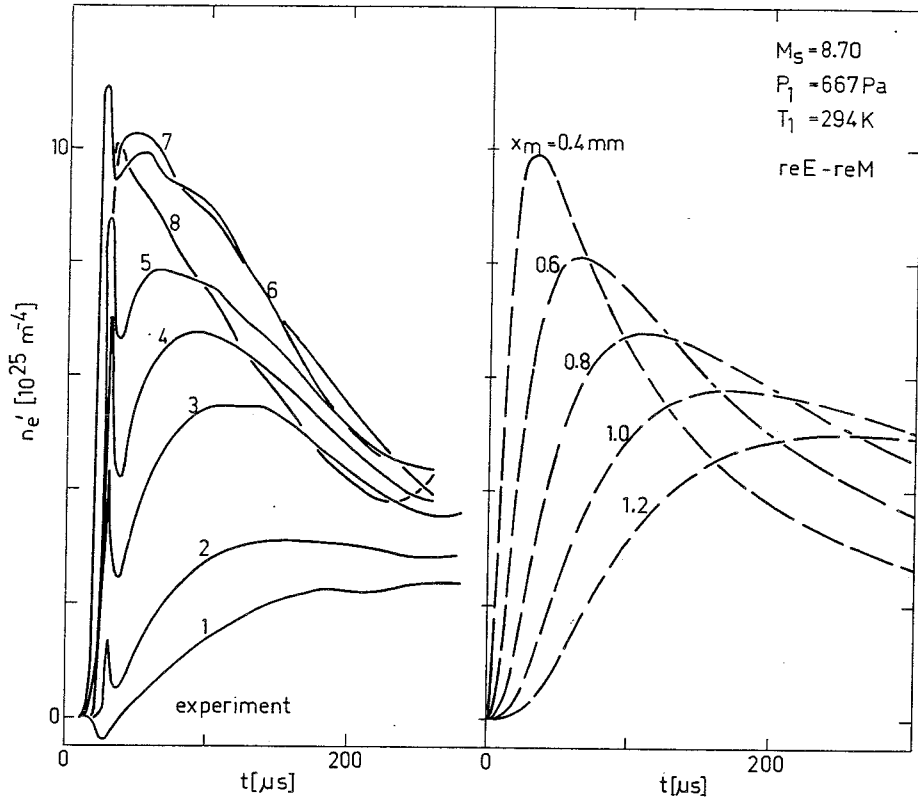
Figure VIII.18 :

Comparison of the measured and theoretical electron and atom density profiles of the thermal boundary layer in pure argon (Ar + 150 ppm air).

Theory :

$M_s = 8.70$, $p_1 = 666.5$ Pa, $T_1 = 294$ K.

Experiment :

N[o]	run	x_m (mm)	$(M_s)_1$	$(M_s)_2$	p_1 (Pa)	T_1 (K)
1	80030304/II	1.203	8.88	8.88	664	294.3
2	80030303/II	1.003	8.80	8.79	666	294.2
3	80030302/II	0.800	8.73	8.71	667	294.1
4	80022803/II	0.703	8.77	8.76	667	294.0
5	80022601/II	0.605	8.60	8.56	669	294.5
6	80022703/II	0.502	8.89	8.85	666	294.4
7	80022702/II	0.412	8.71	8.68	666	294.4
8	80022701/II	0.407	8.59	8.54	668	294.3

$M_s = 8.7$

$t = 100 \mu s$

150

200

250

$n_e \ [10^{22} \ m^{-3}]$

$x_m \ [mm]$

$(\square, \triangle, \triangledown, \circ)$ absorption
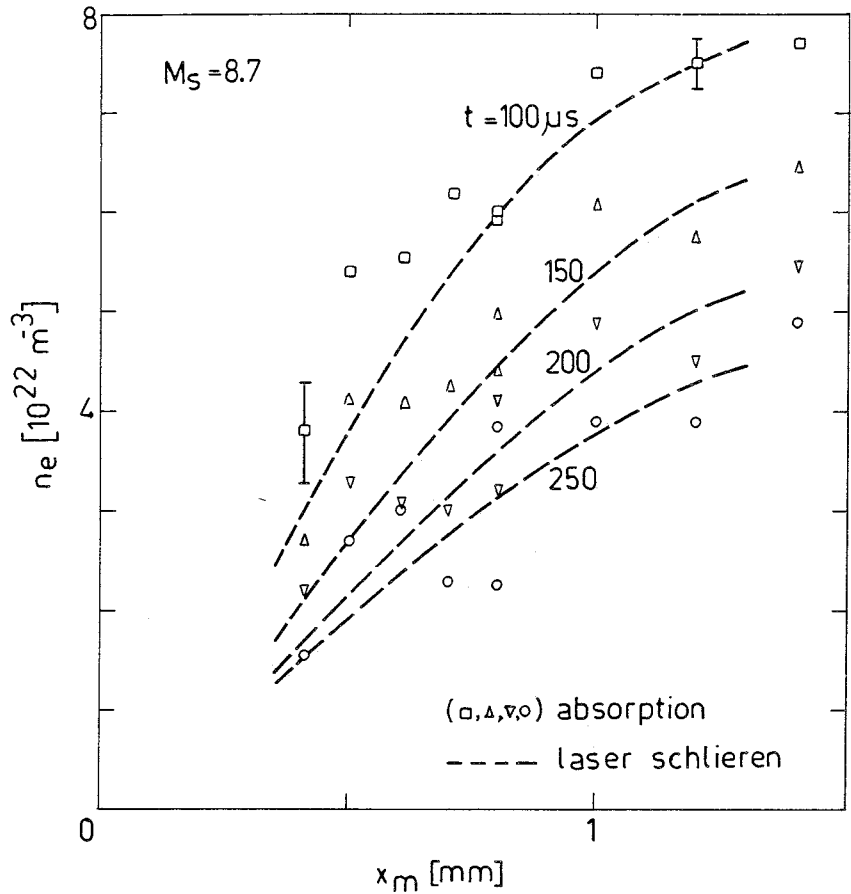
$----$ laser schlieren

Figure VIII.19 : Comparison of the electron density
determined from the absorption measurements with the
integrated laser schlieren data (------)
$M_s = 8.70$, $p_1 = 667$ Pa, $T_1 = 294$ K.

99.5% Ar + 0.5% H_2 mixture :
_____

The influence of the hydrogen addition to the argon is illustrated in
figure VIII.20, in which we compare the pressure, laser schlieren and
absorption signals obtained in pure argon (———) to the signals in
a 99.5% Ar + 0.5% H_2 mixture (-------). We see that the hydrogen
reduces the influence of the ionization relaxation process on the
thermal boundary layer growth. This effect is also observed in the
density gradient data (n_e' and n_a') shown in figure VIII.21. Comparison
of these data to the data obtained in pure argon (figure VIII.14)
shows that n_e' for $t > t_{ion}$ and $x_m \geqslant 0.80$ mm is not significantly

affected by the hydrogen addition. For $x_m \leqslant 0.6$ mm we observe an increase of n_e' due to the hydrogen addition.

Both effects are also observed in figure VIII.22 in which we compare the absorption and laser schlieren data on n_e. The influence of the addition of 0.5% H_2 to the argon can be qualitatively interpreted as an increase of the source terms ε_{eh} and M_i by a factor two. This is illustrated in figure VIII.23.

The good agreement between the data in pure argon and in a 99.5% Ar + 0.5% H_2 mixture in the outer part of the boundary layer $(x_m \geqslant 0.8$ mm) shows that the outer part of the boundary layer is not sensitive to relaxation processes. In section V.e we predicted this fact with the statement that the outer part of the boundary layer is in a state of local thermodynamic equilibrium and that the heat flux towards the wall is determined by the heavy particle heat conductivity in the inner part of the boundary layer. In this inner part the behaviour of the heavy particles is not sensitive to the relaxation processes (low ionization degree).
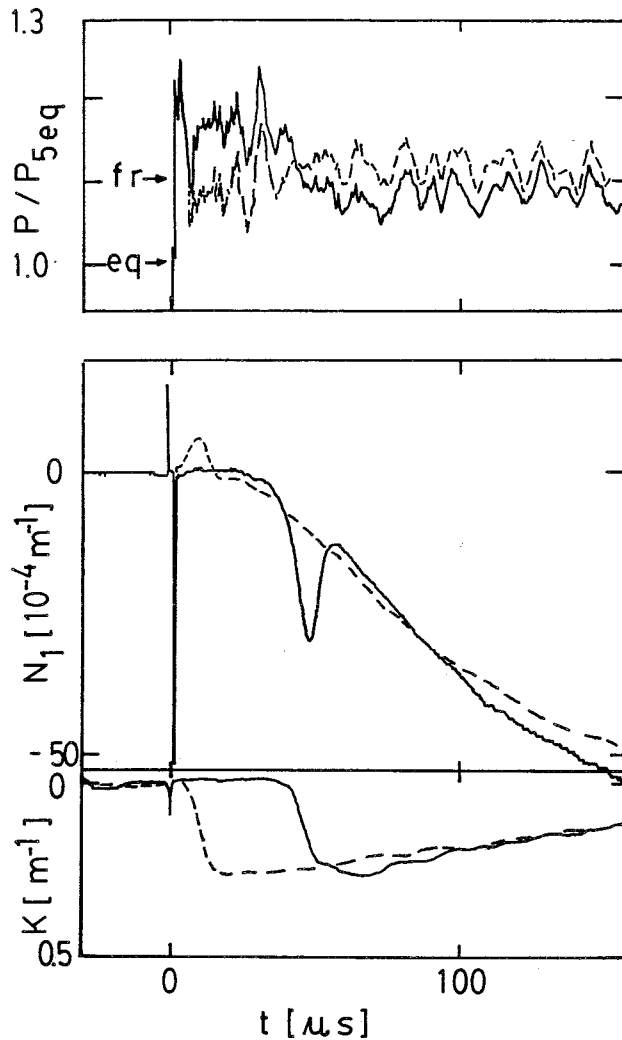
Figure VIII.20 : Comparison of the pressure, laser schlieren (l_1 = 0.6328 μm) and absorption (l_1) signals in pure argon with the signals in a 99.5% Ar + 0.5% H_2 mixture. x_m = 1.2 mm.

Ar :

run (80041602/II), $(M_s)_1$ = 8.25, $(M_s)_2$ = 8.12, p_1 = 668 Pa, T_1 = 296 K. (————)

99.5% Ar + 0.5% H_2 :

run (80042501/II), $(M_s)_1$ = 8.37, $(M_s)_2$ = 8.30, p_1 = 666 Pa, T_1 = 294.5 K. (- - - - -)
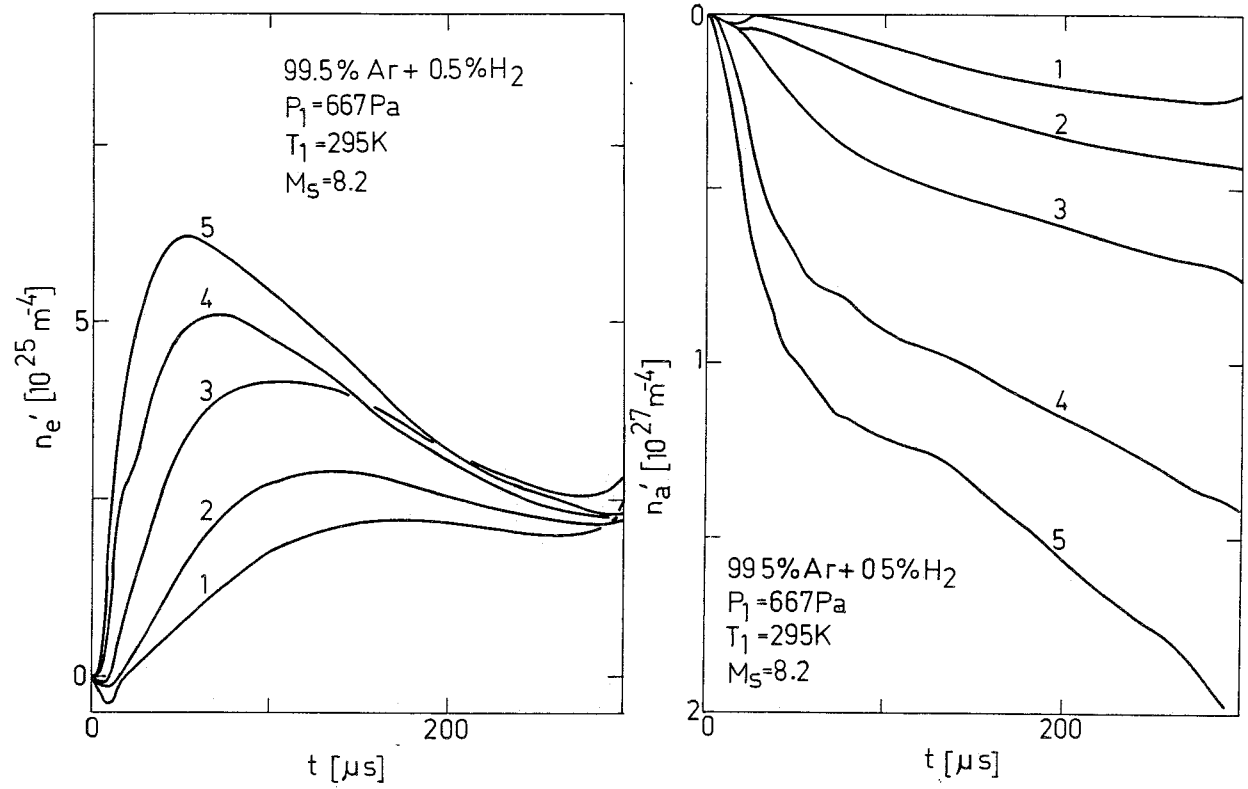
Figure VIII.21 : Electron and atom density gradient
(n_e' and n_a') profiles of the thermal boundary layer in
a 99.5% Ar + 0.5% H_2 mixture.

N^o	run	x_m (mm)	$(M_s)_1$	$(M_s)_2$	P_1 (Pa)	T_1 (K)
1	80042501/II	1.20	8.37	8.30	666	294.5
2	80042402/II	1.00	8.09	7.97	669	294.5
3	80042401/II	0.80	8.26	8.14	668	294.4
4	80042302/II	0.60	8.15	8.08	670	294.4
5	80042301/II	0.50	8.33	8.23	668	294.4
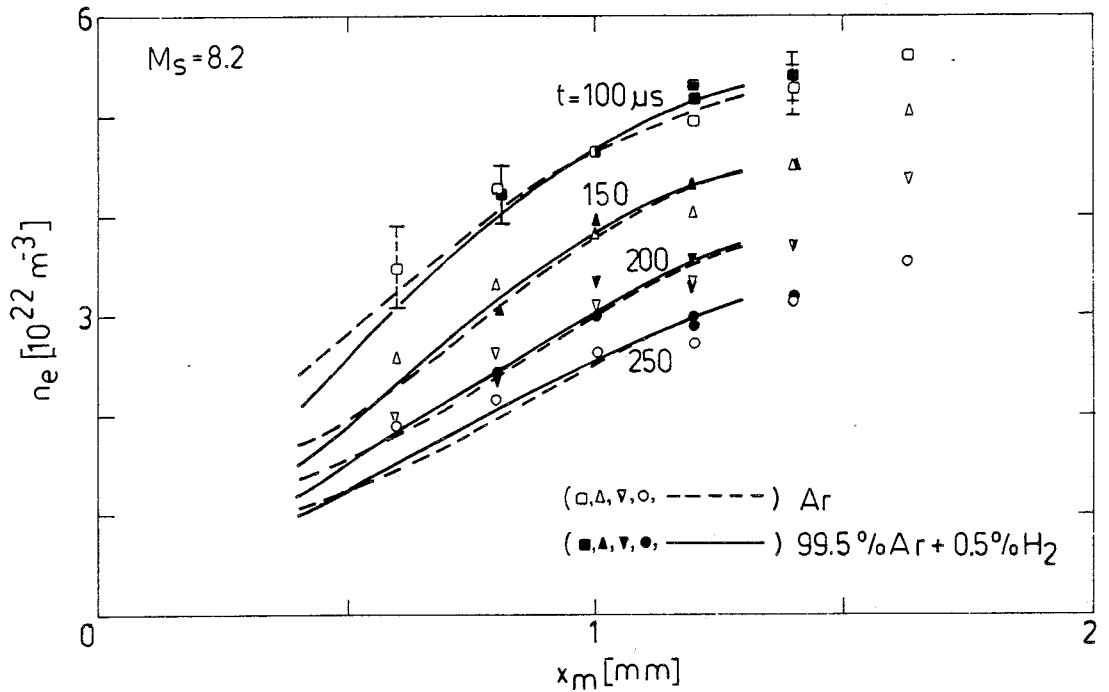
Figure VIII.22 : Comparison of the electron density data for pure argon to the data on a 99.5% Ar + 0.5% H_2 mixture. M_s = 8.2, p_1 = 667 Pa, T_1 = 294.5 K. (———, -----)^2 integrated^s laser schlieren data^1 ($\square$, $\triangle$, $\triangledown$, $\circ$) absorption data. (■, ▲, ▼, ●)
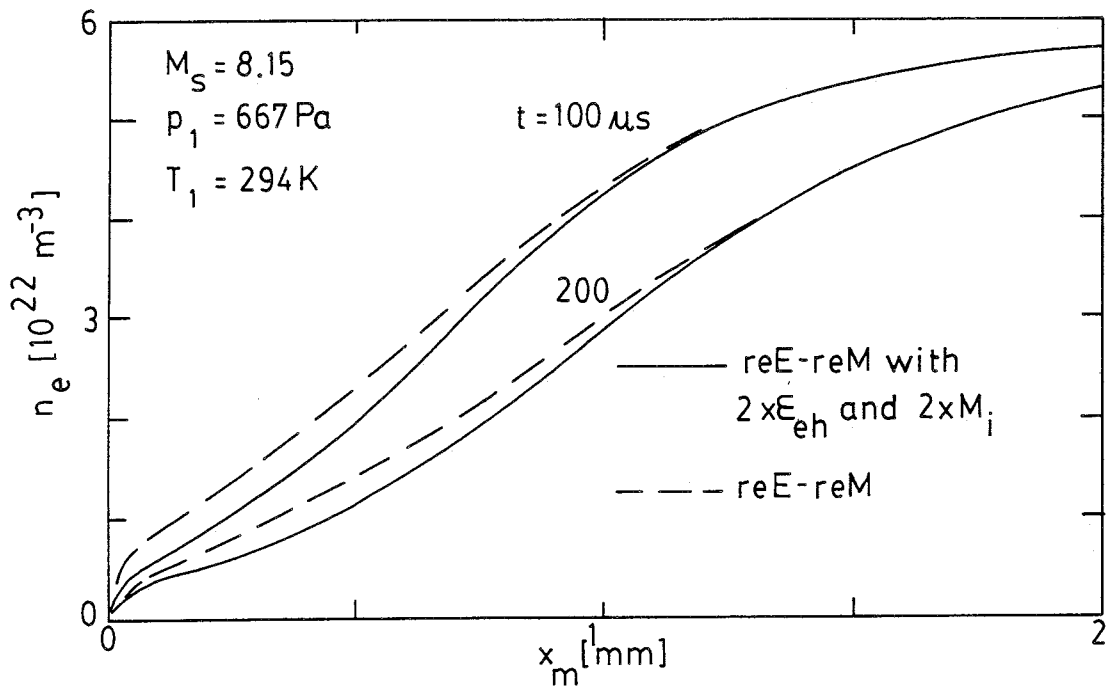
Figure VIII.23 : Influence of the increase of the source terms by a factor two on the electron density profile of the boundary layer.

174

VIII.e. <u>Determination of the heat conductivity</u>

From the data presented in the previous section we have seen
that a quantitative agreement between the relaxation model (reE - reM)
and the experiment is achieved for M_s = 8.15. In the outer part of the
boundary layer corrections of the order of 30% on the n_e' and n_a' data
for the influence of radiation cooling should improve the model
considerably.

We now try to obtain information on the heat conductivity of
the plasma from the experimental data with the procedure described in
section IV.c. We assume a single temperature. The heat conductivity
is thus a function of the temperature and the electron density.
The factors $(T/\lambda)(\partial\lambda/\partial T)$ and $(n_e/\lambda)(\partial\lambda/\partial n_e)$ are estimate on basis of
the theory given in Appendices II and III:

$$(T/\lambda)(\partial\lambda/\partial T) \quad = \quad 1.5 \pm 0.3$$
$$(n_e/\lambda)(\partial\lambda/\partial n_e) \quad = \quad 0.3 \pm 0.1$$

The convective velocity is estimated from the thermal Rayleigh problem
calculations (reE-reM).
We consider here the experimental data in a 99.5% Ar + 0.5% H_2 mixture
because those data agree better with the reE-reM model than the data
in pure argon.

In table VIII.2 we give the data on the state of the plasma
outside the boundary layer (x_m = 3 mm). In table VIII.3 we give the
details of the calculations. In table VIII.4 we compare the results to
the theory (Appendices II and III).

We see that the data obtained are lower than the theoretical
calculated values. We expect that this is due to systematic errors in
our measurements. From an analysis of the various sources of
uncertainties we concluded that the determination of the heat
conductivity depends mainly on the measurements of the atom density.
An improvement of the accuracy of the measurement of the atom density
gradient can be achieved by using instead of the infrared beam
(l_2 = 1.152 μm) a shorter wavelength such as used by Glass (78).

t	p	dp/dt	$(n_e)_\infty$	$(n_a)_\infty$	$d(n_a)_\infty/dt$
(μs)	(10^5Pa)	(10^8Wm^{-3})	(10^{22}m^{-3})	(10^{24}m^{-3})	(10^{26}m^{-3}s^{-1})
100	3.33	-0.3	5.9	2.02	1.5
150	3.18	-1.8	5.3	2.03	-1
200	3.10	-1.5	4.7	2.01	-4
250	3.01	-0.3	4.1	1.99	-2

Table VIII.2 :

State of the plasma outside the boundary layer.

M_s = 8.15, p_1 = 667 Pa, T_1 = 294 K.

x	u	V	T_e/T_h
(mm)	(m s^{-1})	(m s^{-1})	
1.0	-1.91	-0.21	1.002
0.8	-1.60	-0.26	1.005
0.6	-1.35	-0.29	1.019

Data estimated on the basis of the reE-reM model. t = 200 μs.

x	n_e	$\partial n_e/\partial t$	$\partial n_e/\partial x$	$\partial^2 n_e/\partial x^2$	dn_e/dt	Q_r
(mm)	(10^{22}m^{-3})	(10^{26}m^{-3}s^{-1})	(10^{24}m^{-4})	(10^{28}m^{-5})	(10^{26}m^{-3}s^{-1})	(10^8W m^{-3})
1.0	3.0	-1.3	26	-2.6	-1.7	1.8
0.8	2.4	-1.1	32	-1.3	-1.6	1.2
0.6	1.8	-0.8	31	-	-1.2	0.6

Experimental data on the electron density and radiation loss. t = 200 μs.

x	n_a	$\partial n_a/\partial t$	$\partial n_a/\partial x$	$\partial^2 n_a/\partial x^2$	dn_a/dt
(mm)	(10^{24}m^{-3})	(10^{26}m^{-3}/s)	(10^{25}m^{-4})	(10^{30}m^{-5})	(10^{26}m^{-3}/s)
1.0	2.11	-0.5	-36	0.8	6
0.8	2.21	2	-61	1.5	12
0.6	2.38	6	-116	3.5	22

Experimental data on the atom density. t = 200 μs

Table VIII.3 :

Details of the data used for the determination of the heat conductivity.

x	T	n_e	λ	λ_{th}
(mm)	(10^4 K)	(10^{22}m^{-3})	(W K^{-1}m^{-1})	(W K^{-1}m^{-1})
1.0	1.04	3.0	0.3 $\pm$ 0.1	0.43
0.8	0.99	2.4	0.2 $\pm$ 0.1	0.39
0.6	0.93	1.8	0.3 $\pm$ 0.2	0.35

Table VIII.4 :
Experimental data on the heat conductivity of
partially ionized argon obtained from the data
of tables VIII.2 and 3.

In view of the results of the measurements in the non-ionized case
influence of side-wall boundary layer may be important (section VII.d).
Measurements in a larger shock tube facility might show some
improvement.

In figure VIII.24 we show the influence of a variation of 20%
of the electron heat conductivity on the calculated values of the
density gradients n_e' and n_a' (reE-reM model described in section V.e).
From those data we see that in order to obtain information on the
electron heat conductivity one should measure n_e' and n_a' with an
accuracy of about 2%. Further we observe that for $x_m > 1$ mm the
density gradients are much more sensitive to variations in the
electron heat conductivity than close to the wall ($x_m < 1$ mm).

It appears that for $x_m \geqslant 1.00$ mm the time dependence of the
pressure (dp/dt) and the radiation loss term Q_r are of the same order
of magnitude as the other terms. We therefore expect that at higher
temperatures the accuracy of the determination of these terms will
restrict the use of the shock tube method.
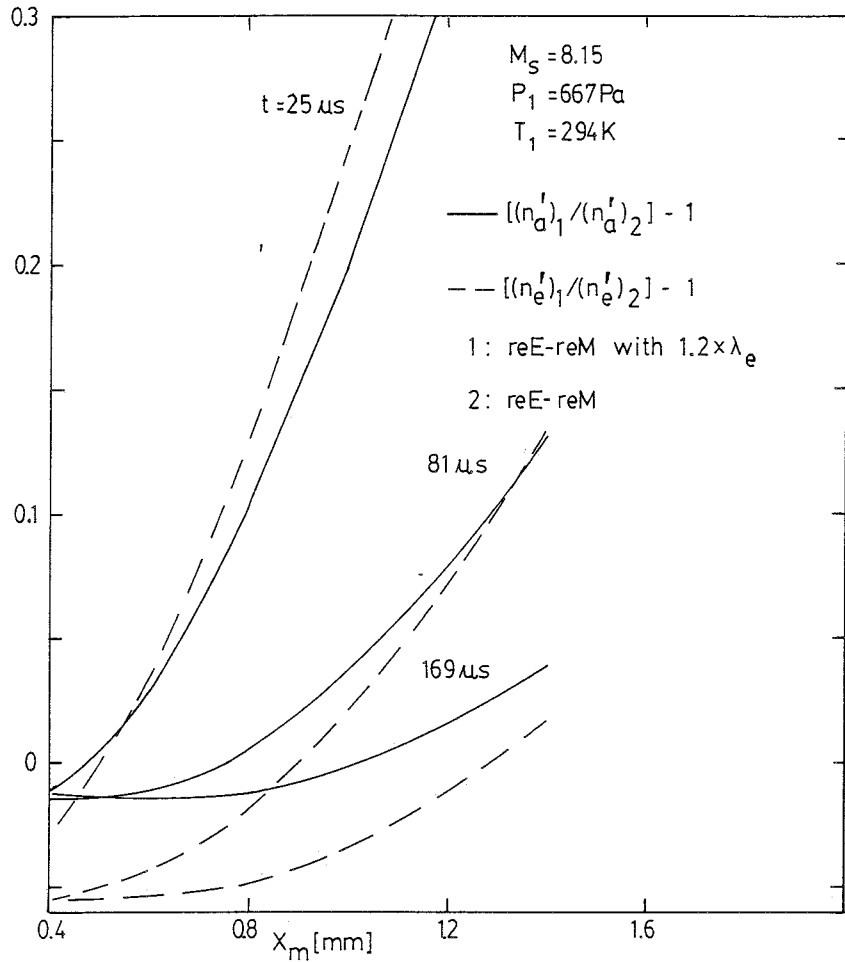
Figure VIII.24 : Comparison of the density gradients $(n_e')_1$ and $(n_a')_1$ calculated with the reE-reM model, with the gradients $(n_e')_2$ and $(n_a')_2$ calculated with the reE-reM model in which the electron heat conductivity is multiplied by a factor 1.2.

IX. CONCLUSIONS

IX.a. Heat conductivity

Non-ionized monatomic gases: (chapters II, III, VII)

Considering the main goal of our study: the improvement of the shock
tube method for the determination of the heat conductivity of gases
at high temperatures we may conclude that for non-ionized monatomic
gases the shock tube method, based on a direct determination of the
terms in the energy equation, yields heat conductivity data with an
accuracy of about 4%.

A significant improvement of this accuracy is expected to result from
a better measurement of the state of the gas outside the boundary
layer and a study of the influence of the side-wall boundary layers
on the flow.

We expect that the improved shock tube method should have an accuracy
comparable to the hot wire column methods with the advantage of a
much more extended temperature range.

For argon, because of the relatively long ionization relaxation time,
one may use the "frozen" reflected shock region in order to determine
heat conductivity of non-ionized argon up to temperatures of the order
of 2×10^4K.

Argon: (chapter VII)

The heat conductivity data on argon obtained for low temperatures
(below 2500 K) agree within 4% with the hot wire column data of
Springer (73), Chen (75) and Shaskov (78).

At higher temperatures (5000 K $\leqslant$ T $\leqslant$ 7000 K) our data agree within 3%
with the data of Aziz (80) calculated on the basis of the
intermolecular potential of Aziz and Chen (77).

Polyatomic gases: (chapter VIII)

Bifurcation of the reflected shock is a severe restriction to the use
of the shock tube method for polyatomic gases.

Some aspects of the heat conductivity of polyatomic gases such as the
influence of dissociation may be studied by considering mixtures of
monatomic gases with a small amount of polyatomic gases.

Ionized monatomic gases: (chapters IV, V, VIII)

In the ionized case the shock tube method may yield valuable data on the heat conductivity. A considerable improvement of the accuracy of the measurements of the atom density, the pressure and the radiation loss has still to be achieved.

IX.b.   Non-equilibrium phenomena in ionized boundary layer:
         (chapters V, VIII).

A quantitative agreement between the two temperatures relaxation model of Hutten (76) and the experiment is achieved at low Mach numbers (electron densities lower than $5 \times 10^{22} m^{-3}$).

At higher electron densities the structure of the reflected shock region is strongly influenced by the radiation cooling.

A considerable improvement of the agreement between theory and experiment is expected if the radiation loss term and the time dependence of the state of the plasma outside the boundary layer are taken into account.

APPENDIX I.

RANKINE-HUGONIOT RELATIONS

A I.a. Rankine-Hugoniot relations for a perfect gas

The different regions of shock tube flow, as defined in figure II.2 are coupled by the following relations:

$$\frac{P_2}{P_1} = 1 + \frac{2\gamma}{\gamma+1}(M_s^2 - 1) \qquad\qquad \text{A I.1}$$

$$\frac{T_2}{T_1} = 1 + \frac{2(\gamma-1)(\gamma M_s^2 + 1)(M_s^2 - 1)}{(\gamma+1)^2 M_s^2} \qquad\qquad \text{A I.2}$$

$$(v_s - u_2)\rho_2 = v_s \rho_1 \qquad\qquad \text{A I.3}$$

$$\frac{P_5}{P_2} = 1 + \frac{2\gamma}{\gamma+1}(M_r^2 - 1) \qquad\qquad \text{A I.4}$$

$$\frac{T_5}{T_2} = 1 + \frac{2(\gamma-1)(\gamma M_r^2 + 1)(M_r^2 - 1)}{(\gamma+1)^2 M_r^2} \qquad\qquad \text{A I.5}$$

$$u_5 = 0 \qquad\qquad \text{A I.6}$$

where the reflected shock Mach number M_r is related to M_s by:

$$M_r^2 = \frac{2\gamma M_s^2 - \gamma + 1}{(\gamma-1)M_s^2 + 2} \qquad\qquad \text{A I.7}$$

Relations A I.1 to 7 can also be used to calculate the "frozen" state 5_{fr}. (section V.b).

A I.2. Rankine-Hugoniot relations for partially ionized argon

Using the integral conservation laws (V.3, 4 and 5) in combination with relations V.6 to 10 we calculate the equilibrium state 5_{eq} behind an "ideal" ionizing reflected shock (section V.c). The numerical procedure is described by Hutten (76). Results are given in tables A I.1, 2 and 3.

M_s	P_{5eq} $(10^5 Pa)$	T_{5eq} $(10^3 K)$	$(n_e)_{5eq}$ $(10^{22} m^{-3})$	α_{eq} (10^{-2})
7.0	0.8706	9.444	0.844	1.264
7.5	0.9853	9.973	1.530	2.138
8.0	1.1047	10.418	2.434	3.169
8.5	1.2296	10.808	3.571	4.334
9.0	1.3607	11.159	4.960	5.616
9.5	1.4980	11.482	6.623	7.009
10.0	1.6421	11.784	8.588	8.509

Table A I.1 : State 5_{eq} as function of M_s for p_1 = 266.6 Pa and T_1 = 295 K.

M_s	P_{5eq} $(10^5 Pa)$	T_{5eq} $(10^3 K)$	$(n_e)_{5eq}$ $(10^{22} m^{-3})$	α_{eq} (10^{-2})
7.0	2.1936	9.690	1.739	1.060
7.5	2.4854	10.289	3.282	1.876
8.0	2.7879	10.790	5.352	2.860
8.5	3.1038	11.227	7.976	3.983
9.0	3.4344	11.618	11.201	5.232
9.5	3.7808	11.978	15.077	6.595
10.0	4.1437	12.313	19.650	8.062

Table A I.2 : State 5_{eq} as function of M_s for p_1 = 666.6 Pa and T_1 = 295 K.

M_s	P_{5eq} $(10^5 Pa)$	T_{5eq} $(10^3 K)$	$(n_e)_{5eq}$ $(10^{22} m^{-3})$	α_{eq} (10^{-2})
7.0	4.4119	9.867	2.960	0.914
7.5	5.0038	10.527	5.786	1.681
8.0	5.6160	11.076	9.637	2.624
8.5	6.2536	11.552	14.564	3.714
9.0	6.9201	11.977	20.642	4.933
9.5	7.6175	12.367	27.966	6.269
10.0	8.3473	12.730	36.645	7.716

Table A I.3 : State 5_{eq} as function of M_s for p_1 = 1333 Pa and T_1 = 295 K.

APPENDIX II

RELATIONS BETWEEN CROSS SECTIONS, FLUXES AND SOURCE TERMS

A II.a. Introduction

　　In section IV.b we reviewed the conservation equations for a
thermal boundary layer in a partially ionized monatomic gas.
In equations IV.1 to 9 we left the expressions of the fluxes and
source terms unspecified. Some general properties of those terms are
given in equations IV.10 to 25. In this appendix we give expressions
relating the fluxes and the source terms to the cross sections for
collisional processes (radiational processes are not considered).
　　Hutten (76) used the formulas of Fay (62) based on a
mean-free-path theory. Those formulas should be equivalent to a first
approximation in the Chapman-Enskog procedure. However the electron
energy source term ε_{eh} used by Hutten (76)(and Hoffert (67))
differs by a factor 4/3 from the expression of Chapman (70). Further
the cross section for electron-atom elastic collisions used by
Hutten (76) (and Jaffrin (65)) is about a factor 4 too low, which is
expected to be due to a confusion in the definition of the cross
section. In addition it appears that a mean-free-path approximation
will only yield an order of magnitude estimate for the electron heat
conductivity (Kruger 68).
　　We therefore used improved expressions based on the studies
of Chapman (70) and Devoto (67, 73). In section A II.b we give the
definition of the cross sections. In section A II.c we consider the
transport coefficients. In section A II.d we consider the source
terms. In appendix III we give the cross section data.

A II.b. Definitions cross sections

　　The "total" cross section $\hat{Q}_{(ij/kl)}$ for a collisional process
(ij/kl) or:

$$i + j \longrightarrow k + 1 \qquad\qquad\qquad \text{A II.1}$$
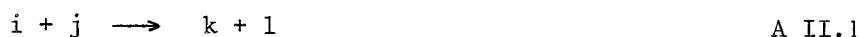
is defined following Mitchner (73) by:

$$\hat{Q}_{(ij/kl)} = \frac{\text{Number of events (ij/kl) per unit of time}}{\text{Flux of test particles i}}$$

$$\text{A II.2}$$

In cases of non-elastic processes k and l are the products and we use the short notation:

$$\hat{Q}_{(ij/kl)} = Q^{i}_{jk} \qquad\qquad \text{A II.3}$$

For elastic processes (ij/ij) we use the notation:

$$\hat{Q}_{(ij/ij)} = \hat{Q}_{ij} \qquad\qquad \text{A II.4}$$

The total cross section is a function of the relative energy e_r given by:

$$e_r = \frac{1}{2} m_{ij} g^2_{ij} \qquad\qquad \text{A II.5}$$

where:

$$m_{ij} = m_i m_j / (m_i + m_j) \qquad\qquad \text{A II.6}$$

and $\underline{g}_{ij}$ is the relative velocity:

$$\underline{g}_{ij} = \underline{v}_j - \underline{v}_i \qquad\qquad \text{A II.7}$$

In addition to the total cross section we also need information on the differential cross section $I_{ij}(X,e_r)$ defined for elastic collisions by:

$$I_{ij}(X,e_r) = \frac{\text{(Number of particles i deflected per unit of time into the solid angle d}\Omega)}{d\Omega \text{ (Flux of particles i)}} \qquad \text{A II.8}$$

where the solid angle element $d\Omega$ is taken in the direction X. $I_{ij}(X,e_r)$ can be calculated from the intermolecular potential V(r). In the cases considered further the data available are given in the form of "weighted" cross sections $Q^{(s)}_{ij}$ defined by:

$$Q^{(s)}_{ij} = 2\pi \int_0^{\pi} (1-\cos^s X)\sin(X) \, I_{ij}(X,y) \, dX \qquad \text{A II.9}$$

and of "average" cross sections $Q^{(s,t)}_{ij}$ related to $Q^{(s)}_{ij}$ by (Devoto 73):

$$Q^{(s,t)}_{ij} = \frac{4(s+1)}{(t+1)! \, (2s+1-(-1)^s)} \int_0^{\infty} y^{2t+3} \exp(-y^2) Q^{(s)}_{ij}(y) \, dy$$

$$\text{A II.10}$$

with

$$y^2 = e_r / (k \, T_m) \qquad\qquad \text{A II.11}$$

and:

$$T_m = (m_j T_i + m_i T_j)/(m_i + m_j) \qquad \text{A II.12}$$

Definition A II.9 and 10 are chosen so that in the case of rigid spheres: $Q_{ij}^{(s,t)} = Q_{ij}^{(s)}$.

A II.c. Transport coefficients

The transport coefficients of partially ionized argon can be estimated on the basis of the Chapman-Enskog procedure (Chapman 70, Devoto 66). In principle this procedure considers only small deviations of the distribution functions of the particles from local Maxwellian distributions with a single temperature. When terms of the order $(m_e/m_h)^{1/2}$ are neglected this procedure can be generalised to the case of a two-temperature plasma (Devoto 67, Kruger 68). In this approximation the influence of the electrons on the heavy particles appears only through the presence of an electric field $\underline{E}$. The heavy particles (atoms and ions) are treated as a binary mixture.[Ω]

The diffusion velocity $\underline{V}_j$ (j = i,a) is given by (Devoto 66):

$$\underline{V}_j = (n_h/n_j) D_{jk}\underline{d}_k - (D_j^T/(n_j m_h))(\nabla \ln T_h) \qquad \text{A II.13}$$

where:

$$\underline{d}_i = \nabla(n_i/n_h) - (n_i e \underline{E})(n_a/n_h)/p_h \qquad \text{A II.14}$$

and:

$$\underline{d}_a = -\underline{d}_i \qquad \text{A II.15}$$

Expressions for the binary diffusion coefficients D_{ij} and the thermo-diffusion coefficient D_j^T based on a second approximation in the Sonine-polynomial expansion of the Chapman-Enskog procedure are given by Chapman (70). The thermo-diffusion appears to be negligible for the conditions considered (p = 3 x 10^5 Pa, T $\leqslant$ 12000 K). This result is confirmed by the study of Devoto (67).

[Ω] Note:
   We neglect the influence of the excited argon atoms on the transport properties.

186

Further it appears that a first approximation for D_{ia} is sufficient (in view of the uncertainties in the cross section data):

$$D_{ia} = \frac{3}{8 \, n_h} \; \left(\frac{\pi k \, T_h}{m_h} \right)^{1/2} \frac{1}{Q_{ia}^{(1,1)}} \qquad\qquad \text{A II.16}$$

The corresponding approximation for the heat fluxes $\underline{q}_j$ ($j = i,a$) is given by equation IV.20. The heat conductivity λ_i^m of the ions appears to be negligible. The heat conductivity λ_a^m of the atoms was calculated by means of the mean-free-path approximation:

$$\lambda_a^m = \lambda_{aa} / \left[\; 1 + \frac{\alpha}{(1 - \alpha)} \; \frac{Q_{ia}^{(2,2)}}{Q_{aa}^{(2,2)}} \; \right] \qquad\qquad \text{A II.17}$$

in which λ_{ij} is given by:

$$\lambda_{ij} = \frac{75 \, k}{64} \left(\pi \, k \, T_h / m_h \right)^{1/2} (1/Q_{ij}^{(2,2)}) \qquad\qquad \text{A II.18}$$

In table A II.1 we compare λ_a^m to the heavy particle heat conductivity $(\lambda_h^m)_{Dev}$ calculated by Devoto (73) for atmospheric argon with a second approximation in the Chapman-Enskog procedure.

T $(10^3 K)$	α	$\lambda_a^m / (\lambda_h^m)_{Dev}$	$(\lambda_e^m / \lambda_h^m)_{Dev}$
6	2.5×10^{-5}	1.000	0.02
8	1.6×10^{-3}	1.003	0.29
10	2.1×10^{-2}	1.011	1.17
12	1.2×10^{-1}	1.275	3.58

Table A II.1: Comparison of λ_a^m obtained [a] from formula A II.17 with the data of Devoto (73). ($p = 1.013 \times 10^5$ Pa).

[a] Note:
  On basis of the cross section data of Devoto (73).

The relatively large discrepancy between formula A II.17 and the data of Devoto (73) at high temperatures is unimportant because in such a case the heat conductivity of the plasma is mainly determined by the electrons (see table A II.1). Further Devoto (73) notices that at high temperatures the second approximation in the Chapman-Enskog procedure underestimates the heavy particles heat conductivity by about 12%. Alternative simplified formulas proposed by Capitelli (72) and Honda (77) have a similar accuracy.

The electron transport properties have been calculated on basis of the simplified theory of Devoto (67).
As shown by Kruger (68) a third approximation in the Sonine-polynomial expansion yields an estimate of the heat conductivity in the fully ionized limit which agrees within 1.2% with the formula of Spitzer (53). In the partially ionized case when electron-atom and electron-charged particle interactions are of the same importance the third approximation agrees within 20% with the twelfth approximation, which can be regarded as exact (Kurger 68). At lower degrees of ionization the Chapman-Enskog procedure fails to converge (T ⩽ 6000 K, p = 10^5 Pa). In the limit of very low degrees of ionization, the Lorentz limit, an analytic expression for the heat conductivity can be derived.
In the partially ionized case Devoto (73) and Kruger (68) use a semi-empirical formula which has the mathematical form of the Lorentz limit. This so called Frost-mixture rule implies a numerical intergration.ᵃ Because the heat conductivity of the electrons below 6000 K will not be of major importance for the structure of the boundary layer (see table A II.1 and section V.e) we decided to use a simple extrapolation between the Lorentz limit and the value of the heat conductivity in the partially ionized case:

$$\lambda_e^m = (\lambda_e^m)_3 \left(1 + \frac{1.5\ F}{F_o + F}\right) \qquad\qquad \text{A II.19}$$

where $(\lambda_e^m)_3$ is the third approximation to λ_e^m, F is the ratio of electron-neutral to electron-ion collision frequencies given by:

$$F = (1 - \alpha)Q_{ea}^{(1,1)}/(\alpha\ Q_{ei}^{(1,1)}) \qquad \text{and } F_o = 50 \qquad \text{A II.20}$$

ᵃ Note: For 4000 K ⩽ T ⩽ 6000 K the Frost-heat conductivity is lower than the twelfth approximation in the Chapman-Enskog procedure. In contradiction with the statement of Mitchner(73) it is therefore not closer to the exact value of the heat conductivity than the twelfth approximation.

With a second approximation for the diffusion and the thermo-diffusion we obtain:

$$\underline{q}_e = \frac{5}{2} k \, T_e \, (1 + q_{ee}^{01}/q_{ee}^{11}) \, n_e \, \underline{V}_e - \lambda_e^m \, \nabla \, T_e \qquad \text{A II.21}$$

The third approximation $(\lambda_e^m)_3$ to λ_e^m is given by:

$$(\lambda_e^m)_3 = \frac{75 \, k \, n_e^2}{8} \, (2\pi k \, T_e/m_e)^{1/2} \, \frac{q_{ee}^{22}}{q_{ee}^{11} q_{ee}^{22} - (q_{ee}^{12})^2} \qquad \text{A II.22}$$

The matrix q_{ee}^{ij} is according to Devoto (67) given by:

$$q_{ee}^{01} = 8 \sum_{j=i,a} n_e n_j \, (\frac{5}{2} Q_{ej}^{(1,1)} - 3 Q_{ej}^{(1,2)}) \qquad \text{A II.23}$$

$$q_{ee}^{11} = 8 \, 2^{1/2} \, n_e^2 \, Q_{ee}^{(2,2)} +$$
$$8 \sum_{j=i,a} n_e n_j (\frac{25}{4} Q_{ej}^{(1,1)} - 15 Q_{ej}^{(1,2)} + 12 Q_{ej}^{(1,3)}) \qquad \text{A II.24}$$

$$q_{ee}^{12} = 8 \, (2)^{1/2} n_e^2 \, (\frac{7}{4} Q_{ee}^{(2,2)} - 2 Q_{ee}^{(2,3)}) +$$
$$8 \sum_{j=i,a} n_e n_j (\frac{175}{16} Q_{ej}^{(1,1)} - \frac{315}{8} Q_{ej}^{(1,2)} + 57 Q_{ej}^{(1,3)} - 30 Q_{ej}^{(1,4)}) \qquad \text{A II.25}$$

$$q_{ee}^{22} = 8(2)^{1/2} n_e^2 (\frac{77}{16} Q_{ee}^{(2,2)} - 7 Q_{ee}^{(2,3)} + 5 Q_{ee}^{(2,4)}) +$$
$$8 \sum_{j=i,a} n_e n_j (\frac{1225}{64} Q_{ej}^{(1,1)} - \frac{735}{8} Q_{ee}^{(1,2)} + \frac{399}{2} Q_{ee}^{(1,3)} - 210 Q_{ee}^{(1,4)} + 90 Q_{ee}^{(1,5)}) \qquad \text{A II.26}$$

From the cross section data available it appears that:

$$q_{ee}^{01}/q_{ee}^{11} = 0(10^{-1}) \qquad \text{A II.27}$$

so that equation A II.21 can be approximated by IV.20.
The interaction of charged particles needs a special treatment because that interaction cannot be considered as strictly binary.
We separate therefore the coefficients q_{ee}^{ij} into a electron-neutral

interaction q_L^{ij} and an electron-charged particle interaction q_F^{ij}:

$$q_{ee}^{ij} \; = \; q_L^{ij} \; + \; q_F^{ij} \qquad\qquad\qquad \text{A II.28}$$

Expressions for q_F^{ij} are given by Itikawa (63), Williams (69), Daybelge (70) and Luchina (78). The theory of Daybelge (70) is appropriate for a two-temperature plasma as considered here. For $T_e/T_h \leqslant 10^2$ in the fully ionized limit the heat conductivity of the electrons in a two-temperature plasma deviates only by a few percents from the one-temperature heat conductivity. This effect was therefore neglected.

The expressions proposed for q_F^{ij} show some discrepancies that are, according to Luchina (78), due to numerical errors. In view of the fact that Luchina (78) dedicates special attention to this problem we decided to use his expressions. It is interesting to notice that in the fully ionized limit the heat conductivity calculated with the expressions of Luchina (78) agrees with the data of Daybelge (70) but does not agree with the previous calculations of Daybelge reported by Kruger (68) and Mitchner (73).

In figure A II.1 we compare the various expressions.
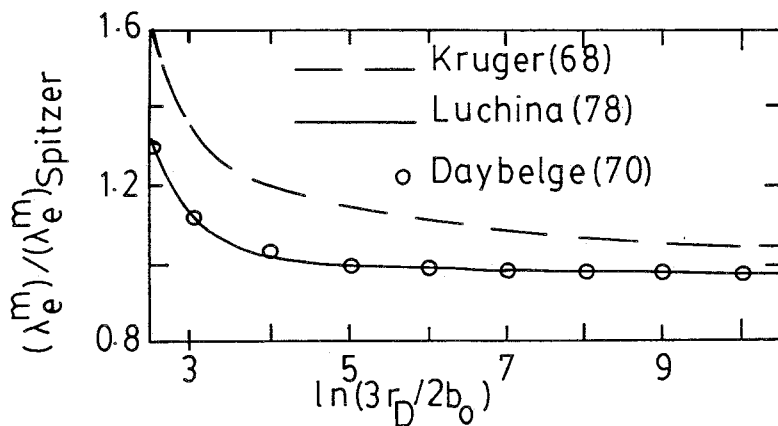
Figure A II.1: Kihara correction to the heat conductivity in the fully ionized case according to Kruger (68), Daybelge (70) and Luchina (78).

Using the expressions of Luchina (78) we found:

$$q_F^{11} = 8 \pi b_o^2 n_e^2 (9.328 \ln(3 \, r_D/2b_o) - 15.405) \qquad \text{A II.29}$$

$$q_F^{12} = 8 \pi b_o^2 n_e^2 (10.746 \ln(3 \, r_D/2b_o) - 25.586) \qquad \text{A II.30}$$

$$q_F^{22} = 8 \pi b_o^2 n_e^2 (21.486 \ln(3 \, r_D/2b_o) - 38.722) \qquad \text{A II.31}$$

where:

$$r_D^2 = \varepsilon_o k \, T_e/(e^2 \, n_e) \qquad \text{A II.32}$$

and

$$b_o = e^2/(8 \pi \varepsilon_o k \, T_e) \qquad \text{A II.33}$$

In appendix III we derive a simplified expression for the electron heat conductivity.

A II.d. Source terms

The ion-mass source term M_i depends on the departure of the state of the gas from local thermodynamic equilibrium and is the net result of various collisional and radiational processes. A model for M_i is described in appendix IV. We consider here only collisional processes.

The rate of production of particles k by a collisional process (ij/kl) is given by:

$$R(ij/kl) = \frac{n_i n_j}{(1+\delta_{ij})} \left(\frac{8 \, k \, T_m}{\pi \, m_{ij}}\right)^{1/2} \int_0^\infty y^3 \exp(-y^2) \, Q_{jk}^i(y) \, dy$$

$$\text{A II.34}$$

In which the factor $(1 + \delta_{ij})^{-1}$ is introduced to prevent that events are counted twice in the case of collisions between identical particles.

The momentum source term P_i is given in first approximation by:

$$P_i = -\frac{8}{3} n_i n_h m_h \, (k \, T_h/\pi \, m_h)^{1/2} V_i \, Q_{ia}^{(1,1)} \qquad \text{A II.35}$$

The expressions for the energy source terms ε_t, ε_e and ε_{eh} have been given in section IV.b.

APPENDIX III

THERMAL RAYLEIGH PROBLEM: EQUATIONS, TRANSPORT COEFFICIENTS
AND SOURCE TERMS.

A III.a Introduction

In this appendix we give information on the equations, the
transport coefficients and the source terms used in the reE-reM model
described in section V.e.

In section A III.b we give the equations. In section A III.c we
describe the expressions used for the transport coefficients and in
section A III.d the expressions used for the source terms.

Note:

For the calculation of the limit cases of the relaxation model
(figures V.9, 10 and 11) the expressions of Hutten (76) have been used.

A III.b Equations

A combined Lagrange-similarity transformation of the form:

$$f(x,t) = t^{-1/2} \int_0^x \rho \ dx'$$ A III.1

is applied to the set of equations IV.1 to 9.

After rearrangement the following set of equations for α, T_e and T_h
is obtained:

$$t \frac{\partial \alpha}{\partial t} = \frac{f}{2} \frac{\partial \alpha}{\partial t} - t^{1/2} \frac{\partial}{\partial f} (\alpha \rho V) + \frac{t \ M_i}{\rho}$$ A III.2

$$\alpha \ t \frac{\partial T_e}{\partial t} - \frac{2}{5} \frac{t}{\rho} \frac{\partial}{\partial t} (\alpha \rho T_e) =$$

$$\alpha \frac{f}{2} \frac{\partial T_e}{\partial f} - \frac{f}{5 \rho} \frac{\partial}{\partial f}(\alpha \rho T_e) + \frac{2}{5 R} \frac{\partial}{\partial f}(\rho \ \lambda_e^m \ \frac{\partial T_e}{\partial f})$$

$$- \frac{1}{\rho}(T_e + \frac{2}{5} T_{ion})M_i \ t - t^{1/2} \ R^2 \alpha \ \rho \ V \frac{\partial T_e}{\partial f}$$

$$+ \frac{2}{5} t^{1/2} V \frac{\partial}{\partial f} (\alpha \rho T_e) + \frac{2}{5 \ \rho R} t \ \varepsilon_{eh}$$ A III.3

192

$$t \frac{\partial T_h}{\partial t} + \frac{2}{5 \rho} t \frac{\partial}{\partial t} (\alpha \rho T_e) =$$

$$\frac{f}{2} \frac{\partial T_h}{\partial f} + \frac{f}{5 \rho} \frac{\partial}{\partial f} (\alpha \rho T_e) + \frac{2}{5 R} \frac{\partial}{\partial f} (\rho \lambda_a^m \frac{\partial T_h}{\partial f})$$

$$- \frac{2}{5} t^{1/2} V \frac{\partial}{\partial f} (\alpha \rho T_e) - \frac{2}{5 \rho R} t \, \varepsilon_{eh}$$

<div align="right">A III.4</div>

The corresponding initial and boundary conditions are given in equations V.16 to 20.

The numerical procedure is described by Hutten (76).

A III.c. <u>Transport coefficients</u>

The relations between the transport coefficients and the cross sections for collisional processes are given in appendix II. We now give the cross section data used and compare our data to data from the literature.

For D_{ia} we used equation A II.16 with:

$$Q_{ia}^{(1,1)} = 3.5 \times 10^{-18} T_h^{-0.14} m^2$$

for $\qquad T_h \leqslant 1.5 \times 10^4 K$ <div align="right">A III.5</div>

which is a compromise between the data of Devoto (73) and Ellis (76).

For λ_a^m we used formula A II.17 with:

$$Q_{aa}^{(2,2)} = 1.33 \times 10^{-18} T_h^{-0.21} m^2$$

<div align="right">A III.6</div>

and

$$\lambda_{aa} = 3.1 \times 10^{-4} T_h^{0.71} \ W \ m^{-1} K^{-1}$$

<div align="right">A III.7</div>

which agree with the data of Aziz (80) within 4% for $T_h \leqslant 10^4 K$, and with:

$$Q_{ia}^{(2,2)} = 3.6 \times 10^{-18} T_h^{-0.30} m^2$$

<div align="right">A III.8</div>

which is a fit of the data of Devoto (73).

The electron heat conductivity λ_e^m was estimated by means of equation A II.19 in which $(\lambda_e^m)_3$ was calculated with equation A II.22.

The Kihara-correction for the charged particle interaction was neglected and the electron-atom cross section $Q_{ea}^{(1)}$ was assumed to be proportional to the energy e_r.

Using the data of Frost (64) and Milloy (77) we obtained:

$$Q_{ea}^{(1)} = 8.6 \times 10^{-2} e_r \ m^2 \qquad\qquad \text{A III.9}$$

for

$$3 \times 10^{-20} J \leqslant e_r \leqslant 2 \times 10^{-18} J.$$

The ratio of electron-atom to electron-ion collision frequencies F is given by:

$$F = \frac{(1-\alpha)}{\alpha} \ \frac{Q_{ea}^{(1,1)}}{2 \pi b_o^2 \ln(3r_D/2b_o)} \qquad\qquad \text{A III.10}$$

and for $(\lambda_e^m)_3$ we find:

$$(\lambda_e^m)_3 = 2.37 (\frac{\pi \ k \ T_e}{8 \ m_e})^{1/2} \ \frac{k}{2 \pi b_o^2 \ln(3r_D/2b_o)} \ \frac{(1 + 1.78 \ F)}{(1 + 10.7 \ F + 3.61 \ F^2)}$$

$$\text{A III.11}$$

T $(10^3 K)$	$(\lambda_e^m)_I$	$(\lambda_e^m)_{II}$ (W/m K)	$(\lambda_e^m)_{III}$	$(\lambda_e^m)_{IV}$
3	8.35–10	8.35–10	7.99–10	9.42–10
4	2.10–6	2.10–6	1.97–6	2.48–6
5	1.71–4	1.72–4	1.65–4	2.13–4
6	2.41–3	2.44–3	2.31–3	3.12–3
7	1.70–2	1.80–2	1.70–2	1.88–2
8	6.22–2	6.80–2	6.52–2	5.86–2
9	0.150	0.162	0.158	0.137
10	0.277	0.293	0.290	0.264
11	0.432	0.451	0.449	0.437
12	0.609	0.631	0.631	0.644

Table A III.1 : Comparison of various expressions for the electron heat conductivity in an atmospheric plasma $(p = 1.013 \times 10^5 Pa)$ (see text).
notation: $8.35 - 10 = 8.35 \times 10^{-10}$.

In table A III.1 we compare data obtained by means of various expressions for λ_e^m :

I. Simplified expression used for our calculations.

The Kihara-correction has been neglected and a linear dependence of $Q_{ea}^{(1)}$ on e_r is used. (A III.9 to 11)

II. Simplified expression based on the assumption of a linear dependence of $Q_{ea}^{(1)}$ on e_r (A III.9) and including the Kihara-correction according to the formulas of Luchina (78).

III. Heat conductivity with the data of Milloy (77) for $Q_{ea}^{(1)}$ in the range $e_r \leqslant 4 \times 10^{-19}$ J and the data of Forst (64) for $e_r > 4 \times 10^{-19}$ J.

The Kihara-correction is applied according to Luchina (78).

IV. Data of Devoto (73) with the data of Forst (64) for the electron-atom interaction and the formulas of Williams (69) for the charged particle interaction. Below 6000K the Forst-mixture rule of Kruger (68) is used.

A III.d. Source terms

The energy source term ε_{eh} was calculated with equation IV.24 in which the expression of Kihara (Mitchner 73) was used for $Q_{ei}^{(1,1)}$:

$$Q_{ei}^{(1,1)} = 2 \pi b_o^2 (\ln(3r_D/2b_o) - 1.37) \qquad \text{A III.12}$$

for the electron-atom interaction formula A III.9 was used.

We calculated the ion-mass source term M_i assuming that electron-atom collisions were dominant. Equation V.15 was used where $_o S^1$ is given by:

$$_o S^1 = C_{ea} T_e^{1/2} (2 T_e + T_{ex}) \exp(- T_{ex}/T_e) \qquad \text{A III.13}$$

with:

$$T_{ex} = 1.35 \times 10^5 \text{K and } C_{ea} = 3 \times 10^{-22} \text{m}^3 \text{K}^{-3/2} \text{s}^{-1}.$$

This formula can be considered as a lower bound for the estimate of M_i. From the comparison of this model with a more detailed model we will show in appendix IV that A III.13 yields a reasonable order of magnitude estimate of M_i outside the boundary layer. However in the inner part of the boundary layer this model is not even expected to yield a correct order of magnitude estimate.

APPENDIX IV.

COLLISION-RADIATION MODEL

A IV.a. Introduction

        In the present study we use a collision-radiation model in
order to estimate the influence of radiation escape on the state of
the plasma outside the boundary layer (section V.d).
The model used is the two-step model of Mitchner (73). (section A IV.b).
When radiation escape is neglected this model yields formula V.15
which has been used for the estimation of the recombination rate in
the boundary layer (see also appendix III, section d).

        This simple model yields a qualitative insight in the
behaviour of the plasma in the outer part of the boundary layer and
outside the boundary layer. This statement is supported by the
comparison with a more detailed (five step) model and with experimental
data of Leclair (77) (section A IV.c).

        For the inner part of the flow (close to the wall) the
reaction model is not expected to yield a realistic order of magnitude
estimate for the recombination rate. We recall here some of the defects
of the model:
From the study of Mitchner (73) it appears that for the conditions
encountered close to the wall the deviation of the electron velocity
distribution from a Maxwellian distribution must be taken into
account for the estimation of the reaction rates.
From the studies of Drawin (69) and Bacri (77, 78) we conclude that
electron-ion-atom three body recombination will not be negligible.[⋈]
The influence of dissociative recombination is not well established.
Close to the wall (T_h = 0(3×10^2K), T_e = 0(5×10^3K)) it will
certainly be dominant. Bates (80) states that dissociative
recombination will overshadow other processes up to 10^4K. This is in
contradiction with the results of Igra (75).

[⋈] Note:
    The expression of Hoffert (67) used by Glass (78) for this reaction
    rate depends only on the heavy particle temperature.
    This seems rather unrealistic. The formula proposed by Drawin (69)
    seems more appropriate.

196

Finally the development of a realistic collision-radiation model
necessitates the estimation of escape factors in a non-uniform
plasma.[@]

In view of those difficulties we did not attempt to develop
a reaction model valid for the entire flow.
Fortunately as shown in section V.e the structure of the outer part
of the boundary layer is rather insensitive to the behaviour of the
electrons close to the wall.

[@] Note:

One may expect that absorption of the light emitted outside the
boundary layer by the inner part of the boundary layer can yield
negative values of the escape factors.

A IV.b. Two step-model

The general formalism of collision-radiation models is
described by Biberman (71), Drawin (69, 72) and Katsonis (76).
A comparative study of various approaches is given bij Drawin (75).
We consider here the simplified two-step model of Mitchner (73) for a
uniform plasma consisting of electrons (e), argon atoms in the ground
state (Ar_o), excited argon atoms (Ar_1) and singly ionized argon in the
ground state (Ar^+ or i). The distribution functions of the particles
are assumed to be Maxwellian. The population of the excited atoms n_1
is assumed to be quasi -stationary, i.e.:

$$\frac{\partial n_1}{\partial t} + \nabla \cdot (n_1 (\underline{u} + \underline{V}_1)) = \dot{n}_1 = 0 \qquad \text{A IV.1}$$

where $\dot{n}_1$ is the volumic rate of production of atoms in the excited
state 1. Using the assumption of quasi-neutrality and the conservation
of charges we have:

$$\dot{n}_e = \dot{n}_i = -\dot{n}_o \qquad \text{A IV.2}$$

Assuming that electron-atom inelastic processes are dominant we can
write:

$$\dot{n}_o = -R(eAr_o/eAr_1)(1 - (n_1/n_o)(n_o/n_1)_{eq}) + n_1 A_{1o} B_{1o}$$

$$-R(eAr_o/eAr^+e)(1 - (n_e^2/n_o)(n_o/n_e^2)_{eq}) + n_e^2 A_{co} B_{co} \qquad \text{A IV.3}$$

and

$$\dot{n}_1 = 0 = R(eAr_o/eAr_1)(1 - (n_1/n_o)(n_o/n_1)_{eq}) - n_1 A_{1o} B_{1o}$$

$$-R(eAr_1/eAr^+e)(1 - (n_e^2/n_1)(n_1/n_e^2)_{eq}) + n_e^2 A_{c1} B_{c1} \qquad \text{A IV.4}$$

Where the equilibrium values of (n_1/n_o) and (n_e^2/n_j) are given by:

$$(n_1/n_o)_{eq} = (Z_1/Z_o) \exp ((e_o - e_1)/kT_e) \qquad \text{A IV.5}$$

and

$$(n_e^2/n_j)_{eq} = (2Z_i/Z_j)(2\pi m_e k T_e/h_p^2)^{3/2} \exp ((e_j - e_{ion})/kT_e)$$

$$\text{A IV.6}$$

The reaction rates are calculated with formula A II.34 in which the following approximations for the cross sections are used:

$$Q_{o1}^e = 3 \times 10^{-3} (e_r - (e_1 - e_o)) \text{ m}^2 \qquad \text{A IV.7}$$

$$Q_{oi}^e = 1.2 \times 10^{-2} (e_r - (e_{ion} - e_o)) \text{ m}^2 \qquad \text{A IV.8}$$

$$Q_{1i}^e = 1.9 \times 10^{-1} (e_r - (e_{ion} - e_1)) \text{ m}^2 \qquad \text{A IV.9}$$

Formulas A IV.7, 8 and 9 are based on the experimental data of Jacob (76), Kieffer (66) and Dixon (73) respectively.
Formula A IV.7 is also used by Glass (78).
e_j is the energy of level j and e_{ion} is the ionization energy. A_{1o} is the rate of spontaneous de-excitation from level 1 to the ground level o. A_{cj} is the two-body radiative recombination rate. The data on e_j, Z_j, A_{1o} and A_{cj} used are given in table A IV.1.

j	Z_j	e_j (1.6×10^{-19} J)	$A_{j(j-1)}$ (10^8/s)	A_{cj} (m^3/s)
o	1	0	–	$1.03 \times 10^{-17} / T_e^{1/2}$
1	12	11.6	3.17	$6 \times 10^{-23} (1.5 \times 10^4 + T_e) / T_e^{1/2}$
i	6	15.76	–	–

Table A IV.1 : Model of the argon atom

These data have been obtained from the studies of Wiese (69), Katsonis (76) and Nishida (77).
The influence of lowering of ionization potential and advance of series limit on the radiative recombination rates has been neglected. Actual values of A_{cj} may be higher by a factor 1.2 to 2 (Vorob'ev (78), Schlüter (80)).

The escape factors B_{1o}, B_{co} and B_{c1} have been calculated by means of the formulas of Drawin (73).

Assuming a Lorentz-line@shape B_{lo} is related to the optical depth t_{lo} by:

$$B_{lo} = (1 + (t_{lo}/(2 + t_{lo}^2)))/(1 + (\pi t_{lo})^{1/2}) \qquad \text{A IV.10}$$

where:

$$t_{lo} = (Z_1/Z_o)(c^2/8 \pi^2 \nu_{lo}^2) A_{lo}/\Delta\nu_{lo} \qquad \text{A IV.11}$$

The line half width $\Delta\nu_{lo}$ is given by:

$$\Delta\nu_{lo} = (\Delta\nu_{lo})_n + (\Delta\nu_{lo})_s + (\Delta\nu_{lo})_r \qquad \text{A IV.12}$$

where the natural line broadening is given by:

$$(\Delta\nu_{lo})_n = A_{lo}/4\pi \qquad \text{A IV.13}$$

the stark broadening is given by Griem (74):

$$(\Delta\nu_{lo})_s = 1.4 \times 10^{-13} n_e \ s^{-1} \qquad \text{A IV.14}$$

and the resonant broadening is calculated by means of the formula of Lindholm-Foley @@ (Traving (68)):

$$(\Delta\nu_{lo})_r = (Z_1/Z_o)(c/4\pi \nu_{lo})^3 A_{lo} n_o \qquad \text{A IV.15}$$

and

$$\nu_{lo} = (e_1 - e_o)/h_p \qquad \text{A IV.16}$$

@ Note:

From the study of Drawin (73) it appears that B_{lo} is mainly determined by the wings of the line. The Doppler broadening will not affect B_{lo} significantly for the experimental conditions considered.

@@ Note:

The formula of Ali (65) yields a value which is a factor 4 lower. Equation A IV.15 can be considered as an upperbound.

According to Irons (79) the formulas of Drawin (73) yield a
qualitative estimate of the escape factor for a cylindrical plasma.
The escape factor at a distance x from a wall in a half infinite
space is about a factor 3 lower than the escape factor at the center
of a cylinder of radius x (for strongly absorbed lines).
The expression used for B_{lo} is thus an upperbound (when considering
the state of the plasma outside the boundary layer in shock tube
experiments).

Using the photo-ionization cross section data of Katsonis (76)
we found:

$$B_{co} = \exp(- t_{co})$$
A IV.17

where the optical depth t_{co} is given by:

$$(n_o x)^{-1} t_{co} = 3.5 \times 10^{-21} m^2$$
A IV.18

For B_{c1} a hydrogenic approximation of the photo-ionization cross
section (Mitchner 73) was used.

For the temperature range considered ($T_e \leqslant 12000$ K) the direct
ionization $R(eAr_o/eAr^+ e)$ is negligible in comparison with the
excitation rate $R(eAr_o/eAr_1)$. The global ionization rate S_g defined by:

$$\dot{n}_e = S_g n_e n_o - A_g n_e^3$$
A IV.19

is in such a case approximatively equal to:

$$_o S^1 = R(eAr_o/eAr_1)/n_e n_o$$
A IV.20

In principle the global ionization rate S_g is not related to the global
recombination rate A_g by the principle of detailed balance.
Equation A IV.19 can also be written as:

$$\dot{n}_e = n_e n_o S_g (1 - (n_e^2/n_o)(n_e^2/n_o)_{st})$$
A IV.21

where the stationary value $(n_e^2/n_o)_{st}$ is in general a function of x, n_e,
n_j and T_e.

When the escape factors are independent of the populations n_j, $(n_e^2/n_o)_{st}$ is a function of n_e and T_e only which can be used as a generalized Saha expression.

In figure A IV.1 we show the behaviour of $(n_e^2/n_o)_{st}$ and $(n_e^2/n_1)_{st}$ for conditions corresponding to our experiments. The escape factors B_{lo} and B_{co} are given as a function of x in figure A IV.2.

From these data we conclude that the influence of radiation escape is negligible so that we may approximate equation A IV.21 by equation V.15:

$$\dot{n}_e = n_e n_o S^1 (1 - (n_e^2/n_o)(n_o/n_e^2)_{eq}) \qquad\qquad V.15$$

In the next section we compare this simplified two-step reaction model with other models and with experimental data.
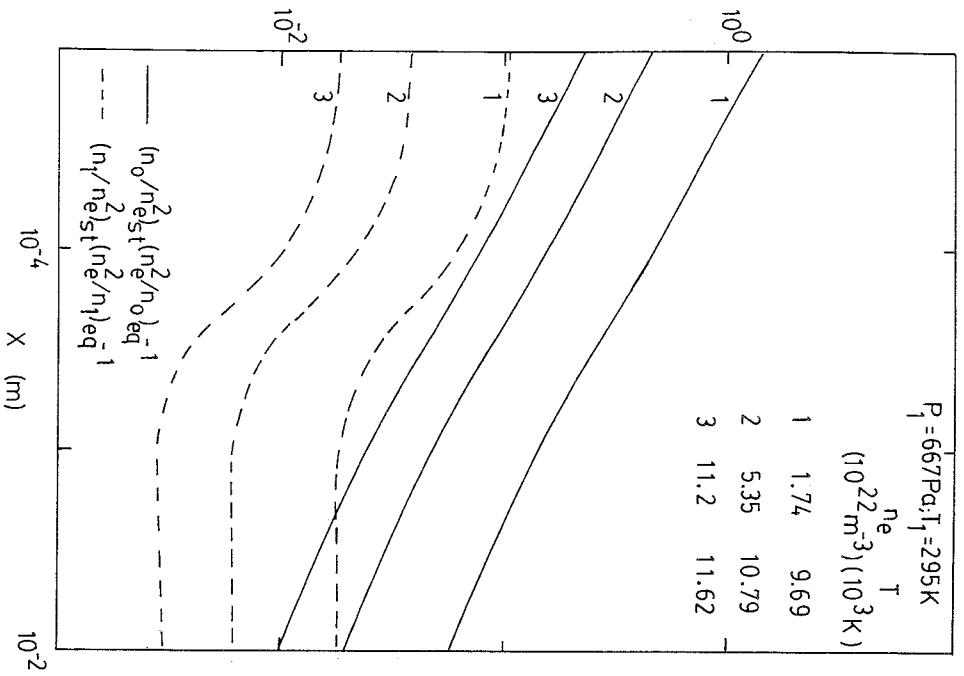
Figure A IV.1 : Stationary state $(n_1/n_e^2)_{st}$ and $(n_o/n_e^2)_{st}$ as function of distance of the wall x in a uniform plasma (two-step model).

Legend (Figure A IV.1):

$(n_o/n_e^2)_{st}(n_e^2/n_o)_{eq}^{-1}$

$(n_1/n_e^2)_{st}(n_e^2/n_1)_{eq}^{-1}$

$P = 667Pa; T_i = 295K$

	n_e $(10^{22}m^{-3})$	T $(10^3 K)$
1	1.74	9.69
2	5.35	10.79
3	11.2	11.62

Figure A IV.2 : Escape factors data corresponding to figure A IV.1.

B_{co}

B_{1o}

203

A IV.c. Comparison of the two-step model with other models

At temperatures of the order of 10^4K and electron densities of $10^{22}m^{-3}$ the two-step model agrees well with the models of Katsonis (76) and Kimura (73, 78). In figure A IV.3 we show the stationary state populations n_o and n_1 calculated by means of a five-step model based on the atomic model of Kimura (73). The additional cross-section data which are not described in section A IV.b are calculated by means of the generalized Thomson formula (Mitchner (73), Kimura (73)). The radiative recombination rates of Katsonis (76) are used. The behaviour of the escape factors is similar to the behaviour shown in figure A IV.2.

The two-step model described in the previous section fails at low temperatures because the atomic model used is too rough and because processes which have not been taken into account become dominant (section A IV.a).

For $T_e = 0(10^3$K) when the two-step model becomes unreliable, Hutten (76) and Liu (79) use both the model of Hinnov (62). Following Igra (75, 77) this model yields a correct order of magnitude estimate for the recombination rate up to temperatures of 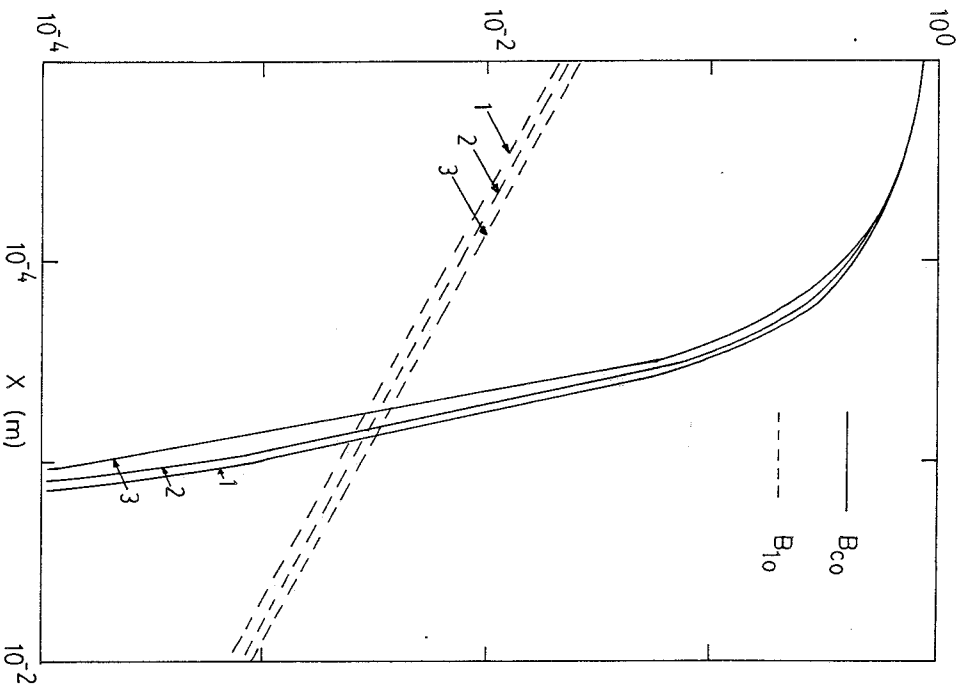10^4K. This conclusion will certainly not hold at low electron densities. As shown by Bacri (77, 78) and according to Massey (74) and Bates (80) the atom-ion-electron three body recombination and the dissociative recombination will overshadow the electron-ion-electron three body recombination. A simple reaction model is not possible because the various processes will interact through their influence on the populations of the excited levels.
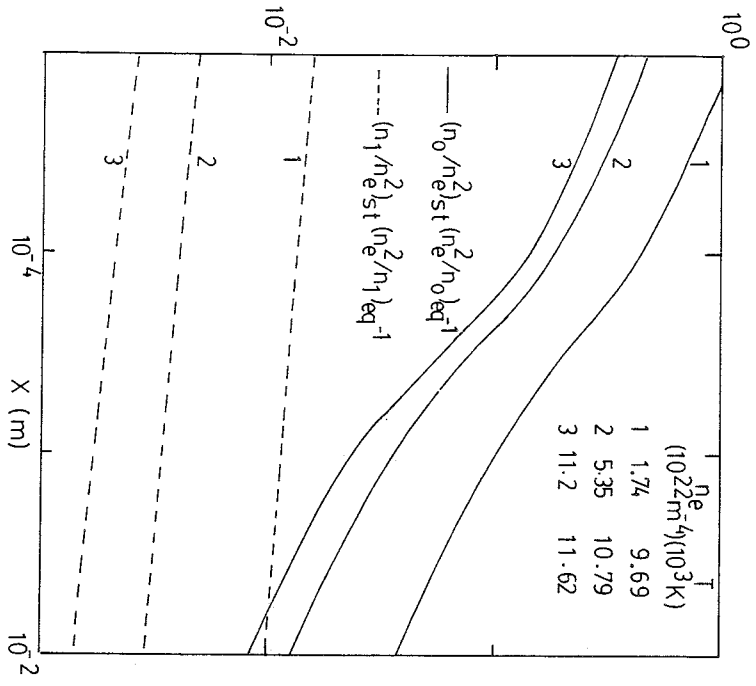
Figure A IV.3 : Stationary state of a uniform plasma (five-step model).

Legend / axes for Figure A IV.3:

$\frac{n_e}{}$ $(10^{22}\,\mathrm{m}^{-4})$ $\quad$ T $(10^3\,\mathrm{k})$

	n_e $(10^{22}\,\mathrm{m}^{-4})$	T $(10^3\,\mathrm{k})$
1	1.74	9.69
2	5.35	10.79
3	11.2	11.62

—— $(n_0/n_e^2)_{st}\,(n_e^2/n_0)_{eq}^{-1}$

---- $(n_1/n_e^2)_{st}\,(n_e^2/n_1)_{eq}^{-1}$

X (m)
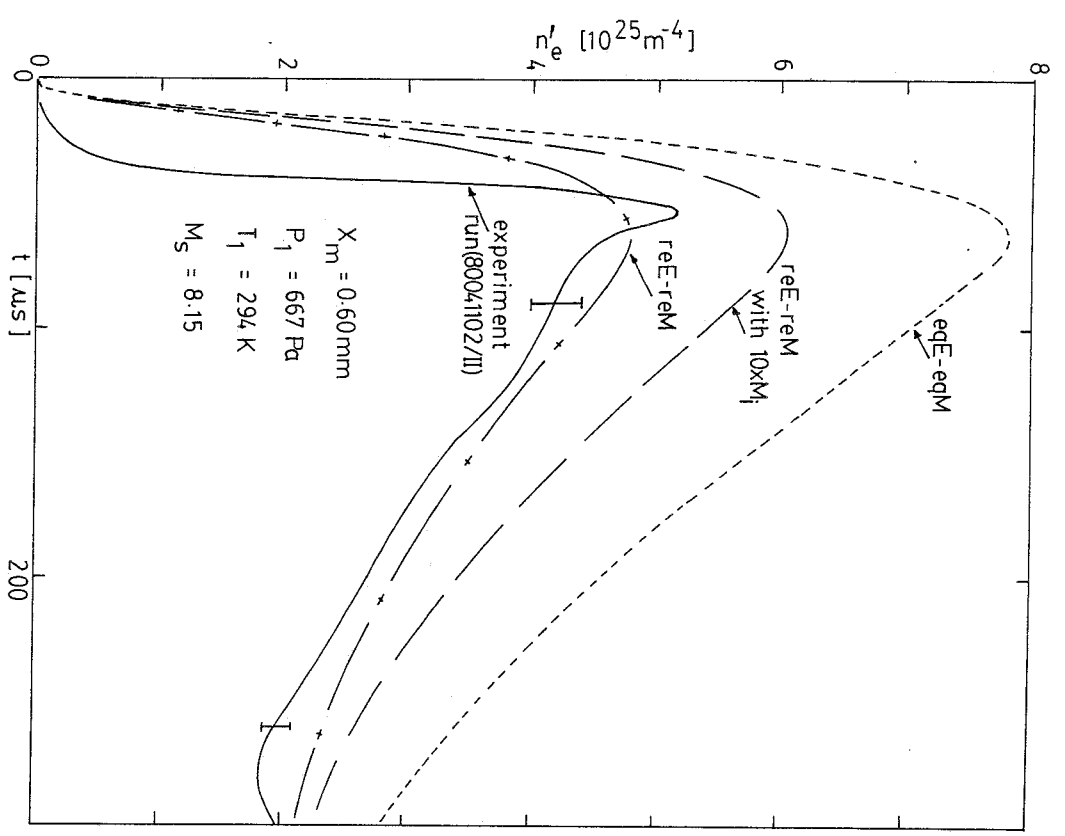
Figure A IV.4 : Influence of an increase of M_i by a factor 10 on the calculated electron density profile.

n'_e $[10^{25}\,\mathrm{m}^{-4}]$

$t\,[\mu s]$

experiment run(80041102/II)

reE-reM

reE-reM with $10\times M_i$

eqE-eqM

$X_m = 0.60$ mm
$P_1 = 667$ Pa
$T_1 = 294$ K
$M_s = 8.15$

205

For instance an extrapolation of the data of Fox (66) for the
dissociative recombination to temperatures of 10^4K would yield a
reaction rate which is 10^3 times greater than the reaction rate
predicted by our two-step model. As shown in figure A IV.4 the
increase of M_i by a factor 10 in the reE-reM model (section V.e)
yields electron density gradients which are significantly higher than
the measured density gradients. Taking into account that the electron
density profile is not sensitive to the behaviour of the electrons in
the inner part of the flow, we may conclude that if dissociative
recombination is important it will not overshadow the three body
electron-electron-ion recombination process (in the outer part of the
flow). Because the electron density profile is not very sensitive to
variation in M_i (figures A IV.4 and A IV.5) this conclusion should
be considered with care. Our conclusion is supported by the studies
of Desai (69) and Igra (75, 77, 80).

The dissociative recombination rates calculated by Desai (69) by
assuming an equilibrium concentration of Ar_2^+ are of the same order of
magnitude as the reaction rates calculated by means of the two-step
model (section A IV.b).

It is also interesting to notice that the recombination rates
measured by Desai (69) and Gaucherel (77) are strongly influenced by
the addition of 100 ppm N_2 to the argon. Gaucherel (77) considers
also the influence of O_2 and H_2.

As shown in figure A IV.6 the addition of 0.5% H_2 to the argon can be
simulated in the reE-reM model by multiplying the recombination rate
by a factor two.

It is also interesting to compare our model to the
experimental data $(n_o/(n_o)_{eq})_{exp}$ of Leclair (77) and Rosado (79).
Those data have been obtained in a stationary electric arc.
In such a case we can write:

$$(n_o/n_e^2)(n_e^2/n_o)_{eq} = (n_o/n_e^2)_{st}(n_e^2/n_o)_{eq}/(1 - \frac{\nabla.(n_e V_e)}{n_e n_o S_g})$$

A IV.23

For the estimation of $(n_o/n_e^2)_{st}$ and S_g we used the five-step model.
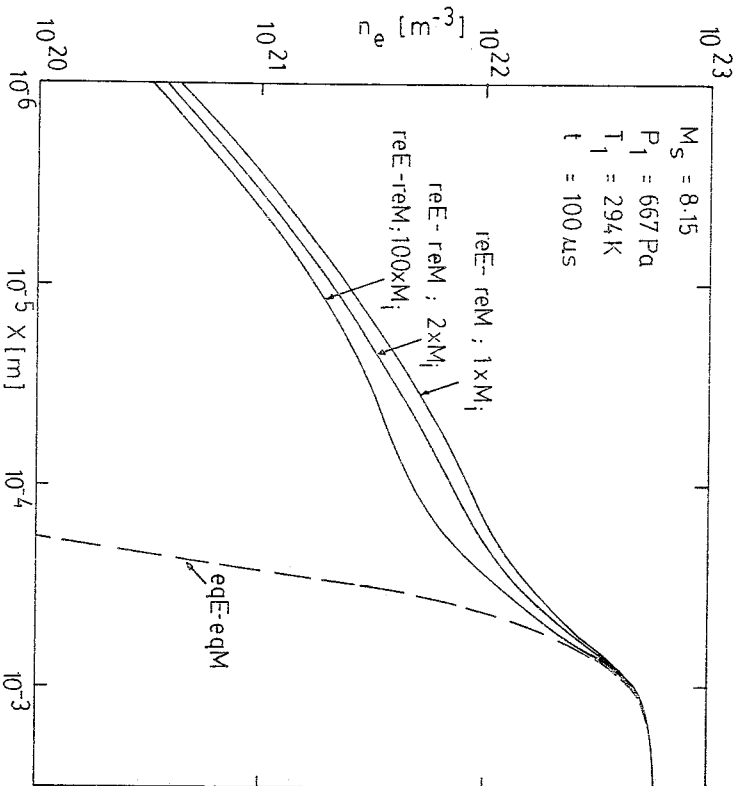The diffusion term $\nabla.(n_e V_e)$ was estimated by means of the formula:

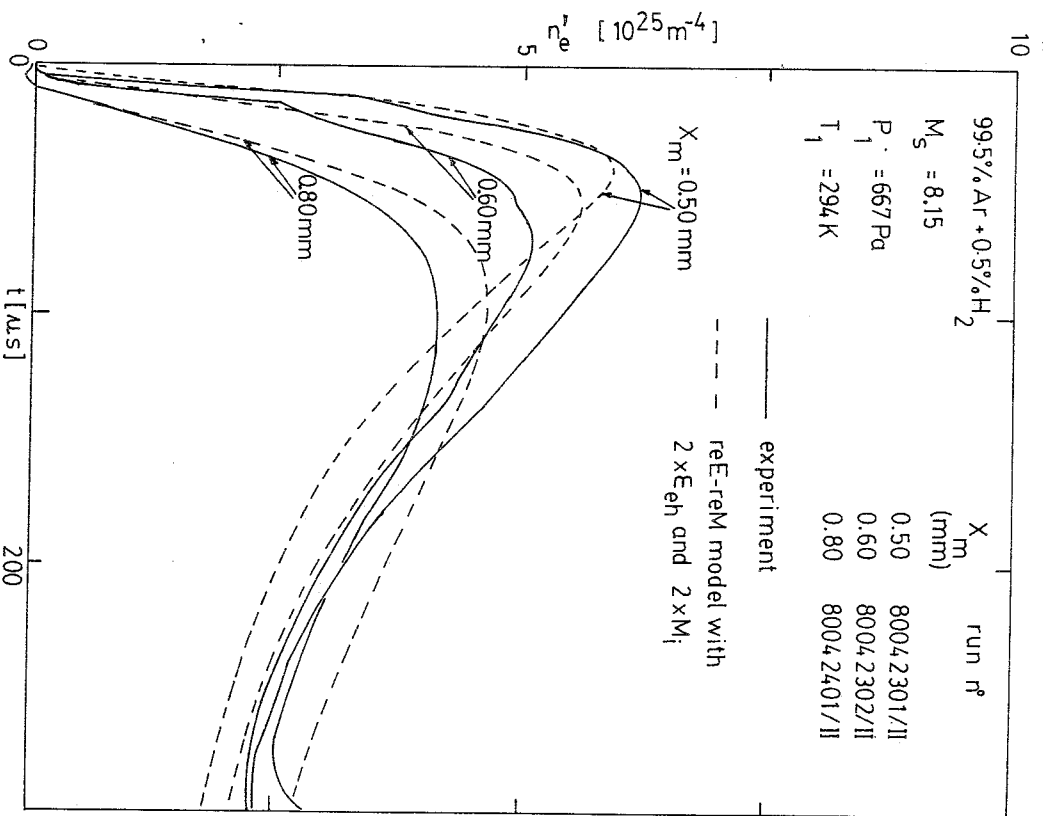Figure A IV.5 : Influence of variation in M_i on the calculated electron density profile.

Figure A IV.6 : Influence of the addition of 0.5% H_2 to the argon on the measured electron density profile.

$$\nabla \cdot (n_e \underline{V}_e) \quad \sim \quad \frac{8 \, n_e D_{ia}}{(1 + \alpha)R^2} \qquad\qquad \text{A IV.24}$$

which is based on a calculation with a parabolic electron density profile:

$$n_e(r) \; = \; n_e(0)(1 - (r/R)^2) \qquad\qquad \text{A IV.25}$$

At low temperatures (currents) it appears from the data of Baum (75) that the constant R is of the order of magnitude of the radius of the arc.

At higher temperature a considerable flattening of the electron density profile is observed. This is due to the strong radiative energy transfer.

In table A IV.2 we compare the calculated value of $(n_o/(n_o)_{eq})_{th}$ to the experimental results of Leclair (77).

T $(10^3 K)$	$(\dfrac{n_o}{(n_o)_{eq}})_{exp}$	$(\dfrac{n_o}{(n_o)_{eq}})_{th}$	$(\dfrac{n_o}{n_e^2})_{st} \dfrac{n_e^2}{n_o}_{eq}$	$\dfrac{\nabla \cdot (n_e \underline{V}_e)}{n_e n_o S_g}$
11	2.0	1.5	1.12	0.25
13	1.5	1.1	1.07	0.03

Table A IV.2 : Deviation from local thermodynamic
equilibrium in an atmospheric electric arc.
$(p = 1.013 \times 10^5 Pa)$.

We see that our model significantly underestimates $(n_o/(n_o)_{eq})$. This as suggested by Rosado (79) may be due to an overestimation of S_g. However one must also consider the fact that the radiative recombination rates calculated by Katsonis (76) do not take into accout the influence of advance of series limits.

Further we see from figure A IV.2 that the escape factor B_{co} is very sensitive to the model used for the density profile and for uncertainties in the cross section data. From equation A IV.24 we see that the influence of diffusion depends strongly on the electron density profile assumed. In view of these difficulties we can state that our collision radiation model yields estimates for $(n_o/(n_o)_{eq})$ that are not in contradiction with the experimental data available.

208

Appendix V

PROPAGATION OF A COHERENT LIGHT BEAM THROUGH A ONE -DIMENSIONAL
INHOMOGENEITY

AV.a   Ray equation

Starting from the Eikonal equation:

$$(\nabla \Sigma)^2 = k^2 \qquad ; \qquad AV.1$$

where k is a function of x only($k = k(x)$), we find
(Courant(62)):

$$(\nabla \Sigma)_x = (k^2 - A^2)^{1/2}$$
$$(\nabla \Sigma)_y = (A^2 - B^2)^{1/2}$$
$$(\nabla \Sigma)_z = B \qquad ; \qquad AV.2$$

The integration constants A and B are determined by the
initial conditions:

$$(\nabla \Sigma)_o = (k_o \sin b, 0, k_o \cos b); \qquad AV.3$$

b is the angle of incidence of the beam.

From the definition of a light ray :

$$d \, \underline{r}_r \, x \, (\nabla \Sigma) = 0 \qquad ; \qquad AV.4$$

we obtain:

$$(dx_r/dz)^2 = ((\nabla \Sigma)_x/(\nabla \Sigma)_z)^2 \qquad ; \, AV.5$$

or:

$$(d^2 x_r/dz^2) = \frac{1}{2 \cos^2 b} \, (\frac{d}{dx}(k/k_o)^2)_{x=x_r} \, ; \, AV.6$$

When $\cos b = 1$ or in the paraxial approximation ($\cos b \approx 1$)
this equation is identical to equation VI.13.

AV.b   Scalar wave theory

As starting point we use the scalar wave equation (section VI.b):

$$(\partial^2 e/\partial x^2) + (\partial^2 e/\partial y^2) + (k^2 - k_o^2) e = 2 i k_o(\partial e/\partial z) ; \quad \text{AV.7}$$

We consider the propagation of a light beam through a slab of gas (thickness L):

$$k = k(x) \quad \text{for} \quad 0 < z < L$$
$$k = k_o \quad \text{for} \quad z \leqslant 0 \text{ and } z \geqslant L; \quad \text{AV.8}$$

The amplitude $e(x,y,0)$ is assumed to be given and we consider $e(x,y,z)$ for $z \geqslant 0$.

In order to determine $e(x,y,z)$ we use a perturbation method based on the mode-theory. The modes e_{jk} are a set of solutions of the wave equation (AV.7), forming a complete set of orthonormal functions. So that we have:

$$\int_{-\infty}^{\infty} \int_{-\infty}^{\infty} e_{jk}^{\pi} e_{lm} \, dxdy = \delta_{jl}\delta_{km} \quad ; \quad \text{AV.9}$$

Considering the gaseous inhomogeneity as a disturbance of the uniform region ($z \leqslant 0$ and $L \leqslant z$) we use the free space modes (Praseti(77)) defined by:

$$e_{jk} = e_{oo} \frac{H_j(2^{1/2}x/W_x)H_k(2^{1/2}y/W_y)}{(2^{j+k} \; j! \; k!)^{1/2}}$$

$$\exp\left\{ i \left(j \; \text{arct}((z - z_{wx})/z_{ox}) + k \; \text{arctg}((z - z_{wy})/z_{oy})\right)\right\};$$

and

AV.10

$$e_{oo} = (\frac{2}{\pi W_x W_y})^{1/2}\exp\left\{ - (x/W_x)^2 - (y/W_y)^2 \right\}$$

$$\exp\left\{ - i k_o(\frac{x^2}{R_x}+\frac{y^2}{R_y})+\frac{i}{2}(\text{arctg}((z-z_{wx})/z_{ox})+ \text{arctg}((z -z_{wy})/z_{oy}))\right\};$$

AV.11

where:

$$W_x^2 = w_{ox}^2 (1 + ((z-z_{wx})/z_{ox})^2) \; ; \; W_y^2 = w_{oy}^2(1+((z-z_{wy})/z_{oy})^2); \text{ AV.12}$$

$$R_x = (z-z_{wx})(1+(z_{ox}/(z-z_{wx}))^2); \; R_y = (z-z_{wy})(1+(z_{oy}/(z-z_{wy}))^2); \text{AV.13}$$

$$z_{ox} = k_o w_{ox}^2 /2 \; ; \; z_{oy} = k_o w_{oy}^2/2 \; ; \qquad\qquad \text{AV.14}$$

w_o is the waist of the beam and z_w is the position of the waist. $H_j(t)$ is the Hermite polynomial of argument t given by: **&**

$$H_j(t) = \sum_{m=0}^{[j/2]} \frac{(-1)^m j! (2 t)^{j-2m}}{(j-2m)! \; m!} \; ; \qquad \text{AV.15}$$

The modes depend on the choice of the coordinate system and of the parameters $w_{ox}, w_{oy}, z_{wx}, z_{wy}$ and k_o.
Because the wave equation AV.7 is linear we can write :

$$e(x,y,z) = \sum_j \sum_k A_{jk}(z) e_{jk} \; ; \qquad\qquad \text{AV.16}$$

where $A_{jk}(z)$ is the "amplitude" of mode e_{jk}.
Using the wave equation AV.7 we find:

$$(dA_{j1}/dz) = - \frac{i}{2k_o} \sum_m \sum_n A_{mn} \int_{-\infty}^{\infty} \int_{-\infty}^{\infty} e_{j1}^{\overline{x}} (k^2-k_o^2) \; e_{mn} dxdy \; ; \qquad \text{AV.17}$$

with the initial conditions:

$$A_{j1}(0) = \int_{-\infty}^{\infty} \int_{-\infty}^{\infty} e_{j1}^{\overline{x}}(x,y,0) \; e(x,y,0) \; dxdy \; ; \qquad \text{AV.18}$$

In the case of a uniform medium ($k=k_o$) the amplitudes are constants . We can thus determine $e(x,y,z)$ for $z > L$ when $e(x,y,L)$ is known.

& Note : $[j/2]$ is the largest integer smaller or equal to $j/2$.

In order to calculate $A_{jl}(L)$ we use a perturbation scheme similar to the procedures described by Schiff( ). We introduce the perturbation parameter θ by stating:

$$(k^2 - k_o^2) \longrightarrow \theta (k^2 - k_o^2); \quad \text{AV.19}$$

and expand the amplitudes A_{jl} in a power series:

$$A_{jl} = \sum_t A_{jl}^{(t)} \theta^t \quad ; \quad \text{AV.20}$$

we write equation AV.17 as:

$$(dA_{jl}^{(0)}/dz) = 0 ;$$

$$(dA_{jl}^{(s+1)}/dz) = -\frac{i}{2k_o} \sum_m \sum_n A_{mn}^{(s)} \int_{-\infty}^{\infty} \int_{-\infty}^{\infty} e_{jl}^{\bar{x}} (k^2 - k_o^2) \, e_{mn} \, dx dy;$$

$$\text{AV.21}$$

This set of equations is equivalent to the wave equation AV.7 and can be solved up to any desired order (s+1) because the right hand side of AV.21 contains only lower order quantities. The amplitudes A_{jl} are estimated by using the (s+1) first terms in equation AV.20 and putting the parameter θ equal to unity.

AV.c   Schlieren signal

The schlieren signal S defined by:

$$S = \int_{-\infty}^{\infty} \int_{0}^{\infty} I(x,y,z_d) \, dxdy - \int_{-\infty}^{\infty} \int_{-\infty}^{0} I(x,y,z_d) \, dxdy \; ; \quad AV.22$$

where:

$$I = \frac{1}{2} k_o \, e_{jl}^x \, e \qquad ; \qquad AV.23$$

has been calculated for the case of a gaussian beam:

$$A_{jl}(0) = \delta_{jo} \, \delta_{lo} \qquad ; \qquad AV.24$$

with:

$$w_{ox} = w_{oy} = w_o \qquad ; \qquad AV.25$$

and

$$z_{wx} = z_{wy} = z_w \qquad ; \qquad AV.26$$

The refractive index profile is given by:

$$\frac{k^2 - k_o^2}{k_o^2} = \sum_{j=1}^{j_{max}} \frac{\eta_j}{j!} (x - x_{mo})^j ; \qquad AV.27$$

In order to calculate the amplitudes $A_{jl}^{(s)}$ by means of formula AV.21 we first calculate the perturbation matrix H_{jlmn} defined by:

$$H_{jlmn} = \int_{-\infty}^{\infty} \int_{-\infty}^{\infty} e_{jl}^x \left(\frac{k^2 - k_o^2}{k_o^2} \right) e_{mn} \, dxdy \; ; \qquad AV.28$$

We notice that because k is a function of x only:

$$H_{jlmn} = \delta_{ln} H_{jnmn} \qquad ; \qquad AV.29$$

Further from the properties of the Gauss-Hermite functions (Rainville(60)) we see that :

$$H_{jnmn} = 0 \quad \text{for} \quad |j - m| > j_{max} \; ; \qquad AV.30$$

The matrix elements used for the derivation of formulas

VI.34 and 35 are:

$H_{0000} = (k_o \eta_2 W^2/2)$;

$H_{1000} = (k_o W/2)(\eta_1 + (\eta_3 W^2/8)) \exp(-i \text{ arctg } \mathcal{Z})$;

$H_{2000} = (k_o \eta_2 W^2/2^{5/2}) \exp(-2 i \text{ arctg } \mathcal{Z})$;

$H_{3000} = (k_o \eta_3 W^3/(8 \, 6^{1/2})) \exp(-3 i \text{ arctg } \mathcal{Z})$;

$H_{1010} = (3 \, k_o \eta_2 W^2/8)$;

$H_{2010} = (k_o W/2^{1/2})(\eta_1 + (\eta_3 W^2/4)) \exp(- i \text{ arctg } \mathcal{Z})$;

$H_{3010} = (6^{1/2} k_o \eta_2 W^2/8) \exp(-2 i \text{ arctg } \mathcal{Z})$;

$H_{4010} = (k_o \eta_3 W^3/(4 \, 6^{1/2})) \exp(- 3 i \text{ arctg } \mathcal{Z})$;

$H_{2020} = (5 \, k_o \eta_2 W^2/8)$;

$H_{3020} = (3^{1/2} k_o W/2)(\eta_1 + (3\eta_3 W^2/8) \exp(- i \text{ arctg } \mathcal{Z})$;

$H_{4020} = (3^{1/2} k_o \eta_2 W^2/4) \exp(-2 i \text{ arctg } \mathcal{Z})$;

$H_{5020} = (5^{1/2} k_o \eta_3 W^3/(8 \, 3^{1/2})) \exp(-3 i \text{ arctg } \mathcal{Z})$;

$H_{3030} = (7k_o \eta_2 W^2/8)$;

$H_{4030} = (k_o W)(\eta_1 + (\eta_3 W^2/2)) \exp(- i \text{ arctg } \mathcal{Z})$;

$H_{5030} = (5^{1/2} k_o \eta_2 W^2/4) \exp(- 2 i \text{ arctg } \mathcal{Z})$;

$H_{6030} = (5^{1/2} k_o \eta_3 W^3/(4 \, 6^{1/2})) \exp(- 3 i \text{ arctg } \mathcal{Z})$; 　　　AV.31

where:

$$W_x = W_y = W \quad ; \qquad\qquad \text{AV.32}$$

and: $\mathcal{Z} = (z - z_w)/z_o;$ 　　　　　　　　AV.33

Taking $j_{max} = 3$ we find in first order (s=1) the amplitudes

for $0 < z < L$:

$$A_{00}^{(1)} = -(i\ k_o \eta_2 w_o^2/8) \left\{ z_o (1 + \frac{z^2}{3}) z \right\}_{z=-z_w/z_o}^{z=(z-z_w)/z_o} \quad ;$$

$$A_{10}^{(1)} = -(i\ k_o w_o/2) \left\{ z_o z (\eta_1 + \frac{\eta_3 w_o^2}{8} (1+z^2/3)) \right.$$
$$\left. - i\frac{z_o z^2}{2} (\eta_1 + \frac{\eta_3 w_o^2}{8}(1+z^2/2)) \right\}_{z=-z_w/z_o}^{z=(z-z_w)z_o} \quad ;$$

$$A_{20}^{(1)} = -(i\ k_o \eta_2 w_o^2/4\ 2^{1/2})) \left\{ z_o z (1 - \frac{z^2}{3} - i\ z) \right\}_{z=-z_w/z_o}^{z=(z-z_w)/z_o} \quad ;$$

$$A_{30}^{(1)} = -(i\ k_o \eta_3 w_o^3/8\ 6^{1/2})) \left\{ z_o z (1-z^2 -i\frac{z}{4}(6-z^2)) \right\}_{z=-z_w/z_o}^{z=(z-z_w)/z_o} \quad ; \text{ AV. 34}^{\otimes}$$

For $z \geq L$ we have:

$$A_{j0}^{(1)}(z) = A_{j0}^{(1)}(L) \quad ; \hspace{3cm} \text{AV.35}$$

The second order (s=2) calculation is rather complex.
We limited ourselves to the case $z_w = L/2$ and $z \geq L$.

Because the schlieren signal is given by:

$$S = 2 \int_{-\infty}^{\infty} \int_{0}^{\infty} (I(x,y,z_d) - I(-x,y,z_d))\ dxdy \quad ; \hspace{1.5cm} \text{AV.36}$$

where (up to second order):

$$I(x,y,z_d) - I(-x,y,z_d) = 2\ k_o\ Re \left\{ (1+A_{00}^{(1)})^x A_{10}^{(1)} e_{00}^x e_{10} \right.$$
$$+ A_{10}^{(1)x} A_{20}^{(1)} e_{10}^x e_{20} + A_{20}^{(1)x} A_{30}^{(1)} e_{20}^x e_{30} + (1+A_{00}^{(1)x}) A_{30}^{(1)} e_{00}^x e_{30}$$
$$\left. + A_{10}^{(2)} e_{00}^x e_{10} + A_{30}^{(2)} e_{00}^x e_{30} + A_{50}^{(2)} e_{00}^x e_{50} \right\} \quad ; \hspace{1cm} \text{AV.37}$$

we need only $A_{10}^{(2)}(L), A_{30}^{(2)}(L)$ and $A_{50}^{(2)}$.

$\otimes$ Note :
$$\left\{ f(z) \right\}_{z=b}^{z=a} = f(a) - f(b)$$

We find:

$$A_{10}^{(2)}(L) = - i(k_o^2 n_2 w_o^3 L^2/32)\left\{ \mathcal{L}[(8\eta_1/3)+(n_3 w_o^2/8)(6+ \frac{4}{5}\mathcal{L}^2)] \right.$$

$$\left. -i[6\eta_1(1+ \frac{\mathcal{L}^2}{9})+(n_3 w_o^2/8)(10+ \frac{2}{3}\mathcal{L}^4)] \right\};$$

$$A_{30}^{(2)}(L) = - i(k_o^2 n_2 w_o^3 L^2/(32\ 6^{1/2}))(n_3 w_o^2/8)\left\{4\ \mathcal{L}\ (5 - \frac{\mathcal{L}^4}{21}) \right.$$

$$\left. + 8\ i\ (- 5 + \frac{4}{3}\mathcal{L}^2 + \frac{\mathcal{L}^4}{3})\right\}$$

$$- (k_o^2 n_2 w_o^3 L^2/(32\ 6^{1/2}))(12\eta_1)(1 - \frac{\mathcal{L}^2}{3}) \qquad ;$$

$$A_{50}^{(2)}(L) = - i(10/3)^{1/2}(k_o^2 n_2 n_3 w_o^5 L^2/128)\left\{\frac{2\ \mathcal{L}^5}{21} - 2i(1-\frac{4}{3}\mathcal{L}^2 + \frac{\mathcal{L}^4}{3})\right\};$$

AV.38

where:

$$\mathcal{L} = (L/2z_o) \qquad ; \qquad\qquad \text{AV.39}$$

AV.d   Digression

        While the influence of higher order derivatives
of the refractive index on the schlieren signal is rather
difficult to interpret, the behaviour of the center of gravity
$\bar{x}$ of the light beam is quite simple.

In analogy to the theorem of **Ehrenfest** we can write(Marcuse 72):

$$(d^2\bar{x}/dz^2) = \frac{1}{2}\left(\overline{\frac{\partial}{\partial x}(k/k_o)^2}\right) \quad ; \quad \text{AV.40}$$

where the average of a scalar F is given by:

$$\bar{F} = \left(\int_{-\infty}^{\infty}\int_{-\infty}^{\infty} F\, I\, dxdy\right)\Big/\left(\int_{-\infty}^{\infty}\int_{-\infty}^{\infty} I\, dxdy\right) \; ; \quad \text{AV.41}$$

Equation AV.40 can also be **written as** :

$$(d^2\bar{x}/dz^2) = \frac{1}{2}\left(\frac{\partial}{\partial x}(k/k_o)^2\right)_{x=\bar{x}}$$

$$+ \frac{1}{2}\left\{ \sum_{j=1}^{\infty} \overline{\frac{x^{j-1}-(\bar{x})^{j-1}}{(j-1)!}}\left(\frac{\partial^j}{\partial x^j}(k/k_o)^2\right)_{x=0}\right\}; \; \text{AV.42}$$

In first approximation we obtain:

$$(d\bar{x}/dz)_{z\geqslant L} = (dx_r/d_z)_{z=L} + \sum_{j=1}^{\infty} \frac{n_{2j+1}}{2^{3j-1}(j-1)!} \int_0^L w^{2j}dz ; \text{AV.43}$$

The simplicity of those expressions makes the direct
measurement of $\bar{x}$ rather attractive. This could be done **by
means of** a diode-array as detection system.

Equation AV.43 was used as a check for the calculations
presented in the previous section.

TECHNICAL DATA

Shock tube I

A sketch of shock tube I is given in figure AVI.1 .

The pattern encarved in the diaphragm is shown in figure

AVI.2. Typical vacuum characteristics are:

$p_{oo} = 10^{-2}$Pa ; $(dp_o/dt) = 2 \times 10^{-3}$Pa s^{-1}.
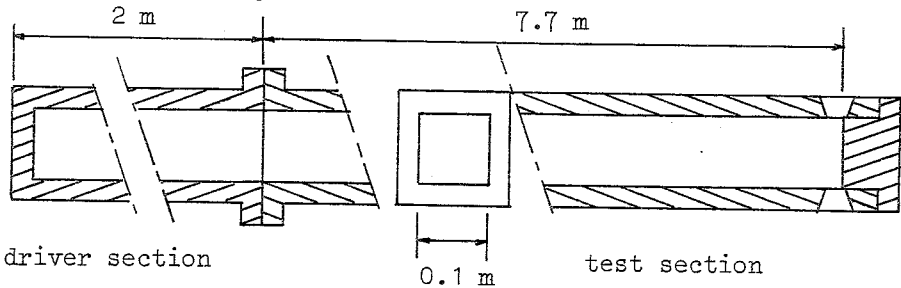
Figure AVI.1: Sketch of shock tube I.

Figure AVI.2:

Pattern encarved in diaphragm
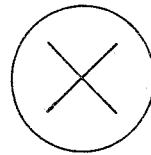
of shock tube I.

Shock tube II

A sketch of shock tube II is given in figure AVI.3.

The pattern encarved in the diaphragm is shown in figure

AVI.4. Typical vacuum characteristics are:

$p_{oo} = 10^{-4}$Pa ; $(dp_o/dt) = 10^{-4}$Pa s^{-1}.
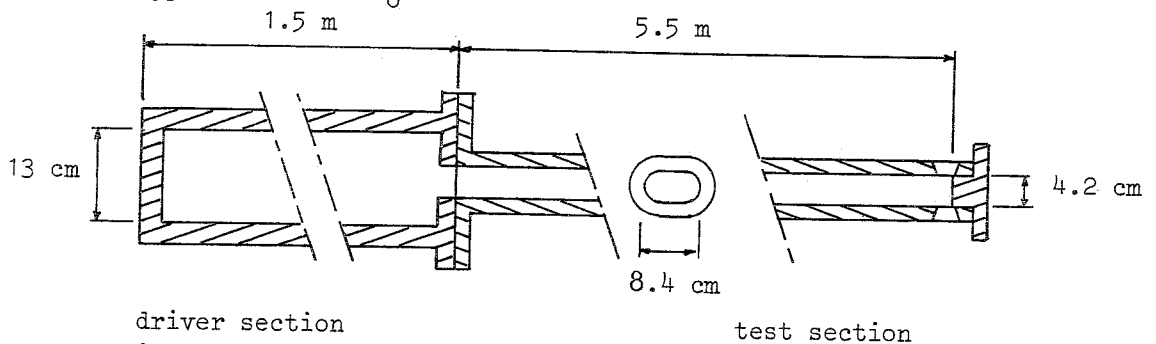
Figure AVI.3: Sketch of shock tube II.

Figure AVI.4:

Pattern encarved in diaphragm

of shock tube II.
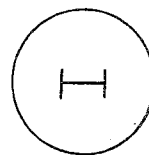
<u>Schlieren set-up:</u>

(shock tube I)

A sketch of the schlieren set-up of shock tube I is
given in figure AVI.5 . The set-up has been built as
compact as possible and is placed on a single optical
bench (which is mounted on rubber blocks). The light
beam before the test section is protected against air
turbulence by means of tubes. The fluctuations in the
position of the beam due to vibrations and air turbulence
were not more than 2×10^{-6}m. The long time drift in
the position appeared to be due to the thermal expansion
of the shock tube. No significant change of direction
was observed for a period of 2×10^{6} s.

laser: Spectra Physics (H_e-N_e) type 120.

lenses: $f_1 = 12$ cm

$f_2 = 30$ cm

orientable

table: see figure AVI.6

detection: see figure AVI.9
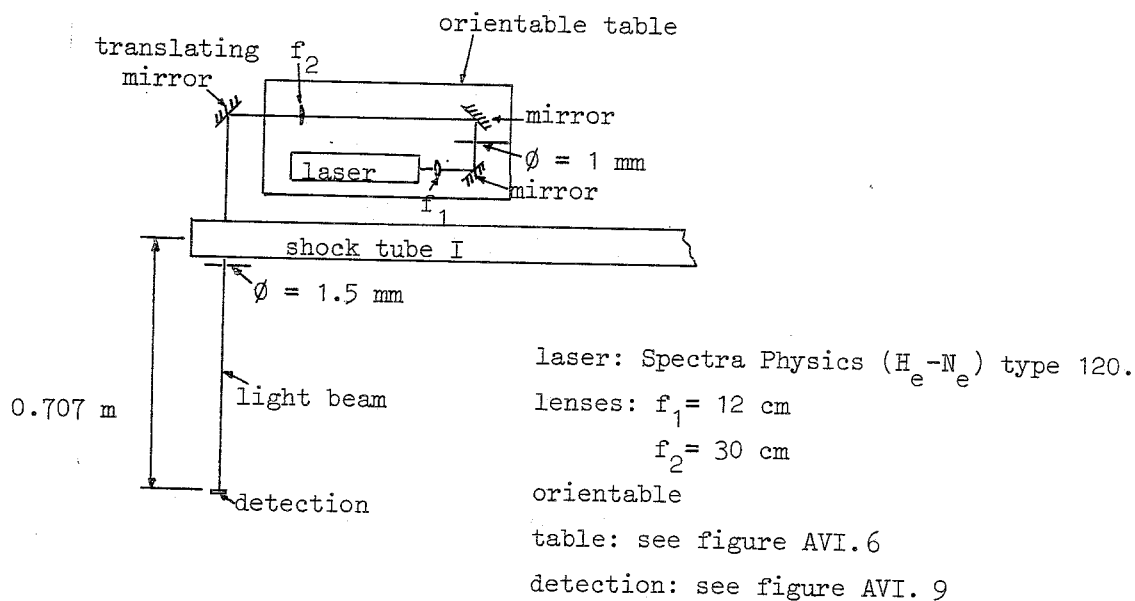
<u>Figure AVI.5:</u>

Laser schlieren set-up of shock tube I.

We now consider step-wise the most important parts of
the set-up.

Adjustment of the laser beam configuration:

The laser beam configuration is determined by the direction
of propagation, the position of the waist and the magnitude
of the waist(chapter VI). The set-up(figure AVI.5) was
designed in order to make it possible to adjust the various
parameters independently. The laser(Spectra Physics He-Ne
type 120) is mounted together with a telescope on an
orientable plate[&]. This plate is supported by three vertical
micrometers(vm) with free rolling balls mounted at the tips
(figure AVI.6). Two of the balls (b) can move freely in a
plane. The movement of the third is restricted to a line(l)
in this plane.
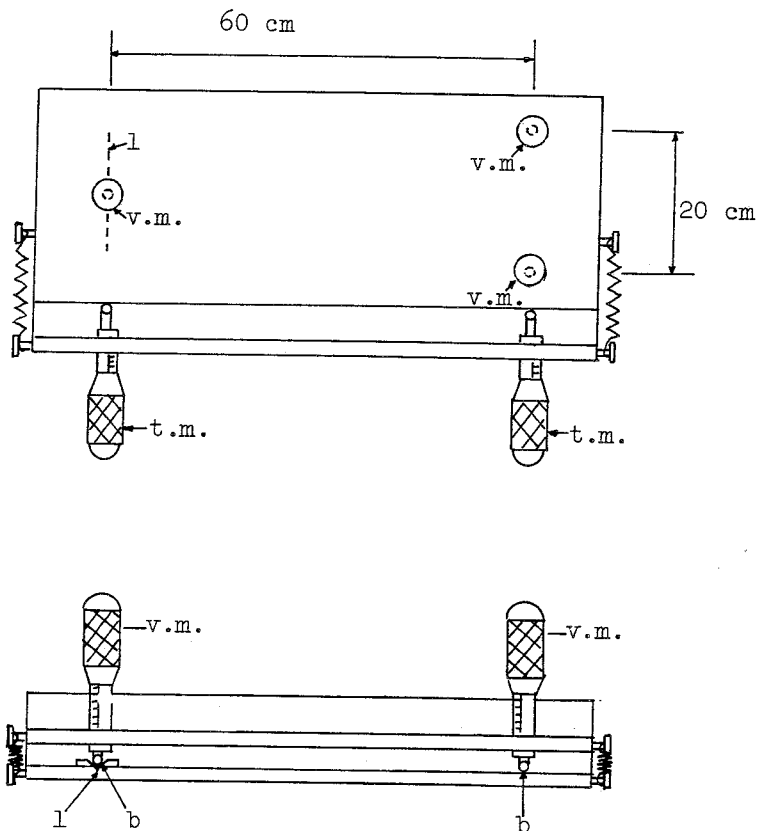
Figure AVI.6: Orientable table.

& Note: Design of laboratory for length measurements
and laboratory for atomic physics (THE).

The two transversal micrometers (tm) are used for translation and rotation of the light beam. Combining this to the translation by means of the translating mirror (see figure AVI.5) we can adjust both the distance to the wall and the position of the waist in the test section.

The first lens f_1 (f = 12 cm) is used to make an "object" waist which has approximately the dimension w_{op} (equation VI.39). The second lens f_2 (f = 30 cm) makes an "image" waist in the test section. Because the image and object distances with respect to f_2 are approximately equal, a translation of f_2 along the beam axis will change the magnitude of the "image" waist without changing its position.

Distance to the wall:

The position of the median x_m of the beam (equation VI.14) is determined by the interception of half of the beam power by means of knife edges mounted on both sides of the test section (figure AVI.7).

Spring blades:
thickness 0.2 mm
surface 70 cm^2

knife

test section

light beam

5 cm

ball bearing

micrometer
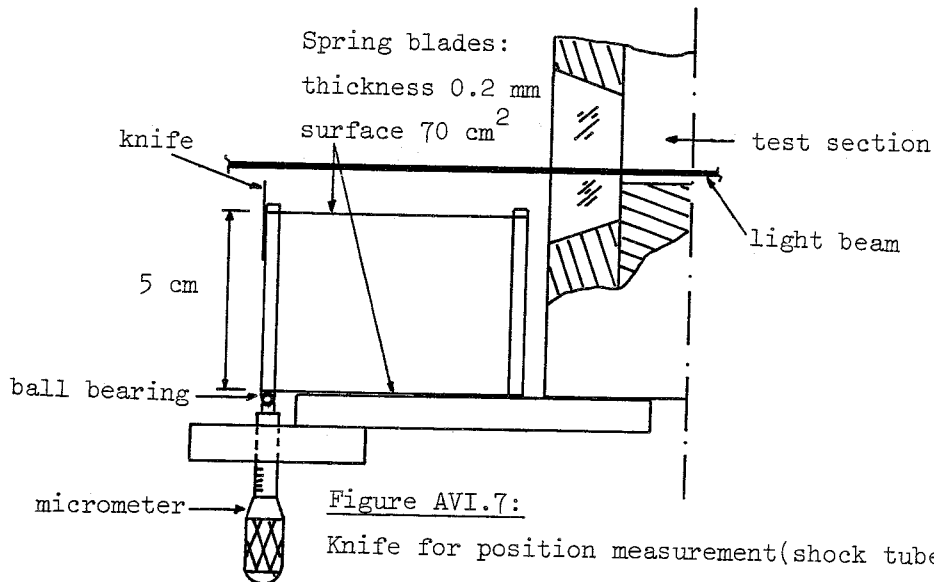
Figure AVI.7:
Knife for position measurement (shock tube II).

221

The system was calibrated by means of a magnetic knife
edge (calibration knife) placed on the end-wall
as shown in figure AVI.8.

incident beam   transmitted beam

_ _ _ _ _ _ _ _ _ _ _ _ _ _ _

                                          wall

∕∕∕∕∕∕∕∕∕∕∕∕∕∕∕∕∕∕∕∕∕∕∕∕∕∕∕∕
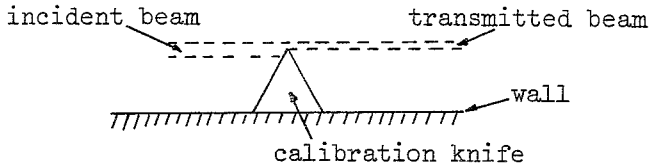
              calibration knife

Figure AVI.8:Calibration of the measurement of x_m
by means of a knife edge attached magnetically to
the end-wall.

The height of the calibration knife was measured within
2×10^{-6}m (Carl Zeiss Universal Messmikroskop 3117).
This uncertainty was reduced to about 10^{-6}m by means of
five different calibration knifes.

        The reproducibility in the measurement of
x_m was 2×10^{-6}m which corresponds to the micro-meter
reading uncertainty. Additional uncertainties in the
position of the beam are:
- 3 μm due to the quality of the end-wall surface,
- 3 μm due to the measurements of the transmitted power,
- 2 μm due to air turbulence and vibrations,
- 2 μm due to the uncertainty in the measurement of the
position of the shock tube during the experiment.
The total uncertainty is estimated to be of the order of
6 μm . Experiments with two wavelengths (chapter VIII)
showed that this can be considered as an upper bound.

<u>Shape of the beam</u>:

In chapter VI we obtained formulas (equations VI.34
and 35) for the schlieren signal in the case of a
gaussian beam. No significant deviation of the
gaussian beam shape was observed.

The beam shape was determined before each
experiment by a measurement of the total beam power and
$(dS_{cal}/dx_d)_{x=x_{mo}}$.
$(dS_{cal}/dx_d)_{x=x_{mo}}$ was calculated from 10 measurements
of S_{cal} as function of x_d by means of linear regression.
Typical determination coefficient was $r^2 = 0.99985$.

<u>Detection system</u>:

The detection system used is similar to the system
described by Diebold(74). The electronic scheme is
given in figure AVI.9.
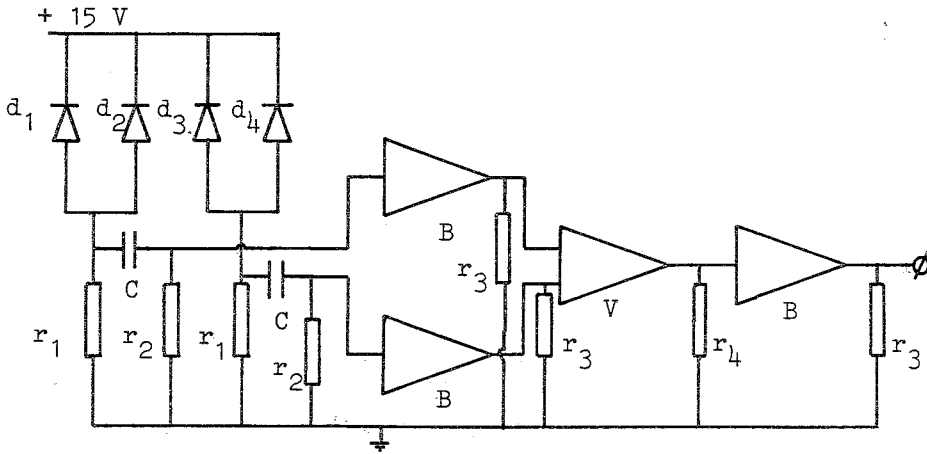
<u>Figure AVI.9</u>:Detection system shock tube I ($1 = 6.328 \times 10^{-7}$m)

d_1, d_2, d_3, d_4 quadrants of UDT 8 diode

$C = 10^{-7}$F

$r_1 = 10^3 \; \Omega \quad ; r_2 = 10^6 \; \Omega$

$r_3 = 10^2 \; \Omega \quad ; r_4 = 10^3 \; \Omega$

B   buffer LH 0033 CG

V   differential amplifier µA 733

<u>Registration</u>:

The signals were recorded by Biomation type 805 digital
memories (DC mode).Graphs of the signals were obtained
by means of a Houston instr. Omnigraphic (X,Y) recorder
type 6. The electronic set-up including recording and
detection systems was calibrated by means of a HP oscillator
type 615B. The amplitude of the sine was measured by a
Fluke universal voltmeter type 8000 A. The procedure
was checked against a Philips electronic reference unit
type PT 2248. The period of the sine was measured with
a HP counter type 5345 A. This calibration procedure
was carried out for frequencies between 50 Hz and 20 kHz
and for various amplitudes. In addition the response
of the system to a step function was checked. As a check
a calibration at 10 kHz was performed after each run.
The accuracy was mainly limited by the reading of the
graphs (2% for S and 0.5% for time).

<u>Schlieren set-up</u>:

(shock-tube II)

The schlieren set-up of shock tube II is shown in figure
VIII.12 . It is similar to the system of shock tube I,
described above, except for the detection systems.
The detection system for $l_1 = 6.328 \times 10^{-7}$m was modified
in order to make absorption measurements possible.
The influence of fluctuations in the intensity of the
laser beam were reduced by comparison of the transmitted
beam power with the intensity of a reference beam.
The two upper quadrants of the UDT 8 diode were used
for the measurements of the schlieren signal and of
the transmitted beam power. The influence of radiation
emitted by the plasma on the power measurement was
compensated by means of the signal measured by the two
lower quadrants of the diode.

The sensitivity of the absorption measurement was limited by the electronic noise (minimum : $K_{min}= 5\times10^{-2}m^{-1}$) and by the quality of the windows. After about 10 runs aluminum dust from the diaphragms may significantly influence the absorption signals for x_m smaller than 0.6 mm. For this reason some of the data obtained are not included in figures VIII.15 & 22.

The detection system for $l_2= 1.152 \times 10^{-6}m$ is shown in figure AVI.10. &
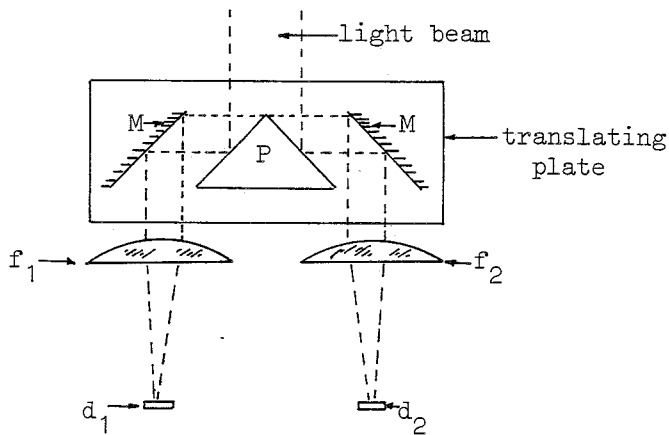
Figure AVI.10: Infrared detection system(l_2).

The reflecting prism(P) splits the beam into two parts. The mirrors(M) at both sides of the prism are placed together with the prism on a translating plate. The lenses (f_1 and f_2) and the diodes (d_1 and d_2) are fixed to the optical bench. A translation of the prism, for the calibration of the schlieren system, will change the ratio of the powers of the beams without affecting the position of the images on the photo-diodes(the optical path lengths do not change).

& Note: Design S.Bruinsma.

In a similar way when the diodes are placed at the
images of the center of the test section, a deflection
of the beam in the test section will not strongly
affect the position of the light spots on the diodes.
However better results are obtained when the diodes
are placed slightly out of the image points (out of
focus). In such a way one avoids the complications
due to the variations in the sensitivity of the
surface of the diodes. The diodes used are germanium
photodiodes (Rofin model 7460 Ge).

NOMENCLATURE [Ω]

LATIN
_____

a   thermal diffusivity ($a = \lambda/(\rho \, c_p)$)

A_j coefficient

b_o Landau length ($b_o = c^2/(8 \, \pi \, \varepsilon_o k \, T_e)$)

c   velocity of sound ($c^2 = \gamma \, R \, T$)

c   velocity of light ($c = 2.998 \times 10^8$ m s^{-1})

c_p specific heat capacity at constant pressure

c_v specific heat capacity at constant volume

c_w specific heat capacity of the wall material

D_{ia} ion-atom binary diffusion coefficient (appendix III)

e   elementary charge ($e = 1.602 \times 10^{-19}$C)

$\underline{e}$,e   amplitude electric field (equation VI.1)

$\underline{E}$,E   electric field

e_{ij} equilibrium

f   focal distance

f(Z)   solution of thermal Rayleigh problem ($\bar{\rho} = f(Z)$)
$f^{(j)}(Z) = (d^j f/dZ^j)$

F(S)   solution of the thermal Rayleigh problem ($\bar{\rho} = F(S)$)
$F^{(j)}(S) = (d^j F/dS^j)$

g(Z)   solution of the simplified thermal Rayleigh problem
          (section III.c)

h   specific enthalpy

$\underline{h}$,h   amplitude of the magnetic field (equation V.1)

$\underline{H}$,H   magnetic field

h_p Planck constant ($h_p = 6.626 \times 10^{-34}$J s)

$\underline{I}$,I   average energy flux density (equations VI.5 and 6)

[Ω] Notes :
  1. Symbols used in the appendices only are not included in this list.
  2. Some of the symbols have been used for different quantities.
     The context should avoid confusion.

k	Boltzmann constant ($k = 1.3807 \times 10^{-23}$ J K^{-1})
k	wave number (equation VI.3)
k_o	wave number at the origin
K	absorption coefficient (equation V.1)
K_o	reference absorption coefficient (equation V.2)
K	Gladstone-Dale coefficient (equation VII.5)
k_{H-Ar}	reaction rate for excitation of hydrogen atoms by collisions with argon atoms (equation VIII.1)
l	wavelength
L	width of the test section (shock tube I: L = 10 cm; shock tube II: L = 4.2 cm)
L_w	thickness of the windows (L_w = 2 cm)
Le	Lewis number (equation V.21)
m_j	mass of particle j (j = e, i, a or h)
M_i	ion mass production source term
M_s	Mach number of the incident shock wave ($M_s = v_s/c_1$)
$(M_s)_1$	Mach number measured over the traject $x_1 \rightarrow x_2$ (table VII.1)
$(M_s)_2$	additional Mach number (section VII.c)
n	total particle density ($n = n_e + n_i + n_a$)
N	refractive index (N = k c/ω)
N_j	$= (d^j N/dx^j)$
N_w	refractive index of the windows
n_j	particle density of species j (j = e, i, a or h)
n_o	reference particle density (equation V.2)
n_o	particle density of the atoms in ground level
n'_j	$= (dn_j/dx)$
$\dot{n}_j$	rate of production of particles j per volume
p	pressure ($p = p_e + p_i + p_a$)
p_j	partial pressure of species j (j = e, i, a of h)
P	power flux of the light beam
P_i	ion momentum source term (equation IV.5)
P_j	polarizability of species j (equation VI.44)
p_o	partical pressure of impurities
p_{oo}	pressure after evacuation of the test section
q	heat flux density
q_w	heat flux density at the wall

q_{ref} reference heat flux (equation V.27)

Q_c contiuum contribution to the transparent radiation loss

Q_r transparent radiation loss (section IV.b)

$Q_{ij}^{(1,s)}$ thermally averaged cross section for elastic collisions between particles i and j (appendix V)

$\underline{r}$ position vector ($\underline{r}$ = (x, y, z))

r_D Debye length ($r_D^2 = \varepsilon_o k \, T/(e^2 n_e)$)

re   relaxation

R   specific gas constant ($R = k/m_a$)

s   optical path length (equation V.1)

S   similarity coordinate ($S = x/(a_R t)^{1/2}$)

S   schlieren signal (equation VI.17)

$_o S^1$ reaction rate for excitation of atoms from ground level o to level 1 by collisions with electrons (appendix IV)

t   time

T   temperature

t_∞ reference time ($t_\infty = 10^{-4}$ s)

$\hat{t}$ normalized stretched time (equation III.62)

T_o reference temperature (equation V.2)

T_{ion} ionization temperature (argon: $T_{ion} = 1.83 \times 10^5$ K)

T_{ex} excitation temperature (argon: $T_{ex} = 1.35 \times 10^5$ K)

$\underline{u}$,u   convective velocity, (mass averaged velocity)

V   ambipolar diffusion velocity (equation IV.19)

V_j diffusion velocity of species j (equation IV.14)

v_j velocity of particle j

V(r)   intermolecular potential

v_s incident shock velocity

v_r reflected shock velocity

W   radius of the gaussian beam $W^2 = w_o^2 (1 + (\dfrac{z - z_w}{z_o})^2)$

w_o waist of the gaussian beam (minimum of W)

w_{op} optimal waist corresponding to a minimum of deformation of the beam (equation VI.39)

w_{min} waist corresponding to the minimum value of the beam radius at the windows of the test section (equation VI.37)

x	distance to the end-wall (figure VI.1)
x_m	midian of the light beam (equation VI.14)
x_r	position of light ray (equation VI.13)
x_∞	reference length scale (equation IV.18)
y	coordinate parallel to end-wall
z	distance along the axis of the undisturbed light beam (figure VI.1)
z_w	position of the waist of the light beam
z_d	position of the detection system
z_o	Rayleigh length ($z_o = k\, w_o^2/2$)
Z	similarity coordinate ($Z = \eta\ /(\eta_R (a_R t)^{1/2})$)
Z_o	coefficient (equation III.54)
Z_j	statistical weight of component j (j = e, i, a)

GREEK

α degree of ionization ($\alpha = n_e/n_h$)

δ_o coefficient in equation III.51

ΔX experimental uncertainty in X, or $X-X_{ref}$

ΔT_{ion} lowering ionization temperature (equation V.9)

$\Delta \Phi$ sheath potential (V.18)

∂z_d correction of z_d for the windows (equation VI.15)

ε electric permittivity

ε_e energy source term in the electron energy equation (IV.23)

ε_{eh} energy source term resulting from the electron-heavy particles elastic collisions (IV.24)

ε_t total energy source term (IV.22)

γ $= c_p/c_v$

Γ sensitivity of the schlieren system (IV.40)

η Lagrangian coordinate (III.3)

η_j $= \dfrac{1}{2\, N^2(x_{mo})} \, (d^j N^2/dx^j)_{x=x_{mo}}$

ζ Biberman factor (section VIII.b)

λ heat conductivity

λ_j^m heat conductivity of species j in the mixture (appendix II)

λ_r radiative heat conductivity (IV.25)

λ_e $= \lambda_e^m$

λ_h $= \lambda_a^m + \lambda_i^m$

μ magnetic permeability

ν $= (d\lambda/dT)/(\lambda/T)$

ρ density (mass)

ρ_e charge density

σ electric conductivity

Σ phase (equation VI.1)

τ stretched time (III.47)

τ_{col} mean free flight time

SUBSCRIPTS

a	atom
Ar	argon
c	continuum
cal	calibration
d	detection
D	Debye
e	electron
eq	equilibrium
ex	excitation
fr	frozen
h	heavy
H	Hydrogen
i	ion
ion	ionization
j	j = e, i, a or h
m	median
min	minimum
max	maximum
o	origin, reference, vacuum
op	optimal
p	constant pressure
r	radiative
r	reflected
r	light ray
re	relaxation
ref	reference
R	reference
RH	Rankine-Hugoniot
s	incident
saha	Saha equation
st	stationary
t	total
th	theoretical

test	test time
v	constant volume
w	waist
w	wall
∞	outside the boundary layer, reference
$(\_)$	vector

1,2,3,4,5 regions 1,2,3,4 and 5 (figure II.2)

SUPERSCRIPTS

$'$	first order derivative
(j)	derivative of order j
$-$	reduced
$\hat{}$	reduced
$-$	averaged
m	in the mixture

NOTE:

SI units are used.

REFERENCES.

Alpher, R.A. and White, D.R.,
        J.Fluid Mech., 3 (1958) 457;
        "Optical Interferometry" in "Plasma diagnostic
        techniques" ed. Huddlestone, R.H. and Leonard, S.L.,
        Academic Press (1965) NY;

Ali, A.W. and Griem, H.R.,
        Phys.Rev., 140 (1965) A 1044;

Arnaud, J.A.
        "Hamiltonian theory of beam mode propagation"
        Progress in Optics XI, ed. Wolf, E.,
        North Holland (1973) Amsterdam;

Asinovsky, E.I., Kirillin, A.V., Pakhomov, E.P. and Shubashov, V.I.
        Proc. IEEE, 59 (1971) 592;

Aziz, R.A. and Chen, H.H.,
        J.Chem.Physics, 67 (1977) 5719;

Aziz, R.A.
        Private communication (1980);

Bacri, J. and Gomes, A.M.,
        J. Phys.D:Appl.Phys., 10 (1977) 2165;
        J. Phys.D:Appl.Phys., 11 (1978) 2185;

Baganoff, D.
        J.Fluid Mech., 23 (1965) 209;

Baryshinkov, A.S. and Skvortsov, G.E.,
        Sov.Phys.Tech.Phys., 49 (1979) 1401;

Batenin, V.M. and Minaev, P.V.,
        J.Quant. Spectrosc.Radiat. Transfer, 18 (1977) 171;

Bates, D.R.,
        J.Phys.B:Atom.Molec.Phys., 13 (1980) L51;

Baum, D., Hackmann, J., and Uhlenbusch, J.,
        Plasma Physics, 17 (1975) 79;

Bengtson, R.D., Miller, M.H., Koopman, D.W. and Wilkerson, T.D.,
        Phys. Fluids, 13 (1970) 372;

Biberman, L.M., Yakubov, I.T. and Vorob'ev, V.S.,
        Proceedings of I.EEE, 59 (1971) 555;

Boer, P.C.T. and Miller, J.A.,
        Proc. 10th Int.Symp. Mod.Dev.Shock tube Research, (1975)
        Kyoto;

Bohm, D.,
        In "Characteristics of Electrical Discharges in Magnetic
        Fields", ed. Cuthrie, A. and Wakerling, R.K.,
        McGraw-Hill (1949);

Born, M. and Wolf, E.,
        "Principles of Optics" Fifth edition, Pergamon Press (1975)
        Oxford;

234

Bristow, N.F.P.,
    UTIAS rep. 158 (1971);

Bunting, J.O. and Devoto, R.S.,
    SUDAAR No. 313 (1967);

Capitelli, M.,
    Z.Naturforsch., $\underline{27a}$ (1972) 809;

Carslaw, H.S. and Jager, J.C.,
    "Operational methos in applied mathematics"
    Dover Publications (1963) NY; republication of
    Oxford University Press (1948);

Carsperson, L.W.,
    Applied Optics, $\underline{12}$ (1973) 2434;
    J.Opt.Soc.Am., $\underline{66}$ (1976) 1373;

Chapman, S., Cowling, T.G. and Burnett, D.,
    "The mathematical theory of non-uniform gases",
    Cambridge Univ.Press (1970);

Chen, F.F.,
    "Plasma Diagnostic Techniques", ed. Huddlestone, R.H.
    and Leonard, S.L., Academic Press (1965);

Chen, S.H.P. and Saxena, S.C.,
    Molecular Physics, $\underline{29}$ (1975) 455;

Clarke, J.F.,
    Proc. Royal Soc., $\underline{299}$ (1967) 221;

Courant, R.,
    "Methods of mathematical physics" Vol. II,
    Intersciene publ. (1962) NY;

Crespo-Martinez, A.
    Ph.D. Thesis, Part I, Cal. Inst.Techn. (1968);

Daybelge, U.,
    Jour.Appl.Phys., $\underline{41}$ (1970) 2130;

Desai, S.V. and Corcoran, W.H.,
    J.Quant.Spectrosc.Radiat.Transfer, $\underline{9}$ (1969) 1371;

Devoto, R.S., Phys.Fluids, $\underline{9}$ (1966)
    Phys.Fluids, $\underline{10}$ (1967) 354;
    Phys.Fluids, $\underline{10}$ (1967) 2105;
    Phys.Fluids, $\underline{10}$ (1967) 2705;
    Phys.Fluids, $\underline{16}$ (1973) 616;

Diebold, G. and Santoro, R.,
    Rev.Sci.Instrum., $\underline{45}$ (1974) 773;

Dixon, A.J., Harrison, M.F.A. and Smith, A.C.H.,
    in "Electronic and atomic collisions",
    ed. Cobic, B.C. and Kupera, M.V. (1973) Belgrado;

Dongen, M.E.H. van, Gils, J.F.M. van, Willems, J.F.H. and Vossers, G.,
    in Proc.10th Int.Shock Tube Symp. (1975) Kyoto;

Dongen, M.E.H. van,
    A.I.A.A. J., $\underline{15}$ (1977) 1210;
    Ph.D. thesis T.H. Eindhoven (1978);

Drawin, H.W.,
>   Z.Physik, $\underline{225}$ (1969) 470;
>   "Thermodynamic properties of the equilibrium and
>   non-equilibrium states of plasmas", in "Reactions
>   under plasma condition", ed. Venugopalan Wiley and
>   Sons (1971);

Drawin, H.W. and Emard, F.,
>   Beitrage aus der Plasmaphysik, $\underline{13}$ (1973) 143;
>   Beit. Plasmaphysik, $\underline{15}$ (1975) 273;

Ellis, H.W., Pai, R.Y., McDaniel, E.W., Mason, E.A. and Viehland, L.A.,
>   Atomic Data, $\underline{17}$ (1976) 177;

Emmons, H.W.
>   Phys. Fluids, $\underline{10}$ (1967) 1125;

Enomoto, Y.,
>   J.Phys.Soc.Japan, $\underline{35}$ (1973) 1228;

Erhardt, K., Meyer, I. and Stritzke, P.,
>   Z.Naturforsch., $\underline{32a}$ (1977) 21;

Ewald, R. and Grönig, H.,
>   AIAA J., $\underline{9}$ (1971) 946;

Ezumi, H.,
>   J.Phys.Soc. Japan, $\underline{46}$ (1979) 1366;

Fay, J.A.,
>   Avco-Everett, Rep. AMP 71 (1962);

Frost, L.S. and Phelps, A.V.,
>   Phys.Rev., $\underline{136}$ (1964) A 1538;

Fox, J.N. and Hobson, R.M.,
>   Phys.Rev.Letters, $\underline{17}$ (1966) 161;

Frohn, A. and Boer, P.C.T. de,
>   Shock tube symposium, Phys.Fluids Sup I (1969) 54;

Gaucherel, P. and Rowe, B.,
>   Int. J.Mass Spectrometry Ion Phys., $\underline{25}$ (1977) 211;

Glass, I.I. and Liu, W.S.,
>   J.Fluid Mech., $\underline{84}$ (1978) 55;

Glasser, J. and Chapelle, J.,
>   Plasma Physics, $\underline{21}$ (1979) 477;

Goldbach, C., Nollez, G. and Plomdeur, P.,
>   J.Phys.B:Atom.Molec.Phys., $\underline{10}$ (1977) 1181;

Groot, J.J. de, Kestin, J. and Sookiazian, H.,
>   Physica, $\underline{75}$ (1974) 454;

Haarman, J.W.,
>   Physica, $\underline{52}$ (1971) 605;
>   AIP Conf.Proc., $\underline{11}$ (1973) 193;

Hanson, R.K.,
>   Phys.Fluids, $\underline{16}$ (1973) 369;

Hashiguchi, S. and Inutake, M.,
        Journal de Physique, Colloque C7, Sup.au n°7, $\underline{40}$ (1979)
        C7-681;

Hinnov, E. and Hirschberg, J.G.,
        Phys.Rev., $\underline{125}$ (1962) 795;

Hirschberg, A., Heugten, W.H.H. van, Willems, J.F.H. and Dongen,
        M.E.H. van,
        Int. J. Heat Mass Transfer, $\underline{23}$ (1980) 799;

Hoffert, M.I. and Lien, M.,
        Phys. Fluids, $\underline{10}$ (1967) 1769;

Hofsaess, D.,
        J.Quant.Spectrosc.Radiat.Transfer, $\underline{19}$ (1978) 339;

Honda, T. and Kanzawa, A.,
        Heat Transfer Japanese Research, $\underline{6}$ (1977) 78;

Horn, K.P.,
        SUDAAR 268 (1966);

Hutten-Mansfeld, A.C.B.,
        PhD thesis, TH Eindhoven (1976);

Igra, O.,
        Prog.Aerospace Sci., $\underline{16}$ (1975) 299;
        Phys.Fluids, $\underline{23}$ (1980) 1513;

Igra, O. and Barcessat, M.,
        Phys.Fluids, $\underline{20}$ (1977) 1449;

Irons, F.E.,
        J.Quant.Spectrosc.Radiat.Transfer, $\underline{22}$ (1979) 1;

Itikawa, Y.,
        J.Phys.Soc.Japan, $\underline{18}$ (1963) 1499;

Jacob, J.H. and Mangano, J.A.,
        Appl.Phys.Letters, $\underline{29}$ (1976) 466;

Jaffrin, M.Y.,
        Phys.Fluids, $\underline{8}$ (1965) 606;

Jain, P.C.,
        J.Phys.D:Appl.Phys., $\underline{13}$ (1980) 29;

Jongen, P.H.M.,
        PhD thesis, TH Eindhoven (1976);

Katsonis, K.,
        Thèse Univ. Paris Sud, Centre d'Orsay (1976);

Kestin, J., R, S.T. and Wakeham, W.A.,
        J.Chem.Phys., $\underline{56}$ (1972) 4119;

Kiefer, J.H. and Lutz, R.W.,
        J.Chem.Physics, $\underline{44}$ (1966) 658;
        Proceedings:Shock tube and Waves, 12th Symposium (1979)
        Jerusalem;

Kieffer, L.J. and Dunn, G.H.,
        Rev.Mod.Phys., $\underline{38}$ (1966) 1;

Kimura, A., Teshima, K. and Nishida, M.,
   Kyoto Univ. Current Papers CP 37 (1973);

Kimura, A., Minomo, M. and Nishida, M.,
   Proc. 11th Int.Symp.Rarefied Gas Dynamics (1978) Cannes;

Knöös, S.P.,
   J.Plasma Physics, 2 (1968) 207;

Kogelnik, H.,
   Bell System Techn.Journ., 44 (1965) 455;

Kon'kov, A.A. and Kulagin, S.G.
   High temperature, 11 (1973) 945;
   High temperature, 12 (1974) 426;

Kon'kov, A.A. and Il'metov, A.V.,
   J.Engin.Physics, 28 (1975) 451;

Kon'kov, A.A. and Sokolov, A.I.,
   High temperature, 14 (1976) 833;

Kopainsky, J.,
   Z.Physik, 248 (1971) 405;
   Z.Physik, 248 (1971) 417;

Kruger, C.H., Mitchner, M. and Daybelge, U.,
   AIAA Jour., 6 (1968) 1712;

Kuiper, R.,
   SUDAAR n°353 (1968);

Landau, L. and Lifchitz, E.,
   "Electrodynamique des milieux continus", Editions MIR
   (1969) Moscou;
   "Mécaniques des fluides", Editions MIR (1971) Moscou;

Lauver, M.R.,
   Phys.Fluids, 7 (1964) 611;

Leclair, J. and Schram, D.C.,
   Proceedings:Phen.ion.gases (1977) Berlin;

Liu, W.S., Whitten, B.T. and Glass, I.I.,
   J.Fluid Mech., 87 (1978) 609;

Liu, W.S. and Glass, I.I.,
   J.Fluid Mech., 91 (1979) 679;

Liu, W.S., Takayama, K. and Glass, I.I.,
   J.Fluid Mech, 97 (1980) 513;

Logan, P.F., Stalker, R.J. and McIntosch, M.K.,
   J.Phys.D:Appl.Phys., 10 (1977) 323;

Luchina, A.A.,
   Phys.Fluids, 21 (1978) 1923;

Marcatili, E.A.J.,
   The Bell sys.tech.Jour., (1967) 149;

Marcuse, D.,
   "Light transmission optics", Bell lab.Series, van Nostran
   (1972) NY;

Massey, H.S.W. and Gilbody, H.B.,
         "Electronic and impact phenomena" vol IV.
         At the Clarendon Press (1974) Oxford;

McLaren, T.I. and Hobson, R.M.,
         Phys.Fluids, 11 (1968) 2162;

Meldau, H.,
         Ph.D. thesis, R.W.T.H., Aachen (1977);

Mirels, H.,
         Phys.Fluids, 9 (1966) 1907;

Mitchner, M. and Kruger, C.H. Jr.,
         "Partially ionized gases", J.Wiley and Sons (1973) NY;

Mondt, J.,
         Ph.D. thesis, TH Eindhoven (1977);

Nieto de Castro, C.A. and Wakeham, W.A.,
         Proceedings:Thermal heat conductivity, plenum Press (1978);

Nishida, M.,
         J.Applied Math.Phys. (ZAMP), 28 (1977) 265;

Oertel, H.,
         in "Chocs et ondes de choc", Tome II, ed.Jaumotte A.L.,
         Masson et C^{le} (1973) Paris;

Peck, E.R. and Fisher, D.J.,
         J.Opt.Soc.Am., 54 (1964) 1362;

Piva, H.O. and Sturtevant, B.,
         in:Proc. 6th Int.Symp.Rarefied Gas Dyn., ed. Trilling, L.
         and Wachman, H.Y., vol.II (1969);

Pratesi, R. and Ronchi, L.,
         J.Opt.Soc.Am., 67 (1977) 1274;

Rainville, E.D.,
         "Special functions", Chelsea publ.Comp. (1960) NY;

Reese, T.,
         in:Proc. 11th Int.Symp. Shock tube and Shock Waves Research.,
         (1977) Seattle;

Rosado, R.J., Schram, D.C. and Leclair, J.,
         in: Proc. Int.Symp.Phen.ion.gases, (1979) Grenoble;

Saxena, S.C.,
         High temperature science, 4 (1972) 517;

Schiff, L.I.,
         "Quantum mechanics", McGraw-Hill (1949) NY;

Schlüter, D.,
         Zeitschrift für Physik, 210 (1968) 80;
         J.Quant.Spectrosc.Radiat.Transfer, 23 (1980) 467;

Schneider, C.P. and Hahne, G.,
         in: Proc. 12th Int.Symp.Shock Tubes and Waves, (1979)
         Jerusalem;

Schram, P.P.J.M.,
         Private communication (1980);

Shashkov, A.G., Marchenkov, E.I. and Aleinikova, V.I.,
        in: "Thermal heat conductivity", Plenum Press (1978);

Smeets, G.,
        Z. Naturforschung, 20a (1965) 683;

Simpson, C.I.S.M. and Chandler, T.R.D.,
        Phys. Fluids, 10 (1967) 1894;

Smiley, E.F.,
        Ph.D. thesis, The Catholic Univ. of America,
        Washington DC (1957);

Smith, J.A.,
        Phys.Fluids, 11 (1968) 2150;

Spitzer, L. Jr. and Härm, R.,
        Phys. Rev., 89 (1953) 977;

Springer, G.S. and Wingeier, E.W.,
        J.Chem.Phys., 59 (1973) 2747;

Stupochenko, Ye., Losev, S.A. and Osipov, A.I.,
        "Relaxation in shock waves", Springer-Verlag (1967) Berlin;

Sturtevant, B. and Slachmuylders, E.,
        Phys.Fluids, 7 (1964) 1201;

Takano, Y., Shimomura, Y. and Akamatsu, T.,
        Proc. 11th Int.Symp.Shock tube and shock waves (1977)
        Seattle;

Takano, Y., Miyoshi, S. and Akamatsu, T.,
        Proc. 12th Int.Symp. Shock tube and Waves (1979) Jerusalem;

Takayama, K. and Liu, W.S.,
        UTIAS Rep.n° 233 (1979);

Teshima
        Proc. 12th Int.Symp.Shock tube and Waves (1979) Jerusalem;

Thor, H.J.,
        Ph.D. thesis, Technische Hochschule Aachen (1978);

Touloukian, Y.S., Liley, P.E. and Saxena, S.C.,
        TPRC Data Series on Thermophysical Properties of Matter,
        3, Plenum Press (1970);

Traving, G.,
        in "Plasma diagnostics", ed. Lochte-Holtgreven,
        North-Holland publ. (1968) Amsterdam;

Uhlenbusch, J.F. and Fischer, E.,
        Proceedings IEEE, 59 (1971) 578;

Vaguin, S.P., Yacobi, Yu.A., Yakovlov, V.V. and Soloukhin, R.I.,
        Revue de Physique Appliquée, 13 (1978) 399;

Vervisch, P., Terrier, M. and Valentin, P.,
        Le Journal de Physique, 38 (1977) 783;
        Le Journal de Physique, 40 (1979) 139;

Vincenti, W.G. and Kruger, Ch. Jr.,
        "Physical Gas Dynamics", J.Wiley and Sons (1965) NY;

Volkov, V.A., Titarov, S.I. and Tkachenko, B.K.,
          High temperature, 16 (1978) 342;

Vorob'ev, V.S.,
          High temperature, 16 (1978) 391;

Vrugt, P.J.,
          Ph.D. thesis, TH Eindhoven (1976);

Wiese, W.L., Smith, M.W. and Miles, B.M.,
          National Stand.Ref.Data.Ser., NSRDS-NBS 22, Nat.Bur. Stand
          (US) (1969);

Wilkerson, T.D. and Miller, M.H.,
          Proceedings IEEE, 59 (1971) 644;

Williams, R.H. and DeWitt, H.,
          Phys.Fluids, 12 (1968) 2326;

Wonnacott, T.H. and Wonnacott, R.J.,
          "Introductory statistics", Wiley int. (1972) NY;

Zeitoun, D. and Imbert, M.,
          AIAA Journal, 17 (1979) 821.

SAMENVATTING

Een procedure is uitgewerkt om de warmtegeleidings-
eigenschappen van éénatomige gassen te bepalen uit metingen van
de structuur van de instationaire thermische grenslaag aan de
eindwand van een schokbuis.

De grenslaagstructuur, bepaald met de laser-schlieren
methode, blijkt beschreven te kunnen worden met een gelijkvormig-
heidsparameter. Na een verbeterde analyse van de laser-schlieren
methode en met gebruik van nauwkeurige druk-metingen is de
warmtegeleidingscoefficient van argon tussen 1000 en 7000 K
bepaald met een nauwkeurigheid van 4% (de druk ligt tussen
3×10^4 en 10^5 Pa). Ten gevolg van de invloed van de zijwand-grens-
lagen en de vereenvoudigingen in de procedure voor de bepaling
van de toestand van het gas buiten de grenslaag, zijn er nog
systematische fouten van enkele procenten aanwezig.

In het geioniseerde geval is een model voor de grens-
laag ontwikkeling voorgesteld. De ionisatie- en thermische
relaxatie worden in het model beschreven. Metingen van de
electron- en atoomdichtheidsgradienten verkregen met behulp van
de laser schlieren methode komen, voor lage waarden van de ion-
isatie graad (3%), binnen 10% overeen met de theorie. Bij hogere
waarden van de ionisatie graad wordt de grenslaag structuur sterk
beinvloed door de stralingsafkoeling die in het model verwaar-
loosd is. Uit absorptie- en druk-metingen is quantitatieve
informatie over de stralingsafkoeling buiten de grenslaag
verkregen. Een aanzienlijke verbetering van de meetnauwkeurigheid
is noodzakelijk voordat quantitatieve informatie over de warmte-
geleidingseigenschappen van geioniseerde gassen op deze wijze
verkregen kan worden.

Uit aanvullende experimenten uitgevoerd aan een meng-
sel van 99.5% Ar + 0.5% H_2 is informatie verkregen over de invloed
van ionisatie relaxatie op de grenslaagstructuur en de ionisatie
snelheid van waterstof ten gevolg van botsingen met argon atomen.

242

LEVENSBERICHT

18-12-1949	geboren te Rehovot (Israël)
september 1966	toelatingsexamen Faculté Polytechnique de Mons (België)
oktober 1975	diploma Natuurkundig Ingenieur Technische Hogeschool Delft. Afstudeer Hoogleraar: prof.dr.ir. H.J.Merk
1976 - 1980	wetenschappelijk medewerker aan de Technische Hogeschool Eindhoven, afdeling Natuurkunde, vakgroep Transportfysica

Sinds 1 januari 1981 werkzaam bij Koninklijke/Shell, Exploratie en Produktie Laboratorium te Rijswijk (Z.H.).